Application of shock-unsteadiness model to hypersonic shock/turbulent boundary-layer interaction

A thesis submitted in partial fulfillment of
the requirements for the degree of

Doctor of Philosophy

by

Amjad Ali Pasha
(Roll No. 05401005)

Under the guidance of
Prof. Krishnendu Sinha

Department of Aerospace Engineering
INDIAN INSTITUTE OF TECHNOLOGY–BOMBAY
2011

To my Ammijaan, Abbajaan and family

Thesis Approval

The thesis entitled

Application of shock-unsteadiness model to hypersonic shock/turbulent boundary-layer interaction

by

Amjad Ali Pasha
(Roll No. 05401005)

is approved for the degree of

Doctor of Philosophy

Examiner	Examiner
Guide	Chairman

Date: ____________

Place: ____________

Declaration

I declare that this written submission represents my ideas in my own words and where others ideas or words have been included. I have adequately sited and referenced the original sources. I also declare that I have adhered to all principles of academic honesty and integrity and I have not misrepresented of fabricated or falsified any idea/data/fact/source in my submission. I understand that any violation of the above will be cause for disciplinary action by the institute and can also evoke panel action from the sources which have thus not been properly cited or from whom proper permission has not been taken when needed.

(Signature)
Amjad Ali Pasha
(Name of the student)
Roll No: 05401005
May 2011

Abstract

Interaction of shock waves with turbulent boundary layer plays an important role in the design and operability of high-speed aerospace vehicles and air-breathing engines. The adverse pressure gradient of the shock is often strong enough to separate the boundary layer. Reynolds-averaged Navier-Stokes simulations using conventional turbulence models do not predict the correct size of the separation bubble in strong shock/turbulent boundary-layer interactions. The corresponding surface predictions exhibit large discrepancy with respect to experimental measurements. The inaccuracies are often attributed to the fact that conventional turbulence models do not account for the unsteady effects in shock/turbulent boundary-layer interaction. Sinha *et al.* (Physics of Fluids, 2003) propose a model for the shock-unsteadiness effect, which gives the correct amplification of turbulence kinetic energy in shock/homogeneous turbulence interaction. The shock-unsteadiness modification is also found to improve model prediction in supersonic compression corner flows, especially in the vicinity of separation point.

In the present work, the shock-unsteadiness modification is applied to a series of canonical shock/boundary-layer interactions at hypersonic Mach numbers. The focus is to predict the separation bubble size accurately using shock-unsteadiness corrected one- and two-equation turbulence models. The configurations studied are: (i) two-dimensional oblique shock/boundary-layer interactions at Mach 5, (ii) three-dimensional single-fin configurations at Mach 5 and (iii) axisymmetric cone-flare geometries at Mach of 11 and 13. A detailed description of the mean flowfield is presented for each case and the computed surface data is compared to experimental measurements. The challenges involved in the implementation of shock-unsteadiness model in the presence of multiple shocks and expansion waves is discussed in detail. It is found that a careful implementation of shock-unsteadiness model results in close matching of the shock structure, separation bubble and wall pressure with the experiments. The shock-unsteadiness model is also applied to a two-dimensional practical scramjet inlet, where the geometric variations add to the complexity of the flowfield. The cowl shock interacts with the boundary layer

on the opposite wall and the simulation yields a reliable prediction of the resulting flow separation inside the duct. Overall, the shock-unsteadiness modification is shown to be a valuable tool for simulating shock/boundary-layer interaction in practically relevant geometries at hypersonic Mach numbers.

Keywords : high-speed flows, shock wave, turbulent boundary layer, separation bubble, turbulence modeling, hypersonic, single-fin, scramjet inlet, cone-flare

Contents

Abstract **i**

List of Tables **vi**

List of Figures **vii**

Nomenclature **xvi**

1 Introduction **1**

1.1 Overview . . . 3

1.2 Scope of the work . . . 4

2 Shock/turbulent boundary-layer interaction flows **6**

2.1 Introduction . . . 6

2.2 Supersonic compression corner . . . 7

2.3 Hypersonic cylinder-flare . . . 11

2.4 Oblique shock impingement . . . 14

2.5 Single-fin configuration . . . 18

2.6 Shock-unsteadiness effects . . . 21

2.7 Summary . . . 24

3 Simulation methodology **25**

3.1 Reynolds averaging . . . 25

3.2 Turbulence closure . . . 27

3.2.1 Spalart-Allmaras model . . . 29

3.2.2 k-ω model . . . 29

3.2.3 Boundary-conditions for turbulence models . . . 30

3.3 Numerical method 31

3.4 Conservation form 32

3.5 Steger-Warming method 35

3.6 Modified Steger-Warming method 38

3.7 Second order method 41

3.8 Boundary conditions 43

3.9 Summary 45

4 Shock-unsteadiness model 46

4.1 Introduction 46

4.2 Problem statement 47

4.3 RANS prediction 50

4.4 Shock-unsteadiness correction 53

4.5 Shock-unsteadiness model implementation 58

4.5.1 Shock-unsteadiness modified k-ω model 58

4.5.2 Shock-unsteadiness modified Spalart-Allmaras model 60

4.6 Summary 61

5 Oblique shock-wave/turbulent boundary-layer interaction 62

5.1 Introduction 62

5.2 Test case 63

5.3 Simulation Methodology 63

5.3.1 Grid convergence 64

5.4 Results and discussions 66

5.4.1 Application of shock-unsteadiness modification 68

5.4.2 $\theta = 10^\circ$ and 6° cases 76

5.5 Summary 78

6 Simulation of a practical scramjet inlet 79

6.1 Introduction 79

6.2 Inlet configuration 80

6.3 Computational grid 81

6.4 Simulation methodology 83

6.5 Flowfield and wall data . . . 84
6.6 Comparison of separation bubble size with experiments . . . 89
6.7 Inlet performance parameters . . . 91
6.8 Summary . . . 93

7 Three-dimensional single-fin configuration 94
7.1 Introduction . . . 94
7.2 Test case . . . 94
7.3 Simulation methodology . . . 95
7.4 Flow physics . . . 96
7.5 Comparison of computed wall data with experiments . . . 99
7.6 Summary . . . 104

8 Shock/boundary-layer interaction on a cone-flare geometry 105
8.1 Introduction . . . 105
8.2 Test cases . . . 106
8.3 Simulation methodology . . . 107
8.3.1 Grid refinement study . . . 108
8.4 Simulation results . . . 113
8.4.1 $36°$ flare at Mach 13.1 . . . 113
8.4.2 $36°$ flare at Mach 10.97 . . . 123
8.4.3 $30°$ flare at Mach 12.92 . . . 127
8.4.4 $30°$ flare at Mach 10.98 . . . 130
8.4.5 Heat flux predictions . . . 132
8.5 Summary . . . 133

9 Conclusions 134

A Navier-Stokes equations 137

References 139

Publications/conferences based on present work 149

List of Tables

5.1 Average values of upstream Mach number normal to shock waves M_{1n} and shock-unsteadiness damping factor b_1'. 71

5.2 Comparison of computed separation and reattachment points and separation bubble size with experiments. [a,b]all distances are measured from origin in upstream direction. 75

6.1 Freestream conditions for scramjet inlet simulations. 81

6.2 Comparison of flow parameters between the scramjet inlet simulations and oblique shock impingement cases [14]. 90

6.3 Inlet efficiency parameters for inviscid and viscous simulations of inlet duct. . . 91

7.1 Computed primary separation point S1 and reattachment point R1 compared with the experiments [14] at different x-sections on the flat plate. 102

8.1 Freestream conditions and flare-angles for hypersonic cone-flare configurations. 107

8.2 Shock/boundary-layer characteristics for the cone-flare configuration. The subscripts *1* and *2* correspond to inviscid conditions upstream and downstream of an assumed oblique shock at the cone-flare junction. 114

8.3 Experimental and computed separation shock locations. 123

List of Figures

2.1 (a) Inviscid supersonic flow over compression corner generating an oblique shock at the corner. (b) Viscous flow over compression corner with separation shock, reattachment shock and separation bubble (reproduced from [25]). . . . 8

2.2 Comparison of computed [12] (a) normalized surface pressure (b) skin-friction coefficient along a 24° compression corner at Mach 2.84 obtained using the standard k-ϵ and k-ω models with experimental data [28]. 9

2.3 Comparison of computed [12] (a) normalized surface pressure (b) skin-friction coefficient along a 24° compression corner at Mach 2.84 obtained using the standard Spalart-Allmaras model with experimental data [28]. 9

2.4 (a) Inviscid hypersonic flow over cylinder-flare generating a more inclined oblique shock at the corner. (b) Viscous hypersonic flow over cylinder-flare with separation shock, reattachment shock, shock-shock interaction and separation bubble (reproduced from [39]). 11

2.5 Experimental [42] and computed [6] (a) wall pressure and (b) heat transfer rate for hypersonic cylinder-flare with $M_{\infty} = 7$ and flare angle = 35° using standard two-equation models. 12

2.6 Comparison of computed [50] surface pressure with experiments [22] for hypersonic flare at Mach 7.2 and deflection angle of 33°. 13

2.7 (a) An oblique incident shock from external shock generator impinges on inviscid flow over flat plate and gets reflected. (b) An oblique incident shock from shock generator impinges on boundary layer over flat plate to generate separation shock, reattachment shock, expansion fan and separation bubble. . . 15

2.8 Comparison of computed [32] (a) wall pressure and (b) skin friction for oblique shock/turbulent boundary-layer interaction with experiments [51, 52, 53], for M_∞ = 2.89, deflection angle $\theta = 13°$ and unit Reynolds number $Re_1 = 5.73 \times 10^7 \mathrm{m}^{-1}$. 16

2.9 Comparison of computed [8] surface pressure with experiments [54] for hypersonic oblique shock/turbulent boundary-layer interaction with M_∞ = 11 and deflection angle $\theta = 17.6°$. 17

2.10 Single-fin geometry with fin mounted on flat plate, making an angle of θ with the flow direction. The fin edge generates a planar inviscid shock over the flat plate. 18

2.11 Proposed flow model of Kubota and Stollery [57] for single-fin geometry with deflection angle, θ = $15°$, $Re_{\delta_0} = 5 \times 10^4$ and $M_\infty = 2.3$. 19

2.12 (a) Single-fin flowfield model, proposed by Alvi and Settles [58] for deflection angle = $16°$ and $M_\infty = 2.95$, depicting a lambda shock structure in a cross plane. 19

2.13 Comparison of computed [65] (a) normalized surface pressure and (b) skin friction with fin angle θ = $20°$ and M_∞ = 4, with experiments [59]. 20

2.14 Comparison of computed [65] (a) normalized surface pressure and on plate for fin deflection angle θ = $30.6°$ and M_∞ = 4, with the experiments [60]. 21

2.15 Comparison of computed [12] (a) normalized surface pressure (b) skin-friction coefficient along a $24°$ compression corner obtained using the standard and modified k-ϵ and k-ω models with experimental data [28]. 23

3.1 (a) Two-dimensional control volume used in finite volume formulation, where the grid points are represented by solid circles with small indices of i and j and cell centers are shown by crosses represented by caps indices of I and J. (b) Calculation of normal surface vector $\vec{S}_{i,j+1/2}$. 34

3.2 The conservative variable $U_{I,J}$ at cell center calculated from the fluxes F and G passing through the cell boundaries in the x- and y-directions. 34

3.3 Comparison of computed velocity profile using modified Steger-Warming [85] method (diamond symbols) and Steger-Warming method [13] (square symbols) with Blasius theory [91] (solid line). 39

3.4 Physical interpretation for evaluation of conservative variable at cell-center, using fluxes at cell-interfaces, for the first-order method (reproduced from Hirsch [78]). 40

3.5 Physical interpretation for evaluation of fluxes for the second-order method (reproduced from Hirsch [78]). 42
3.6 Computational domain along with boundary conditions for flat-plate configuration. 44

4.1 Homogeneous isotropic turbulence interacting with a shock-wave with upstream Mach of 2 at particular instant of time [93]. The normal shock is represented by dilatation contours at the center of domain. The positive mean turbulence vorticity contours are depicted by solid lines and negative contours by dash lines. 47
4.2 Schematic sketch of homogeneous isotropic turbulence/shock interaction. $\overline{u}_1$ and $\overline{u}_2$ are the mean uniform velocities and u' and v' are the fluctuating velocities, upstream and downstream of shock. The shock represented by solid line is displaced by x = ξ(y,t) from its mean position (represented by dash line). 48
4.3 Variation of turbulent kinetic energy across a shock wave [11] interacting with homogeneous isotropic turbulence for upstream Mach of 1.29. 49
4.4 Comparison of standard k-ϵ and modified turbulence models results with DNS data across a normal shock-wave. (a) Variation of turbulent kinetic energy k in the streamwise direction at M_1 = 1.29. (b) k amplification at varying Mach numbers. 53
4.5 Homogeneous isotropic turbulence/shock interaction. Enlarged view depicting the velocity diagram with ζ-η co-ordinate system attached to the oblique shock. The normal and tangential components of velocity upstream and downstream of shock are shown. 54
4.6 Variation of $\overline{u'\xi_t}/\overline{u'^2}$ as a function of upstream Mach number predicted by linear analysis [11], used to obtain model parameter b_1. 56
4.7 Comparison of k-amplification with linear analysis [11] for homogeneous turbulence interacting with shock with varying upstream Mach numbers. 57
4.8 Comparison of turbulent kinetic energy with DNS data [11] for homogeneous isotropic turbulence interacting with shock with upstream Mach of 1.29. 57

5.1 Oblique shock-wave/turbulent boundary-layer interaction on a flat plate. (a) Experimental configuration with shock generator deflection angle θ° and (b) computational domain with appropriate boundary-conditions. 63

5.2 Variation in (a) y_2^+ at the wall and (b) skin friction coefficient for deflection angle θ = $14°$ obtained using computational grids with varying wall normal spacing at the flat plate. 65
5.3 Variation of (a) wall pressure and (b) skin friction coefficient for θ = $14°$ with changing number of wall-parallel grid points upstream of origin. 65
5.4 Effect of varying number of wall-normal grid points on computed (a) pressure and (b) skin friction coefficient for θ = $14°$. 66
5.5 Computed (a) normalized mean dilatation (b) pressure and (c) Mach number contours showing different shocks, expansion waves and separation bubble for $\theta = 14°$ and $M_\infty = 5$. 67
5.6 Computed (a) wall pressure and (b) skin friction with $\theta = 14°$ using standard k-ω with $M_\infty = 5$, compared with experiments. 68
5.7 Distribution of (a) normalized mean dilatation and (b) f_s showing different shock regions in $\theta = 14°$ interaction. (c) Points are identified in the shock-waves and upstream Mach number is obtained along the corresponding stream-lines. 69
5.8 Normalized eddy viscosity contours obtained using (a) standard k-ω (b) original shock-unsteadiness [12] and (c) present shock-unsteadiness models for $\theta = 14°$. 72
5.9 Computations showing (a) normalized mean dilatation and (b) pressure contours using shock-unsteadiness modified k-ω model for $\theta = 14°$, compared with (c) experimental shadowgraph and schematic [14]. 73
5.10 Comparison of (a) wall pressure and (b) skin friction coefficient for $\theta = 14°$ computed using standard k-ω and shock-unsteadiness modified k-ω models over a larger domain up to 500 mm downstream of interaction region, compared with experimental data of Schulein [14]. 74
5.11 Normalized eddy viscosity contours obtained using (a) standard k-ω and (b) shock-unsteadiness modified k-ω models downstream of reattachment for $\theta = 14°$. 74
5.12 Normalized eddy viscosity profiles at different stream-wise stations downstream of interaction region computed using (a) standard k-ω and (b) shock-unsteadiness modified k-ω models for $\theta = 14°$. 75

5.13 Computed (a) wall pressure and (b) skin friction coefficient for $\theta = 14^\circ$ using standard k-ω and shock-unsteadiness modified k-ω models with different values of b_1', compared with experiments from Schulein [14]. 76
5.14 (a) Normalized mean dilatation contours computed using shock-unsteadiness modified k-ω model for $\theta = 10^\circ$ and $M_\infty = 5$, compared with (b) experimental shadowgraph from Schulein [14]. 77
5.15 (a) Normalized mean dilatation contours computed using shock-unsteadiness modified k-ω model for $\theta = 6^\circ$ and $M_\infty = 5$, compared with (b) experimental shadowgraph from Schulein [14]. 77
5.16 Computed (a) wall pressure and (b) skin friction coefficient for $\theta = 10^\circ$ at $M_\infty = 5$ using standard k-ω and shock-unsteadiness modified k-ω models, compared with experiments from Schulein [14]. 77
5.17 Computed (a) wall pressure and (b) skin friction coefficient for $\theta = 6^\circ$ at $M_\infty = 5$ using standard k-ω and shock-unsteadiness modified k-ω models. 78

6.1 (a) Geometric configuration with (b) flow schematic, for practical scramjet inlet. 80
6.2 Computational grid with every second point in each direction along with boundary conditions used in forebody. The inset shows enlarged view of the grid in the ramp corner and cowl tip regions. 82
6.3 Computational grid with every second point in each direction for inlet duct along with boundary conditions. 82
6.4 Computed normalized dilatation contours identifying shock regions in cowl region, using standard Spalart-Allmaras model [75] with M_∞ = 6.5. 83
6.5 Computed normalized dilatation contours identifying shock regions using standard Spalart-Allmaras model [75] for isolated oblique shock/boundary-layer interaction with deflection angle of 14° and M_∞ = 5. 84
6.6 Computations showing normalized density contours using (a) standard Spalart-Allmaras model [75] and (b) shock-unsteadiness modified Spalart-Allmaras model [12] for oblique shock/boundary-layer interaction with deflection angle of 14° and M_∞ = 5, compared with (c) experimental shadowgraph [14]. 85
6.7 Computed wall pressure using standard Spalart-Allmaras model [75] and shock-unsteadiness modified Spalart-Allmaras model [12] with deflection angle of 14° and $M_\infty = 5$, compared with experiments [14]. 85

6.8 Computations showing variation of Mach contours in forebody with M_∞ = 6.5. The inset shows the enlarged view of shock-shock interaction region. 86
6.9 Computations showing normalized pressure jump across ramp-1 and ramp-2 shocks in the inviscid region of forebody with M_∞ = 6.5. 87
6.10 Inviscid computations showing normalized pressure contours in inlet duct. . . . 87
6.11 Computations showing (a) normalized pressure and (b) Mach contours in inlet duct using shock-unsteadiness modified Spalart-Allmaras model [12]. 88
6.12 Computed (a) normalized wall pressure and (b) skin friction on vehicle wall of inlet duct using shock-unsteadiness modified Spalart-Allmaras model [12]. . . . 89
6.13 Computed flow variable profiles for inviscid and viscous simulations at exit of inlet duct: (a) velocity (b) Mach number and (c) static pressure. 92

7.1 (a) Three-dimensional single-fin configuration with fin mounted on the flat-plate. The surface measurements [14] were taken along the dashed lines. (b) Computational domain with appropriate boundary conditions. 95
7.2 Flow solution in a single-fin shock/boundary-layer interaction in terms of the computed surface streamlines on the plate. The shock structure is shown by normalized pressure contours at x-sections = 92 mm and 183 mm. 97
7.3 Computed stream-surfaces starting at z/δ_0 = 0.8 and z/δ_0 = 0.25 showing vortex region, and the normalized pressure contours at x-section = 83 mm, as viewed from the downstream direction. 97
7.4 (a) Experimental [106] pictorial diagram for deflection angle $\alpha = 16^\circ$ and $M_\infty = 3.95$. (b) Computed normalized stagnation pressure contours at x-section = 123 mm, for $\theta = 23^\circ$ and $M_\infty = 5$. 98
7.5 (a) Enlarged region of computed (a) pressure contours (b) Mach contours at x-section = 123 mm. 99
7.6 Computed (a) normalized pressure contours overlapped with normalized wall pressure and (b) normalized velocity contours overlapped with skin-friction coefficient, at x-section = 123 mm. 100
7.7 Comparison of computed (a) wall pressure at x-section = 154 mm and (b) skin friction at x-section = 123 mm with experiments [14] using standard Spalart-Allmaras model [75] and modified Spalart-Allmaras model [12]. 101

7.8 Computed normalized eddy-viscosity contours at x-section = 123 mm using (a) standard SA model and (b) shock-unsteadiness modified SA model with c'_{b_1} = -2.0. 101
7.9 Computed (a) surface pressure and (b) skin-friction at different x-sections for single-fin configuration with $M_\infty = 5$ and deflection angle, θ = $8°$. 103
7.10 Variation of computed peak pressures at reattachment point R1 with inviscid shock strength p_2/p_1 compared with experiments [14] for different fin angles θ = $23°$, $18°$, $12°$ and $8°$. 103

8.1 Geometric configuration with flow schematic for hypersonic shock-wave turbulent boundary-layer interaction test cases of Holden [15]. 106
8.2 (a) Computational domain and boundary conditions used in the simulations. (b) A typical computational mesh showing every third point in each direction. Inset shows a magnified view of the cone-flare junction. 108
8.3 Effect of variation in wall-normal spacing on (a) wall pressure and (b) skin friction, using modified Spalart-Allmaras model for $36°$ flare at Mach 13.1. . . 109
8.4 Effect of varying the number of wall-normal grid points on (a) wall pressure and (b) skin friction, using modified Spalart-Allmaras model for $36°$ flare at Mach 13.1. 109
8.5 Effect of varying wall-normal spacing on computed (a) wall pressure and (b) skin-friction coefficient, using modified k-ω model for $36°$ flare at Mach 13.1. . 111
8.6 Effect of varying number of wall-normal grid points on computed (a) wall pressure and (b) skin-friction coefficient, using modified k-ω model for $36°$ flare at Mach 13.1. 111
8.7 Effect of varying wall-parallel grid points on computed (a) wall pressure and (b) skin-friction coefficient, using modified k-ω model for $36°$ flare at Mach 13.1.112
8.8 Shock-wave/boundary-layer interaction on a $36°$ flare at Mach 13.1: (a) experimental schlieren image [15] and (b) computed density contours using standard Spalart-Allmaras model. 115
8.9 Comparison of computed wall pressure with experiments [15] for $36°$ flare at Mach 13.1. The standard Spalart-Allmaras and standard k-ω models are used in the simulations. 116

8.10 (a) Distribution of upstream Mach number, M_1, normalized velocity, U/U_∞ and normalized temperature T/T_∞ in the undisturbed boundary-layer upstream of the shock/boundary-layer interaction region. (b) Variation of shock-normal upstream Mach number M_{1n} and shock-unsteadiness model parameter b_1' in the boundary layer. 117
8.11 Normalized pressure contours showing the shock wave in the interaction region of the 36° flare geometry. A set of points are identified along the shock wave and M_{1n} is calculated using the upstream values along the respective streamlines. 117
8.12 Variation of (a) normalized mean dilatation, S_{ii} and (b) shock-identifying function, f_s showing different shocks and compression waves in the shock/boundary-layer interaction region. 118
8.13 Computed flow pattern using shock-unsteadiness modified Spalart-Allmaras model [12] for 36° flare at Mach 13.1: (a) normalized pressure contours, and (b) magnified view of the reattachment region and (c) normalized density contours. 120
8.14 Schematic sketch of Edney type-VI shock-shock interaction [40]. 121
8.15 Computed wall pressure is compared with experiments [15] for 36° flare at Mach 13.1. Shock-unsteadiness correction [12] applied to (a) Spalart-Allmaras model and (b) k-ω model. 122
8.16 Shock-wave/boundary-layer interaction on a 36° flare at Mach 10.97: (a) experimental schlieren image [15], and computed normalized pressure contours using (b) standard k-ω model and (c) shock-unsteadiness modified k-ω model. . 125
8.17 Comparison of computed wall pressure using (a) standard and (b) shock-unsteadiness modified turbulence models with experimental measurements [15] for 36° flare at Mach 10.97. 126
8.18 Shock-wave/boundary-layer interaction on a 30° flare at Mach 12.92: (a) experimental schlieren image [15], and computed normalized pressure contours using (b) standard k-ω model and (c) modified k-ω model. 128
8.19 Comparison of computed wall pressure using (a) standard and (b) shock-unsteadiness modified Spalart-Allmaras and k-ω turbulence models with experimental measurements [15] for 30° flare at Mach 12.92. 129

8.20 Shock/wave boundary-layer interaction on a $30°$ flare at Mach 10.98: (a) experimental schlieren image [15] and (b) computed density and pressure field using standard Spalart-Allmaras model. 131
8.21 Shock-unsteadiness correction [12] applied to (a) Spalart-Allmaras and (b) k-ω turbulence models. Computed wall pressure is compared with experimental measurements [15] for $30°$ flare at Mach 10.98. 131
8.22 Comparison of computed heat flux using standard and shock-unsteadiness modified k-ω turbulence models with experimental measurements [15] for $36°$ flare at Mach 13.1. 132

Nomenclature

Roman Symbols

A	Jacobian matrix
$\tilde{a}$	Mean speed of sound = $\sqrt{\gamma R\tilde{T}}$
b_1'	Shock-unsteadiness damping parameter
c_{b_1}'	Shock-unsteadiness parameter
C_f	Skin-friction coefficient
C_p	Specific heat at constant pressure
C_v	Specific heat at constant volume
C_μ, c_{b1}, c_{b2}	Model closure coefficients
f_s	Shock-identifying function
F	Flux-vector
e	Specific internal energy, = $C_v\tilde{T}$ for perfect gas
h	Specific enthalpy = $C_p\tilde{T}$ for perfect gas
k	Turbulent kinetic energy
l	Turbulent length scale
M_∞	Free stream Mach number
M_{1n}	Upstream Mach number normal to a shock wave

M_t	Turbulent Mach number, $\sqrt{2k}/\tilde{a}$
P_k	Production of turbulent kinetic energy
Pr	Prandtl number, 0.72 for air
Pr_T	Turbulent Prandtl number, 0.92 (boundary-layer) for air
p	Instantaneous static pressure
P_0	Stagnation pressure
$\overline{p}$	Mean pressure
p_w	Mean wall pressure
q_j	Heat flux vector
q	Turbulent velocity, $\sqrt{2k}$
$\overline{R}$	Universal gas constant equal to 8.314 $\mathrm{kJ/(kgmol.K)}$
R	Characteristic gas constant, for perfect gas air = 287.1 $\mathrm{J/K}$
Re	Reynolds number
Re_1	Unit Reynolds number or Reynolds number per meter length
Re_λ	Reynolds number based on Taylor microscale, λ
s	arc length measured from cone-flare junction
s_{ij}	Instantaneous strain rate tensor
S_{ij}	Mean strain rate tensor
S_{ii}	Mean dilatation
S	Mean strain rate parameter, $S = [2S_{ij}S_{ji} - \frac{2}{3}S_{ii}^2]^{\frac{1}{2}}$
$\overline{t}_{ij}$	Average viscous stress tensor
T_0	Stagnation temperature

$\tilde{T}$	Mean flow temperature
T_w	Mean wall temperature
u_i	Instantaneous velocity in tensor notation, i = x,y,z in Cartesian coordinates
$\overline{u}_i$	Reynolds time average velocity in tensor notation
u_i'	Reynolds fluctuating velocity in tensor notation
$\tilde{u}_i$	i^{th} component of the Favre mean velocity
u_i''	Favre fluctuating velocity in tensor notation
U	Mean velocity in the streamwise direction
U	Conservative variable vector
$\vec{x}$	Position vector in vector notation
y_2^+	Wall-normal distance to the nearest point in wall coordinates

Greek Symbols

α	Turbulence model constant
β, β^*, β_1	Turbulence model constants
θ	Deflection angle, momemtum thickness
δ	Boundary-layer thickness
δ^*	Displacement thickness
δ_{ij}	Kronecker delta function, δ_{ij} = 1 if $i = j$ and δ_{ij} = 0 if $i \neq j$
η	Coordinate normal to shock direction
γ	Specific heat ratio
ϵ	Dissipation rate of turbulent kinetic energy
ω	Specific dissipation of turbulent kinetic energy

κ	von-Karman constant, standard value equal to 0.41
κ_T	Eddy thermal conductivity
Ω_{ij}	Vorticity tensor
μ	Molecular viscosity
μ_T	Turbulent viscosity or eddy viscosity
ν	Kinematic viscosity
ν_T	Kinematic eddy-viscosity
$\overline{\rho}$	Reynolds time average density
τ	Integral time scale
τ_{ij}	Reynolds stress tensor
θ	Momentum thickness
σ, σ^*	Turbulence model constants
ξ_t	Linear shock velocity
ξ(y,t)	Shock displacement from its mean position
ξ_z, ξ_y	Shock distortion
ζ	Dimensionless mean strain rate, S/ω
ζ	Coordinate tangential to shock

Subscript

i, j, k	x, y, z components of vector
n	Normal to shock wave
0	Stagnant conditions
0	Upstream of interaction

w Wall conditions

∞ Free stream conditions

Superscript

$'$ Reynolds fluctuating variable

$''$ Favre fluctuating variable

$\circ$ Angle measurement in degrees

Abbreviations

CFD Computational Fluid Dynamics

CFL Courant-Friedrichs-Lewy

DNS Direct Numerical Simulation

FORTRAN FORmula TRANslation

SA Spalart-Allmaras Turbulence Model

TKE Turbulent Kinetic Energy

RANS Reynolds-averaged Navier-Stokes

Chapter 1

Introduction

High-speed aerospace vehicles, flying at supersonic and hypersonic Mach numbers, generate shock waves. The shocks from different parts of the vehicle interact with the boundary layer on the walls. The abrupt change of flow quantities across a shock result in sever distortion of the boundary layer. If the adverse pressure gradient at the shock is strong enough, it can cause local flow separation and attachment of the boundary layer. The viscous effects in a separated boundary layer are not only confined to near wall region, but flow separation can cause additional shocks, expansion waves and shear layers, and thus can result in significant distortion of the inviscid flowfield around the vehicle.

Shock/boundary-layer interactions are observed in many parts of high-speed aerospace vehicles. For example, deflected control surfaces, intakes of air-breathing engines, wing-body junctions, supersonic combustors, and nozzles. It is common in case of multi-body aerodynamics, where the bow shock from one body can impinge on the boundary layer on the neighboring body surface. Local flow separation in these applications can alter the characteristics of the vehicle. It can also result in reduced performance of engine components. For example, flow separation caused by cowl shock impingement is found to be major concern for inlet unstart of a real-life scramjet engine [1].

At high Reynolds number, the boundary-layer on the vehicle surface is often turbulent. The turbulent fluctuations in a boundary layer get amplified on passing through a shock wave. The interaction of turbulent fluctuations with a shock wave involves complex physical processes, which determine the magnitude of turbulent fluctuations downstream of the shock. The level of turbulence amplification at the shock has a significant effect on shock/boundary-layer interaction, specifically on the extent of flow separation and the peak heating at reattachment.

Reynolds-averaged Navier-Stokes (RANS) methods are usually employed to simulate such flows, where the effect of turbulent fluctuations on the mean flowfield is accounted by using turbulence models. Most of the conventional turbulence models are developed in low-speed flows and they cannot reproduce the complex physical effects involved in shock/turbulence interaction. This puts severe limitation on the accuracy of the computed flow solution in the presence of strong shock waves [2, 3, 4]. The separation bubble size is often predicted incorrectly, and it results in a flow topology that does not match experimental observations. Many modifications have been proposed [5, 6, 7, 8] to extend the low-speed turbulence models to high-speed applications. The modifications are often heuristic and their performance vary from one test case to another.

In a shock-wave/turbulent boundary-layer interaction, the shock wave oscillates about its mean position in response to the unsteady turbulent fluctuations passing through it. The scale of turbulent motion is a function of the boundary layer conditions, like Reynolds number, which in turn is expected to influence the scale of shock motion. Turbulence models used in RANS treat the shock wave as steady, and do not account for the unsteady motion of the shock. This has been pointed out as one of the major limitations of existing turbulence models [2, 9].

Sinha *et al.* [10] study the effect of shock-unsteadiness on turbulence amplification across a shock wave. An additional source term is identified in the turbulent kinetic energy (TKE) equation that is proportional to the correlation of the shock speed and the streamwise velocity fluctuations. An in-phase coupling of the unsteady shock motion with the upstream turbulent fluctuations is found to have a damping effect on TKE amplification. They develop a model for the shock-unsteadiness effect based on results from linear interaction analysis [11]. The new model matches direct numerical simulation data for the evolution of TKE, when a homogeneous isotropic turbulence field interacts with a normal shock. By comparison, standard models like k-ϵ and k-ω, which neglect the shock-unsteadiness damping effect, overly amplify the turbulent kinetic energy across a shock wave.

The shock-unsteadiness modified turbulence models were applied to a canonical shock boundary-layer interaction in a series of compression corner configurations [12]. The implementation was based on identifying the regions of shock and strong compression. The correction was then applied in terms of the local upstream Mach number at a given shock location. The shock-unsteadiness modification was found to result in significant improvement in the size of the separation bubble. The predicted separation bubble size for strong interactions matched with the experimental measurements, and it had negligible effect in case of weak interactions, where the existing model predictions are reasonable. Thus, the correction reproduced the correct trends with varying Mach number that is observed in the experiments. Also, its basis on an important physical phenomena, along with a simple implementation in existing CFD codes, make it appealing to adopt the shock-unsteadiness correction for turbulent high-speed flows dominated by shock waves.

Earlier applications of shock-unsteadiness correction are limited to simple compression corner configurations at supersonic Mach numbers. In this work, the correction is applied to other, more complex configurations at significantly higher Mach numbers to study the following.

1. Assess the performance of the shock-unsteadiness corrected turbulence models in two and three-dimensional shock/boundary-layer interactions.

2. Study the implementation of the shock-unsteadiness correction in the presence of complex shock structure involving multiple shock/expansion waves.

3. Apply the shock-unsteadiness correction to a realistic scramjet intake flow simulation to accurately predict the size of the separation bubble inside the inlet duct.

1.1 Overview

The report is divided into ten chapters. Chapter 2 presents a literature survey on commonly studied canonical shock/boundary-layer interactions. The flow topology is described and available experimental measurements are surveyed. A brief literature survey on evaluation of commonly used one- and two-equation turbulence models in shock-wave/turbulent boundary-layer interactions is discussed. The limitations of standard one- and two-equation turbulence models are documented. The shock-unsteadiness effects in these interactions and its modeling is also presented.

Chapters 3 and 4 describe the simulation methodology. Chapter 3 describes the governing equations and the turbulence models. It also presents the numerical method used in the in-house CFD code. Specifically, the flux-vector splitting algorithm of Steger and Warming [13] is described. The time-integration and boundary-conditions are also presented. The development of shock-unsteadiness model and its evaluation to shock/turbulence interaction is described in

Chapter 4. The implementation of shock-unsteadiness correction to one- and two-equation models is also presented.

Chapters 5, 6, 7 and 8 describe the current research work. The application of shock-unsteadiness model to four shock-wave/turbulent boundary-layer interaction configurations is studied. These include (i) two-dimensional oblique shock impingement, (ii) three-dimensional single-fin, (iii) two-dimensional practical scramjet inlet and (iv) axisymmetric cone-flare. The flow physics details are emphasized and the computed wall data in the interaction region is compared with experimental measurements. The focus is to predict the flowfield topology accurately using the shock-unsteadiness model in these shock/turbulent boundary-layer interactions.

Chapter 9 describes the conclusions based on the research work. The contributions of the current research work are also presented.

1.2 Scope of the work

Chapter 5 presents the two-dimensional interaction of an incident oblique shock with turbulent boundary-layer on flat plate. The shock/boundary-layer interactions at Mach 5, span a range of deflection angles with large flow separation for strong shocks to attached flow for weak shock. A detail description of computed flowfield is presented and the wall data is compared with experiments [14]. Presence of multiple shock waves and flow expansion in the interaction region make it more challenging to implement the shock-unsteadiness correction than earlier compression corner applications. The shock identifying function is appropriately altered and the calculation of the variation of upstream Mach number normal to differnet shocks with varying shock strengths is included in the simulations. The results show that a robust implementation of the shock-unsteadiness model yields significant improvement in prediction of flowfield and wall pressure.

Chapter 6 describes the shock/boundary-layer interaction in a practical inlet. The focus is to study the separation bubble size resulting from the impingement of the cowl shock on the opposite wall. The resulting separation bubble can lead to blockage and inlet unstart, total pressure loss and degrade the quality of flow entering the combustion chamber. The shock-unsteadiness parameter is calibrated to match the experimental separation location closely for a range of oblique shock/boundary-layer interactions presented in Chapter 5, and is used in the simulation of the present inlet duct configuration. Simulations predict a complex flowfield inside a inlet duct including a large separation separation bubble, and multiple shock waves, expansion waves and their reflections. The size of the separation bubble is validated against experimental data of canonical flows.

Chapter 7 describes the computed results of three-dimensional single-fin configuration. The inviscid shock generated by the fin interacts with boundary layer on the adjacent flat plate to form a complex three-dimensional flowfield. The boundary layer separates to a conical vortex. The inviscid shock bifurcates and forms a lambda shock structure, one edge being the separation shock and the other being the rear shock. Application of the shock-unsteadiness correction leads to improved prediction of separation location. The computed surface pressure distribution is also predicted accurately.

Chapter 8 studies computed results for shock/boundary-layer interaction on a cone-flare configuration at Mach 11 and 13. Four test cases are studied which span the range from weak shock strength with no flow separation at the corner to strong shock strength with a large separation bubble at the cone-flare junction. A naturally developing turbulent boundary layer on a long cone interacts with an oblique shock generated at the cone-flare junction to form shock/boundary-layer interaction. A local pressure peak is observed immediately downstream of the reattachment point. This is caused by the interaction of separation shock and reattachment shock in this region. Using the shock-unsteadiness correction the size of the separation bubble and the peak wall pressure compare well with the experimental measurements [15]. This, in turn results in close matching of the shock structure with the experimental shadowgraph.

The above applications show that the shock-unsteadiness model if implemented correctly yields significant improvement in predicting the separation bubble, shock structure and the wall pressure for a range of shock-boundary layer interactions for high Mach numbers.

Chapter 2

Shock/turbulent boundary-layer interaction flows

2.1 Introduction

Shock/boundary-layer interactions occur in many high-speed flow applications. The geometric complexity in a realistic aerospace vehicle makes it difficult to understand and analyze the shock/boundary-layer interactions. The complex configuration can be broken down into simpler geometries, which can isolate different kinds of shock/boundary-layer interactions. These simplified geometries are called canonical configurations. These include compression corner, oblique shock-wave impingement, cylinder-flare, cone-flare and three-dimensional configurations like single-fin, axial corner and double-fin. In these canonical flows, the shock-strength and boundary layer can be controlled by varying flow deflection angles, Mach numbers and Reynolds numbers. Also, both the shock-wave and upstream boundary layer to interaction are clearly characterized in these flows.

The canonical flow geometries have been extensively studied by experimental and computational methods [16, 17, 9, 4, 18]. The articles by Panaras [19], Thivet *et al.* [20], Knight *et al.* [21, 9], Holden *et al.* [22, 23], Arnal and Delery [24, 25], Zheltovodov *et al.* [26, 27], Dussauge *et al.* [18] and Roy *et al.* [4] give insight into the flow physics and surface properties. Experimental schlieren flowfield images, velocity profiles, wall pressure, skin-friction and heat transfer rate measurements are available. As an engineering approach, the computations are performed using Reynolds-averaged Navier-Stokes (RANS) methods. Wide range of turbulence models are used in the computations like zero-equation, one-equation, two-equation and their modified versions to predict flowfield, wall pressure and skin-friction coefficient.

In this chapter, we summarize the experimental and computational studies for shock/boundary-layer interactions in four canonical geometries: compression corner, oblique shock impingement on a flat plate, axisymmetric cylinder-flare and three-dimensional single-fin. The objective is to evaluate the accuracy of the existing computational results. Specifically, we focus on one- and two-equation turbulence models that are most commonly used in practical applications.

2.2 Supersonic compression corner

The two-dimensional compression corner is the simplest case of shock/boundary-layer interaction and is shown in Fig. 2.1. It consists of a flat plate followed by a ramp inclined at an angle of θ with respect to the flow direction. An inviscid supersonic flow over the compression corner generates a single oblique shock at the corner (see Fig. 2.1a) due to flow compression by the ramp surface. In Fig. 2.1b, the shock at the corner interacts with the upstream turbulent boundary layer to from shock/boundary-layer interaction region. The compression corner finds application in many areas, like flap controls, fuselage junctures, and engine inlet, whose study is important from aerodynamic point of view.

The boundary layer on the flat plate experiences an adverse pressure gradient across the shock wave and separates the flow. The streamline showing the extent of separation region is plotted and the separation and reattachment points are identified by S and R. The size between S and R determines the size of the separation bubble. The velocity profile gets reversed in the separation bubble and is plotted in the figure. The separation bubble acts as a blockage to the upstream flow and generates an oblique separation shock at S. The boundary layer goes over the separation bubble to form a free shear layer. As the free shear layer attaches on the ramp, it generates compression waves. The compression waves coalesce to form a reattachment shock. The flow remains subsonic inside the separation bubble.

Experiments [28] have been performed for different compression flow configurations. Flowfield schlieren images, and surface measurements like pressure and skin-friction have been studied. Compression corners with Mach numbers in the vicinity of 2.9 and deflection angles of $8°$, $16°$, $20°$, $24°$ and $25°$ span the range from attached flow to large boundary layer separation. The unit Reynolds number lies in the vicinity of $Re_1 = 7 \times 10^7 \mathrm{m}^{-1}$ for the experiments. These configurations have been computed by different authors [21, 9] using different turbulent models

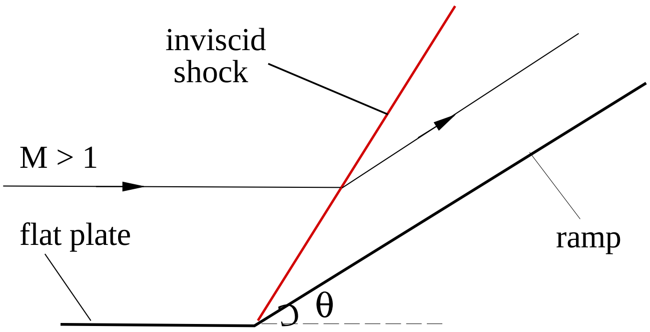

(a)

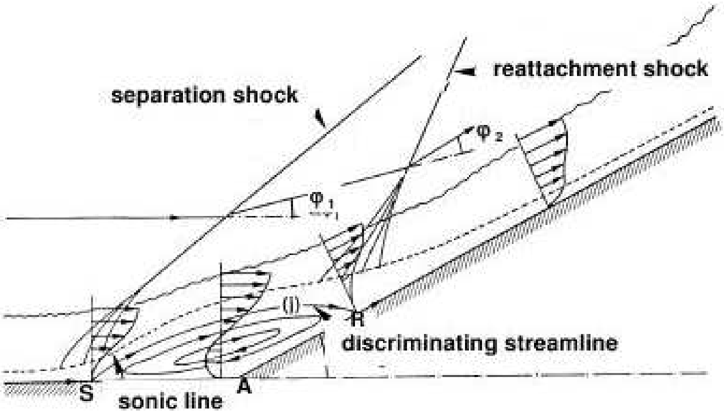

(b)

Figure 2.1: (a) Inviscid supersonic flow over compression corner generating an oblique shock at the corner. (b) Viscous flow over compression corner with separation shock, reattachment shock and separation bubble (reproduced from [25]).

for predicting surface-pressure and skin-friction.

Many researchers have studied for the strong interaction case of $24°$ compression corner at Mach 2.84. The shock/boundary layer interaction results in large flow separation. The normalized surface pressure distribution and skin friction coefficient C_f are shown in Fig. 2.2, where experimental data of Settles *et al.* [28] is also plotted with open circles. The streamwise distance s along the plate and the ramp is normalized by the incoming boundary-layer thickness δ_0, where s = 0 represents the corner. The wall pressure remains constant in the boundary layer before the shock/boundary layer interaction region. The initial pressure rise location is at s/δ_0 = -2. The pressure rises across the separation shock and it remains constant in the plateau region of the separation bubble. Next, it rises further in the reattachment region and remains constant over the ramp surface. The skin friction remains constant up to s/δ_0 = -2 before the interaction region. The C_f drops at s/δ_0 = -2 which is same as initial pressure rise location. There is no experimental data available in the recirculation region and the separation S and reattachment

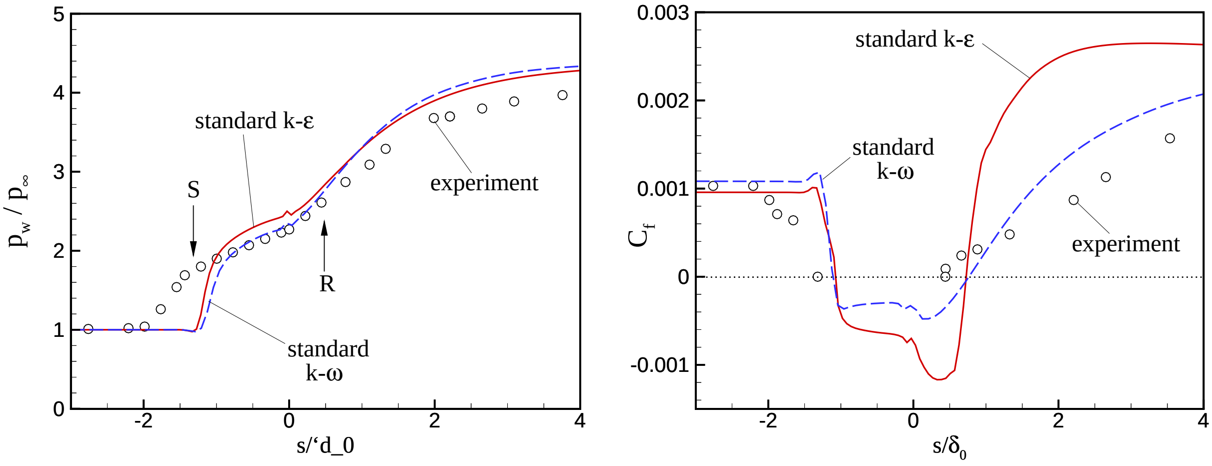

(a) (b)

Figure 2.2: Comparison of computed [12] (a) normalized surface pressure (b) skin-friction coefficient along a $24°$ compression corner at Mach 2.84 obtained using the standard k-ϵ and k-ω models with experimental data [28].

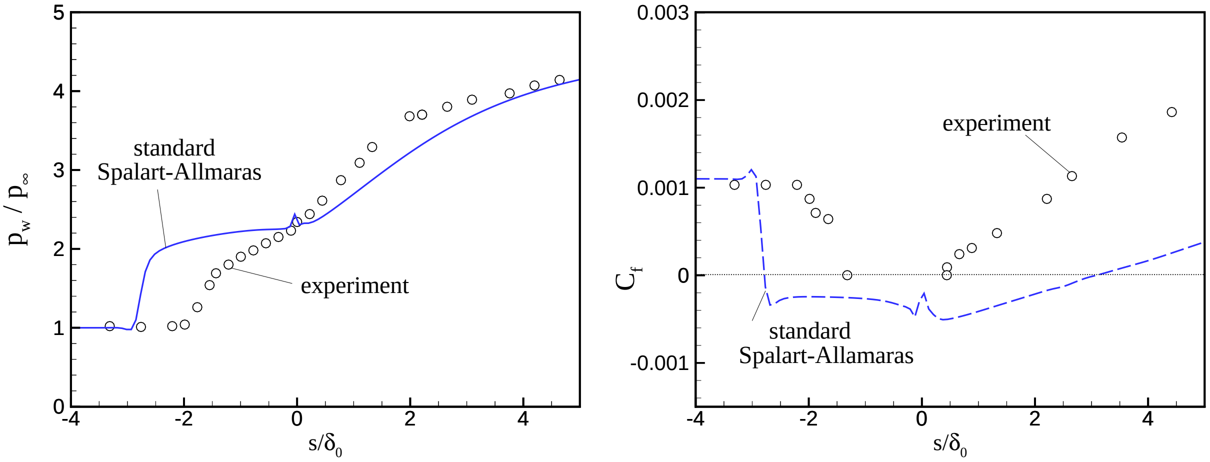

(a) (b)

Figure 2.3: Comparison of computed [12] (a) normalized surface pressure (b) skin-friction coefficient along a $24°$ compression corner at Mach 2.84 obtained using the standard Spalart-Allmaras model with experimental data [28].

points R are marked where C_f = 0. The boundary layer is compressed across the reattachment shock wave and results in a higher skin friction downstream of the reattachment point (s/δ_0 = 0.4).

Computations have been performed by Wilcox *et al.* [29], Coakley *et al.* [6], Haidinger *et al.* [30], Forsythe *et al.* [31], Liou *et al.* [32], Gerolymos *et al.* [33], Sinha *et al.* [12] and Oliver *et al.* [34] for this flow configuration using standard one- and two-equation turbulence models. The computed [12] wall pressure and skin-friction using standard k-ω-88 [35] and

k-ϵ [36] models is shown in Fig. 2.2. Both models predict the separation shock location downstream of the experiment. The reattachment pressure rise on the ramp is also overpredicted by both models. The skin friction plot shows that the models predict a later separation than the experiment. The reattachment location is also downstream of the experimental data. The k-ϵ model overpredicts C_f on the ramp, whereas the k-ω model predictions are higher than the measurements downstream of reattachment. A similar trend is observed by the low-Reynolds number k-ϵ Chein model [37] and k-ω-91 [38] and k-ω-98 [76] models computed by the above researchers.

The computed results in Fig. 2.3 show that the standard Spalart-Allmaras model predicts the separation shock location upstream of the experiment. The pressure plateau is overpredicted and the pressure on the ramp is lower than in the experimental data. The C_f drops earlier (s/δ_0 = 2.7) and reattaches later (s/δ_0 = 3.2) as compared to the experiment. This results in large size of separation bubble. The C_f on the ramp is much lower than the experimental measurement.

Various authors [9] have studied for lower deflection angles of $8°$, $16°$ and $20°$ compared to the above $24°$ case. With the same Mach number of 2.84 and lower deflection angles, the shock strength reduces, hence reduces pressure gradient across the shock wave. The lower pressure gradient reduces the size of the separation bubble. Also, the peak load at reattachment region decreases with reduction in shock strength. In $20°$ deflection angle case, the standard k-ϵ, k-ω and Spalart-Allmaras models show similar trends of wall pressure and skin-friction as observed in $24°$ case. The two-equation turbulence models predict initial pressure rise location downstream. The wall pressure and C_f is high at the reattachment region. Also a small separation bubble is predicted. The standard Spalart-Allmaras model overpredicts the separation bubble size and underpredicts C_f at the reattachment region.

An incipient separation bubble is observed in the $16°$ case. When the flow across the shock wave just begins to separate it results in very small separation bubble size called incipient separation bubble. The pressure variation does not have the distinct pressure plateau in this case as observed in higher ramp angle cases. The standard turbulence models predict wall pressure and skin-friction close to the experiments in this case, but still show higher values of skin friction at reattachment. The flow remains attached and no separation bubble is formed in the weakest interaction case of $8°$. The flowfield and wall data predicted by the standard turbulence models matches well with the experimental data.

2.3 Hypersonic cylinder-flare

The geometry of axisymmetric cylinder-flare shown in Fig. 2.4a is similar to the compression corner. The plate and ramp in compression corner (Fig. 2.1a) correspond to cylinder and flare respectively. The flare makes a deflection angle of θ with the cylinder. The inviscid hypersonic Mach flow over cylinder-flare in Fig. 2.4a causes the shock to be more inclined compared to the supersonic compression corner case (Fig. 2.1a). This is because for the same deflection angle, as the Mach number increases the shock angle decreases. The flow structure in shock boundary layer interaction in cylinder-flare configuration (see Fig. 2.4b) is similar to that of compression corner (see Fig. 2.1b). A separation shock, reattachment shock and separation bubble is formed in the shock/boundary-layer interaction region.

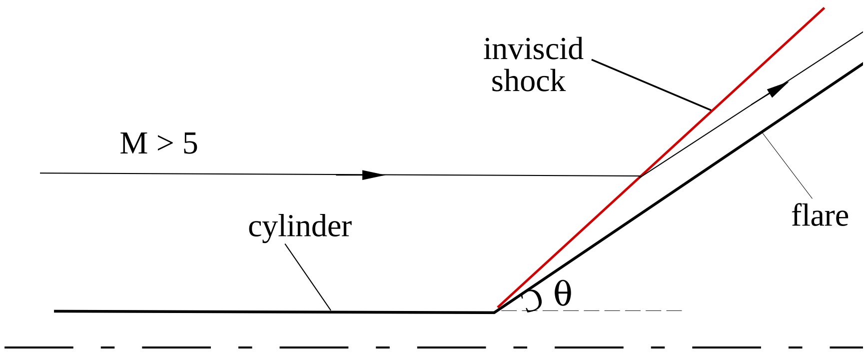

(a)

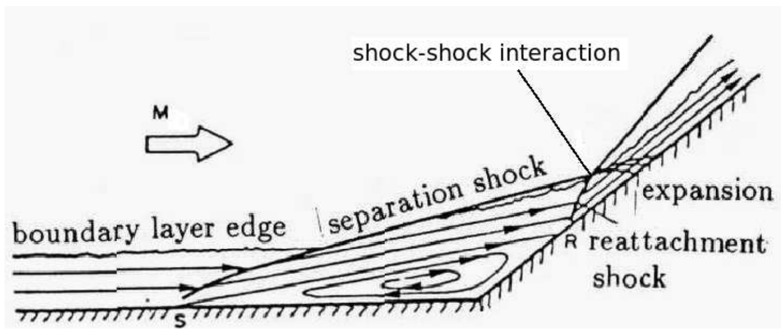

(b)

Figure 2.4: (a) Inviscid hypersonic flow over cylinder-flare generating a more inclined oblique shock at the corner. (b) Viscous hypersonic flow over cylinder-flare with separation shock, reattachment shock, shock-shock interaction and separation bubble (reproduced from [39]).

In hypersonic flows, due to high Mach number there exist some differences in the flow topology as compared to supersonic flows. The high Mach numbers results in stronger shock waves than supersonic cases. The high shock strength and higher pressure gradient results in a large separation bubble. Also, the high Mach numbers generate thicker boundary layer on the

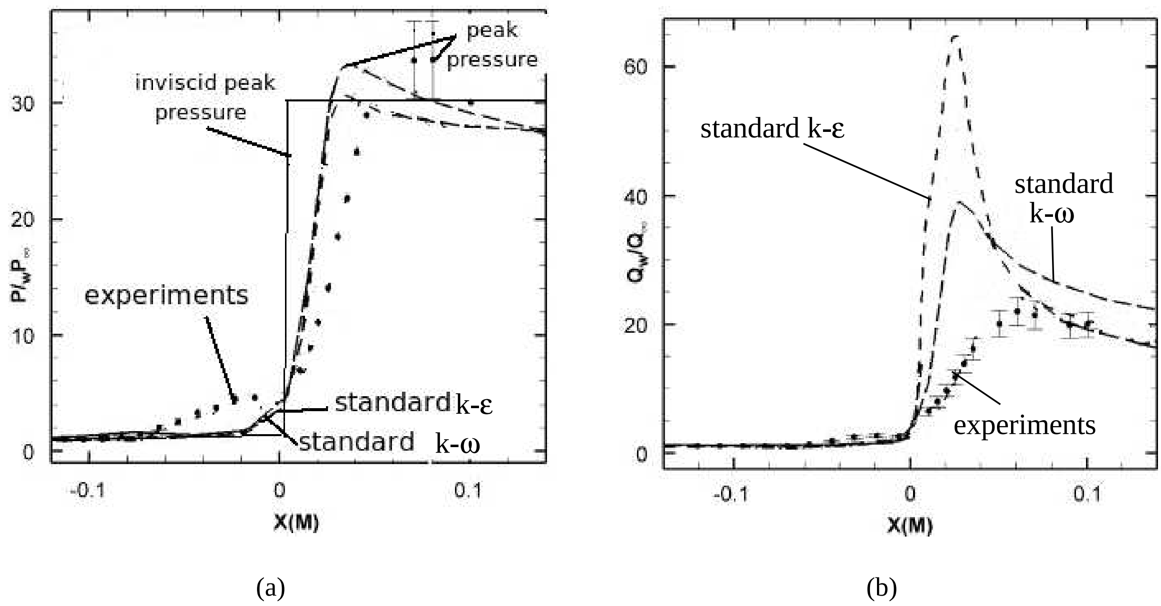

Figure 2.5: Experimental [42] and computed [6] (a) wall pressure and (b) heat transfer rate for hypersonic cylinder-flare with $M_\infty = 7$ and flare angle = $35°$ using standard two-equation models.

upstream of the interaction region. The separation and reattachment shocks are more inclined to the flare surface. The separation shock interacts with the reattachment shock and often forms type VI shock-shock interaction [40]. A shear-layer and an expansion fan is generated at the triple point. This shock-shock interaction affects the wall pressure and heat transfer rate as described below.

Experiments [41, 42] and computations [6, 45, 3, 46] have been performed for different flare angles of $20°$, $27°$, $30°$, $33°$ and $35°$ and Mach numbers in the vicinity of Mach 7 for cylinder-flare configuration. Hypersonic two-dimensional compression corner and axisymmetric cone-flare configurations result in a similar kind of interaction compared to cylinder-flare. Experiments [44, 43, 28] and computations [6, 3] were performed for compression corner with Mach numbers in the vicinity of 7, 8 and 9 with deflection angles of $15°$, $27°$, $30°$, $33°$, $36°$ and $38°$. Also, cone-flare geometries have been studied experimentally [15] and computationally [45, 107, 47, 48] for $6°$ cone angle and flare angles of $30°$ and $36°$ at Mach of 11, 13 and 16. Flowfield schlieren images, and surface measurements like pressure and heat transfer rate measurements have been done. The computations using standard one- and two-equation turbulence models and modified version of these models have been carried.

The normalized wall pressure is shown in Fig. 2.5a for cylinder-flare at $M_\infty = 7$ and flare angle = $35°$. The experimental data [28, 42] is shown by solid circles. There are some key dif-

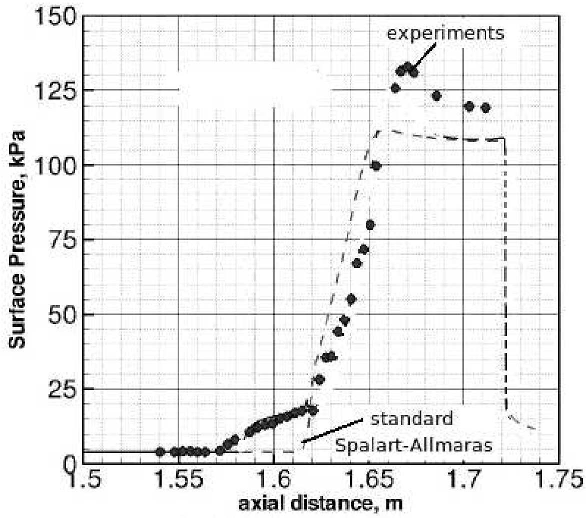

Figure 2.6: Comparison of computed [50] surface pressure with experiments [22] for hypersonic flare at Mach 7.2 and deflection angle of $33°$.

ferences between the current hypersonic shock/boundary-layer interaction case and supersonic compression corner case (see Fig. 2.2). First, the pressure rise across the separation shock is 10 - 20% of the inviscid pressure rise in hypersonic case, whereas in supersonic case the separation shock pressure contributes to 30 - 40% of the overall pressure rise. This is because the separation bubble in hypersonic case is much thinner than the supersonic case and therefore results in a smaller flow deflection and hence a smaller pressure rise. Secondly, the interaction between the separation and reattachment shocks in hypersonic case is more inclined and much closer to the flare surface and causes a local peak in surface pressure in the reattachment region (see Fig. 2.5a). This local peak pressure is not observed in the supersonic compression corner wall pressure (see Fig. 2.2a). The overall pressures in hypersonic cases are always higher compared to supersonic cases. The heat transfer data in Fig. 2.5b also shows a similar variation to skin friction (Fig. 2.2b) in supersonic flows where the standard two-equation k-ϵ and k-ω models show higher values at reattachment point. The standard two-equation versions of k-ϵ and k-ω models in Fig. 2.5b shows peak values of heat transfer at the reattachment point.

Simulations by Huang and Coakley [6] have been done using standard k-ω and k-ϵ turbulence models. The standard k-ϵ-LS [36], k-ϵ-JL [49] and k-ω [35] models predict initial pressure location later than experiments, hence show small separation region. The shock-shock interaction region is predicted upstream. This causes the peak value to underpredict at the reattachment region. Also, the location of the peak pressure is shifted upstream. Later we will see in Chapter 8 that prediction of separation location correctly is important to get the location of peak pressure.

Figure 2.6 shows a comparison of the computed [50] normalized wall pressure with experiments [22], for flare at M_∞ = 7.2 and $\theta = 33^\circ$ The standard Spalart-Allmaras model predicts initial pressure location close to corner, hence predicts negligible separation bubble. The local maxima at reattachment is not predicted. This is because, the separation bubble is negligible and results in no shock-shock interaction, thereby no peak pressure is predicted at reattachment. In Sec. 2.2 we have seen that the standard Spalart-Allmaras model overpredicts the separation bubble in supersonic shock/boundary-layer interaction cases (see Fig. 2.3), whereas in case of hypersonic shock/boundary-layer interaction, the separation bubble size is underpredicted by the same model. The cause for these differences is explained in Sec. 8.4.1.

2.4 Oblique shock impingement

The two-dimensional oblique shock impingement case is shown in Fig. 2.7a with flat plate and an external shock wave generator with deflection angle of θ. The oblique shock impingement case finds application in analysis of internal flows such as air intakes of high speed air-breathing engines. An inviscid supersonic flow over the shock generator produces an incident oblique shock (see Fig. 2.7a). This incident shock impinges on flat plate and is reflected. The shock strength at impingement point is given by the total inviscid pressure rise across the incident shock and the reflected shock. Whereas in case of compression corner (see Fig. 2.1a) the inviscid shock strength is given by the pressure rise across the single oblique shock at the corner. The incident oblique shock (see Fig. 2.7b) interacts with the turbulent boundary layer on the plate and results in a complex flow pattern as explained below.

The adverse pressure gradient across the incident oblique shock causes the boundary layer to separate on flat plate and forms a separation bubble. The separation point (S) and reattachment point (R) are identified in the Fig. 2.7b. An oblique separation shock is generated at S due to the blockage caused by the separation bubble. The interaction of incident shock and separation shock generates additional shocks. The boundary layer turns to form a shear layer over the separation bubble. The shear layer attaches back on the plate and forms compression waves, which coalesce to form a reattachment shock. The correct prediction of separation bubble size determines the correct flow topology in terms of shock angles, strength of shock waves and expansion fan formation.

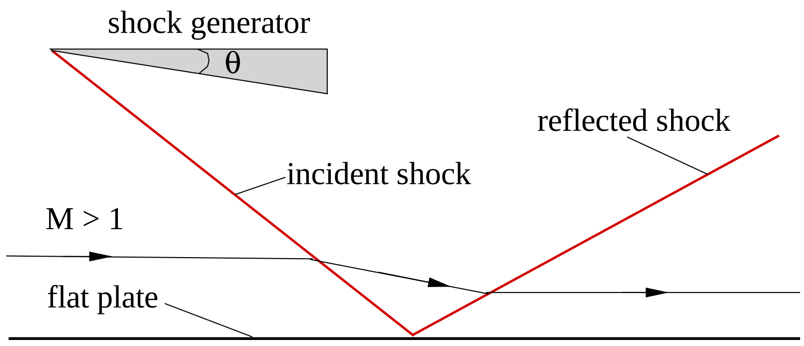

(a)

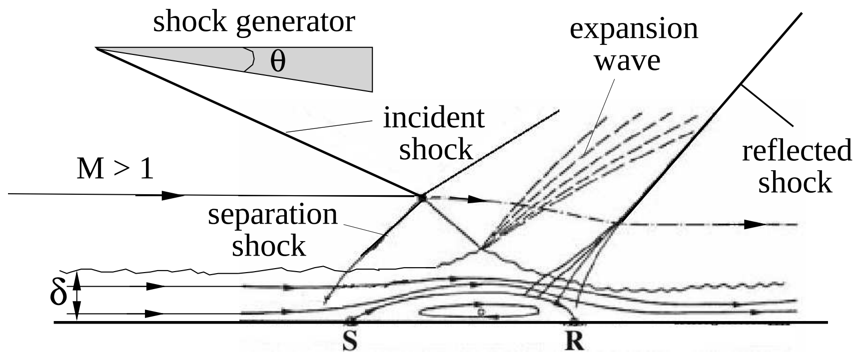

(b)

Figure 2.7: (a) An oblique incident shock from external shock generator impinges on inviscid flow over flat plate and gets reflected. (b) An oblique incident shock from shock generator impinges on boundary layer over flat plate to generate separation shock, reattachment shock, expansion fan and separation bubble.

Experimental [51, 52, 53] investigations were done for different deflection angles of 7°, $10°$ and $13°$ with Mach number in the vicinity of 2.9. The unit Reynolds number $Re_1 = 5.73 \times 10^7 \mathrm{m}^{-1}$ is taken in the experiments. Flowfield schlieren images, wall pressure and skin friction measurements have been carried. These configurations have been computed by different researchers [9] using different turbulent models for predicting surface pressure and skin friction. In general it was observed that the computed wall pressure and skin friction values match closely for lower deflection angles and show large variation for larger angles when compared to experimental data.

Many researchers have computed for the strong interaction case of large flow separation at $13°$ deflection angle and Mach 2.84. The experimental [51, 52, 53] normalized surface pressure and skin-friction coefficient distribution is shown in Fig. 2.8 with open circles. The streamwise distance x along the plate is normalized by the incoming boundary-layer thickness δ_0, where x/δ_0 = 0 represents the location of inviscid shock impingement. The wall pressure remains

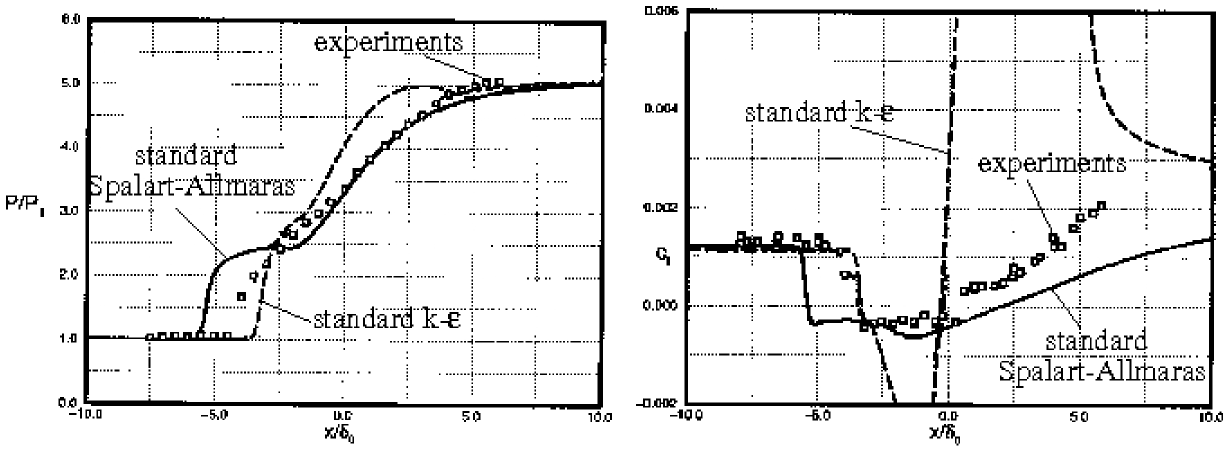

(a) (b)

Figure 2.8: Comparison of computed [32] (a) wall pressure and (b) skin friction for oblique shock/turbulent boundary-layer interaction with experiments [51, 52, 53], for M_∞ = 2.89, deflection angle $\theta = 13°$ and unit Reynolds number $Re_1 = 5.73 \times 10^7 \mathrm{m}^{-1}$.

constant in the boundary layer before the shock/boundary-layer interaction region. The initial pressure rise location is at x/δ_0 = -4. Similar to the compression corner case (Sec. 2.2), the pressure rises across the separation shock and it remains constant in the plateau region of the separation bubble. Next, it rises further in the reattachment region and remains constant in the downstream. The skin friction remains constant up to x/δ_0 = -4 before the interaction region. The C_f drops at x/δ_0 = -4 which is same as initial pressure rise location. The distance between S and R gives the size of the separation bubble. The boundary layer is compressed across the reattachment shock wave and results in a higher skin friction downstream of the reattachment point.

Computations have been performed by Liou *et al.* [32], Haidinger *et al.* [30], Gerolymos *et al.* [33] and Wilcox [8] for this configuration using standard one- and two-equation turbulence models. Some compressibility corrections have been incorporated to these turbulence models, but only a small improvement is observed in flow predictions compared to standard models. The computed [32] wall pressure and skin friction using standard low-Reynolds number k-ϵ Chein [37] model is shown in Fig. 2.8. The separation shock location is predicted downstream of the experiment. The reattachment pressure rise is also overpredicted. The skin friction plot shows that the model predicts later separation than the experiment. The reattachment location is just upstream of the experimental data. The C_f is overpredicted at the reattachment region. A similar trend is observed in the computations using the k-ω-88 [35] model. The standard k-ω model predicts initial pressure rise location downstream, small separation bubble and high

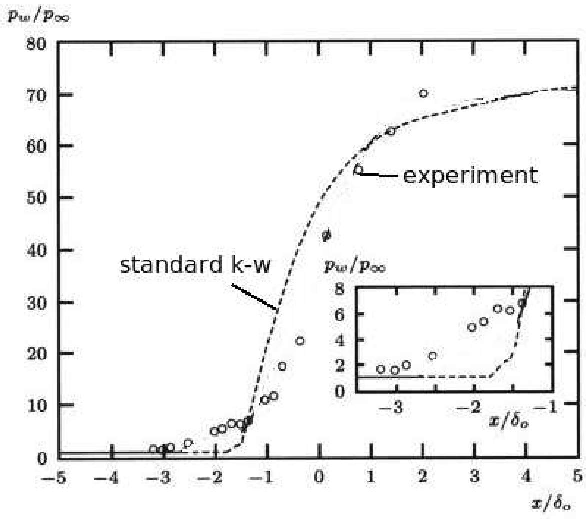

Figure 2.9: Comparison of computed [8] surface pressure with experiments [54] for hypersonic oblique shock/turbulent boundary-layer interaction with M_∞ = 11 and deflection angle $\theta = 17.6°$.

values of C_f at the reattachment region.

The computed results in Fig. 2.8 show that the standard Spalart-Allmaras model predicts the separation shock location significantly upstream of the experiment. The pressure plateau is overpredicted and the pressure downstream of the reattachment region is lower than experimental data. The C_f drops earlier (x/δ_0 = -6) and reattaches later (x/δ_0 = 2.5) as compared to the experiment. This results in a large separation bubble. The C_f at the reattachment region and downstream of it is much lower than the experimental measurement.

In lower deflection angle case of $\theta = 10°$ and M_∞ = 2.89, the low Reynolds number k-ϵ Chein and Spalart-Allmaras models show similar trend to the above $13°$ case. The k-ϵ model predicts small separation bubble and shows high values of C_f downstream of the reattachment region. The Spalart-Allmaras model overpredicts size of the separation bubble and C_f values are underpredicted downstream of the interaction region. The flow remains attached in the weakest interaction case of 7° at Mach 2.89. The k-ϵ Chein and Spalart-Allmaras models matches surface pressure well with the experiments, whereas the C_f variation shows similar trend to the above $10°$ case.

Fig. 2.9 shows the comparison of computed [8] normalized wall pressure for a hypersonic oblique shock/boundary-layer interaction at Mach 11 and $17.6°$, with the experiments [54]. The standard k-ω model [76] shows similar trend to the above supersonic case. The initial pressure rise location is predicted later than experiments and gives a small separation bubble. The small separation bubble results in upstream location of reattachment pressure rise as compared to experiments. In the current case, no local reattachment pressure peak is observed as compared to hypersonic cylinder flare case (see Fig. 2.5a). This is because in the present case there is no interaction of separation shock and reattachment shock. The hypersonic shock impingement with θ = $14°$ and $10°$ at Mach 5 were computed by Lindbad [55] using k-ω [56] and low Reynolds number Chien k-ϵ [37] turbulence models. Similar trend in wall pressure and C_f is observed by these turbulence models as above supersonic and hypersonic cases.

2.5 Single-fin configuration

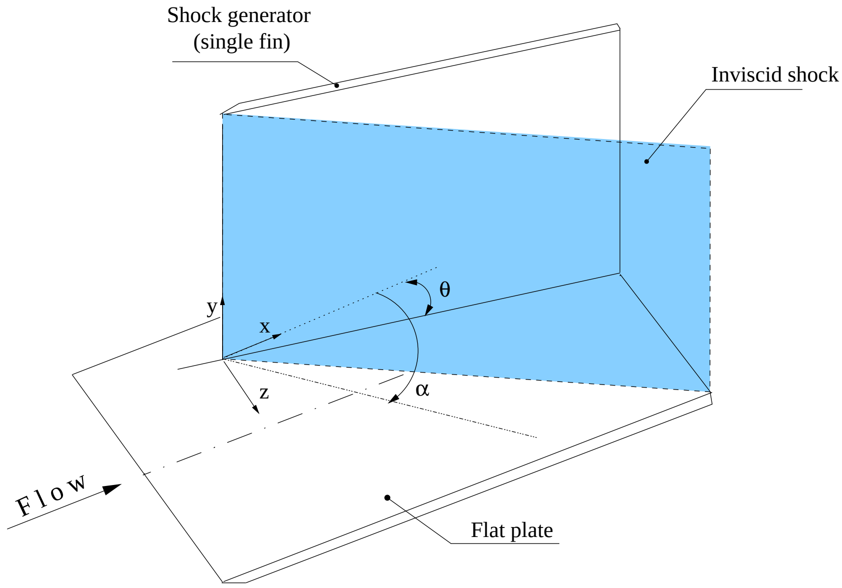

Figure 2.10: Single-fin geometry with fin mounted on flat plate, making an angle of θ with the flow direction. The fin edge generates a planar inviscid shock over the flat plate.

The single-fin configuration is the simplest and most fundamental case of three-dimensional shock/boundary-layer interaction. It consists of a flat plate with a sharp fin mounted perpendicular to it (see Fig. 2.10). An inviscid supersonic flow generates a planar oblique shock at the fin leading edge. The oblique shock wave interacts with the turbulent boundary-layer developed on the plate. The single-fin configuration finds application in inlets of scramjet engine where the cowl acts as a fin. The cowl shock interacts with the side-wall (acts as plate) boundary layer to result in a three-dimensional interaction.

The flowfield generated by a single-fin interaction is shown in terms of the surface streamlines over the plate in Fig. 2.11. The parallel streamlines represent the undisturbed boundary layer. Due to the adverse pressure gradient of the oblique shock wave, the boundary layer sep-

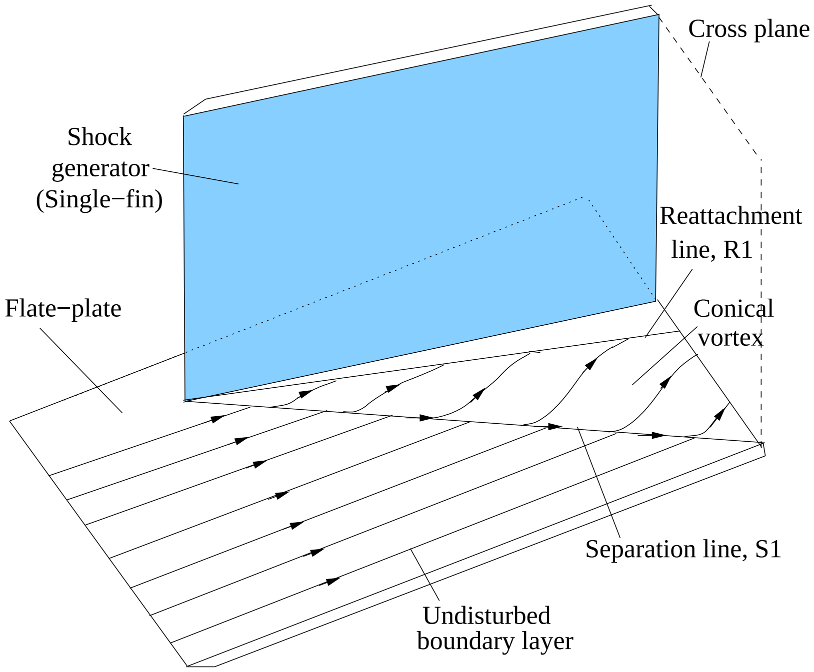

Figure 2.11: Proposed flow model of Kubota and Stollery [57] for single-fin geometry with deflection angle, θ = $15°$, $Re_{\delta_0} = 5 \times 10^4$ and $M_\infty = 2.3$.

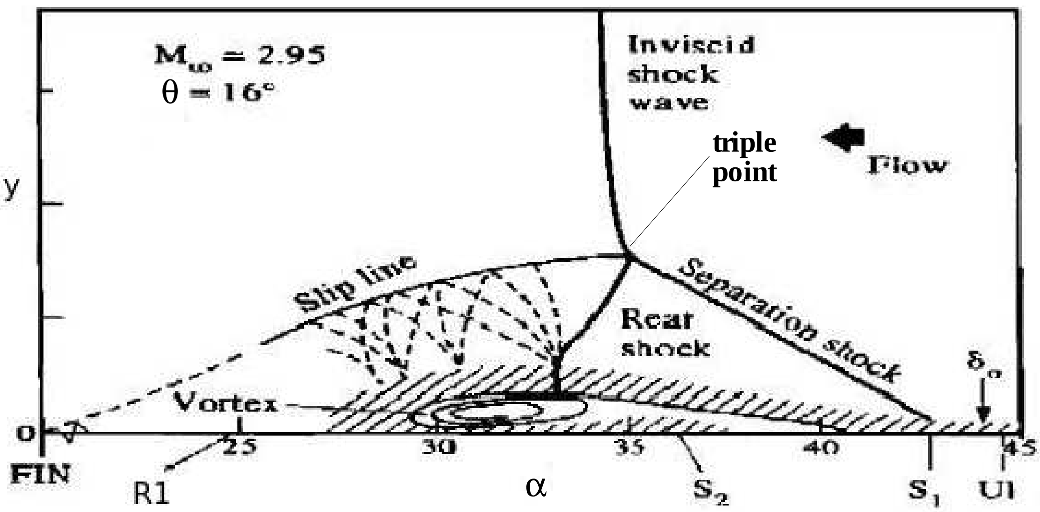

Figure 2.12: (a) Single-fin flowfield model, proposed by Alvi and Settles [58] for deflection angle = $16°$ and $M_\infty = 2.95$, depicting a lambda shock structure in a cross plane.

arates along the separation line S1 and attaches along the reattachment line R1. The region between S1 and R1 corresponds to a conical vortex. The inviscid shock bifurcates and forms a separation shock and a rear shock representing a lambda structure (see Fig. 2.12) in a cross plane perpendicular to the flow direction. The separated conical vortical flow region is formed underneath the lambda shock structure. A slip line is generated from the triple point of intersection of three shock waves and a set of compression and expansion waves are formed between

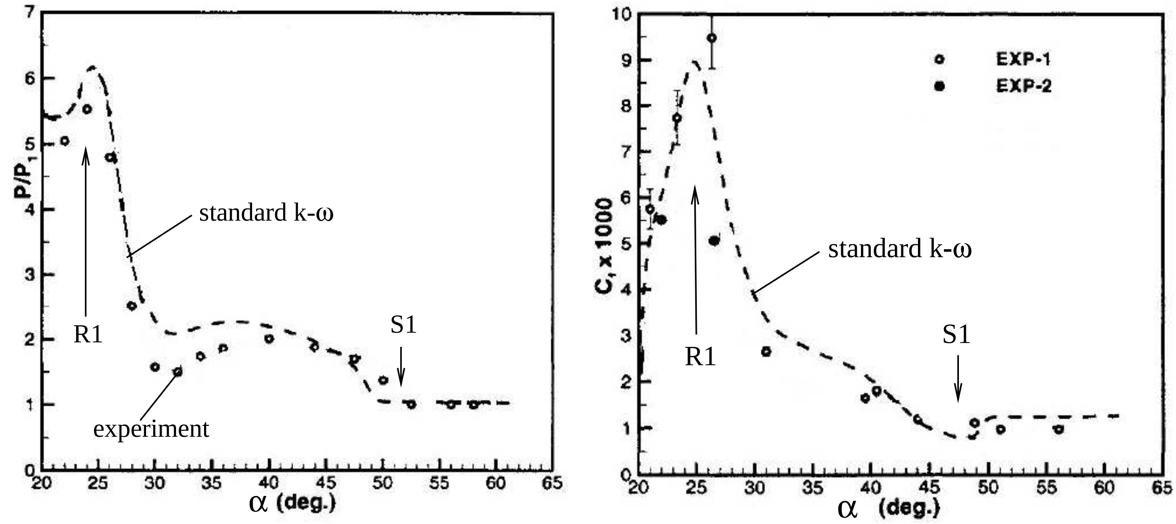

(a) (b)

Figure 2.13: Comparison of computed [65] (a) normalized surface pressure and (b) skin friction with fin angle θ = 20° and M_∞ = 4, with experiments [59].

the shear layer and the slip line.

Experiments [59, 57, 60, 14] have been performed for different configurations with deflection angles of $8°$, $12°$, $15°$, $16°$, $18°$, $20°$, $24°$, $31°$ and Mach numbers in the vicinity of 3, 4, 5 and 8. The Reynolds number based on the boundary-layer thickness upstream of the interaction region lies in the vicinity of 2×10^5 for most of the cases. Surface oil flow patterns, wall pressure and skin friction measurements have been studied. These configurations have been computed by different authors [17, 21, 9, 27] using standard one- and two-equation turbulence models for predicting surface-pressure and skin-friction. Detailed experimental and computational flow-field three-dimensional shock-wave/boundary-layer interaction in single-fin interactions can be found in articles by Settles [63], Degrez [64], Dolling [62], Knight [61] and Panaras [19].

The experimental [59] wall pressure and skin friction variation in a cross plane is shown in Fig. 2.13. The wall data is measured on the plate with varying conical angle α measured from the tip (see Fig. 2.10). α varies from fin surface with $20°$ and spans up to the region of undisturbed boundary layer with its increasing value. The wall pressure remains constant in the undisturbed boundary-layer before the interaction region for $\alpha > 51°$. The wall pressure rises across the separation shock at the primary separation point S1. It remains approximately constant in the conical recirculation region and rises to peak values at the primary reattachment point R1. The C_f shows similar variation to wall pressure.

Figure 2.13 shows computed [65] results for $20°$ at M_∞ = 4. The k-ω model shows a

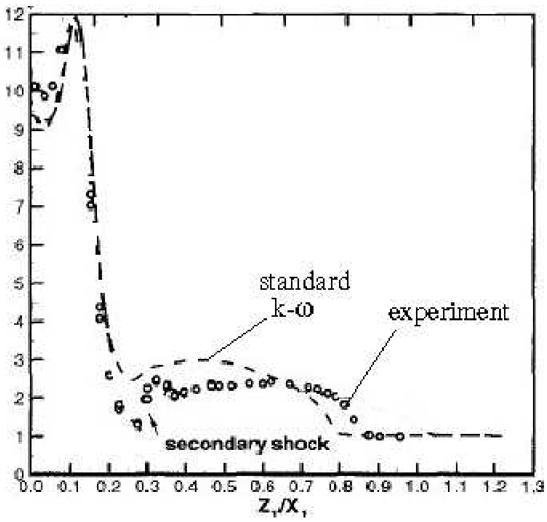

Figure 2.14: Comparison of computed [65] (a) normalized surface pressure and on plate for fin deflection angle θ = $30.6°$ and M_∞ = 4, with the experiments [60].

delayed separation and higher values of wall pressure and C_f in the plateau of conical recirculation region. The standard k-ϵ and Spalart-Allmaras models shows similar trend to k-ω model predictions [17]. Similar trend in wall data is observed by these turbulence models for the weaker interaction case of $15°$ at Mach 3 [17].

The computed [65] wall pressure for $30.6°$ and M_∞ = 4 is compared with experiments [60] in Fig. 2.14. The distance along z-axis (see Fig. 2.10), is normalized with the corresponding x-section distance measured from the fin-tip. The k-ω [35] model shows more delay in separation compared to above $20°$ case (see Fig. 2.13) and other trends are similar. The secondary separation shock in formed in the current case but is is not predicted by the model. The computations [66, 17] were done for higher Mach number = 8 and $15°$ using Spalart-Allmaras model. The SA model predicts separation location downstream of experiments and C_f is underpredicted at the reattachment region.

2.6 Shock-unsteadiness effects

The turbulence flow is inherently unsteady in nature and when interacts with a shock wave makes the shock unsteady. In canonical flows like compression corner, the shock-unsteadiness has been observed experimentally by many researchers [9]. In supersonic compression corner flows, shock deformation was observed by Zheltovodov *et al.* [67, 68] using Schlieren images and hot wire anemometer and shock-unsteadiness was observed by Dolling *et al.* [69] by measuring wall pressure fluctuation time history. Andreopoulos *et al.* [70] experimentally investigate for possible mechanism of shock-unsteadiness in compression corner flow. In their finding they observe that shock velocity is of the order of turbulence fluctuation. It is suggested that the fluctuations in the upstream boundary layer is the cause for triggering shock wave oscillation. The particle image velocimetry measurements by Beresh *et al.* [71] show that upstream turbulence in boundary layer is responsible for shock-unsteadiness in compression corner at Mach 5. Qualitatively it was based on the physical principle that a fuller velocity profile with positive velocity fluctuations imparts increased resistance to separation to the boundary layer and hence causes downstream shock motion, and a less-full velocity profile with lower resistance to separation causes upstream shock motion.

The Reynolds-averaged Navier-Stokes (RANS) simulations are based on time averaged quantities. They calculate the mean flow and take the average effect of fluctuating turbulence on mean flow. RANS simulations of shock/boundary-layer interaction, for example, a compression ramp flow, results in a steady mean shock at the corner. Unsteadiness shock motion is not captured in the simulations. The conventional turbulence models have no mechanism to include the shock-unsteadiness effect on the mean flow. This is argued [9, 72] to be a major limitation of RANS models which result in significant deficiency in predicting shock/boundary-layer interaction flowfields, as described in earlier Sections.

Sinha *et al.* [10] were the first to model the shock-unsteadiness in the RANS framework. The turbulent kinetic energy transport equation was derived in the reference frame of the unsteady shock. This equation includes a term corresponding to the shock-unsteadiness effect. The unclosed term is modelled using theoretical analysis and the results were evaluated with DNS data. The shock-unsteadiness term is found to have a damping effect on turbulent kinetic energy amplification and including this effect accurately predicts k-amplification across shock wave. The shock-unsteadiness correction is incorporated in standard one-/two-equation turbulence models.

The shock-unsteadiness modification is applied to k-ϵ and k-ω models to compression corner configuration with 24° at Mach 2.84. In Sec. 2.2, we have seen that the location of separation shock predicted by standard k-ϵ and k-ω models is much downstream when compared to experimental data. The pressures and C_f deviate from measurement near the separation point. An important improvement observed by modification, is in the vicinity of separation zone, where the lower amplification of turbulent kinetic energy is predicted and also it is observed that the

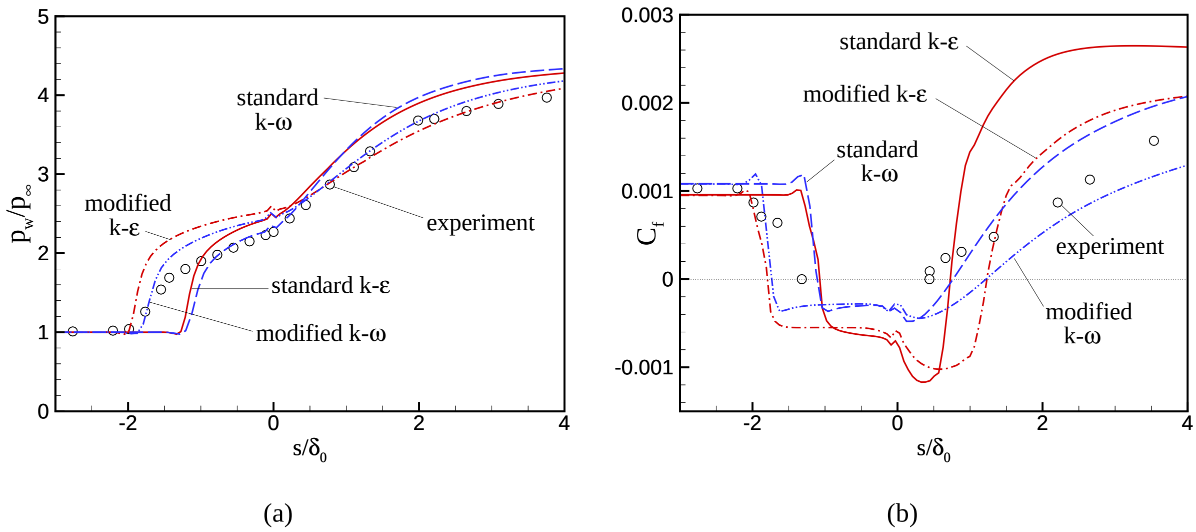

Figure 2.15: Comparison of computed [12] (a) normalized surface pressure (b) skin-friction coefficient along a 24° compression corner obtained using the standard and modified k-ϵ and k-ω models with experimental data [28].

shock unsteadiness modification moves the separated shock upstream and predicts the separation point closer to experiment. The separation pressure rise at s/δ_0 = -2 and the drop in C_f matches experiment (Fig. 2.15). It is also observed that both the modified models show very good agreement with pressure over the ramp. The modification also reduces C_f on reattachment, which brings the RANS predictions closer to experiment.

Simulations using modified Spalart-Allmaras model of Sinha *et al.* [10] shows improvement in the prediction of separation point than standard Spalart-Allmaras model. Figure 2.3 shows that the Spalart-Allmaras model predicts separation point upstream of experiments. The modified Spalart-Allmaras model predicts the separation point downstream, close to experiments, the reason for this is the model predicts higher eddy viscosity across the separation shock.

The new Wilcox k-ω model [8] and realizable corrected models [73, 74] in above sections also dampens the turbulent kinetic energy across the shock wave. Hence, show improvement in size of the separation bubble. But often, these models are based on heuristic methods and it is unclear how these corrections improve for different Mach numbers and flow configurations. The shock unsteadiness model of Sinha *et al.* [10] has evolved by considering the effect of flow physics of shock-unsteadiness and is based on analytical reasoning. This is why we have chosen to use the shock-unsteadiness model to apply for different shock/boundary-layer configurations in our work.

2.7 Summary

In this chapter, we study the performance of turbulence models, applied to different canonical configurations of shock/turbulent boundary-layer interactions. These include compression-corner, hypersonic cylinder-flare, oblique shock impingement and single-fin. Different Mach numbers and deflection angles are considered which span the range of strong interactions with flow separation to weak interactions with attached flow. Correct prediction of the separation bubble size in shock/turbulent boundary-layer interactions is essential to obtain the correct flow-field topology and wall data. Predicting the correct size of separation bubble is also critical for many high speed flow applications like supersonic inlets.

It is found that standard one- and two-equation turbulence models cannot predict the size of the separation bubble correctly for strong shocks. This may be because of the fact that the standard turbulence models do not account for the shock-unsteadiness effects that are inherent in shock/turbulent boundary-layer interactions. The shock-unsteadiness modification of Sinha *et al.* [10] has shown significant improvement in the prediction of separation bubble size for the range of deflection angles and Mach numbers in compression corner flows. Unlike other modifications which are often based on heuristic methods, the shock-unsteadiness modification is based on physics and theoretical analysis. Also, the shock-unsteadiness model is simple to implement and therefore is appealing to use for computing different shock/turbulent boundary-layer interactions.

Chapter 3

Simulation methodology

This chapter describes the conservation equations and boundary conditions for three-dimensional flow of a compressible fluid. This is followed by the numerical method for solving the governing equations.

3.1 Reynolds averaging

Turbulent motion comprises of mean and fluctuating parts. Conservation equations for mean part is written and they have terms containing the effect of fluctuations. One of the most commonly adapted approaches in turbulence applied for incompressible flows is called Reynolds averaging and that which is applied for compressible flows is called Favre averaging.

In Reynolds averaging the instantaneous variables are time averaged to get mean variables. The governing equations for instantaneous variables is presented in Appendix A. For statistically steady and stationary incompressible turbulence flow, the instantaneous variables are written as,

$$u_i(\vec{x},t) = \overline{u}_i(\vec{x}) + u_i'(\vec{x},t)$$
$$\overline{u}_i(\vec{x}) = \lim_{T\to\infty} \frac{1}{T}\int_t^{t+T} u_i(\vec{x},t)dt \tag{3.1}$$

where $u_i(\vec{x},t)$, $\overline{u}_i(\vec{x})$ and $u_i'(\vec{x},t)$ are instantaneous velocity, time average velocity and fluctuating velocity respectively. The instantaneous variables for velocity, density, pressure and temperature are written in shorthand as,

$$
\begin{aligned}
u_i &= \overline{u}_i + u_i' \\
\rho &= \overline{\rho} + \rho' \\
p &= \overline{p} + p' \\
T &= \overline{T} + T'
\end{aligned}
\tag{3.2}
$$

In Favre averaging the instantaneous variables are mass weighted averaged. For statistically steady and stationary compressible turbulence flow, the instantaneous variables are written as,

$$
\begin{gathered}
u_i(\vec{x},t) = \tilde{u}_i(\vec{x}) + u_i''(\vec{x},t) \\
\tilde{u}_i(\vec{x}) = \tfrac{1}{\bar{\rho}} \lim_{T\to\infty} \tfrac{1}{T} \int_t^{t+T} \rho(\vec{x},t) u_i(\vec{x},t) dt
\end{gathered}
\tag{3.3}
$$

where $\tilde{u}_i(\vec{x})$ and $u_i''(\vec{x},t)$ are mass weighted average velocity and fluctuating velocity. In shorthand, instantaneous variables for velocity, density, pressure, temperature, specific enthalpy and specific internal energy are written as,

$$
\begin{aligned}
u_i &= \overline{u}_i + u_i'' \\
\rho &= \overline{\rho} + \rho' \\
p &= \overline{p} + p' \\
T &= \tilde{T} + T'' \\
h &= \tilde{h} + h'' \\
e &= \tilde{e} + e''
\end{aligned}
\tag{3.4}
$$

The variables with overline, tilde, single prime and double prime represent the Reynolds average, Favre average, Reynolds fluctuating and Favre fluctuating variables respectively.

The Favre average conservation law of mass, momentum and energy for steady, stationary and compressible turbulent flow can be derived by time averaging Eqs. A.1, A.2 and A.3 and are stated as,

$$
\frac{\partial \overline{\rho}}{\partial t} + \frac{\partial}{\partial x_i}(\overline{\rho}\tilde{u}_i) = 0 \tag{3.5}
$$

$$
\frac{\partial}{\partial t}(\overline{\rho}\tilde{u}_i) + \frac{\partial}{\partial x_j}(\overline{\rho}\tilde{u}_i\tilde{u}_j) = -\frac{\partial \overline{p}}{\partial x_i} + \frac{\partial(\bar{t}_{ij} - \tau_{ij})}{\partial x_j} \tag{3.6}
$$

$$
\begin{aligned}
\frac{\partial}{\partial t}(\overline{\rho}\tilde{E}) + \frac{\partial}{\partial x_j}(\overline{\rho}\tilde{u}_j\tilde{H}) = & -\frac{\partial}{\partial x_j}(q_{L_j}) - \frac{\partial}{\partial x_j}(q_{T_j}) + \frac{\partial}{\partial x_j}(\tilde{u}_i\bar{t}_{ij}) + \frac{\partial}{\partial x_j}(\tilde{u}_i\tau_{ij}) \\
& -\frac{\partial}{\partial x_j}\overline{\rho u_i'' u_i'' u_j''} + \frac{\partial}{\partial x_j}\overline{(t_{ij}' u_i')} + \frac{\partial}{\partial x_j}\bar{t}_{ij}\overline{u_i''}
\end{aligned}
\tag{3.7}
$$

Here $\tilde{E}$ and $\tilde{H}$ represent the total energy and total enthalpy which are given as,

$$\tilde{E} = \tilde{e} + \frac{1}{2}\tilde{u}_i\tilde{u}_i + k \tag{3.8}$$

$$\tilde{H} = \tilde{h} + \frac{1}{2}\tilde{u}_i\tilde{u}_i + k \tag{3.9}$$

$$\tilde{e} = C_v\tilde{T} \tag{3.10}$$

$$\tilde{h} = \tilde{e} + \bar{p}/\bar{\rho} \tag{3.11}$$

where,

$$k = \frac{1}{2}\frac{\overline{\rho u_i'' u_i''}}{\overline{\rho}} \tag{3.12}$$

is the turbulent kinetic energy. The LHS terms of Eqs. 3.5, 3.6 and 3.7 represent the transient and convective transport terms. The first term in the RHS of Eq. 3.6 represents the pressure force and the second and and third term represent forces due to average viscous stress $\bar{t}_{ij}$ and Reynolds stresses τ_{ij}, which are given as

$$\bar{t}_{ij} = 2\mu(S_{ij} - \frac{1}{3}S_{kk}\delta_{ij}) \tag{3.13}$$

$$\tau_{ij} = -\overline{\rho u_i'' u_j''} \tag{3.14}$$

The first and second terms on RHS of Eq. 3.7 represent the conduction heat flux and turbulent heat flux. The conduction heat flux is calculated from Fourier's assumption of heat conduction which is given as

$$q_{L_j} = -\frac{\mu}{Pr_L}\frac{\partial\tilde{h}}{\partial x_j} = -\frac{\mu C_p}{Pr_L}\frac{\partial\tilde{T}}{\partial x_j} = -\kappa\frac{\partial\tilde{T}}{\partial x_j} \tag{3.15}$$

and the turbulent heat flux vector is defined as,

$$q_{T_j} = \overline{\rho u_j'' h''} \tag{3.16}$$

In terms of mean variables the equation of state for perfect gas is expressed as

$$\overline{p} = \overline{\rho}R\tilde{T} \tag{3.17}$$

The above equations can be solved to obtain the mean flow variables, but these equations are not closed as described below.

3.2 Turbulence closure

As Favre averaging is done, it introduces new turbulent terms in the mean flow equations, which need to be modeled to close them. As there are 6 equations i.e. one continuity, three momentum, one energy and one perfect gas equation. In these equations there are six unknown mean variables; $\tilde{u}_i$, $\overline{\rho}$, $\overline{p}$, $\tilde{T}$ and additional turbulent terms like Reynolds stress terms in momentum equation 3.6 and turbulent heat flux term in energy equation 3.7, which need to be calculated. These turbulent terms are modeled in terms of turbulent and mean variables which can be solved, thus closing the problem i.e. satisfying the requirement of equality of number of equations and number of unknowns.

The ‘n-equation’ turbulent model means that n turbulent transport equations, in addition to mean conservation equations of mass, momentum and energy. Some of the examples are zero, one and two equation turbulent models. All of these models use the Boussinesq assumption [76], which states that the turbulent shear stress is linearly related to the mean strain rate and is given by the following expression.

$$\tau_{ij} = -\overline{\rho u_i'' u_j''} = 2\mu_T \left(S_{ij} - \frac{1}{3}\frac{\partial \tilde{u}_k}{\partial x_k}\delta_{ij} \right) - \frac{2}{3}\overline{\rho} k \delta_{ij} \tag{3.18}$$

where μ_T is the turbulent or eddy viscosity and S_{ij} is the Favre averaged strain rate expressed in terms of mean variables as,

$$S_{ij} = \frac{1}{2}\left[\left(\frac{\partial \tilde{u}_i}{\partial x_j} \right) + \left(\frac{\partial \tilde{u}_j}{\partial x_i} \right) \right] \tag{3.19}$$

The turbulent heat flux vector is modeled as,

$$q_{T_j} = \overline{\rho u_j'' h''} = -\frac{\mu_T}{Pr_T}\frac{\partial \tilde{h}}{\partial x_j} = -\frac{\mu_T C_p}{Pr_T}\frac{\partial \tilde{T}}{\partial x_j} = -\kappa_T \frac{\partial \tilde{T}}{\partial x_j} \tag{3.20}$$

Here the turbulent Prandtl number is defined as $Pr_T = (\mu_T C_p)/\kappa_T$, where μ_T is eddy viscosity and κ_T is turbulent conductivity, Pr_T = 0.9 is used in turbulent boundary layer flows and a value of 0.7 is used for free shear flows. The third and fourth terms in Eq. 3.7 RHS represent the work done due to viscous stresses and work done due to turbulent stresses. The fifth and sixth terms represent the turbulent transport of turbulent kinetic energy and viscous diffusion of turbulent kinetic energy and are modeled as,

$$\overline{\rho u_i'' u_i'' u_j''} = \mu_T \frac{\partial k}{\partial x_j} \tag{3.21}$$

$$\overline{(t_{ij}' u_i')} = \mu \frac{\partial k}{\partial x_j} \tag{3.22}$$

The last term is due to compressible effects and is neglected.

In the above Eqs. 3.18, 3.20, 3.21, and 3.22 we need to calculate μ_T and k for which we use turbulence models like zero, one and two equation, which are discussed below.

3.2.1 Spalart-Allmaras model

In one equation Spalart-Allmaras or SA Model [75] the eddy viscosity ν_T is related to the intermediate variable, $\tilde{\nu}$ by a damping function, f_{v1} as $\nu_T = \tilde{\nu} f_{v1}$, and the equation for $\tilde{\nu}$ is written as,

$$\frac{\partial \tilde{\nu}}{\partial t} + \frac{\partial \tilde{\nu}\tilde{u}_j}{\partial x_j} = c_{b1}\tilde{S}\tilde{\nu} - c_w f_w \left(\frac{\tilde{\nu}}{d}\right)^2 + \frac{1}{\sigma}\frac{\partial}{\partial x_k}\left[(\nu + \tilde{\nu})\frac{\partial \tilde{\nu}}{\partial x_k}\right] + \frac{c_{b2}}{\sigma}\frac{\partial \tilde{\nu}}{\partial x_k}\frac{\partial \tilde{\nu}}{\partial x_k} \tag{3.23}$$

In shorthand this is written as,

$$\frac{D\tilde{\nu}}{Dt} = \mathrm{Prod}(\tilde{\mathrm{S}}, \tilde{\nu}, \mathrm{d}) - \mathrm{Dest}(\tilde{\nu}, \mathrm{d}) + \frac{1}{\sigma}\left[\nabla.((\nu + \tilde{\nu})\nabla\tilde{\nu}) + \mathrm{c_{b2}}(\nabla\tilde{\nu})^2\right] \tag{3.24}$$

Here,

$$f_w = g\left[\frac{1 + c_{w3}^6}{g^6 + c_{w3}^6}\right], \quad f_{v1} = 1 - \left[\frac{\chi^3}{\chi^3 + c_{v1}^3}\right], \quad f_{v2} = 1 - \frac{\chi}{1 + \chi f_{v1}} \tag{3.25}$$

where,

$$\chi = \frac{\tilde{\nu}}{\nu}, \quad g = r + c_{w2}(r^6 - r), \quad r = \frac{\tilde{\nu}}{\tilde{S}\kappa^2 d^2}, \quad \tilde{S} = \bar{S} + \frac{\tilde{\nu}}{\kappa^2 d^2} f_{v2} \tag{3.26}$$

d is the normal distance from the wall and the vorticity magnitude is represented as $\bar{S} = \sqrt{2\Omega_{ij}\Omega_{ij}}$, in which the rotation tensor is given as $\Omega_{ij} = \frac{1}{2}\left[(\partial\tilde{u}_i/\partial x_j) - (\partial\tilde{u}_j/\partial x_i)\right]$ and the constants are given as $c_{b1} = 0.1355$, $c_{b2} = 0.622$, $c_{v1} = 7.1$, $\sigma = 2/3$, $\kappa = 0.41$, $c_{w1} = c_{b1}/\kappa^2 + (1 + c_{b2})/\sigma$, $c_{w2} = 0.3$, $c_{w3} = 2$.

The terms on the LHS of Eq. 3.23 represent the transport terms. The first and second terms on RHS of Eq. 3.23 represent the production and destruction of eddy viscosity. The last two terms on RHS represent the molecular and eddy diffusivity terms. The quantities embraced within them represents the major variables dependency of these source terms.

3.2.2 k-ω model

In two-equation k-ω turbulence model by Wilcox [76], the turbulent kinetic energy k and the specific dissipation rate of turbulent kinetic energy ω are calculated from conservation equations where $\omega = \epsilon/k$. The eddy viscosity is given by,

$$\mu_T = \overline{\rho}k/\omega \tag{3.27}$$

In the Eq. 3.27, k and ω are found from their modeled governing equations by

$$\frac{\partial(\overline{\rho}k)}{\partial t} + \frac{\partial(\overline{\rho}\tilde{u}_j k)}{\partial x_j} = \tau_{ji}\frac{\partial \tilde{u}_i}{\partial x_j} - \beta^*(\overline{\rho}k)\omega + \frac{\partial}{\partial x_j}\left[\mu\frac{\partial k}{\partial x_j}\right] + \frac{\partial}{\partial x_j}\left[(\sigma^*\mu_T)\frac{\partial k}{\partial x_j}\right] \tag{3.28}$$

$$\frac{\partial(\overline{\rho}\omega)}{\partial t} + \frac{\partial(\overline{\rho}\tilde{u}_j\omega)}{\partial x_j} = \alpha\frac{\omega}{k}\tau_{ji}\frac{\partial \tilde{u}_i}{\partial x_j} - \beta\overline{\rho}\omega^2 + \frac{\partial}{\partial x_j}\left[\mu\frac{\partial \omega}{\partial x_j}\right] + \frac{\partial}{\partial x_j}\left[(\sigma\mu_T)\frac{\partial \omega}{\partial x_j}\right] \tag{3.29}$$

The terms on LHS of Eq. 3.28 represents the time rate of change of turbulent kinetic energy and contribution of convection fluxes, which need no modeling. The first term on RHS represents the rate of production of turbulent kinetic energy by the mean flow i.e. a transfer of kinetic energy from the mean flow to the turbulence. It also represents transfer of mean kinetic energy to turbulence i.e. the work done by turbulent stress against mean strain. It is postulated that this transfer of energy takes place from mean flow to large size scale eddies in turbulent flow. The second term on RHS is the product of the density and specific turbulent dissipation rate, which represents the rate at which turbulent kinetic energy is destructed and converted into internal energy. It is postulated that this mechanism occurs in small size eddies. The third and fourth term on RHS represents the molecular and turbulent diffusion of kinetic energy. They are modeled by using gradient diffusion assumption. The units of turbulent kinetic energy k are $\mathrm{m}^2/\mathrm{s}^2$. The terms on LHS of Eq. 3.29 represent the unsteady and transport terms. The first term on RHS represents the rate of production of specific dissipation rate. The second term represents the destruction of specific dissipation rate and the third and fourth terms on RHS represent the molecular and turbulent diffusion. The units of ω are s^{-1}. The constants in Eq. 3.28 and 3.29 are, $\alpha = 5/9$, $\beta = 3/40$, $\beta^* = 0.09$, $\sigma = 0.5$, $\sigma^* = 0.5$.

3.2.3 Boundary-conditions for turbulence models

The free stream and wall boundary conditions for various turbulence models [77, 12] are stated below with subscript ∞ and w representing the freestream and wall conditions.

Spalart-Allmaras model

$\tilde{\nu}_\infty = \frac{0.1\mu_\infty}{\bar{\rho}_\infty}$, and $(\nu_T)_w = 0$.

k-ω **model**

$\omega_\infty = (10\tilde{u}_\infty)/L$ and $k_\infty = 0.01\nu_\infty\omega_\infty$ and $\omega \to 6\nu_w/(\beta y^2)$ as $y \to 0$; $(\omega)_w = 106\nu_w/(\beta_1 \triangle y_1^2)$ as $y \to 0$; for $\triangle y_1^+ < 3$ (for smooth wall), where $\triangle y_1$ is the normal distance to the next point nearest from the wall, $\beta_1 = 3/40$ and L is the length of the domain.

3.3 Numerical method

The governing equations for any fluid flow can be expressed in form of partial differential equations or integral equations. The exact analytical solutions of these equations is difficult to obtain for complex flows such as shock-wave turbulent boundary-layer interactions. As an engineering approach, these partial differential equations or integral equations are discretized to system of algebraic equations. Generally the Taylor series [78] is used to approximate the partial differential equations to system of algebraic linear equations. There are different discretization techniques like finite difference, finite element and finite volume [79]. In this chapter, we restrict ourselves to the finite volume method approach and for more details of it, we can refer to textbooks by Hirsch [78], Laney [78], Toro [78], Leveque [80] and Blazek [81]. We use Reynolds-Averaged Navier-Stokes (RANS) equations [76] for solving the high-speed supersonic flows. Basically the terms in RANS equations can be viewed as three terms, the inviscid or convective terms, the viscous terms and the source terms.

The shock-wave/turbulent boundary-layer interaction cases [16, 9, 4] includes different high gradient regions such as separation bubble, shock-waves, expansion waves, shear-layer and boundary-layer flow separation point and re-attachment point and, all of these physical features in the flowfield has to be captured accurately using appropriate CFD methods. For steady-state solution of the supersonic flows the hyperbolic and elliptic nature dominate the flow. For supersonic steady flows the convective terms dominate in the inviscid regions and the flow is hyperbolic in nature in space. For boundary-layer flows and separated flows the diffusive terms dominate. In a separation bubble the flow is diffusive in nature hence the information can flow in all the directions and the flow posses elliptic nature in this confined region. The central differencing scheme can be used to discretize the viscous terms.

In-house code [84] is used in our simulations in Chapters 5, 6, 7 and 8. The code is capable to run on parallel machines. Reynolds-averaged Navier-Stokes equations are used in either two-dimensional, three-dimensional or axisymmetric. The Spalart-Allmaras and k-ω turbulence models are included in the code. The governing equations are discretized in a finite volume formulation where the inviscid fluxes are computed using a modified (low-dissipation) form of the Steger-Warming flux splitting approach [85]. The turbulence model equations are fully coupled to the mean flow equations. The details of the formulation are given in Ref. [84]. The method is second order accurate both in stream-wise and wall normal directions. The viscous fluxes and the turbulent source terms are evaluated using central difference method. The implicit Data Parallel Line Relaxation method of Wright *et al.* [86] is used in two-dimensional and axisymmetric simulations and Data-Parallel Lower-Upper Relaxation method [87] is used in three-dimensional simulations to integrate in time and to reach steady-state solution. The code has been used successfully in several supersonic and hypersonic applications [12, 88, 90, 89].

In the following, we briefly discuss about the finite volume formulation and flux-vector splitting scheme of Steger-Warming [13] and modified Steger-Warming [85], for solving RANS equations using k-ω model for perfect gas. Next, we discuss the explicit time integration method to obtain steady state solution followed by the numerical boundary conditions.

3.4 Conservation form

The RANS equations in tensor notation are given by Eqs. 3.5, 3.6, 3.7, 3.18, 3.20, 3.21, 3.22, 3.28 and 3.29 (see Section 3.1). In this section we use standard two-equation k-ω model [76] to calculate the eddy viscosity (see Subsection 3.2.2). In two-dimensional RANS equations we solve for one continuity, two momentum, one energy, one turbulent kinetic energy, and one dissipation of turbulent kinetic energy, equation along with turbulent closure equations. A total of six equations are solved simultaneously to obtain six conservative variables $\overline{\rho}$, $\overline{\rho}\tilde{u}$, $\overline{\rho}\tilde{v}$, $\overline{\rho}\tilde{E}$, $\overline{\rho}k$ and $\overline{\rho}\omega$. From these conservative variables, the six primitive mean flow quantities are derived as, $\tilde{u}$, and $\tilde{v}$, density $\overline{\rho}$, temperature $\tilde{T}$, and k and ω. The mean pressure $\overline{p}$ is calculated from perfect gas law. The two-dimensional system of RANS equations can be written by single equation in conservation form by,

$$\frac{\partial U}{\partial t} + \nabla.(\vec{F} + \vec{G}) = Q \tag{3.30}$$

Where U is the set of conservative vector variables, $\vec{F}$ is the flux vector in x-direction and $\vec{G}$ is the flux vector in the y-direction and, Q is the source term. The total fluxes are written as inviscid part and viscous part. The subscripts I and V represent the inviscid and viscous terms. These equations are written in Cartesian form.

$$\frac{\partial U}{\partial t} + \frac{\partial F}{\partial x} + \frac{\partial G}{\partial y} = Q \tag{3.31}$$

$$F = F_I + F_V; \qquad\qquad G = G_I + G_V \tag{3.32}$$

$$U = \begin{bmatrix} \overline{\rho} & \overline{\rho}\tilde{u} & \overline{\rho}\tilde{v} & \overline{\rho}\tilde{E} & \overline{\rho}k & \overline{\rho}\omega \end{bmatrix}^T \tag{3.33}$$

$$F_I = \begin{bmatrix} \overline{\rho}\tilde{u} \\ \overline{\rho}\tilde{u}^2 + \overline{p} + \frac{2}{3}\overline{\rho}k \\ \overline{\rho}\tilde{u}\tilde{v} \\ (\overline{\rho}\tilde{E} + \overline{p} + \frac{2}{3}\overline{\rho}k)\tilde{u} \\ \overline{\rho}\tilde{u}k \\ \overline{\rho}\tilde{u}\omega \end{bmatrix}; \qquad G_I = \begin{bmatrix} \overline{\rho}\tilde{v} \\ \overline{\rho}\tilde{u}\tilde{v} \\ \overline{\rho}\tilde{v}^2 + \overline{p} + \frac{2}{3}\overline{\rho}k \\ (\overline{\rho}\tilde{E} + \overline{p} + \frac{2}{3}\overline{\rho}k)\tilde{v} \\ \overline{\rho}\tilde{v}k \\ \overline{\rho}\tilde{v}\omega \end{bmatrix} \tag{3.34}$$

$$F_V = \begin{bmatrix} 0 \\ \overline{t}_{xx} + \tau_{xx} \\ \overline{t}_{xy} + \tau_{xy} \\ (\overline{t}_{xx} + \tau_{xx})\tilde{u} + (\overline{t}_{xy} + \tau_{xy})\tilde{v} + (\kappa + \kappa_T)\frac{\partial \tilde{T}}{\partial x} + (\overline{\mu} + \sigma\mu_T)\frac{\partial k}{\partial x} \\ (\overline{\mu} + \sigma_k^*\mu_T)\frac{\partial k}{\partial x} \\ (\overline{\mu} + \sigma_k\mu_T)\frac{\partial \omega}{\partial x} \end{bmatrix} \tag{3.35}$$

$$G_V = \begin{bmatrix} 0 \\ \overline{t}_{xy} + \tau_{xy} \\ \overline{t}_{yy} + \tau_{yy} \\ (\overline{t}_{xy} + \tau_{xy})\tilde{u} + (\overline{t}_{yy} + \tau_{yy})\tilde{v} + (\kappa + \kappa_T)\frac{\partial \tilde{T}}{\partial y} + (\overline{\mu} + \sigma\mu_T)\frac{\partial k}{\partial y} \\ (\overline{\mu} + \sigma{\mu_T}^*)\frac{\partial k}{\partial y} \\ (\overline{\mu} + \sigma\mu_T)\frac{\partial \omega}{\partial y} \end{bmatrix} \tag{3.36}$$

$$Q = \Big[0 \quad 0 \quad 0 \quad 0 \quad (P_k - \beta^*\overline{\rho}k\omega) \quad (\alpha\tfrac{\omega}{k}P_k - \beta\overline{\rho}\omega^2)\Big]^T \tag{3.37}$$

Here $\overline{\rho}$ is the mean density of fluid, $\tilde{u}$, $\tilde{v}$ are the mean velocities in the x and y direction, $\overline{p}$ is the mean pressure and, $\overline{t}_{xx}$, $\overline{t}_{xy}$ are the mean viscous stresses acting on a fluid and, τ_{xy}, τ_{xy} are the Reynolds stresses. $\tilde{E}$ represents the averaged total energy, $\tilde{e}$ is averaged specific internal energy, and P_k represents the production of turbulent kinetic energy. The superscript T represents the transpose of the matrix. The other details of the terms in the above matrices are presented in Sections 3.1 and 3.2. The Eq. 3.30 is integrated over the control surface area (CS) of control volume (CV) in Fig. 3.1a to give,

$$\frac{\partial}{\partial t}\iiint\limits_{CV} U dV + \iint\limits_{CS} \Big[(\vec{F_I} + \vec{G_I}) + (\vec{F_V} + \vec{G_V})\Big].(\hat{n}dS) = Q \tag{3.38}$$

$$\frac{\partial U}{\partial t} = -\frac{1}{V_{i,j}}\Big[\vec{F}_{i+1/2,j}.\vec{S}_{i+1/2,j} + \vec{F}_{i-1/2,j}.\vec{S}_{i-1/2,j} + \vec{G}_{i,j+1/2}.\vec{S}_{i,j+1/2} + \vec{G}_{i,j-1/2}.\vec{S}_{i,j-1/2}\Big] + Q \tag{3.39}$$

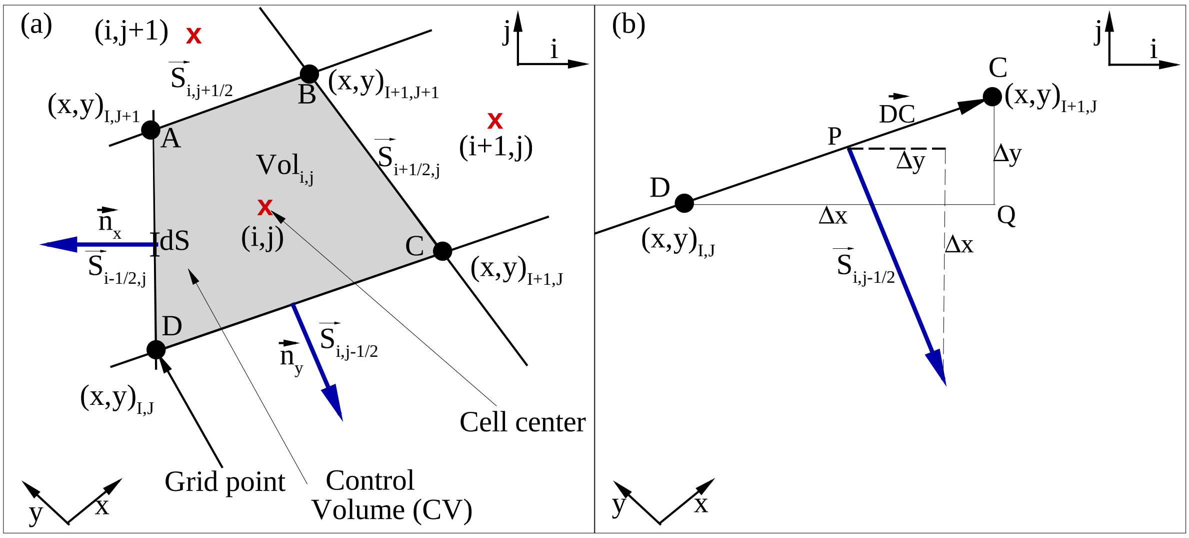

Figure 3.1: (a) Two-dimensional control volume used in finite volume formulation, where the grid points are represented by solid circles with small indices of i and j and cell centers are shown by crosses represented by caps indices of I and J. (b) Calculation of normal surface vector $\vec{S}_{i,j+1/2}$.

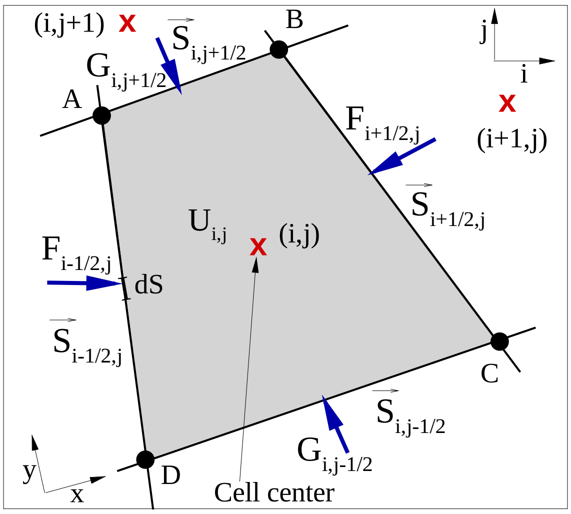

Figure 3.2: The conservative variable $U_{I,J}$ at cell center calculated from the fluxes F and G passing through the cell boundaries in the x- and y-directions.

$$\begin{aligned}\vec{S}_{i+1/2,j} &= +(y_{i+1,j+1} - y_{i+1,j})\hat{i} - (x_{i+1,j+1} - x_{i+1,j})\hat{j} \\ \vec{S}_{i-1/2,j} &= -(y_{i,j+1} - y_{i,j})\hat{i} + (x_{i,j+1} - x_{i,j})\hat{j}\end{aligned} \tag{3.40}$$

$$\begin{aligned}V_{i,j} = [&|(x_{i,j} - x_{i+1,j})y_{i+1,j+1} + (x_{i+1,j} - x_{i+1,j+1})y_{i,j} + (x_{i+1,j} - x_{i,j})y_{i+1,j}| \\ &+|(x_{i,j} - x_{i+1,j+1})y_{i,j+1} + (x_{i+1,j+1} - x_{i,j+1})y_{i,j} + (x_{i,j+1} - x_{i,j})y_{i+1,j+1}|]\end{aligned} \tag{3.41}$$

$\hat{n}$ is the unit normal vector to surface area dS as shown in Fig. 3.1a. Here $\vec{S}_{i+1/2,j}$ and $\vec{S}_{i-1/2,j}$ are the surface area vectors and, $\hat{i}$ and $\hat{j}$ are unit vectors in i and j direction. x and y are the coordinates of the grid points and $V_{i,j}$ is the control volume. The evaluation of $\vec{S}_{i,j-1/2}$ is shown in Fig. 3.1b. The vector $\vec{DC} = \Delta x\hat{i} + \Delta y\hat{j}$. where $\Delta x = x_{i+1,j} - x_{i,j}$ and $\Delta y = y_{i+1,j} - y_{i,j}$. Hence the normal vector is calculated as $\vec{S}_{i,j-1/2} = \Delta y\hat{i} - \Delta x\hat{j}$. Similarly $\vec{S}_{i,j+1/2}$ is evaluated. The control volume in Fig. 3.1a is calculated as summation of area of triangles ABD and BCD.

There are several methods for evaluation of fluxes using finite volume method. The detail formulation of the flux discretization schemes like Mac-Cormack, Steger-Warming, Van-Leer, Advection Upstream Splitting Method (AUSM), Total Variation Diminishing (TVD), Roe, and Weighed Essentially Non-Oscillating (WENO), can be found in standard textbooks [78, 82, 83, 80, 81]. In the below sections we discuss the brief formulation of Steger-Warming [13] and modified Steger-Warming methods [85].

3.5 Steger-Warming method

In this section we describe briefly about the Steger-Warming method [13] applied to one-dimensional Euler equations, which are used to solve inviscid supersonic flows. The Euler equations are hyperbolic in nature. The basic requirement for hyperbolic flow is that the eigen values should be real, distinct and positive [80]. Some of the basic discretization techniques [78, 82, 83, 80, 81] used in solving the the governing equations are forward difference, backward difference, central difference and upwind difference. In an upwind scheme spatial differencing is done on the mesh points on the side from which the information or wind flows. Upwind schemes use information of the local wave propagation explicitly. The eigen values provide the direction of information in the flow. Central difference schemes even though they are simple to discretize for complex equations, they are unstable compared to the upwind scheme.

Basically the Steger-Warming method [13] was formulated for high speed inviscid flows to capture shocks by taking the advantage of the hyperbolic nature of the Euler equations. The physics of the characteristic waves is taken into consideration in its formulation. Simple one-sided up-winding (as applied to linear-advection equation), cannot be used to discretize the system of the Euler equations. Since the Euler equations has mixed nature of eigen values, the information can propagate in either direction and depends not only the velocity terms but also the pressure terms in the fluxes. The flux-vectors and the eigen values are splitted according to the upwind direction of information propagation. We consider one-dimensional Euler equations to evaluate the fluxes. The same methodology can be extended to the two- and three-dimensional flows. In this section we do not take co-ordinate transformations into consideration for simplicity.

$$U = \begin{bmatrix} \rho \\ \rho u \\ E \end{bmatrix} = \begin{bmatrix} U_1 \\ U_2 \\ U_3 \end{bmatrix} \tag{3.42}$$

$$F_I = \begin{bmatrix} \rho u \\ \rho u^2 + p \\ (E+p)u \end{bmatrix} = \begin{bmatrix} F_1 \\ F_2 \\ F_3 \end{bmatrix} \tag{3.43}$$

where E=$\rho e + 1/2\rho u^2$ is the total energy and $e = C_v T$ is the internal energy. The flux vector is function of the conservative variable vector and is evaluated as,

$$[F] = [A][U] \tag{3.44}$$

where A is the Jacobian matrix and U is the conservative variable vector. The Jacobian matrix, A is calculated by taking the partial derivative of the flux-vector with respect to vector of conservative variable.

$$A = \frac{\partial F}{\partial U} \tag{3.45}$$

$$A = \begin{bmatrix} \frac{\partial F_1}{\partial U_1} & \frac{\partial F_1}{\partial U_2} & \frac{\partial F_1}{\partial U_3} \\ \frac{\partial F_2}{\partial U_1} & \frac{\partial F_2}{\partial U_2} & \frac{\partial F_2}{\partial U_3} \\ \frac{\partial F_3}{\partial U_1} & \frac{\partial F_3}{\partial U_2} & \frac{\partial F_3}{\partial U_3} \end{bmatrix} = \begin{bmatrix} 0 & 1 & 0 \\ (\gamma-3)u^2/2 & (3-\gamma)u & \gamma-1 \\ (\gamma-1)u^3 - \gamma e u/\rho & [\gamma e/\rho - 3(\gamma-1)u^2/2] & \gamma u \end{bmatrix} \tag{3.46}$$

With this Jacobian matrix we write the characteristic equation to find the eigen values.

$$det[A - \lambda I] = 0 \tag{3.47}$$

where I is the identity matrix. The three eigen values (λ_k, k = 1,2,3) of the above matrix are

$$\Lambda = diag(u, u+a, u-a)$$

Here u is speed of the flow and a corresponds to the speed of the sound. The corresponding left eigen vector matrix and right eigen vector matrix is evaluated as T and T^{-}. For each eigen value of λ_1, λ_2 and λ_3 the corresponding eigen vectors are calculated as given by Eqs. 3.48, 3.49 and 3.50. Each of the these single column 1×3 matrix of eigen vectors are arranged in three columns of a 3×3 square matrix to form a right eigen vector matrix T as given by Eqs. 3.51.

Here r is 1×3 single column eigen vector with $p = (1, 2, 3)$ and $k = (1, 2, 3)$. $|r_k^p|$ corresponds to the right eigen vector single column matrix formed by calculating the three eigen vectors r_1^1, r_1^2, r_1^3 in Eqs. 3.48, for corresponding eigen value λ_1. Similarly other terms in Eqs. 3.49 and 3.50 are defined.

$$[A][r_1^1 r_1^2 r_1^3] = \lambda_1 [r_1^1 r_1^2 r_1^3]^T \tag{3.48}$$

$$[A][r_2^1 r_2^2 r_2^3] = \lambda_2 [r_2^1 r_2^2 r_2^3]^T \tag{3.49}$$

$$[A][r_3^1 r_3^2 r_3^3] = \lambda_3 [r_3^1 r_3^2 r_3^3]^T \tag{3.50}$$

$$[T] = [|r_k^p||r_k^p||r_k^p|] \tag{3.51}$$

The left eigen vector matrix is calculated by taking the inverse matrix of the right vector matrix. Using T and T^- the negative and positive Jacobian matrices are calculated. The Jacobian is splitted into positive and negative parts by splitting the eigen values into positive and negative parts. The diagonal matrix Λ_+ contains only positive eigen values and diagonal matrix Λ_- has only negative eigen values.

$$A = A_+ + A_- \tag{3.52}$$

$$\lambda_k = \lambda_{k+} + \lambda_{k-} \tag{3.53}$$

$$\lambda_{k+} = \frac{\lambda_k + |\lambda_k|}{2} \tag{3.54}$$

$$\lambda_{k-} = \frac{\lambda_k - |\lambda_k|}{2} \tag{3.55}$$

$$\Lambda = \Lambda_+ + \Lambda_- \tag{3.56}$$

$$\Lambda_+ = diag(\frac{\lambda_k + |\lambda_k|}{2}, \frac{\lambda_k + |\lambda_k|}{2}, \frac{\lambda_k + |\lambda_k|}{2}) \tag{3.57}$$

$$\Lambda_- = diag(\frac{\lambda_k - |\lambda_k|}{2}, \frac{\lambda_k - |\lambda_k|}{2}, \frac{\lambda_k - |\lambda_k|}{2}) \tag{3.58}$$

$$A_+ = T\Lambda_+ T^{-1} \qquad A_- = T\Lambda_- T^{-1} \tag{3.59}$$

The fluxes are then splitted according to the sign of the Jacobians as positive and negative parts as below.

$$F = F_+ + F_- \tag{3.60}$$

$$F_+ = A_+ U \qquad F_- = A_- U \tag{3.61}$$

The above fluxes are evaluated for subsonic flows. For supersonic flows the information flows in downstream direction and there is no information flows is upstream direction. Hence for supersonic flows $F_+ = F$ and $F_- = 0$. The information in a flow can come from upstream or downstream direction and depending on it, the discretization is done to the fluxes. In a control volume these fluxes are calculated at the cell faces with the help of the Jacobian and the values of conservative variables are taken from the cell center. The up-winding scheme is applied, where the positive and negative fluxes are calculated in the direction from which the information (wind) flows. In the Steger-Warming method the Jacobians are calculated at the cell-centers and the fluxes are evaluated using this Jacobians and is given by Eq. 3.62.

First-order method

$$\begin{aligned} F_{+_i} &= A_{+_i} U_i \\ F_{-_{i+1}} &= A_{-_{i+1}} U_{i+1} \end{aligned} \tag{3.62}$$

For hyperbolic nature of the Euler equations, the eigen values are real and distinct. In the Steger-Warming method, the modification is made to the eigen values when they become either zero or one. This can happen when the flow becomes sonic for local Mach number = 1 or stagnant for M = 0 in some regions. One of the examples is the regions at blunt-nose the of the vehicle. To overcome this problem, the eigen values are corrected ($\tilde{\lambda}$), with the use of a small value of a constant, ε = 0.3.

$$\tilde{\lambda}_{\pm} = \left[\lambda_{\pm} \pm \sqrt{(\lambda_{\pm} + \varepsilon^2 a^2)} \right] \tag{3.63}$$

The high quality solutions of supersonic undisturbed boundary-layers are obtained by setting ε = 0, than the original eigen values are restored from this modified eigen value.

3.6 Modified Steger-Warming method

The Steger-Warming [13] method when applied to the viscous flows results in large numerical dissipation [85] across the boundary-layer. Also it creates fictitious pressure gradient which causes the unrealistic convection within the layer. It has similar problems across free shear-layers. MacCormack and Candler [85] modified the Steger-Warming method to reduce the excessive numerical mixing in the boundary-layer and free shear-layer flows. In the Steger-Warming method the evaluation of Jacobians at the cell centers resulted in excessive numerical dissipation in the boundary-layer. In the modified Steger-Warming method the Jacobians are modified and are calculated at cell-interfaces (see Fig. 3.4) and from these values the fluxes were calculated as given by Eq. 3.64. This formulation reduces the numerical dissipation in the boundary layer. Fig 3.3 shows the the velocity profile distribution in boundary-layer computed using the the modified Steger-Warming [85] is represented by diamond symbols and the Steger-Warming method [13] is represented by square symbols. The results are compared with the Blasius theory [91] depicted by solid line. The modified Steger-Warming method predicts realistic velocity profile and is close to the theory. The standard Steger-Warming method predicts unphysical excessive velocity gradients near the wall and deviates from Blasius theory [91].

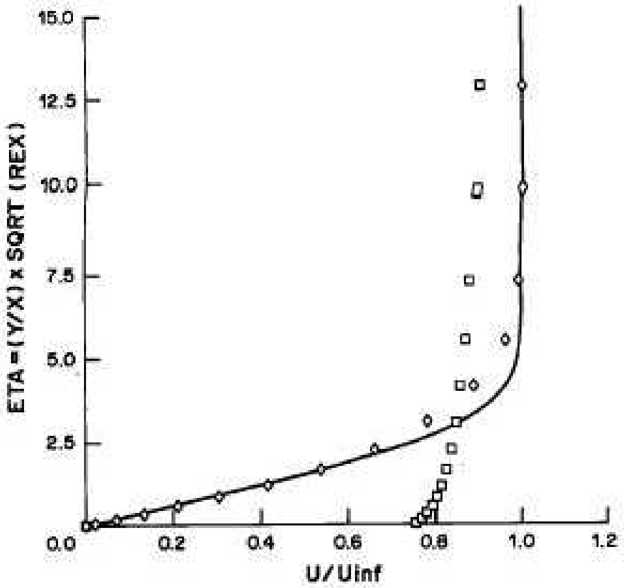

Figure 3.3: Comparison of computed velocity profile using modified Steger-Warming [85] method (diamond symbols) and Steger-Warming method [13] (square symbols) with Blasius theory [91] (solid line).

First-order method

$$\begin{aligned} F_{+_i} &= A_{+_{i+1/2}} U_i \\ F_{-_{i+1}} &= A_{-_{i+1/2}} U_{i+1} \\ A_{\pm_{i+1/2}} &= A_{\pm}\left[\tfrac{1}{2}\left(U_i + U_{i+1}\right)\right] \end{aligned} \tag{3.64}$$

Time integration

$$U_i^{n+1} = U_i^n - \frac{\triangle t}{\triangle x}[F_{i+1/2} - F_{i-1/2}]^n \tag{3.65}$$

$$U_i^{n+1} = U_i^n - \frac{\triangle t}{\triangle x}[(F_{+_i} + F_{-_{i+1}}) - (F_{+_{i-1}} + F_{-_i})]^n \tag{3.66}$$

$$U_i^{n+1} = U_i^n - \frac{\triangle t}{\triangle x}\left[(F_{+_i} - F_{+_{i-1}}) + (F_{-_{i+1}} - F_{-_i})\right]^n \tag{3.67}$$

The one-dimensional Euler equation is solved using the explicit method as in Eq. 3.66, where the forward differencing is used. In this explicit formulation the conservative variables at time step $n+1$ are evaluated as U_i^{n+1} from the known conservative varables U_i^n and fluxes at time step n, and the solution is marched in time to obtain steady state solution. Here, n represents the former time step and $n+1$ represents the updated or new time step. The only unknown term is U_i^{n+1} and is calculated explicitly in the from the known terms on RHS, hence the name explicit method is coined to this approach.

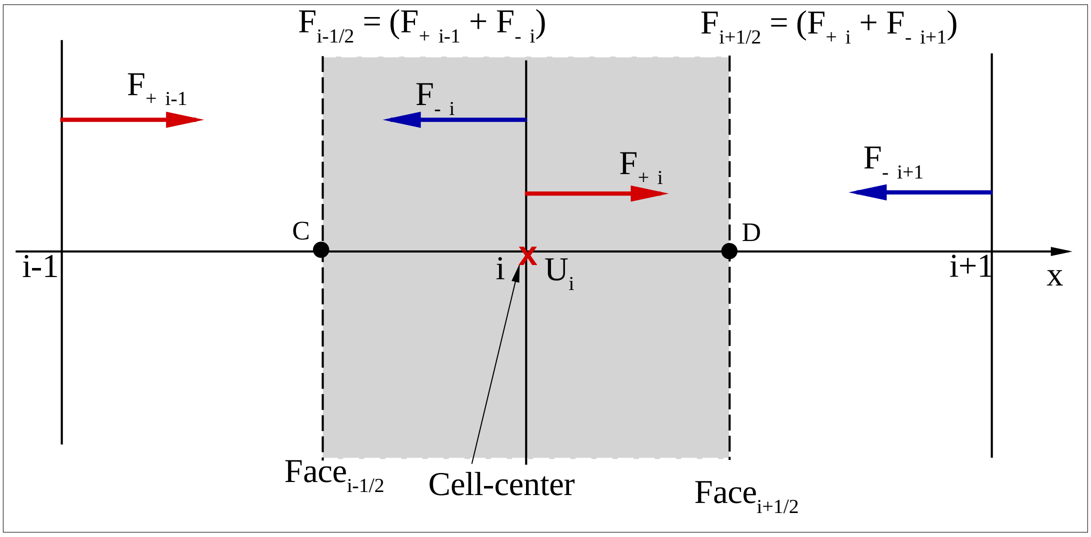

Figure 3.4: Physical interpretation for evaluation of conservative variable at cell-center, using fluxes at cell-interfaces, for the first-order method (reproduced from Hirsch [78]).

Fig. 3.4 shows the physical interpretation for evaluating the fluxes with the first order scheme of Eq. 3.67. The positive and negative fluxes in Fig. 3.4 are attached to the characteristics of positive and signs (eigen values). To evaluate the conservative variable at cell center the fluxes are evaluated at cell faces $i+1/2$ and $i-1/2$. Fig. 3.4 shows that the flux at interface $F_{i+1/2}$, at D is calculated from the positive flux vector F_{+_i} coming from left hand side and negative flux vector $F_{-_{i+1}}$ coming from right hand side of U_i. Similarly the flux at interface $F_{i-1/2}$, at C is evaluated. Both of these fluxes, $F_{i+1/2}$ and $F_{i-1/2}$ contribute to the conservative variable U_i at cell center. Fig. 3.4 shows that for an upwind direction of positive fluxes the backward difference method is used and for negative fluxes of downwind direction, the forward difference method is used (see Eq. 3.67). Hence the discretization of the fluxes is done on the side of wind flow (information).

Stability analysis had been carried by Steger and Warming [13] for one-dimensional Euler equations using Von-Neuman stability condition [78]. In this analysis the Jacobian matrix is freezed and and decoupling is done to system of simple advection equations. The Fourier analysis is done by assuming the solution in the form of waves and satisfying the condition of ratio of amplification of solution error to be less than 1. It is shown that the taking only positive direction of eigen values in the upwind scheme resulted in instability. Taking the mixed signs of eigen values resulted in stable solution. From stability analysis the CFL (Courant-Friedrichs-Lewy) is restricted to less than 1, in the explicit method due to which only small timesteps can be taken while solving the flow.

3.7 Second order method

The first-order upwind schemes are less accurate as they contain less number of points in a stencil. They are more dissipative and do not give any oscillations across the high gradient regions such as shock-waves. The second order central differencing schemes are more accurate than first order upwind schemes and are less dissipative, but they are unstable across the shock-waves. The second order upwind schemes possess less numerical dissipation compared to the upwind first order schemes and are more accurate because of more points in the stencil. By increasing the number of points in the stencil (or order) minute details of flow physics can be accurately captured by the numerical method.

Second order Steger-Warming method [13]

$$\begin{aligned} F_{+_i} &= A_{+_i} U^L_{i+1/2} \\ F_{-_{i+1}} &= A_{-_{i+1}} U^R_{i+1/2} \end{aligned} \tag{3.68}$$

$$\begin{aligned} U^L_{i+1/2} &= \tfrac{3}{2} U_i - \tfrac{1}{2} U_{i-1} \\ U^R_{i+1/2} &= \tfrac{3}{2} U_{i+1} - \tfrac{1}{2} U_{i+2} \end{aligned} \tag{3.69}$$

Second order modified Steger-Warming method [85]

$$\begin{aligned} F_{+_i} &= A_{+_{i+1/2}} U^L_{i+1/2} \\ F_{-_{i+1}} &= A_{-_{i+1/2}} U^R_{i+1/2} \end{aligned} \tag{3.70}$$

$$\begin{aligned} U^L_{i+1/2} &= \tfrac{3}{2} U_i - \tfrac{1}{2} U_{i-1} \\ U^R_{i+1/2} &= \tfrac{3}{2} U_{i+1} - \tfrac{1}{2} U_{i+2} \end{aligned} \tag{3.71}$$

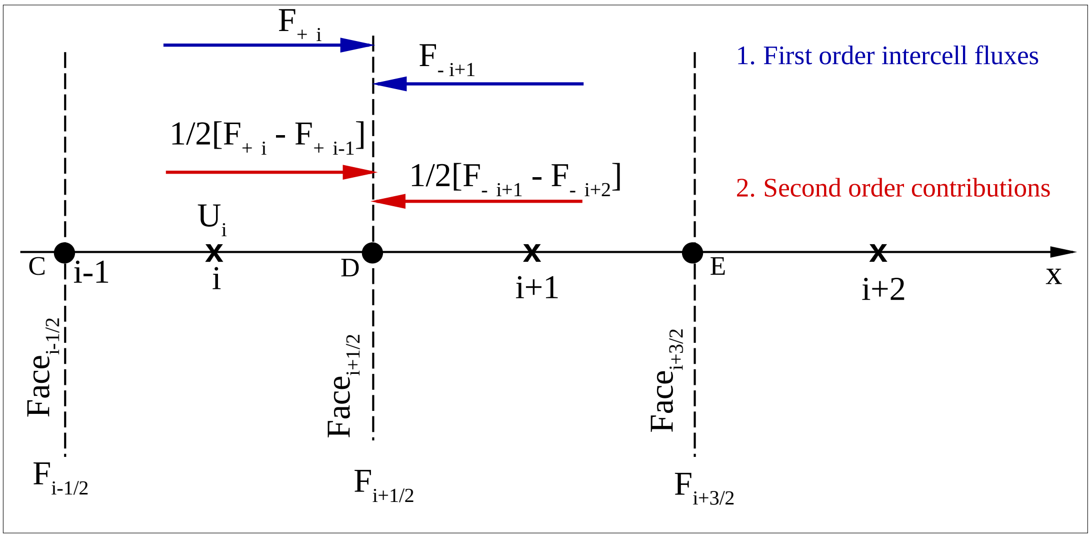

Figure 3.5: Physical interpretation for evaluation of fluxes for the second-order method (reproduced from Hirsch [78]).

Eqs. 3.68, 3.69, 3.70 and 3.71 represent the flux evaluations using second-order schemes. Here U_L and U_R correspond to the left and right states. Fig. 3.5 gives the physical interpretation for evaluating the fluxes using second order scheme. The fluxes are extrapolated to the interfaces [78] defining the flux equal to the numerical scheme. Fig. 3.5 shows that at cell interface $i + 1/2$ the flux is evaluated as summation of the contribution from first order scheme and contribution from second order from left and right states.

The second order schemes give spurious non-physical oscillations across high gradients such as shock-waves. To avoid these spurious oscillations they are converted to first order schemes across the shock-waves. The flux limiters are used to avoid spurious oscillations or wiggles across the shocks. The second order modified Steger-Warming method is converted to first order method by applying the pressure limiter [88]. Flux limiters are used to limit the spatial derivatives to physically realistic values. They come in to operation when sharp gradients like shocks occur. For smooth gradient regions these flux limiters are not active. The shock-wave regions are detected if the pressure jump is greater than 50% across grid points.

The modified Steger-Warming method [85] gives less dissipation in the boundary-layers and result in oscillations in the high gradient regions such as shock-waves. Whereas the standard Steger-Warming gives more numerical dissipation in the boundary-layers and is stable across the shock-waves. To take the advantage of both the methods, a hybrid scheme is used to evaluate the fluxes and the pressure limiter [88] is used to switch from modified Steger-Warming scheme to the standard Steger-Warming scheme across the shock-waves. When the pressure gradient is more than 50% across the shock-waves the scheme is reverted to Steger-Warming method and when the pressure gradient is less the scheme is reverted to modified Steger-Warming method in the boundary-layer regions. The pressure jump across high gradients is detected with the use of pressure limiter.

The modified Steger-Warming has been applied to supersonic flows of shock-wave boundary-layer interaction cases [12, 90] and to the hypersonic cases [85, 86, 92, 89]. The numerical experiments [88] were done on the double cone geometry for hypersonic flows, where different flux evaluation techniques like modified Steger-Warming [85], Roe [78], and HLLC methods [83] were applied to predict the heat transfer rates. Amongst these flux evaluation methods, the modified Steger-Warming [85] method was found to give less numerical dissipation and predicted accurate results compared to the experiments.

3.8 Boundary conditions

Fig. 3.6 shows computational domain with different boundaries for supersonic flow over flat-plate at zero angle of attack. Total number of cells are $mx \times my$, where mx is number of cells in flow-parallel direction and my is total number of cells in flow-normal direction. The dummy cells are represented by dashed-lines and their cell centers are marked by circles. The inner cells are represented by solid-lines and their cell centers are marked by crosses. No computations are done at dummy cells. They serve to calculate the fluxes at cell faces of inner cells along the boundaries as shown in Fig. 3.6. The boundary conditions applied to turbulent variables is discussed in Subsection. 3.2.3. The boundary-conditions applied at dummy cells for other variables are discussed below.

Inlet

The free-stream conditions are assigned at i = 1 with j varying from 1 to my.

$$\begin{aligned} u(1,j) &= V_\infty, \quad v(1,j) = 0 \\ \rho(1,j) &= \rho_\infty, \quad T(1,j) = T_\infty \end{aligned} \tag{3.72}$$

Here, u and v are velocity components in the flow-parallel and flow-normal direction, ρ is the density, and T is the temperature. The subscript ∞ represent the freestream conditions. The pressure is calculated from the equation of state.

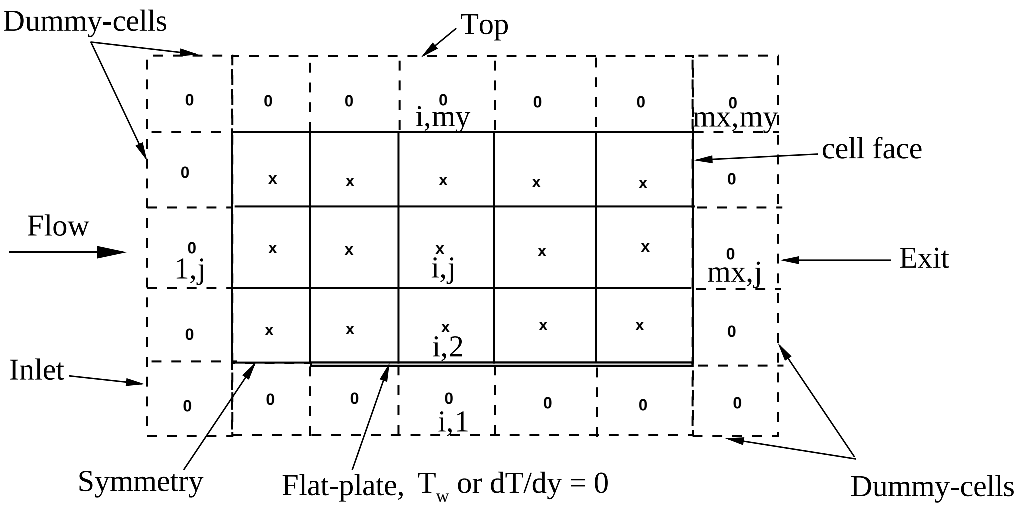

Figure 3.6: Computational domain along with boundary conditions for flat-plate configuration.

Symmetry

The symmetry conditions are assigned at j = 1 and i = 2. The variables are mirrored over symmetry boundary.

$$\begin{aligned} u(2,1) &= u(2,2), \quad v(2,1) = -v(2,2) \\ \rho(2,1) &= \rho(2,2), \quad T(2,1) = T(2,2) \end{aligned} \tag{3.73}$$

Wall

The physical boundary conditions applied at stationary flat-plate for the viscous flow are,

$$\begin{array}{ll} \vec{v} = 0, & \text{no slip condition} \\ \partial P/\partial n, & \text{constant pressure boundary layer} \\ T_w = \text{constant}, & \text{isothermal wall} \\ \partial T/\partial n, & \text{adiabatic wall} \end{array} \tag{3.74}$$

Here, $\vec{v}$ is the velocity vector with components u and v and n is the normal direction to plate. The above conditions are applied numerically at j = 1 with i varying from 3 to mx. The density is calculated using the equation of state.

$$\begin{aligned} u(i,1) &= -u(i,2),\ v(i,1) = -v(i,2) \\ \rho(i,1) &= \frac{\rho(i,2)\ T(i,2)}{T(i,1)} \\ T(i,1) &= 2T_w - T(i,2) \\ T(i,1) &= T(i,2) \end{aligned} \tag{3.75}$$

Top

The free-stream conditions are assigned at top boundary at j = my with i varying from 2 to (mx -1).

$$\begin{aligned} u(i,my) = V_\infty, \quad & v(i,my) = 0 \\ \rho(i,my) = \rho_\infty, \quad & T(i,my) = T_\infty \end{aligned} \tag{3.76}$$

Exit

At the exit, the supersonic extrapolation condition is applied where the computed flow variable values are extrapolated from inner cells with i = mx and j varying from 2 to my.

$$\begin{aligned} u(mx,j) = u(mx-1,j), \quad & v(mx,j) = v(mx-1,j) \\ \rho(mx,j) = \rho(mx-1,j), \quad & T(mx,j) = T(mx-1,j) \end{aligned} \tag{3.77}$$

3.9 Summary

Reynolds-averaged Navier-Stokes equations are described for simulation of high-speed flows. Commonly used one- and two-equation turbulence models are used for turbulence closure. They provide a balance between computational efficiency and accuracy of the solution. A finite-volume based numerical method is described. It uses modified Steger-Warming flux splitting approach for computing the inviscid fluxes, and second order central differencing for the viscous fluxes and turbulent source terms. An in-house code based on the above methodology is used for the computations presented in this thesis. The method and the code has been validated for a series of hypersonic flow applications.

Chapter 4

Shock-unsteadiness model

4.1 Introduction

Shock-wave/turbulent boundary-layer interaction is a complex process and some of the mechanisms like shock-unsteadiness, shock-distortion and turbulence amplification across shock are dominant. The unsteady nature of shock wave is these interaction is caused by turbulence which is unsteady is nature. RANS models are based on average quantities in the turbulent flow and do not account for unsteady motion of shock in shock-wave/turbulent boundary-layer interactions. Hence, they predict inaccurate flow in these interaction cases [9]. In-depth understanding of the flow is required to study the mechanisms in shock-wave/turbulent boundary-layer interaction. This helps in knowing the limitations of standard and existing turbulence models and these models can be improved by including the missing flow physics. When the average effect of shock-unsteadiness is modeled and included in the RANS models, it is found to improve the flow predictions [10].

Homogeneous isotropic turbulence interacting with a normal shock wave is taken to be the model problem to study the flow physics. A typical flow image is shown in Fig. 4.1. This shock turbulence interaction is an isolated problem and does not include any flow gradients in transverse direction, flow separation, streamline curvature and no additional compression behind the shock. This is a fundamental problem to study how different mechanisms change the turbulence across a shock wave. Since the mean flow is uniform no vorticity is generated from it in the upstream. Vorticity is generated solely from the turbulence. The overlapped contours of turbulent vorticity and mean flow dilatation are shown in Fig. 4.1 at a particular instant of time. The solid lines represents positive values of vorticity contours and dash lines

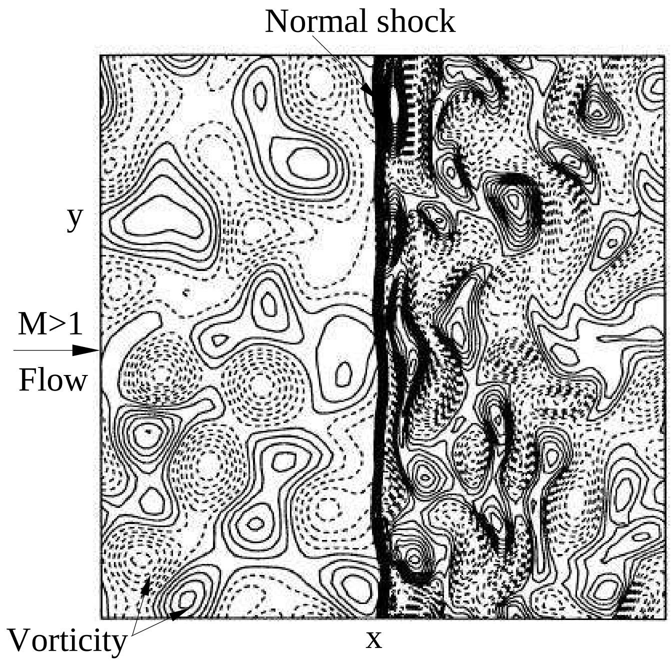

Figure 4.1: Homogeneous isotropic turbulence interacting with a shock-wave with upstream Mach of 2 at particular instant of time [93]. The normal shock is represented by dilatation contours at the center of domain. The positive mean turbulence vorticity contours are depicted by solid lines and negative contours by dash lines.

show negative vorticity contours. The normal shock is represented at the center of domain by dilatation contours. Linear inviscid theory can be used to predict the above described flow across the shock [94, 95, 96]. Many researchers [97, 98, 99] have studied this problem using direct numerical simulations (DNS) to explore the underlying flow physics.

In this chapter, first we describe model flow problem. Next, turbulence model prediction of amplification of turbulent kinetic energy across a shock wave is presented. Next, we describe the shock-unsteadiness correction and improvement in results over existing turbulence models. Finally, the implementation of shock-unsteadiness correction to one- and two-equation models is presented.

4.2 Problem statement

A uniform mean flow in the stream-wise x direction interacts with a normal shock. The upstream flow is supersonic and the conditions are denoted by subscript 1. The downstream flow is subsonic and denoted by subscript 2. The Rankine-Hugoniot relations are applied to calculate the jump in flow variables, such as pressure ratio p_2/p_1 across a shock wave. Here u, ρ and T

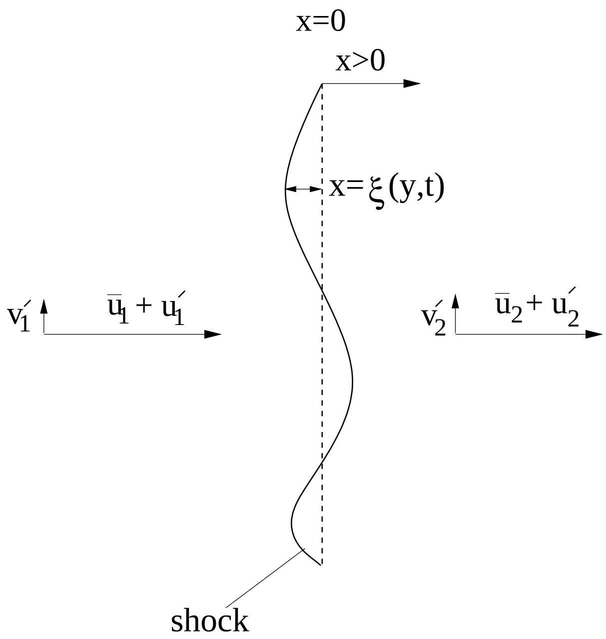

Figure 4.2: Schematic sketch of homogeneous isotropic turbulence/shock interaction. $\overline{u}_1$ and $\overline{u}_2$ are the mean uniform velocities and u' and v' are the fluctuating velocities, upstream and downstream of shock. The shock represented by solid line is displaced by x = ξ(y,t) from its mean position (represented by dash line).

are velocity, density and temperature.

$$\begin{aligned} \rho_1 u_1 &= \rho_2 u_2 \\ \rho_1 u_1^2 + p_1 &= \rho_2 u_2^2 + p_2 \\ C_p T_1 + \tfrac{1}{2} u_1^2 &= C_p T_2 + \tfrac{1}{2} u_2^2 \end{aligned} \tag{4.1}$$

The components of mean velocity in the transverse y and span-wise direction z are taken as zero. The incoming turbulence is assumed to be homogeneous and isotropic. In homogeneous turbulence the average of the properties are uniformly distributed over the domain and statistically they are independent of position in space. Isotropic means the turbulence is statistically independent of direction, for example $\overline{u'^2}$ = $\overline{v'^2}$ = $\overline{w'^2}$. In addition, only vortical fluctuations are considered in the upstream flow, i.e., u', v', $w' \neq$ 0 and ρ' = T' = p' = 0. Physically, it means that the turbulence fluctuations u', v', w' are small compared to mean speed of sound, such that the turbulence fluctuations are incompressible. where $\overline{\rho}$ is the mean density. Further acoustic fluctuations are found to be negligible in supersonic boundary-layer (p' = 0). The same is assumed to hold in the upstream flow.

The inflow turbulence and shock wave have effect on each other and are modified due to their mutual interaction. First, the effect of turbulence on shock wave is described. When the upstream fluctuations interact with the shock front, it oscillates with time hence making it

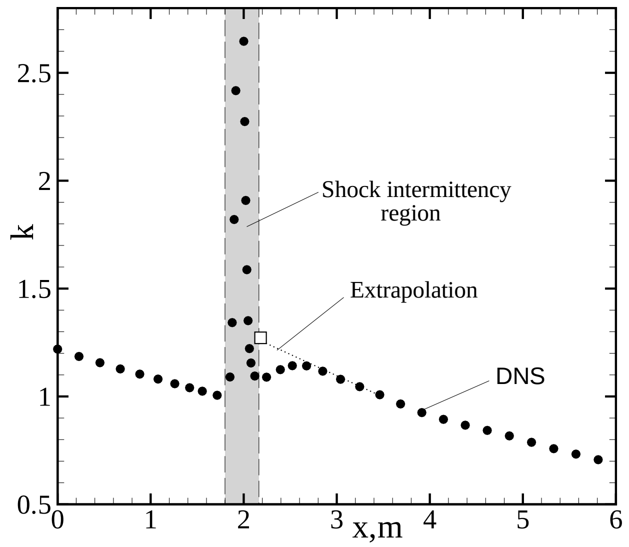

Figure 4.3: Variation of turbulent kinetic energy across a shock wave [11] interacting with homogeneous isotropic turbulence for upstream Mach of 1.29.

unsteady in nature [10]. The shock is stationary in the mean and is displaced by a distance of x = ξ(y,t) in the flow direction as shown in Fig. 4.2. The shock gets distorted in the mean flow due the blobs of turbulence interacting with it as shown in Fig. 4.2. The unsteady shock distortions about its mean position is assumed to be small. In the absence of turbulence, the shock is straight, as predicted by inviscid theory.

Next, the effect of shock on turbulence is described. The velocity fluctuations u' and v' are amplified across a shock-wave. Also vorticity fluctuations are intensified in the immediate downstream of shock because of the shock wave. Later in the far downstream the amplification of vorticity diminishes. The turbulent kinetic energy $k = \overline{u_i' u_i'}/2$ is amplified because of the amplifications in the velocity fluctuations. Fig. 4.3 shows the evolution of turbulent kinetic energy, k along the normalized shock-normal direction, x. Here, $k = \frac{1}{2}(\overline{u'u'} + \overline{v'v'} + \overline{w'w'})$ is normalized by its value immediate upstream of shock. The flow is similar to as shown in Fig. 4.1 and differs in the inflow conditions. In this flow, upstream Mach M_1 = 1.29, turbulent Mach number, M_t = 0.14 and Reynolds number, Re_λ = 19.1.

The turbulence is sustained because of mean velocity gradients. As there are no mean flow gradients outside the shock, there is no means for production of k in the upstream of shock, hence k decays up to x = 2 as shown in Fig. 4.3. Across the shock, k is amplified up to about 1.3. Immediately downstream of shock wave, k exhibits non-monotonic behavior because of transfer of energy between different modes. Acoustic energy is generated at the shock. A part of it decays rapidly behind the shock and is transferred to the vortical mode. This results in an increase in k between x = 2.1 m and x = 2.7 m. Further downstream (for x $>$ 2.7 m), k decays monotonically because of turbulent dissipation.

For canonical flows the normal Mach number can be calculated. For example, Smits *et al.* [100] performed experiments for compression corner flows with M_∞ = 2.9 and corner angle = $8°$. An oblique shock is generated at corner with interacts with turbulent boundary layer over plate. If it is assumed that the flow is across the a single normal shock, it yields a normal Mach number of 1.29.

4.3 RANS prediction

The standard k-ϵ model [76] is used to compute homogeneous isotropic turbulence interacting with normal shock with upstream Mach of 1.29. The turbulent Mach number, M_t = 0.14 and Reynolds number based on Taylor micro-scale, Re_λ = 19.1. The one-dimensional steady mean flow for this problem is given by,

$$\overline{\rho}\bar{u}\frac{\partial k}{\partial x} = P_k - \overline{\rho}\epsilon \tag{4.2}$$

$$\overline{\rho}\bar{u}\frac{\partial \epsilon}{\partial x} = -c_{\epsilon_1} P_k \frac{\epsilon}{k} - c_{\epsilon_2}\frac{\epsilon^2}{k} \tag{4.3}$$

Here, the diffusion terms are assumed to be negligible across shock wave. $\bar{u}$ is the mean component of velocity in the x-direction, ϵ is the turbulent kinetic energy dissipation rate and, c_{ϵ_1} = 1.35 and c_{ϵ_1} = 1.8 are model constants. The production of turbulent kinetic energy is given by,

$$P_k = \tau_{ij}\frac{\partial \overline{u}_i}{\partial x_j} \tag{4.4}$$

where $\tau_{ij} = 2\mu_T[S_{ij} - (1/3)(\partial\overline{u}_k/\partial x_k)\delta_{ij}] - (2/3)\overline{\rho}k\delta_{ij}$. In two-dimensions the production term can be written as,

$$P_k = \tau_{xx}\frac{\partial \overline{u}}{\partial x} + \tau_{xy}\frac{\partial \overline{u}}{\partial y} + \tau_{yx}\frac{\partial \overline{v}}{\partial x} + \tau_{yy}\frac{\partial \overline{v}}{\partial y} \tag{4.5}$$

Across a normal shock-wave the first term is higher in order of magnitude compared to the other terms, therefore the production of turbulent kinetic energy becomes,

$$P_k = \left[2\mu_T\frac{\partial \overline{u}}{\partial x} - \frac{2}{3}\mu_T\nabla.\vec{u} - \frac{2}{3}\overline{\rho}k\right]\frac{\partial \overline{u}}{\partial x} \tag{4.6}$$

In a normal shock $\nabla.\vec{u} \approx \partial\overline{u}/\partial x$, therefore the above equation simplifies to

$$P_k = \frac{4}{3}\mu_T\left(\frac{\partial \overline{u}}{\partial x}\right)^2 - \frac{2}{3}\overline{\rho}k\frac{\partial \overline{u}}{\partial x} \tag{4.7}$$

or

$$P_k = \frac{4}{3}\mu_T S_{ii}^2 - \frac{2}{3}\overline{\rho} k S_{ii} \tag{4.8}$$

From this expression it shows the production of turbulent kinetic energy across a shock is proportional to $S_{ii}^2 \propto (\partial\overline{u}/\partial x)^2 \propto 1/\delta^2$, where S_{ii} is the dilatation and δ is the thickness of shock. Since this dilatation term is large across a shock-wave it predicts high values of turbulent kinetic energy. The mean dilatation is proportional to the upstream Mach number. The standard models are sensitive to the thickness of shock waves hence the grid and as the thickness of shock reduces they predict higher amplification of k. Fig. 4.4a shows that the standard k-ϵ model predicts over amplified values of k across a shock at x = 2 compared to DNS data. Also, higher values of k are predicted downstream of a shock wave. Therefore, k-amplification predicted by standard k-ϵ model is a function of upstream Mach number and thickness of a shock wave.

$$k_2/k_1 = \mathrm{f}(\delta, M_1) \tag{4.9}$$

Boussinesq approximation [76] states that the turbulent stresses are linearly related to the mean strain rates via the eddy viscosity. This linear relation holds well for equilibrium flows in which, the time scales of mean strain rate are of the same order of magnitude as that of turbulence time scales. But this expression does not hold for highly non-equilibrium flows such as shock-waves. Across shock wave the mean strain rate changes very fast but turbulence requires time to get adjusted for this sudden change, i.e. the mean flow time scale and turbulence time scales are not of the same order. Therefore the Boussinesq approximation [76] breaks down in a shock-wave.

The standard models were modified [73, 74] to suppress the turbulent kinetic energy k across a shock-wave by applying the realizable condition $0 \le \overline{u'u'} \le 2k$, where u' is the fluctuating velocity in the streamwise direction. The Reynolds stress and eddy viscosity across normal shock are given by,

$$\tau_{xx} = -\overline{\rho}\overline{u'u'} = \frac{4}{3}\mu_T \frac{\partial\overline{u}}{\partial x} - \frac{2}{3}\overline{\rho} k \tag{4.10}$$

$$\mu_T = \overline{\rho} C_\mu \frac{k^2}{\epsilon} \tag{4.11}$$

where C_μ = 0.09 is the model constant. Applying the realizable condition, the eddy viscosity μ_T is corrected by altering the model constant.

$$C_\mu = \min\left[C_\mu^o, C_\mu^o/\zeta\right] \tag{4.12}$$

where, C_μ^o = 0.09 is the standard value, $\zeta = Sk/\overline{\epsilon}$ is the dimensionless mean strain rate. The parameter S = $\left[2S_{ij}S_{ji} - \frac{2}{3}S_{ii}^2\right]^{\frac{1}{2}}$ and mean strain rate tensor, $S_{ij} = 1/2(\partial\overline{u}_i/\partial x_j + \partial\overline{u}_j/\partial x_i)$. $\partial\overline{u}/\partial x$ is negative across a shock wave, $S = -(2/\sqrt{3})\partial\overline{u}/\partial x$. Substituting S in Eq. 4.12 and using this value of C_μ in Eq. 4.11, the Reynolds stress simplifies to

$$\tau_{xx} = -\overline{\rho}\overline{u'u'} = -(0.35\overline{\rho}k + \frac{2}{3}\overline{\rho}k) \tag{4.13}$$

The production of turbulent kinetic energy modifies to,

$$P_k = -(0.35 + \frac{2}{3})\overline{\rho}kS_{ii} \tag{4.14}$$

When above equation is substituted in Eq. 4.2 in place of Eq. 4.8 it yields lower values of k across shock wave. Fig. 4.4a shows that inspite of suppressing eddy viscosity by the relalizablility correction, k shows higher values across shock-wave. Substituting above Eq. 4.13 in Eq. 4.2 and integrating, k-amplification is obtained.

$$\frac{k_2}{k_1} = \left(\frac{\overline{u}_1}{\overline{u}_2}\right)^{\frac{2}{3}+0.35} \tag{4.15}$$

The dissipation term on RHS of Eq. 4.2 has negligible effect on evolution of k across a shock-wave. Hence only the production term is considered to obtain above expression. The k-amplification given by Eq. 4.15 is independent of shock thickness and depends only on the upstream Mach number.

The flow is highly non-equilibrium across a shock wave since the mean flow changes rapidly and turbulence cannot adjust to this sudden change. Hence the linear relation between the Reynolds stress and mean strain rate via eddy viscosity breaks down. Therefore, Sinha *et al.* [10] argue that more accurate amplification of k is obtained by setting $\mu_T = 0$.

On this basis the production of turbulent kinetic energy reduces to

$$P_k = -\frac{2}{3}\overline{\rho}kS_{ii} \tag{4.16}$$

The above relation shows that $P_k \propto S_{ii}$ and therefore a lower amplification of turbulent kinetic energy than the original model (see Eq. 4.8). Substituting the above equation in Eq. 4.2 and integrating yields,

$$\frac{k_2}{k_1} = \left(\frac{\overline{u}_1}{\overline{u}_2}\right)^{\frac{2}{3}} \tag{4.17}$$

In this extreme limiting case of suppressing eddy viscosity to zero value, Fig. 4.4b shows that the k-amplification matches for low $M_1 < 1.5$ and shows higher values for $M_1 > 1.5$ as compared to DNS data.

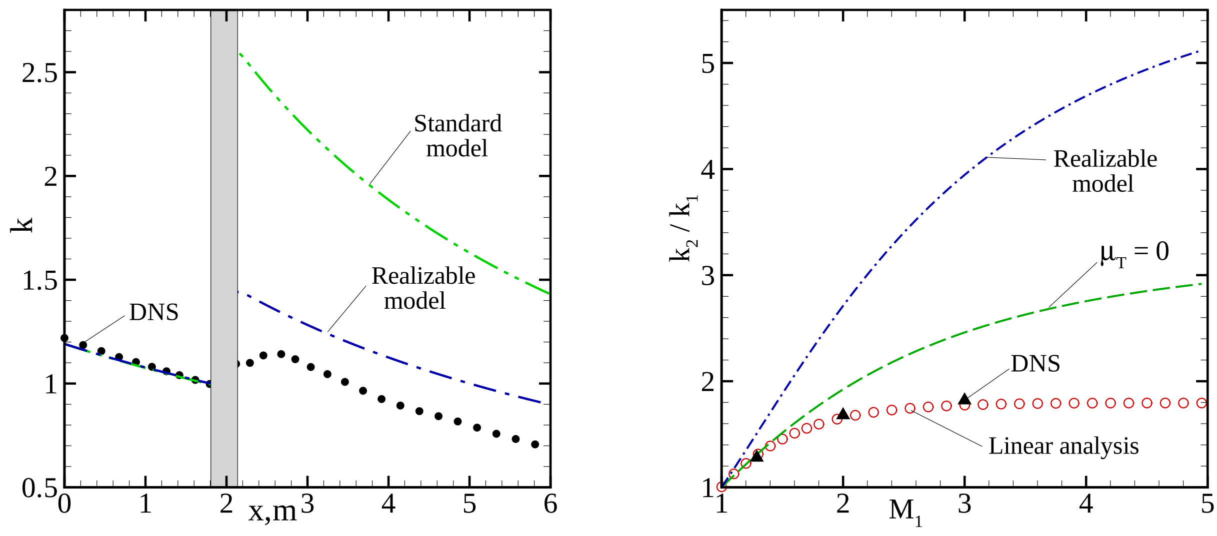

(a)

(b)

Figure 4.4: Comparison of standard k-ϵ and modified turbulence models results with DNS data across a normal shock-wave. (a) Variation of turbulent kinetic energy k in the streamwise direction at M_1 = 1.29. (b) k amplification at varying Mach numbers.

Therefore from above modifications it is observed that suppressing the eddy viscosity alone is not enough for accurate prediction of k across a shock. The question now arises is that what physical mechanisms would be responsible that could suppress k across a shock-wave so as to accurate predict the k-amplification. Next step would be how do we include these physical effects in the turbulence models. The unsteady shock motion is found to have a damping effect on turbulent kinetic energy amplification at the shock. Sinha *et al.* [10] study this mechanism using linear theory and propose the model for the production of turbulent kinetic energy at the shock wave whose details are presented below.

4.4 Shock-unsteadiness correction

The fluctuations in turbulent flow when interacts with a shock wave creates shock-unsteadiness. Sinha *et. al.* [10] derived the turbulent kinetic energy equation based on the reference frame attached to the instantaneous shock. The shock-unsteadiness correction term in k-equation has damping effect on k amplification across a shock and is modeled using linear analysis. The model is evaluated using DNS data. The details are presented below.

The unsteady problem is converted to steady state by fixing the co-ordinates to the shock.

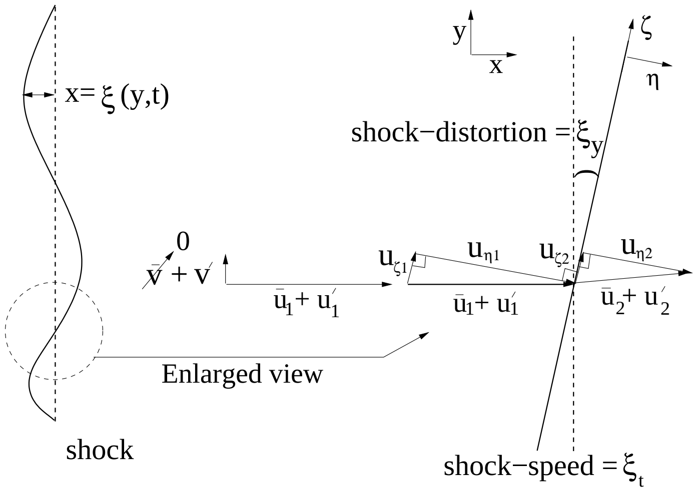

Figure 4.5: Homogeneous isotropic turbulence/shock interaction. Enlarged view depicting the velocity diagram with ζ-η co-ordinate system attached to the oblique shock. The normal and tangential components of velocity upstream and downstream of shock are shown.

Imagine that we are sitting on the shock and in this frame of reference the shock is steady. The linearized conservation equations of mass and momentum in the ζ-η co-ordinates are written. The ζ-direction is tangential to shock and η is normal to it. The viscous terms are neglected across shock and it is assumed that gradients in the shock parallel direction are negligible. In Fig. 4.5 the part of the instantaneous shock is enlarged and shown. For small shock-distortion ξ_y, $\cos\xi_{\rm y} \approx 1$ and $\sin\xi_{\rm y}$ = ξ_y. Dropping the higher order terms the velocity components in ζ and η direction are given by,

$$
\begin{aligned}
u_\eta &= (u\ \cos\xi_{\rm y} - v\ \sin\xi_{\rm y}) - \xi_t = (u - v\xi_y) - \xi_t = (\overline{u} + u') - \xi_t \\
u_\zeta &= u\ \sin\xi_{\rm y} + v\ \cos\xi_{\rm y} = u\xi_y + v = (\overline{u} + u')\xi_y + v' = \overline{u}\xi_y + v'
\end{aligned}
\tag{4.18}
$$

Here, ξ_t is the linear shock velocity in the streamwise direction, overbar represents the Reynolds averaged and prime represents the fluctuation quantities. The continuity and momentum equations in the steady state ζ-η coordinate system are given by,

$$\frac{\partial}{\partial \eta}(\rho u_\eta) = 0 \tag{4.19}$$

$$(\rho u_\eta)\frac{\partial u_\eta}{\partial \eta} = -\frac{\partial p}{\partial \eta} \tag{4.20}$$

$$(\rho u_\eta)\frac{\partial u_\zeta}{\partial \eta} = 0 \tag{4.21}$$

Applying the chain rule of differentiation and substituting Eqs. 4.18 in above equations we obtain,

$$\begin{aligned}
\frac{\partial}{\partial x}(\bar{\rho}+\rho')(\overline{u}+u'-\xi_t) &= 0 && (4.22)\\
(\bar{\rho}+\rho')(\overline{u}+u'-\xi_t)\frac{\partial}{\partial x}(\overline{u}+u'-\xi_t) &= -\frac{\partial}{\partial x}(\overline{p}+p') && (4.23)\\
(\bar{\rho}+\rho')(\overline{u}+u'-\xi_t)\frac{\partial}{\partial x}(\overline{u}\xi_y+v') &= 0 && (4.24)
\end{aligned}$$

Multiplying the x-momentum equation with u' and Reynolds averaging we obtain,

$$\bar{\rho}\bar{u}\frac{\partial}{\partial x}\frac{\overline{u'^2}}{2} = -\overline{\rho u'^2}\frac{\partial \bar{u}}{\partial x} + \bar{\rho}\overline{u'\xi_t}\frac{\partial \bar{u}}{\partial x} - \overline{u'}\frac{\partial \bar{p}}{\partial x} - \overline{u'\frac{\partial p'}{\partial x}} \tag{4.25}$$

The y-momentum equation is multiplied with v' and Reynolds averaged. In three-dimensional flow similar equation for z-momentum equation is obtained and multiplying it with w' and Reynolds averaging gives,

$$\begin{aligned}
\bar{\rho}\bar{u}\frac{\partial}{\partial x}\frac{\overline{v'^2}}{2} &= -\bar{\rho}\bar{u}\overline{v'\xi_y}\frac{\partial \overline{u}}{\partial x} && (4.26)\\
\bar{\rho}\bar{u}\frac{\partial}{\partial x}\frac{\overline{w'^2}}{2} &= -\bar{\rho}\bar{u}\overline{w'\xi_z}\frac{\partial \overline{u}}{\partial x} && (4.27)
\end{aligned}$$

It is assumed that w' = v' and for small shock distortion ξ_z = ξ_y, hence $\overline{w'\xi_z}$ = $\overline{v'\xi_y}$. Summing Eqs. 4.25-4.27 and accounting for turbulent dissipation we obtain,

$$\bar{\rho}\bar{u}\frac{\partial k}{\partial x} = -\overline{\bar{\rho}u'^2}\frac{\partial \bar{u}}{\partial x} + \bar{\rho}\overline{u'\xi_t}\frac{\partial \bar{u}}{\partial x} - 2\bar{\rho}\bar{u}\overline{v'\xi_y}\frac{\partial \overline{u}}{\partial x} - \overline{u'}\frac{\partial \bar{p}}{\partial x} - \overline{u'\frac{\partial p'}{\partial x}} - \bar{\rho}\epsilon \tag{4.28}$$

The above equation represents the transport of turbulent kinetic energy equation for homogeneous isotropic turbulence interacting with a normal shock. The term on LHS is the convection of turbulent kinetic energy. The first term on RHS is the production of turbulent kinetic energy, the second term is the shock-unsteadiness term, the third gives the shock-distortion, the fourth is the production due to mean pressure gradient, fifth is the velocity pressure correlation and the last term is the dissipation.

The shock-unsteadiness term is $\propto \overline{u'\xi_t}$ and from linear analysis,

$$\overline{u'\xi_t} > 0 \tag{4.29}$$

and the dilatation S_{ii} = $\partial\bar{u}/\partial x$ is negative across shock wave. Hence the shock-unsteadiness term,

$$S_k^1 = \overline{u'\xi_t}\frac{\partial \bar{u}}{\partial x} < 0 \tag{4.30}$$

This shows that S_k^1 has damping effect on k across shock. From above Eq. 4.29, it follows that if $u' > 0$ then $\xi_t > 0$ and if $u' < 0$ then $\xi_t < 0$. It implies that there is in-phase coupling between

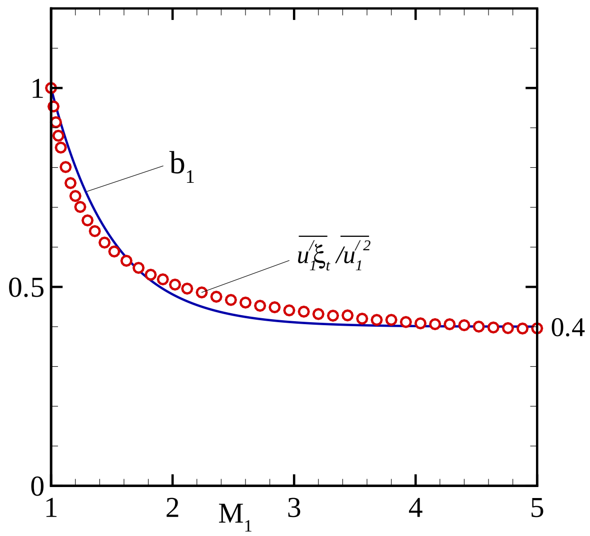

Figure 4.6: Variation of $\overline{u'\xi_t}/\overline{u'^2}$ as a function of upstream Mach number predicted by linear analysis [11], used to obtain model parameter b_1.

incoming turbulent fluctuations and shock motion. The ξ_t is written in terms of model constant b_1 times u', based on the assumption that shock unsteadiness is caused by turbulent fluctuation. Therefore the term $\overline{u'\xi_t}$ is modeled as,

$$\overline{u_i'\xi_t} = b_1\overline{u'^2} \tag{4.31}$$

Linear analysis [11] is used to obtain the ratio $\overline{u_i'\xi_t}/\overline{u'^2}$ with varying Mach numbers as shown in Fig. 4.6. The shock-unsteadiness model closure constant $b_1 = 0.4 + 0.6e^{2(1-M_1)}$ is obtained by curve-fit, to match the linear theory results. Substituting Eq. 4.31 in Eq. 4.30 we obtain,

$$S_k^1 = \overline{u'^2}\frac{\partial\bar{u}}{\partial x}b_1 \tag{4.32}$$

Considering the k convection, production, shock-unsteadiness and dissipation terms in Eq. 4.28, the transport of turbulent kinetic energy reduces to,

$$\overline{\rho u_i}\frac{\partial k}{\partial x} = \overline{\rho}\overline{u'^2}\frac{\partial\overline{u}}{\partial x}(1-b_1) - \overline{\rho}\epsilon \tag{4.33}$$

The Reynolds stress $\rho\overline{u'^2} = (2/3)\overline{\rho}k$ is obtained by substituting $\mu_T = 0$ in Eq. 4.10. The model parameter b_1 is modified to b_1' to accommodate effects of shock-distortion effect, production due to mean pressure gradient and velocity pressure correlation.

$$b_1' = b_{1\infty}(1 - e^{1-M_1}) \tag{4.34}$$

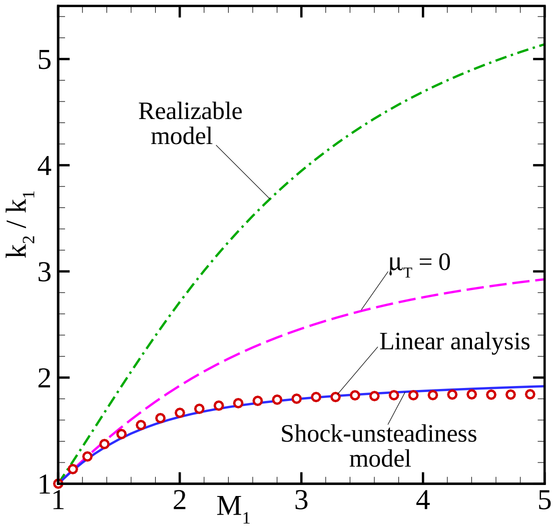

Figure 4.7: Comparison of k-amplification with linear analysis [11] for homogeneous turbulence interacting with shock with varying upstream Mach numbers.

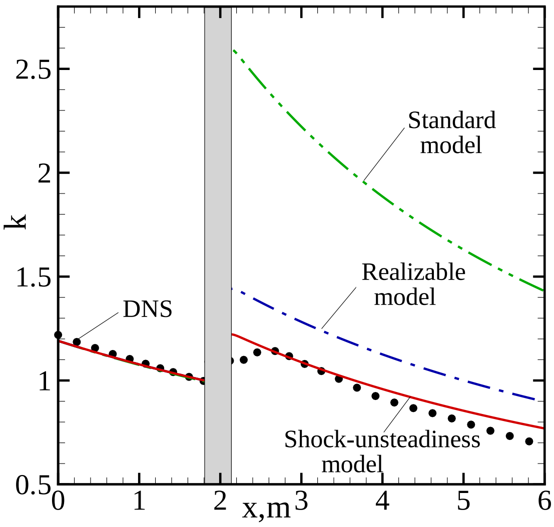

Figure 4.8: Comparison of turbulent kinetic energy with DNS data [11] for homogeneous isotropic turbulence interacting with shock with upstream Mach of 1.29.

$b_{1\infty}$ = 0.4 is the high Mach number limiting value of b_1 (see Fig. 4.6). Hence the final form of turbulent kinetic energy transport equation is given by,

$$\overline{\rho u}_i \frac{\partial k}{\partial x_i} = -\frac{2}{3}\overline{\rho} k S_{ii}(1 - b_1') - \overline{\rho}\epsilon \tag{4.35}$$

From above equation the production term is given by,

$$P_k = -\frac{2}{3}\overline{\rho} k S_{ii}(1 - b_1') \tag{4.36}$$

Hence, the the production term predicted by shock-unsteadiness correction is less compared to predicted by standard and modified models given by Eqs. 4.8 and 4.14. Integrating Eq. 4.35 by neglecting the dissipation across a shock wave we obtain,

$$\frac{k_2}{k_1} = \left(\frac{\overline{u}_1}{\overline{u}_2}\right)^{\frac{2}{3}(1-b_1')} \tag{4.37}$$

The above equation shows that the k-amplification predicted by shock-unsteadiness model is less compared to predicted by realizable model (see Eq. 4.15). Fig. 4.7 shows that he shock-unsteadiness model matches with linear analysis results over wide range of Mach numbers.

In the above analysis, the shock-unsteadiness term is modeled using linear analysis and the results are compared with linear analysis. The model has to be validated with the available experimental or DNS data. The shock-unsteadiness model evaluation is done with DNS results [11] for upstream normal Mach number of 1.29 and is depicted in Fig. 4.8. The shock-unsteadiness model matches k-amplification at the shock wave at x = 2. Hence, the missing physics of shock-unsteadiness in standard and realizable models has been modeled by Sinha *et al.* [10] and shows improved prediction of k-amplification across a shock wave.

4.5 Shock-unsteadiness model implementation

The shock unsteadiness model was subsequently incorporated in one- and two-equation turbulence models applied to shock/boundary-layer interaction [12]. The simplicity of the shock-unsteadiness correction term and its basis in underlying physical phenomena makes it attractive to use in practical applications. The model is briefly discussed below and more details can be found in the original references. Shock-unsteadiness correction is a function of upstream normal Mach number to shock-waves M_{1n} and shock identifying function f_s. In this section we discuss the formulation of shock-unsteadiness model to one- and two-equation turbulence models like k-ω and Spalart-Allmaras model.

4.5.1 Shock-unsteadiness modified k-ω model

The production of turbulent kinetic energy in the standard k-ω turbulence model [76] is given by,

$$P_k = \mu_T S^2 - \frac{2}{3}\overline{\rho}k[S_{ii}] \tag{4.38}$$

here the eddy viscosity is,

$$\mu_T = \overline{\rho}C_\mu \frac{k}{\omega} \tag{4.39}$$

where, k is the turbulent kinetic energy, ω is the specific dissipation rate and constant C_μ = 1.

$$S = \left[2S_{ij}S_{ji} - \frac{2}{3}S_{ii}^2\right]^{\frac{1}{2}} \tag{4.40}$$

Here, $S_{ij} = 1/2(\partial\overline{u}_i/\partial x_j + \partial\overline{u}_j/\partial x_i)$ is the mean strain rate tensor. For two-dimensional flows the parameter S and mean dilatation S_{ii} takes the form,

$$S^2 = \frac{4}{3}\left[\left(\frac{\partial\overline{u}}{\partial x}\right)^2 + \left(\frac{\partial\overline{v}}{\partial y}\right)^2 + \left(\frac{\partial\overline{u}}{\partial y} + \frac{\partial\overline{v}}{\partial x}\right)^2 - \left(\frac{\partial\overline{u}}{\partial x}\right)\left(\frac{\partial\overline{v}}{\partial y}\right)\right] \tag{4.41}$$

$$S_{ii} = \left(\frac{\partial\overline{u}}{\partial x}\right) + \left(\frac{\partial\overline{v}}{\partial y}\right) \tag{4.42}$$

In Sec. 4.3 it is shown that in a shock wave, the standard model predicts $P_k \propto S_{ii}^2$ (see Eq. 4.8). This results in excessively high values of turbulent kinetic energy behind the shock, which may be the reason why the standard k-ω model often predicts delayed separation in shock/boundary-layer interaction flows. Sinha *et al.* [10] argue that the eddy viscosity assumption breaks down in the highly non-equilibrium flow through a shock wave and a more realistic amplification of k is obtained by setting $\mu_T = 0$ in the production term. This results in $P_k \propto S_{ii}$ (see Eq. 4.16) and therefore a lower amplification of turbulent kinetic energy than the original model.

The turbulent fluctuations in the incoming flow make the shock wave unsteady. The unsteady shock motion is found to have a damping effect on turbulent kinetic energy amplification at the shock. Sinha *et al.* [10] study this mechanism using linear theory and propose the following model for the production of turbulent kinetic energy at the shock wave,

$$P_k = -\frac{2}{3}\bar{\rho}kS_{ii}\left(1 - b_1'\right) \tag{4.43}$$

where, the first term is obtained by setting $\mu_T = 0$ in Eq. (4.38) and the second term corresponds to the shock-unsteadiness damping mechanism. The model parameter b_1' represents the coupling between the unsteady shock motion and the upstream velocity fluctuations, and is given by,

$$b_1' = \max\left[\,0,\ 0.4\left(1 - e^{1-M_{1n}}\right)\right] \tag{4.44}$$

It is zero for subsonic flows without shock waves and it reaches an asymptotic value of 0.4 for high Mach numbers.

The shock-unsteadiness correction (see Sec. 4.4) is applied in the k-ω framework by multiplying the eddy viscosity term in Eq. 4.38 by the factor,

$$c_\mu' = 1 - f_s\left[1 + \frac{b_1'}{\sqrt{3}\zeta}\right] \tag{4.45}$$

where, $\zeta = S/\omega$ is dimensionless mean strain rate and f_s is the empirical function that locates the region of shock wave in terms of the ratio S_{ii}/S. It is defined as

$$f_s = \frac{1}{2} - \frac{1}{2}\tanh\left[5(\mathrm{S_{ii}/S}) + 3\right] \tag{4.46}$$

Incorporating the shock-unsteadiness modification in k-ω model, the production of turbulent kinetic energy is modified as

$$P_k' \;=\; c_\mu' \mu_T S^2 - \frac{2}{3}\overline{\rho} k S_{ii} \tag{4.47}$$

The function f_s takes a value of one in shock and high compression regions of the flow field, such that $c_\mu' = -b_1'/\sqrt{3}\zeta$ and the modified production term in the k-ω model matches with that in Eq. 4.36. Otherwise, $f_s = 0$ and the standard form of k-ω model is recovered. The shock-unsteadiness modification is applied across the shock to predict the correct amplification of turbulent kinetic energy and is applied only to the k equation only, the other governing ω equation, does not alter.

4.5.2 Shock-unsteadiness modified Spalart-Allmaras model

In standard Spalart-Allmaras model [75], the mean flow influences the turbulence field via the production term that is a function of the mean vorticity.

$$P_{\mu_T} = c_{b_1}\overline{\rho}\tilde{\nu}\tilde{S} \tag{4.48}$$

Here, the parameter $\tilde{S} = \bar{S} + (\tilde{\nu}/\kappa^2 d^2) f_{v2}$. The vorticity magnitude is represented as $\bar{S} = \sqrt{2\Omega_{ij}\Omega_{ij}}$, in which the rotation tensor is given as $\Omega_{ij} = \frac{1}{2}\left[(\partial\tilde{u}_i/\partial x_j) - (\partial\tilde{u}_j/\partial x_i)\right]$, d is the normal distance from the wall, f_{v2} is the damping function and the constants $c_{b1} = 0.1355$ and $\kappa = 0.41$. Therefore, the eddy viscosity is insensitive to mean dilatation in a shock wave. However, the mean vorticity field in a turbulent boundary layer changes across a shock wave. This can alter the production term and thus can change $\tilde{\nu}$ in the vicinity of the shock. In a 24° compression corner flow [12] at Mach 2.84, for example, the interaction of a turbulent boundary layer with an oblique shock results in a small increase in $\tilde{\nu}$ (less than 5% of the local $\tilde{\nu}$ magnitude).

Interaction with a shock wave enhances the turbulent fluctuations in a flow. Sinha *et al.* [10] propose the following model for the amplification of the turbulent kinetic energy and the turbulent dissipation rate ϵ, when homogeneous isotropic turbulence interacts with a shock wave.

$$\frac{k_2}{k_1} = \left(\frac{\bar{u}_{n,1}}{\bar{u}_{n,2}}\right)^{\frac{2}{3}(1-b_1')} \qquad \text{and} \qquad \frac{\epsilon_2}{\epsilon_1} = \left(\frac{\bar{u}_{n,1}}{\bar{u}_{n,2}}\right)^{\frac{2}{3}c_{\epsilon 1}'} \tag{4.49}$$

where, b_1' is given by Eq. (4.44) and $c_{\epsilon 1}' = 1.25 + 0.2(M_{1n} - 1)$. The subscripts 1 and 2 refer to the locations upstream and downstream of the shock, respectively, and $\bar{u}_n$ is the mean flow velocity normal to the shock. The kinematic eddy viscosity $\tilde{\nu} \propto k^2/\epsilon$, which yields

$$\frac{\tilde{\nu}_2}{\tilde{\nu}_1} = \left(\frac{k_2}{k_1}\right)^2 \frac{\epsilon_1}{\epsilon_2} = \left(\frac{\bar{u}_{n,1}}{\bar{u}_{n,2}}\right)^{c_{b_1'}} \tag{4.50}$$

where,

$$c_{b_1}' = 4/3(1 - b_1') - 2/3c_{\epsilon 1} \tag{4.51}$$

This can be achieved by a production term of the form $-c_{b_1}'\overline{\rho}\tilde{\nu}S_{ii}$ in the transport equation for $\rho\tilde{\nu}$.

$$P_{\mu_T} = c_{b_1}\overline{\rho}\tilde{\nu}\tilde{S} - c_{b_1}'\overline{\rho}\tilde{\nu}S_{ii} \tag{4.52}$$

Note that this additional term is effective only in regions of strong dilation, and therefore does not alter the standard Spalart-Allmaras model elsewhere.

4.6 Summary

The mechanisms involved in the fundamental problem of homogeneous isotropic turbulence interacting with shock are discussed. Linear theory can be used to predict the turbulent kinetic energy amplification across shock wave for this problem. Different variations of the k-ϵ model are compared with DNS data. The standard k-ϵ model predicts very high amplication of turbulent kinetic energy, k across shock. The realizable k-ϵ model reduces amplication of k across and it is further reduced by using $\mu_T = 0$. Both the standard and realizable models do not include the key physical process of unsteady motion of shock-wave in these interaction. The shock-unsteadiness mechanism is found to reduce the the amplification of turbulent kinetic energy and a model is developed to bring in this damping effect. The shock-unsteadiness model improves the k predictions across shock-wave. Hence, the shock-unsteadiness corrected Spalart-Allmaras and k-ω models are used in the simulations.

Chapter 5

Oblique shock-wave/turbulent boundary-layer interaction

5.1 Introduction

In this chapter, the application of shock-unsteadiness correction to the interaction of a canonical two-dimensional oblique impingement configuration is studied. Presence of multiple shock-waves and flow expansion in the interaction region make it more challenging to implement the shock-unsteadiness correction [90] than earlier compression corner applications [12]. The function used to identify the location and extent of shock waves need to be altered. Also, the variation of flow quantities upstream of the different shock-waves cannot be prescribed *a priori*, as in the compression corner cases. The current chapter addresses these issues is detail and presents an improved implementation of the shock-unsteadiness modification for practical flows.

The chapter is organized as follows. First, the experimental test cases and simulation methodology is described. Next, the computed results obtained using standard k-ω model [35] are presented. Next, the application of shock-unsteadiness correction to the k-ω model is studied in detail. A comparison of the computed results using standard and shock-unsteadiness modified k-ω turbulence models with experimental data is presented.

5.2 Test case

Experiments were performed by Schulein [14] for oblique shock wave/turbulent boundary layer interaction flows. The geometry, shown schematically in Fig. 5.1a, consists of a flat plate and a shock generator with three different deflection angles of 6, 10 and $14°$. The strength of the incident shock wave increases with deflection angle, resulting in a stronger interaction with the boundary layer. The inviscid shock from tip of shock generator interacts with the turbulent boundary layer developed over the flat plate. Free stream conditions are $M_\infty = 5$, $T_\infty = 68.3$ K and $p_\infty = 4008.5$ N/m^2 with unit Reynolds number $Re_\infty = 37 \times 10^6$ m^{-1}. The plate is maintained under isothermal conditions of 300 K. Initially the experiments were done for flow over flat plate to obtain undisturbed turbulent boundary layer properties like δ, δ^*, θ and C_f at different locations. Wall data like pressure, skin friction and heat transfer rates were measured along the flat plate in the interaction region.

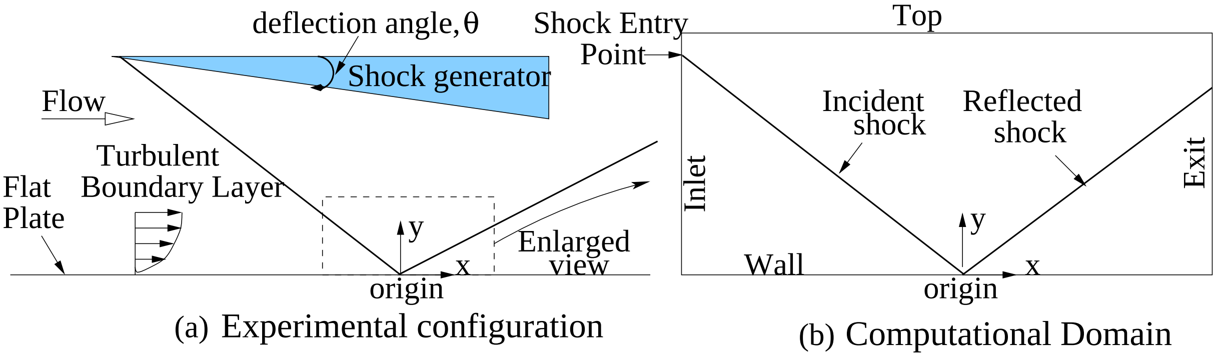

Figure 5.1: Oblique shock-wave/turbulent boundary-layer interaction on a flat plate. (a) Experimental configuration with shock generator deflection angle $\theta°$ and (b) computational domain with appropriate boundary-conditions.

5.3 Simulation Methodology

Two-dimensional Reynolds-averaged Navier-Stokes (RANS) equations are solved for the mean flow, as presented in Ref. [76]. The two-equation k-ω model of Wilcox [35] and the recent shock-unsteadiness corrected k-ω model of Sinha *et al.* [10] are used in the simulations. Both the standard and shock-unsteadiness corrected models do not include any compressibility corrections. The RANS equations are discretized using a finite volume discretization, where the inviscid fluxes are computed using a modified, low-dissipation form of the Steger-Warming flux splitting approach [85]. The discretization method is second order accurate in space. The implicit Data Parallel Line Relaxation method [86] is used to integrate the equations in time and reach a steady-state solution. Other details of the numerical method are discussed in Section 3.3.

The computational domain is schematically shown in Fig. 5.1b. It extends 85 mm upstream and 150 mm downstream of the interaction region in the wall parallel i-direction. In the wall normal j-direction, it extends to 44 mm such that the top boundary is above the oblique shock entry and exit locations. The experiments [14] were done over a 500 mm long flat plate and the inviscid shock was adjusted to impinge at a fixed location of 350 mm from the tip of shock generator. Inviscid simulations were done to locate the shock impingement point. This point is taken as origin in the computational domain such that negative values of x are assigned upstream and positive values in the downstream side. The inviscid shock impingement point is matched between computation and experiment for comparing surface pressure and skin friction data.

The boundary conditions are identified in Fig. 5.1b. Inlet profiles for the computations are obtained from separate flat plate simulation at freestream and wall boundary conditions identical to those listed above. The value of the momentum thickness reported in the experiments [14] is matched to obtain the mean flow and turbulence profiles at the inlet boundary of the computational domain. The inlet profile for the mean flow variables are modified at the shock entry point to post-shock conditions calculated analytically. Post-shock conditions are also prescribed at the top boundary. At the wall, isothermal ($T_w = 300$ K), no-slip boundary conditions are applied and extrapolation condition is used at the exit boundary of the domain. The freestream and wall boundary-conditions for the turbulence model variables are discussed in Subsection 3.2.3. For the oblique shock-wave/turbulent boundary-layer interaction simulations, k and ω values at the boundary-layer edge in the inlet profile are prescribed as the freestream conditions at the top boundary.

5.3.1 Grid convergence

A FORTRAN (FORmula TRANslation) code is used to generate a single-block structured Cartesian grid in the computational domain shown in Fig. 5.1b. The mesh with exponential stretching normal to the wall is used to span the computational domain. Along the wall, the grid points are clustered at the origin and the mesh is stretched exponentially in the upstream and downstream directions. A careful grid refinement study is performed by systematically varying the number of grid points in each direction, as well as refining the cell size in critical regions.

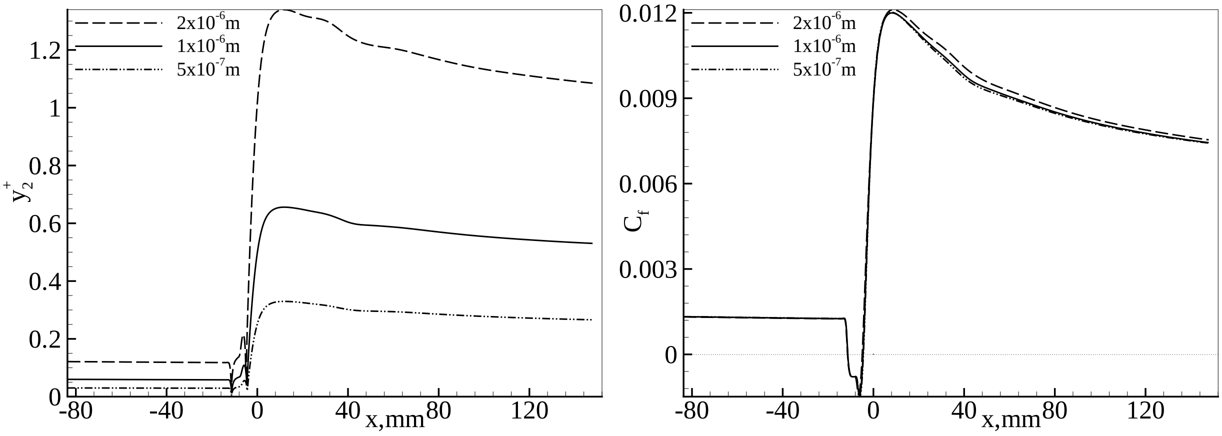

(a)

(b)

Figure 5.2: Variation in (a) y_2^+ at the wall and (b) skin friction coefficient for deflection angle θ = $14°$ obtained using computational grids with varying wall normal spacing at the flat plate.

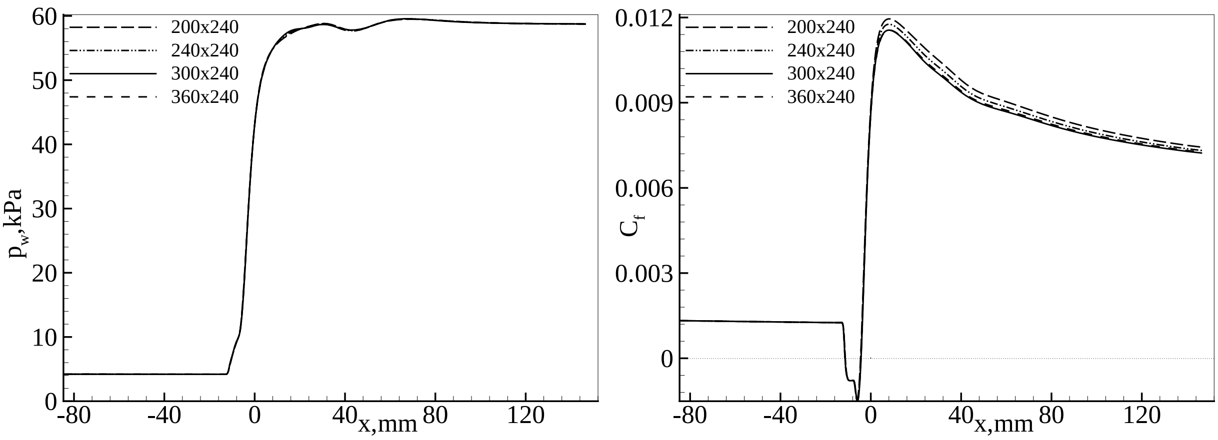

(a)

(b)

Figure 5.3: Variation of (a) wall pressure and (b) skin friction coefficient for θ = $14°$ with changing number of wall-parallel grid points upstream of origin.

The skin friction coefficient is found to be most sensitive to the computational mesh and is used to identify a grid converged solution.

The grid refinement study for the $\theta = 14°$ strongest interaction is presented below. First, the distance of the first cell center from the wall is successively halved from its initial value of 2×10^{-6} m. The corresponding values in wall units, y_2^+, are presented in Fig. 5.2a. C_f plotted in Fig. 5.2b indicate that 1×10^{-6} m is sufficient for an accurate solution. Next, the number of points in the wall parallel direction is refined until the two finest grids, 300×240 and 360×240, yield overlapping results in Fig. 5.3. Finally, the number of points in the wall normal direction is increased to arrive at the 300×400 grid. Figure 5.4 shows that further refinement to 300×460 grid points yields less than 2% variation in wall pressure and skin friction. Based

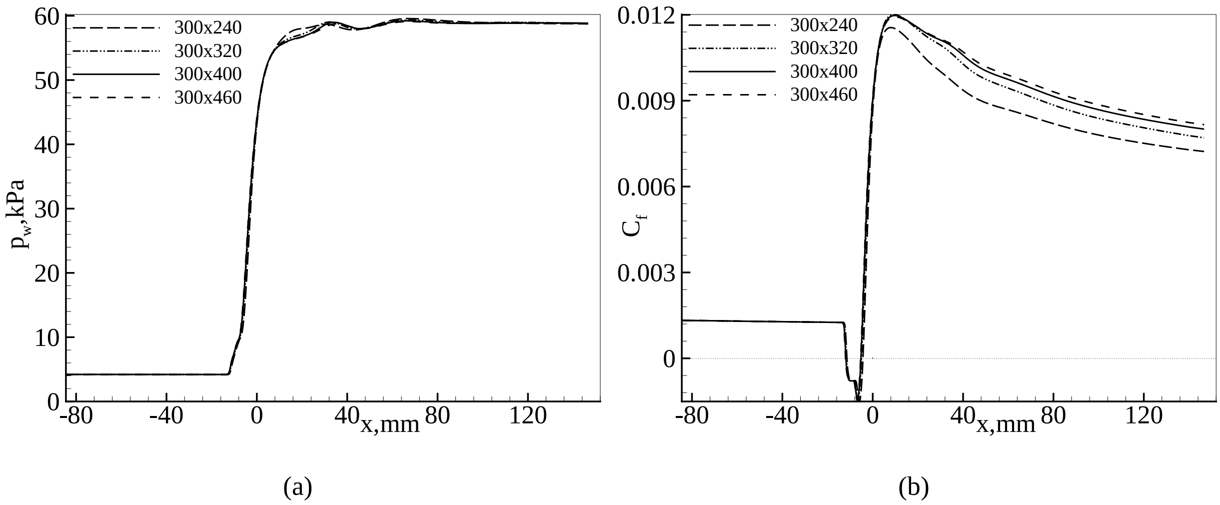

Figure 5.4: Effect of varying number of wall-normal grid points on computed (a) pressure and (b) skin friction coefficient for θ = $14°$.

on the foregoing study, the solution obtained on the 300×400 grid is considered to be grid converged.

Different Courant-Friedrichs-Lewy (CFL) numbers are used in the computations. In the computations, a CFL of 0.05 is used at the beginning and it is gradually increased to 10 in the first 100 iterations. It is further increased to 500 at 1000 iterations and to 1000 at 500 iterations, and to 5000 at 5000 iteration. A maximum CFL of 8000 is used after 10000 iterations. The computation converges in 14 cpu hrs and it takes 20000 iterations to reach the steady state solution. The computed solutions are checked for iterative convergence by plotting the C_f variation. The drop of local residue is approximately from 10^5 to 10^{-5}.

5.4 Results and discussions

The oblique shock-wave/turbulent boundary-layer interaction for 14$°$ shock deflector is shown in Fig. 5.5. The flow in the interaction region is complex due to the presence of multiple shock and expansion waves along with local flow separation and reattachment. A magnified view of the interaction region is shown in terms of the computed pressure and Mach number contours. The adverse pressure gradient of the incident shock separates the boundary layer on the flat plate. The streamline showing the extent of separation region is plotted and the separation and reattachment locations are identified by S and R respectively. The separation shock and incident shock intersect and form induced and transmitted shock waves. The transmitted shock is short in length and terminates at the expansion waves generated by the flow turning over

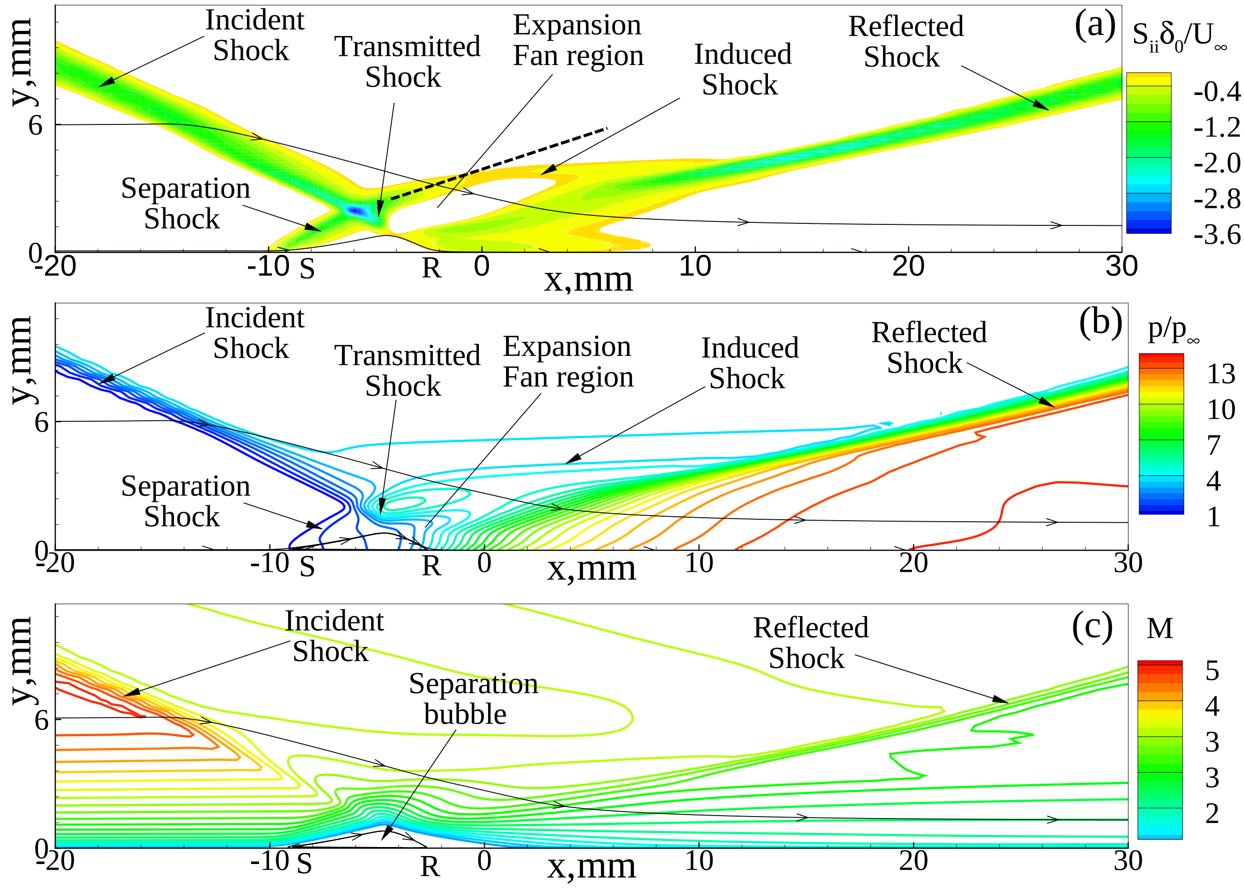

Figure 5.5: Computed (a) normalized mean dilatation (b) pressure and (c) Mach number contours showing different shocks, expansion waves and separation bubble for $\theta = 14°$ and $M_\infty = 5$.

the separation bubble. The expansion fan is embedded between the induced and reflected shock waves. It interacts with and weakens the induced shock. It also causes the induced shock to bend and merge with the reflected shock. The compression waves generated by flow reattachment coalesce to form the reflected shock. The Mach number decreases from its freestream value of 5 ahead of the incident shock to about 3.6 at the induced shock and is further reduced to 2.7 by the reflected shock. In parallel, the flow is compressed through these shock waves with a decrease in the boundary layer thickness from its undisturbed value of 5.9 mm to 4 mm.

Figure 5.6 shows the variation in pressure and skin friction coefficient along the plate. The experimental pressure measurements remain at freestream value up to the separation point. It rises to about 16 kPa across the separation shock and rises further to about 58 kPa at flow reattachment. Adverse pressure gradient of the separation shock decreases the skin friction coefficient from its undisturbed boundary layer value. C_f is negative in the re-circulation bubble and attains high values downstream of the interaction region.

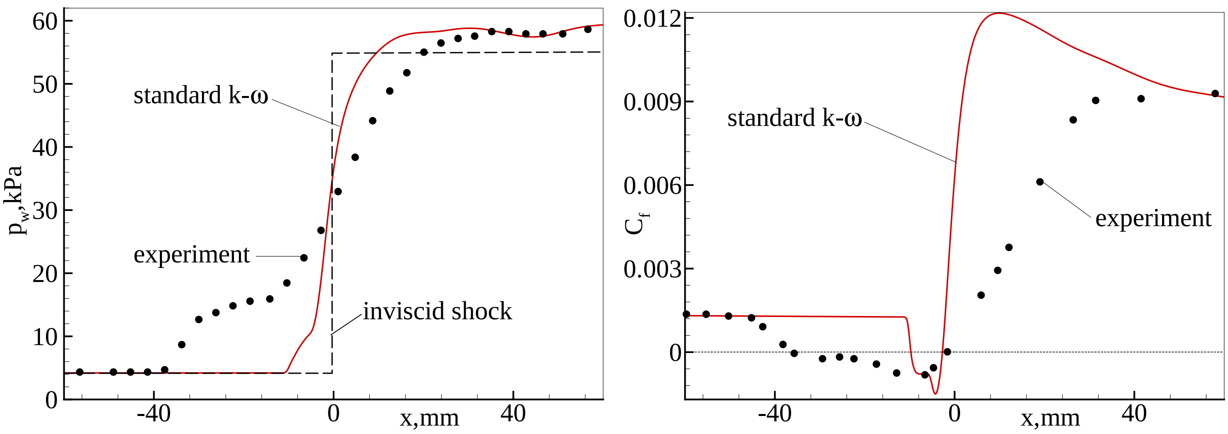

(a) (b)

Figure 5.6: Computed (a) wall pressure and (b) skin friction with $\theta = 14°$ using standard k-ω with $M_\infty = 5$, compared with experiments.

The computations using the standard k-ω model shows similar trends in surface pressure and skin friction coefficient variation. The major differences compared to the experimental data are in the size of the separation bubble and the skin friction at reattachment. The predicted separation point is far downstream of its experimentally measured location. The pressure rise at the separation shock is smaller, followed by a higher pressure gradient in the reattachment region. The computed results show some waviness in the pressure distribution downstream of reattachment. The experimental pressure data also shows similar trend. This may be due to reflection of compression/expansion waves between the wall and the reflected shock. The zero crossing of the computed C_f determines the separation bubble size as 7.6 mm. The corresponding experimental value is 34 mm. The steep rise in skin friction at reattachment grossly over-predicts the measurements. C_f decreases further downstream to values closer to the experimental data. Similar results have been reported in literature [55, 101, 33, 102]. The shock-unsteadiness correction significantly improves the model predictions. The issues involved in the application of the modification and the results obtained are discussed in detail below.

5.4.1 Application of shock-unsteadiness modification

In order to incorporate shock-unsteadiness effects, we need to identify the shock waves and high compression regions in the flow. This is done by the function f_s. The correction term is to be applied at all grid points with non-zero f_s. The shock unsteadiness damping parameter b'_1 is a function of M_{1n}. The shock-normal upstream Mach number M_{1n} is calculated by taking dot

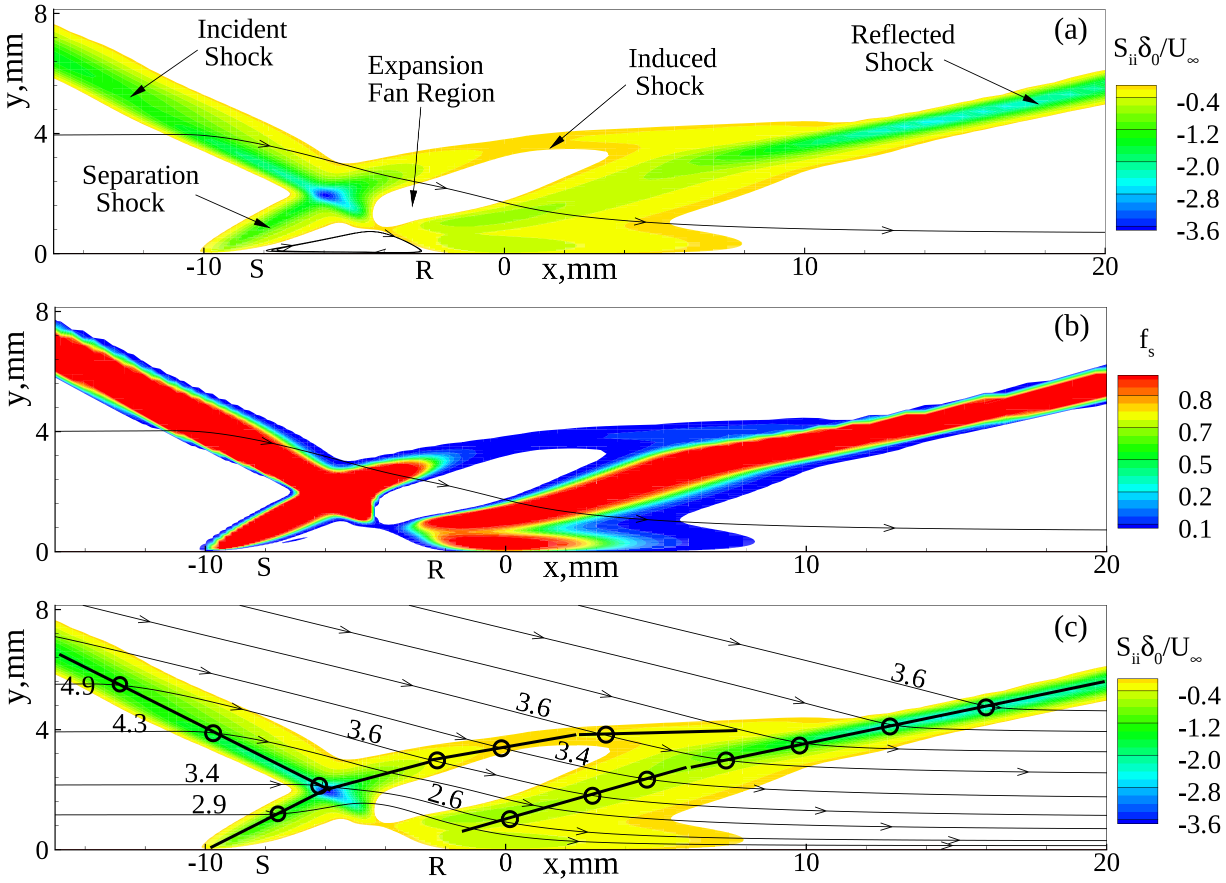

Figure 5.7: Distribution of (a) normalized mean dilatation and (b) f_s showing different shock regions in $\theta = 14°$ interaction. (c) Points are identified in the shock-waves and upstream Mach number is obtained along the corresponding streamlines.

product of vector $\vec{u}_1/a_1$ with unit pressure gradient vector $\nabla p/|\nabla p|$.

$$M_{1n} = \frac{\vec{u}_1.\nabla p}{a_1|\nabla p|} \tag{5.1}$$

Here $\vec{u}_1$ and a_1 are the velocity vector and speed of sound upstream of shock wave.

The shock waves and high compression regions in the standard k-ω solution are presented in terms of the mean dilatation S_{ii} in Fig. 5.7. The quantity S_{ii} is normalized by the freestream velocity U_∞ and boundary layer thickness δ_0 upstream of the interaction region. S_{ii} becomes negative across the incident and separation shocks and attains large negative values at the intersection of these two shock waves. S_{ii} also identifies the induced and transmitted shock waves. It is positive in the expansion fan. A large region of relatively low negative value of S_{ii} is observed in the reattachment region. This corresponds to the compression waves generated by gradual flow turning.

The original form of f_s proposed by Sinha *et al.* [12] is a function of S_{ii}/S. This function when applied to the current configuration did not capture the separation shock well. This is because S attains high values in the lower part of the boundary layer and therefore reduces the magnitude of the ratio S_{ii}/S, such that $f_s < 0.65$. In an alternate form S_{ii}/S is replaced by $S_{ii}\delta_0/V$, where V is the magnitude of the local velocity vector. This yields better reproduction of the separation shock. However small velocities very close to the wall causes difficulties in numerical evaluation of f_s. Next, the maximum magnitude of mean dilatation $|S_{ii}|_{max}$ over the computational domain is used to normalize S_{ii} in the definition of f_s. Although this function identifies the shock well, it requires additional coding to identify the maximum value $|S_{ii}|_{max}$, especially for parallel simulations run on multiple processors. Finally, the ratio of S_{ii} to U_∞/δ_0 is used to define a function of the form given below. The characteristic length δ_0 and velocity U_∞ are a priori known for a given simulation and can be specified as user input.

$$f_s = \frac{1}{2} - \frac{1}{2}\tanh[12(\mathrm{S_{ii}}\delta_0/\mathrm{U_\infty}) + 4] \tag{5.2}$$

The constants chosen are such that f_s takes values close to one in strong shock regions and goes to zero outside shock waves. Depending on the level of compression, it smoothly varies between 0 and 1. Care is taken to make f_s negligible in boundary layer flows where the standard model predictions are well validated. Fig. 5.7b shows the distribution of the above function in the interaction region and it captures the shock waves identified in Fig. 5.7a correctly. Note that the definition of f_s is based on identifying the shock waves in the computational solution and no attempt has been made to tailor the function so as to match the pressure and skin friction measurements.

In the compression ramp flow [12], the modification is active only in the separation shock. The flow upstream of the separation shock is well characterized and the variation of Mach number in the incoming boundary layer is readily available. By comparison, the regions of non-zero f_s in the current configuration correspond to the incident, separation, induced and reflected shock waves. Obtaining the local upstream Mach number at grid points at these shocks is much more challenging than the compression ramp case. Some of these values depend on the shock pattern in the intersection region and cannot be prescribed *a priori*. For example, for points in reattachment region upstream Mach number depends on the strength of the incident shock, induced shock and expansion waves.

The values of upstream Mach number at different shocks are calculated manually by identifying an upstream location along the local streamline in Fig. 5.7c. For the separation shock upstream Mach number varies approximately from 1.1 to 3.4 and it increases from 3.4

Shock	M_1	M_{1n}	b'_1
Incident	3.4 - 5.0	1.89	0.23
Separation	1.1 - 3.4	1.28	0.09
Induced	3.4 - 3.6	1.61	0.18
Reflected	2.0 - 3.6	1.85	0.2

Table 5.1: Average values of upstream Mach number normal to shock waves M_{1n} and shock-unsteadiness damping factor b'_1.

to freestream value of 5 near the boundary layer edge for the incident shock. Downstream of the incident shock wave Mach number decreases to around 3.6 for the induced shock. For the reflected shock wave, the upstream Mach number varies from around 2.0 near the reattachment point to 3.6 at the boundary layer edge. The average values of M_{1n} and b'_1 at the different shocks are listed in Table. 5.1. As expected, b'_1 approaches zero in the near wall region and attains high values at the boundary layer edge. Incorporating the exact distribution of b'_1 in the code is a cumbersome task. A representative average value of 0.188 is used to apply the shock-unsteadiness modification and sensitivity of the flow solution to variation of b'_1 is presented.

The grid refinement study using shock-unsteadiness modified k-ω model, for the deflection angle θ = $14°$ strongest interaction is done. The results are similar to that obtained in Sec. 5.3.1. The solution obtained on the 300×400 mesh is considered to be grid converged. The distance of the first cell center from the wall = 1×10^{-6} m is sufficient for an accurate solution.

The main effect of the shock-unsteadiness modification is to reduce the amplification of turbulent kinetic energy across a shock-wave. This effect can be seen in the normalized eddy viscosity contours plotted in Fig. 5.8. Standard k-ω model results in high level of eddy viscosity across incident shock and in the re-attachment region. By comparison the current shock-unsteadiness model yields much lower eddy viscosity levels in the interaction region. The computed eddy viscosity distribution using the original shock-unsteadiness modification of Sinha *et al.* [12] is also shown in Fig. 5.8b. This is very similar to the present model, except near the separation point, where μ_T/μ_∞ values are somewhat higher than that observed in Fig. 5.8c.

Lower turbulence levels with the shock-unsteadiness model results in earlier separation and thus a larger separation bubble than standard k-ω model. The shock pattern obtained using shock-unsteadiness modified k-ω model is shown in Fig. 5.9 in terms of dilatation S_{ii} and

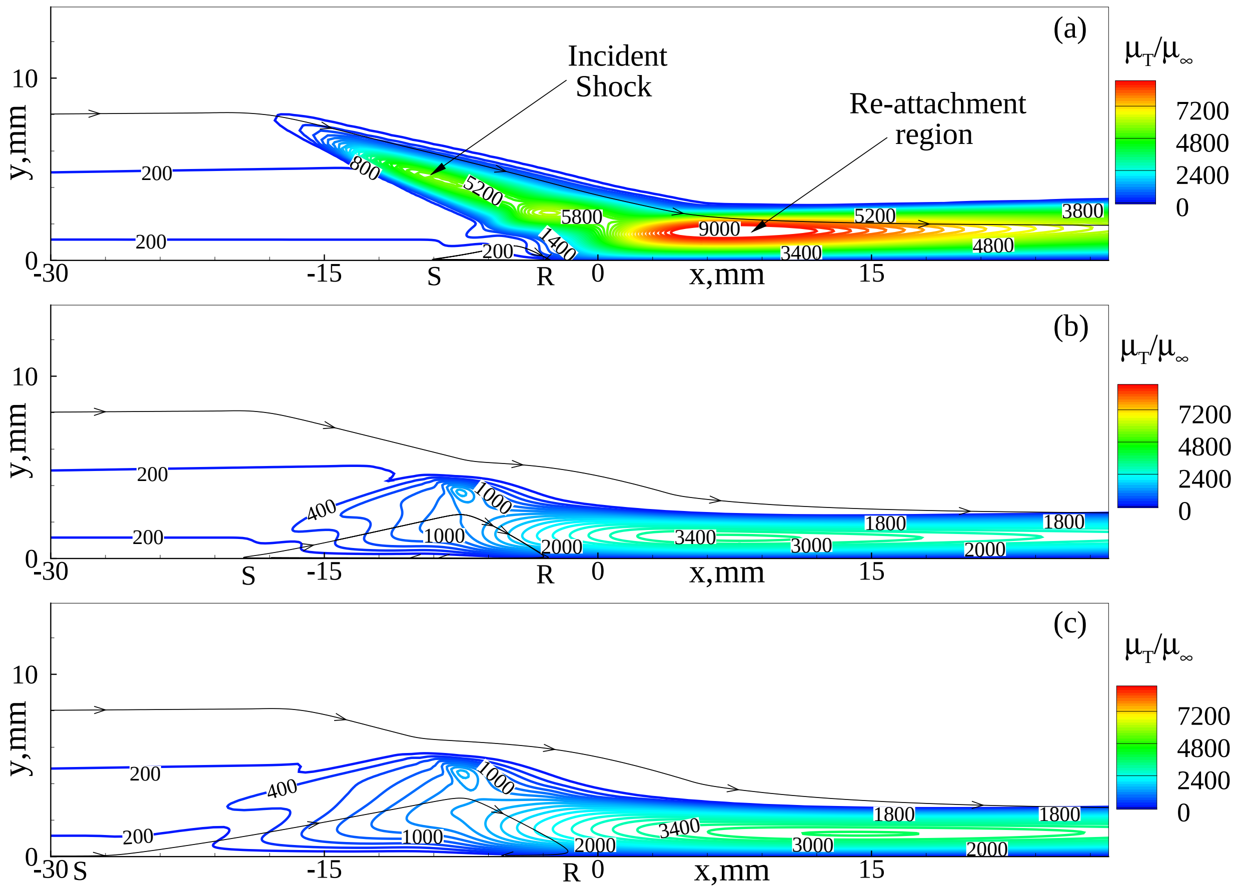

Figure 5.8: Normalized eddy viscosity contours obtained using (a) standard k-ω (b) original shock-unsteadiness [12] and (c) present shock-unsteadiness models for $\theta = 14°$.

pressure contours. It is qualitatively similar to that obtained using the standard k-ω model in Fig. 5.5, but the location and shape of the different shock-waves are altered by the shock-unsteadiness correction. Earlier separation using the modified k-ω model causes the separation shock to shift upstream closer to experiment. It also increases the length of the separation and transmitted shocks. The transmitted shock is very small and is not clear in the standard k-ω solution. Larger size of the interaction region also leads to a more prominent expansion fan in Fig. 5.9b than that obtained using the standard k-ω model.

The shock structure obtained using the current shock-unsteadiness correction has striking resemblance to the experimental shadowgraph [14] presented in Fig. 5.9c. The high compression (negative S_{ii}) regions match the corresponding dark lines in experimental shadowgraph. These include the incident, separation, induced and transmitted shocks as well as the curved pattern of the reflected shock. The experimental shadowgraph is explained in the flow diagram in Fig. 5.9c. The expansion fan generated over the separation bubble curves the induced shock downwards. The reflected shock on the other hand is curved upwards by the expansion fan. The

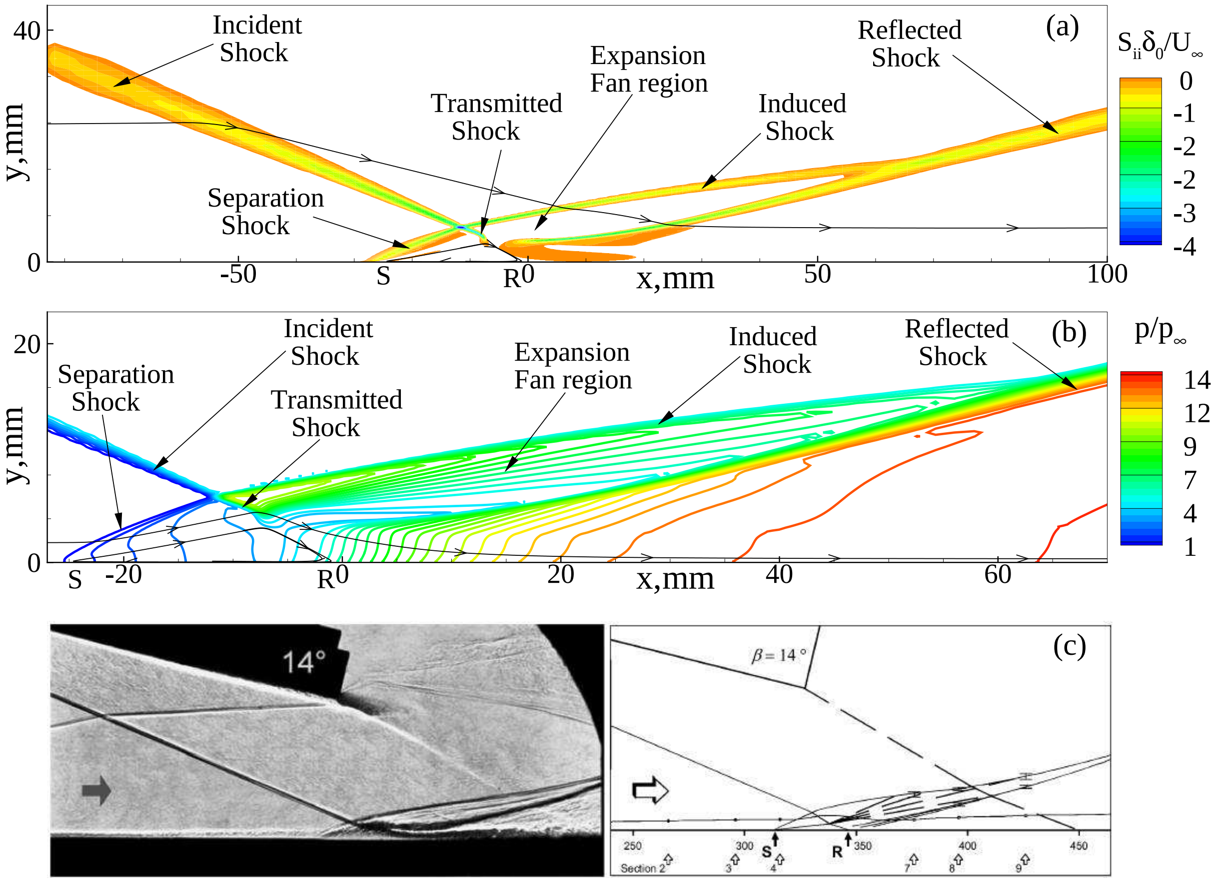

Figure 5.9: Computations showing (a) normalized mean dilatation and (b) pressure contours using shock-unsteadiness modified k-ω model for $\theta = 14°$, compared with (c) experimental shadowgraph and schematic [14].

pressure contours in Fig. 5.9b clearly show the interaction of the expansion fan with the shock-waves. The only difference between experiment and computation being the upward curving of the induced and reflected shocks caused by a second expansion fan emanating from the end of the shock generator. This effect and the resulting delay in the intersection of the two shocks is not reproduced in the computed solution. This is because the shock generator geometry is not included in the current simulations.

Wall pressure and skin friction coefficient computed using the shock-unsteadiness modified k-ω model are compared with the experiment and standard k-ω model in Fig. 5.13. The shock-unsteadiness modification appreciably improves the flow predictions in the interaction region. The location of the separation shock pressure rise is much closer to the experiment than the standard model. This results in a better comparison of the pressure plateau as well as the pressure rise in the reattachment region with the measurements. A similar trend is observed in the skin-friction results with the drop in C_f at separation point being closer to the experi-

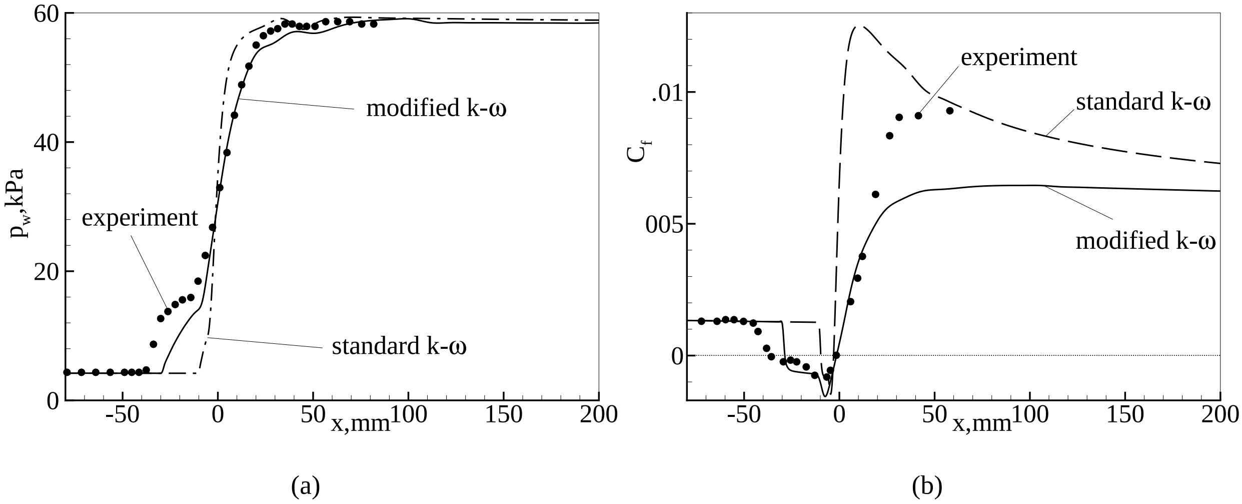

Figure 5.10: Comparison of (a) wall pressure and (b) skin friction coefficient for $\theta = 14°$ computed using standard k-ω and shock-unsteadiness modified k-ω models over a larger domain up to 500 mm downstream of interaction region, compared with experimental data of Schulein [14].

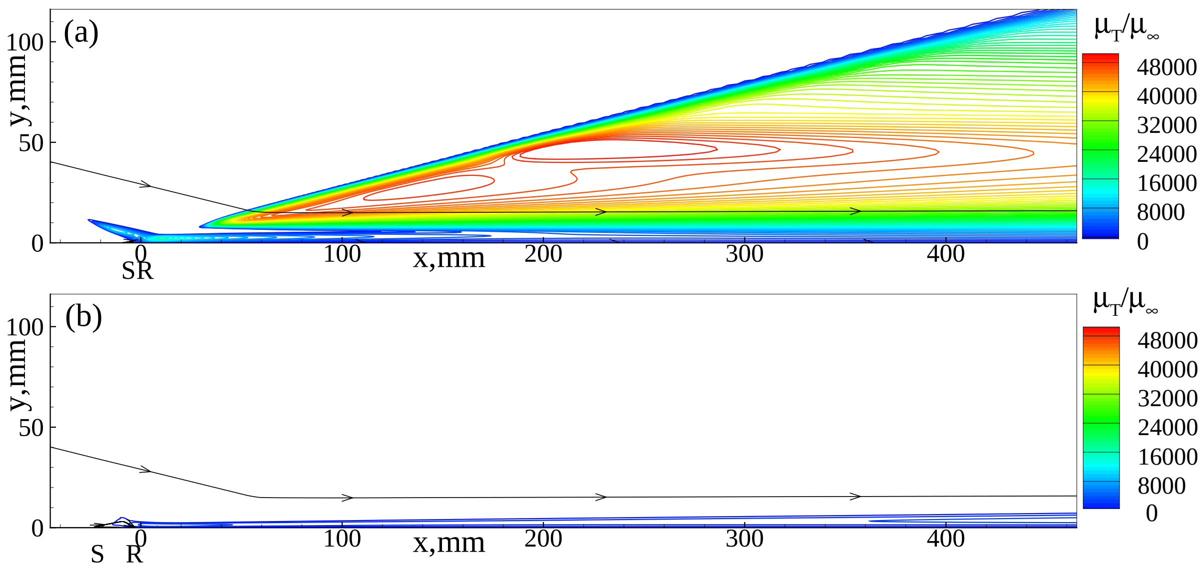

Figure 5.11: Normalized eddy viscosity contours obtained using (a) standard k-ω and (b) shock-unsteadiness modified k-ω models downstream of reattachment for $\theta = 14°$.

mental data. The reattachment point is not affected much by the modification and both models predictions compare well with experiment. Past reattachment point, the shock-unsteadiness modified k-ω model reproduces the initial build-up of C_f well, but saturates at a value lower than the experimental data. By comparison, the standard k-ω model predicts a steep rise in C_f at reattachment followed by a gradual decrease. The maximum C_f predicted at x = 10 mm is significantly higher than the measurement.

The close match of experimental skin friction value and standard k-ω prediction at x $\sim$ 50 mm is fortuitous. Computation over a larger domain extending up to x = 500 mm (Fig. 5.10)

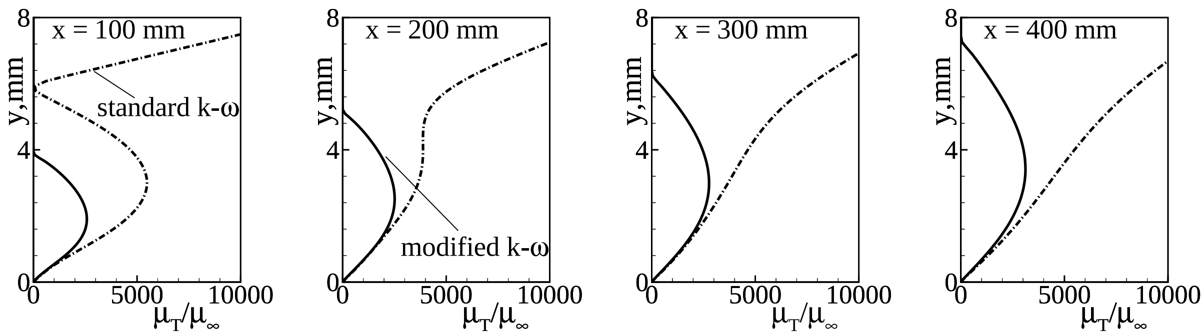

Figure 5.12: Normalized eddy viscosity profiles at different stream-wise stations downstream of interaction region computed using (a) standard k-ω and (b) shock-unsteadiness modified k-ω models for $\theta = 14°$.

	Separation point[a],mm			Reattachment point[b],mm			Separation bubble size,mm		
$\theta°$	experi-ment	standard k-ω	modified k-ω	experi-ment	standard k-ω	modified k-ω	experi-ment	standard k-ω	modified k-ω
14	35.7	9.9	27.1	1.7	2.3	-0.4	34	7.6	27.5
10	16.2	6.9	13.5	4.2	3.5	2.6	12	3.4	10.9
6	-	5.7	7.8	-	4.7	3.9	-	1.0	3.9

Table 5.2: Comparison of computed separation and reattachment points and separation bubble size with experiments. [a,b]all distances are measured from origin in upstream direction.

shows that the standard k-ω results eventually asymptote to a value close to the modified k-ω model prediction. The small difference between the two asymptotic C_f values is caused by a build-up of eddy viscosity outside the boundary-layer in the standard k-ω solution. Figure 5.11 shows the eddy viscosity distribution downstream of the interaction region. The standard k-ω model yields very high turbulence amplification across the reflected shock, with μ_T/μ_∞ levels in the post-shock inviscid flow exceeding its value in the boundary-layer. Profiles of eddy viscosity plotted at different stream-wise locations downstream of reattachment point (Fig. 5.12) show this effect more clearly. High values of μ_T/μ_∞ at the boundary-layer edge distorts the eddy viscosity distribution in the boundary-layer, and this non-physical effect persists far downstream of the interaction region. By comparison, the eddy viscosity distribution in the modified k-ω solution resembles that of a unperturbed zero pressure gradient turbulent boundary-layer for $x > 150$ mm.

The location of separation and re-attachment points computed using the standard k-ω and current shock-unsteadiness modified k-ω models is listed in Table 5.2. The corresponding points

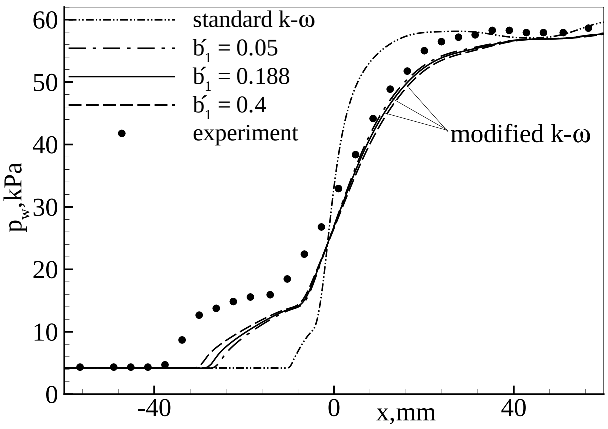

(a)

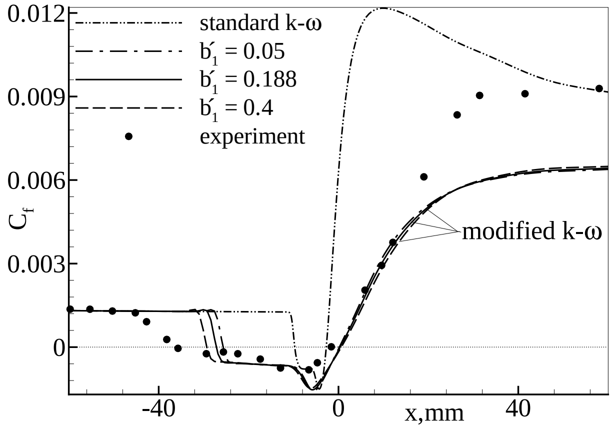

(b)

Figure 5.13: Computed (a) wall pressure and (b) skin friction coefficient for $\theta = 14°$ using standard k-ω and shock-unsteadiness modified k-ω models with different values of b'_1, compared with experiments from Schulein [14].

from oil flow visualization in the experiment are also tabulated. Quantitative comparison shows that the shock-unsteadiness correction markedly improves separation location. As a result, the separation bubble size is increased from 22% to 81% of the experimental measurement.

The sensitivity of pressure and skin friction prediction to the choice of shock-unsteadiness model parameter b'_1 is presented in Fig. 5.13. The value of b'_1 is varied from lowest to highest attainable values of 0.05 to 0.4. There is negligible effect of b'_1 variation on the surface properties except for the location of the separation shock. A higher b'_1 enhances the damping of turbulent kinetic energy, resulting in lower turbulence at the shock and thereby earlier separation. However, the variation in separation location is within 7% of that obtained using the average value of b'_1.

5.4.2 $\theta = 10°$ and $6°$ cases

Shock generator angles of $10°$ and $6°$ are simulated using the standard and modified k-ω models and results are compared with experimental shadowgraphs and surface measurements. A 240×400 computational grid is used in these simulations, which is based on a grid refinement study similar to the $14°$case. Details are omitted for the sake of brevity. The shock-unsteadiness correction is implemented in these flows using the same values of b'_1 and f_s as discussed above.

The shadowgraphs in Fig. 5.14 and Fig. 5.15 show a reduction in the intensity of the interaction than the $14°$ case, in terms of smaller separation bubble size. The pressure and skin friction data in Fig. 5.16 reflect the same trend with the values of separation and reattachment

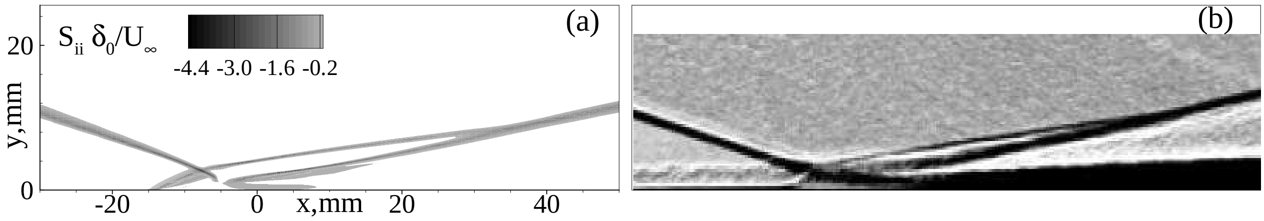

Figure 5.14: (a) Normalized mean dilatation contours computed using shock-unsteadiness modified k-ω model for $\theta = 10^\circ$ and $M_\infty = 5$, compared with (b) experimental shadowgraph from Schulein [14].

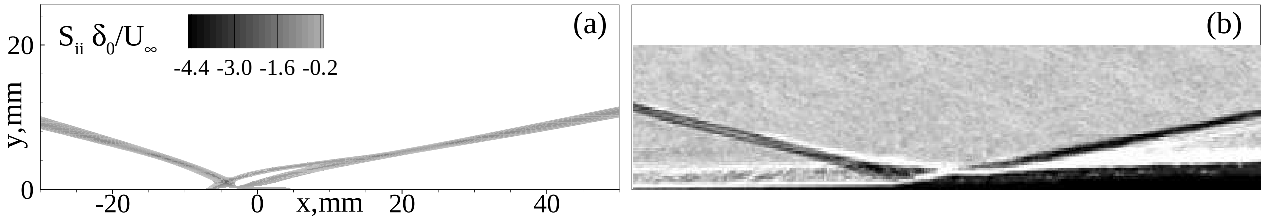

Figure 5.15: (a) Normalized mean dilatation contours computed using shock-unsteadiness modified k-ω model for $\theta = 6^\circ$ and $M_\infty = 5$, compared with (b) experimental shadowgraph from Schulein [14].

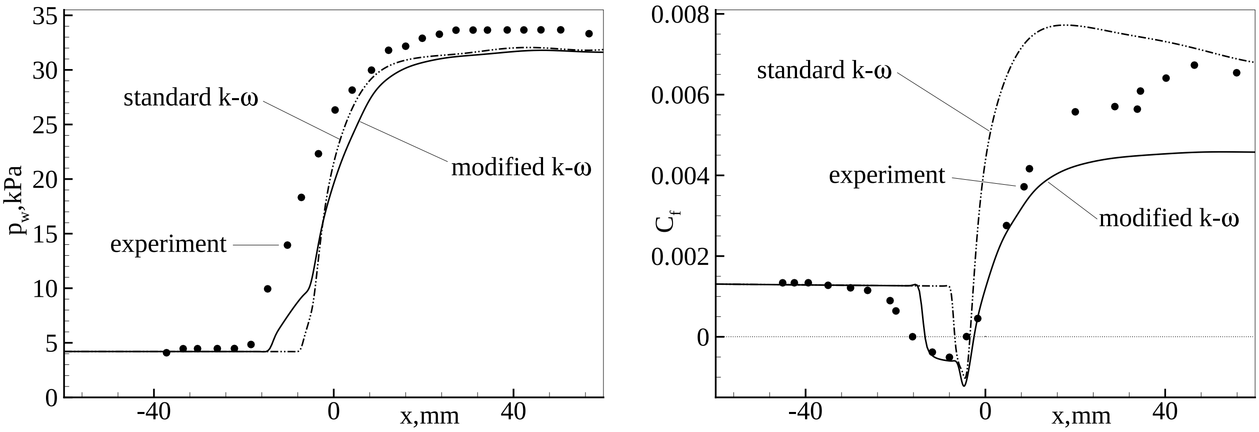

(a) (b)

Figure 5.16: Computed (a) wall pressure and (b) skin friction coefficient for $\theta = 10^\circ$ at $M_\infty = 5$ using standard k-ω and shock-unsteadiness modified k-ω models, compared with experiments from Schulein [14].

points listed in Table 5.2. As in the case of 14° shock generator, the standard k-ω model underpredicts the separation bubble size and over predicts the skin friction coefficient at reattachment. The shock-unsteadiness modification moves the separation location closer to experiment for $\theta = 10^\circ$ and increases the bubble size from 28% to 91% of the experimental value. For the 6° case a separation bubble was not identified in the oil flow pattern. The standard model predicts an incipient separation in this flow as in Fig. 5.17 and the modification increases the size of the bubble by a small amount. The computed pressure and C_f matches well with experiments.

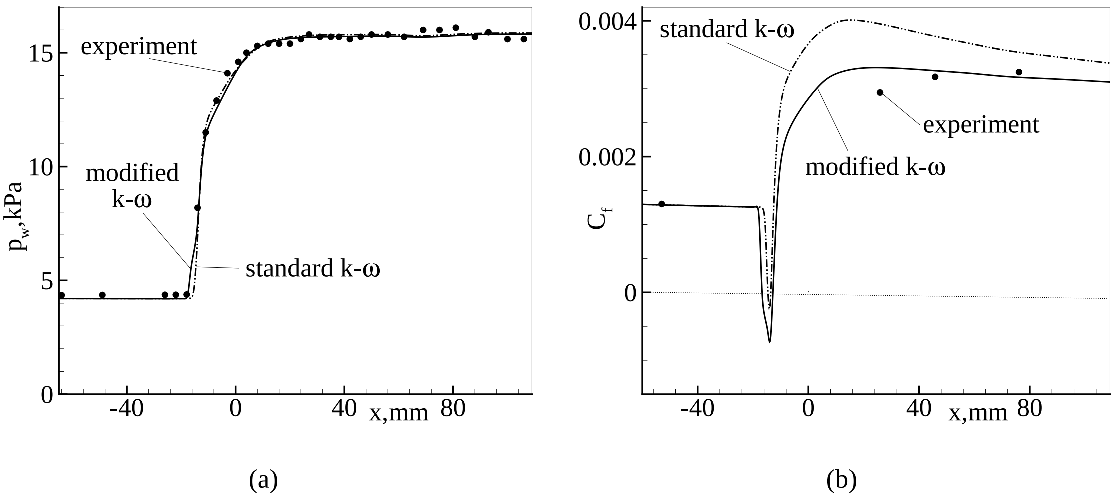

Figure 5.17: Computed (a) wall pressure and (b) skin friction coefficient for $\theta = 6^\circ$ at $M_\infty = 5$ using standard k-ω and shock-unsteadiness modified k-ω models.

5.5 Summary

In this chapter, we study the impingement and reflection of an oblique shock wave on a turbulent boundary layer. Three configurations with shock generator angles of 14, 10 and 6° are chosen at Mach 5. These cases span the range from weak shock strength with no flow separation to strong shock strength with a large separation bubble at the shock/boundary-layer interaction region. Both standard k-ω model and shock-unsteadiness modified k-ω models are applied and results are compared to experimental data.

In spite of the geometric simplicity, presence of multiple shock waves and flow expansion in the interaction region, makes implemention of shock-unsteadiness correction challenging. The standard k-ω model predicts delayed flow separation and yields too high skin-friction at reattachment. The damping effect of shock-unsteadiness correction moves the separation location much closer to the experiment. This in turn results in close matching of the shock structure with the experimental shadowgraph. Comparison with surface measurements show that the shock-unsteadiness modification yields appreciable improvement over the standard k-ω model, especially near the separation point and in the reattachment region. It however under-predicts the skin-friction coefficient in the recovering boundary-layer downstream of the interaction.

For the weakest interaction case, the effect of shock-unsteadiness correction reduces and both the standard and modified models predict the wall pressure and skin-friction well with the experiments.

Chapter 6

Simulation of a practical scramjet inlet

6.1 Introduction

A scramjet engine consists of an inlet, isolator, combustor and nozzle. The main function of a scramjet inlet is to capture air flow from the incoming hypersonic stream, compress it through a series of shocks or compression waves, and provide uniform flow to the combustor. There should be maximum mass capture along with a minimum stagnation pressure loss in the inlet. The shocks generated in the inlet and isolator replace the conventional mechanical compressors, which are required for compressing air before combustion.

A typical inlet consists of a forebody portion, which ranges from the nose of the vehicle to the cowl tip. The shocks generated on the forebody ramps compresses the air and meet very close to the cowl tip. This ensures maximum mass capture for a given geometry. The internal compression portion of the inlet is comprised of the inlet duct downstream of the cowl tip. It can have different cross sections like circular, rectangular and other intricate shapes. There are several shock waves generated in the supersonic or hypersonic flow in a scramjet inlet. These shock waves impinge on the vehicle body and have multiple reflection to form a train of shocks and expansion waves between the vehicle body and the cowl plate.

The shock waves in the inlet duct interact with the boundary layer on the walls and can result in flow separation due to strong adverse pressure gradient across the shock wave. The shock/boundary-layer interaction often results in a complex flow pattern, comprising of additional shocks, expansion waves, shear layer and separation bubble. The separation bubbles are highly viscous, and hence increase the stagnation pressure loss. Peak values of pressure, skin friction and heat transfer rates are found at reattachment point. Also, the separation bubble acts as a blockage to the flow inside the inlet duct and can result in inlet unstart. It is therefore important to predict the shock/boundary-layer interactions in a scramjet inlet, including the size of the recirculation region, accurately.

In a practical inlet configuration, presence of geometric variations add to the overall complexity of the flowfield. In the absence of experimental data, CFD is often relied upon to predict and improve the performance of scramjet inlets. It is therefore essential to perform detailed CFD simulations of the flowfield inside an inlet duct. The focus of the current work is to study the reflection of the cowl and hinge shocks from the opposite wall and to predict the resulting size of the separation bubble accurately using the shock-unsteadiness model.

6.2 Inlet configuration

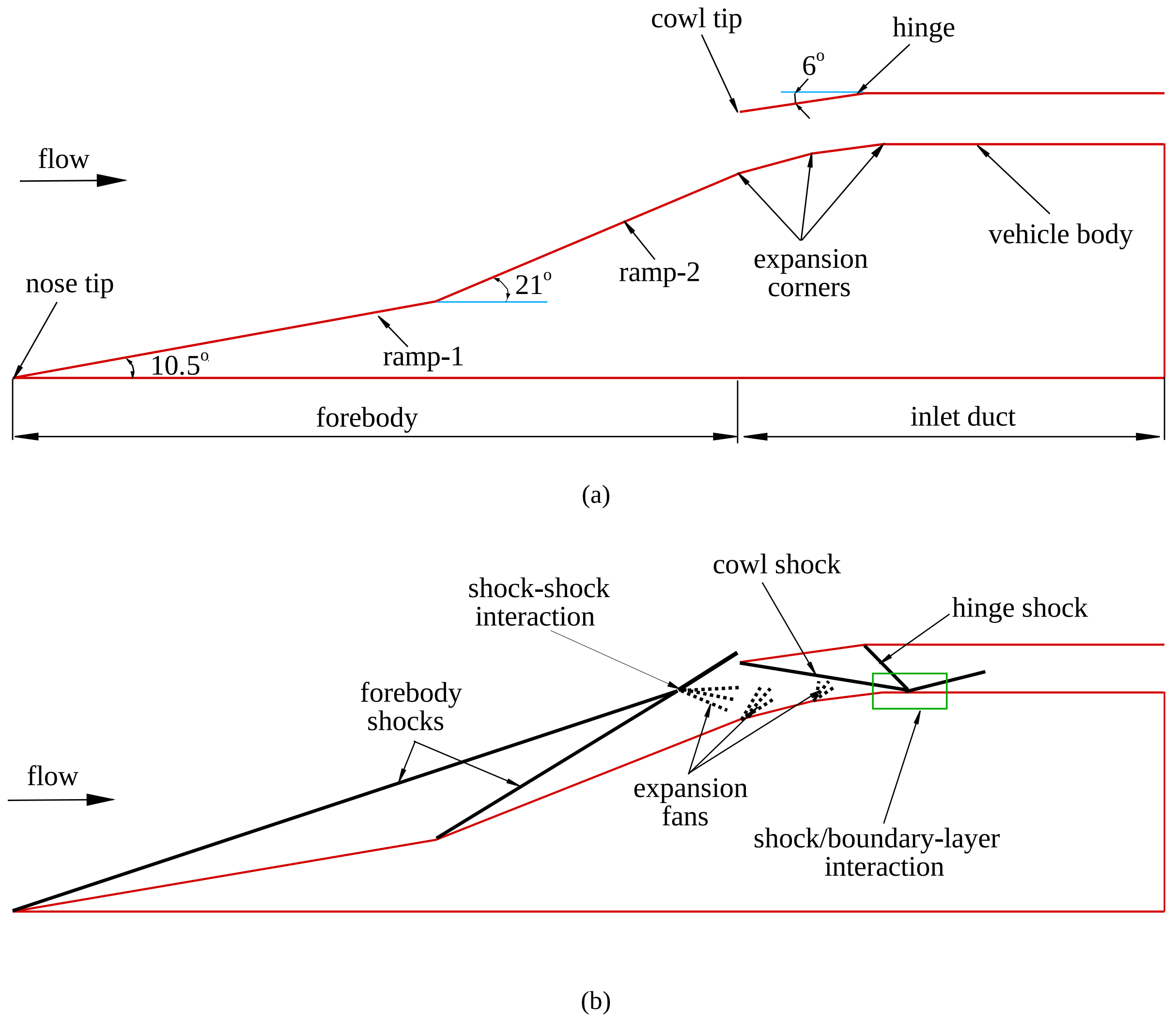

Figure 6.1: (a) Geometric configuration with (b) flow schematic, for practical scramjet inlet.

Mach number M_∞	6.5
Temperature (K)	219.3
Pressure (N/m^2)	2163.2
Density ($\mathrm{kg/m^3}$)	0.03436
Velocity U_∞ ($\mathrm{m/s}$)	1930

Table 6.1: Freestream conditions for scramjet inlet simulations.

A scramjet inlet of the mixed-compression type is shown in Fig. 6.1. The geometry is inverted in this figure and consists of two forebody ramps of $10.5°$ and $21°$ respectively, followed by three expansion corners, each of $7°$, leading to the inlet duct. The cowl is bent by $6°$ and results in formation of oblique shocks from the cowl tip and hinge location. The shock/boundary-layer interaction due to the impingement of the cowl and hinge shocks on the opposite wall is marked in the figure. The freestream conditions listed in Table. 6.1 correspond to an altitude of 26 km.

6.3 Computational grid

The grid and boundary conditions for forebody and inlet duct are shown in Figs. 6.2 and 6.3. Structured Cartesian grids are generated using Gridgen package [103]. Based on the grid convergence study, a grid of 337×190 is used for the whole geometry. There are 21 grid points upstream of the nose tip, 126 points in the forebody and 190 points in the inlet duct. In the flow-normal direction 190 points are used to span the region between the wall and the outer boundary. The grids are clustered in high gradient regions of shock waves, expansion corners and boundary layer regions of forebody and inlet duct. A minimum cell size of 1×10^{-6} m is taken in wall-normal direction of forebody and inlet duct. The corresponding y_2^+ value varies between 0.15 and 0.35 on the forebody and is less than 1.7 on the vehicle wall of inlet.

These conditions are specified upstream of the nose tip and along the top boundary, except for the region close to the cowl tip, where extrapolation condition is used to avoid reflection of forebody shock waves. At forebody, cowl and vehicle walls: isothermal ($T_w = 300$ K), no-slip and zero pressure gradient boundary conditions are assigned. An extrapolation condition is specified for the supersonic flow at the exit of the inlet duct. The freestream and wall boundary conditions for the turbulence model variables are discussed in Subsection 3.2.3.

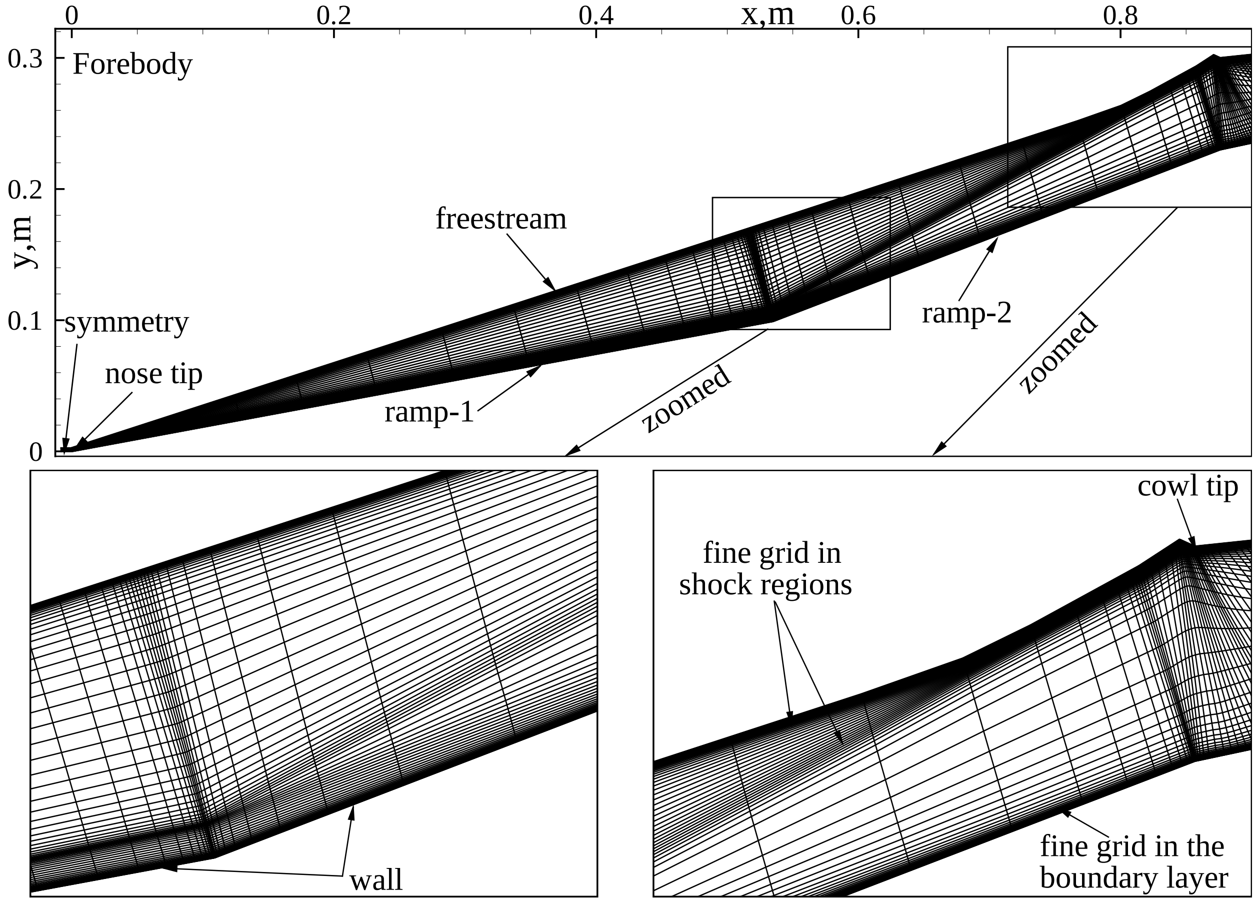

Figure 6.2: Computational grid with every second point in each direction along with boundary conditions used in forebody. The inset shows enlarged view of the grid in the ramp corner and cowl tip regions.

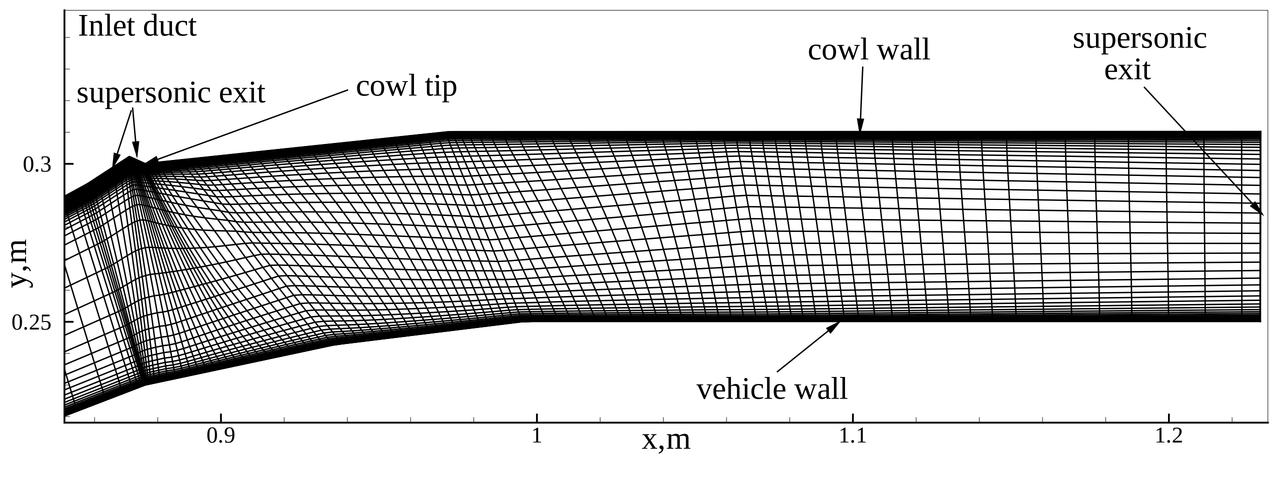

Figure 6.3: Computational grid with every second point in each direction for inlet duct along with boundary conditions.

6.4 Simulation methodology

We solve two-dimensional Reynolds-averaged Navier-Stokes equations [76]. The standard Spalart-Allmaras model [75] and shock-unsteadiness corrected Spalart-Allmaras turbulence model [12] are used in the simulations. The RANS equations are discretized using a finite volume discretization, where the inviscid fluxes are computed using a modified, low-dissipation form of the Steger-Warming flux splitting approach [85] (second order accurate). The implicit Data Parallel Line Relaxation method [86] is used to integrate the equations in time and reach a steady-state solution. Other details of the numerical method are discussed in Section 3.3. The CFL numbers used in the current simulations follow the same trend as discussed in Sec. 5.3.1. A maximum CFL number of 1000 is used in the simulations and it takes 40 cpu hours (1,50,000 iterations) to obtain the steady-state solution.

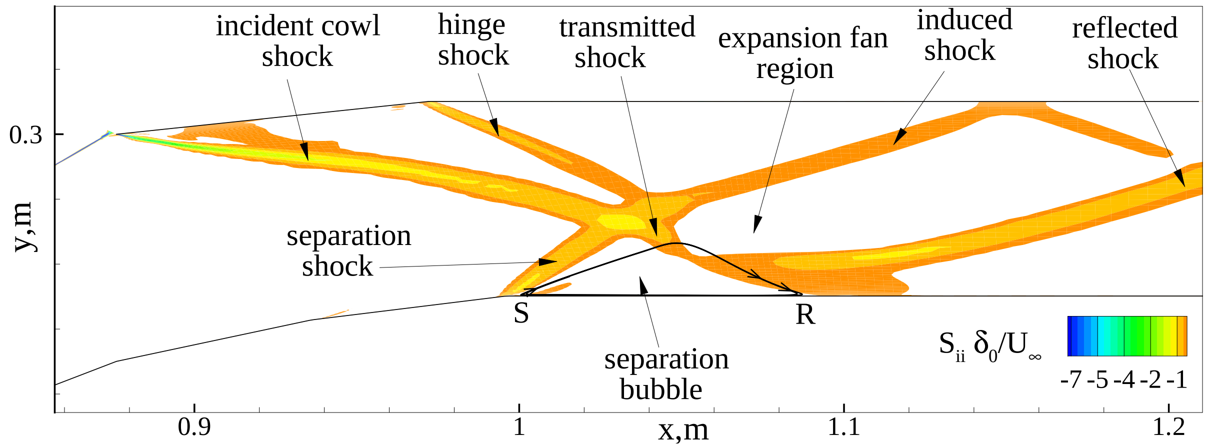

Figure 6.4: Computed normalized dilatation contours identifying shock regions in cowl region, using standard Spalart-Allmaras model [75] with M_∞ = 6.5.

Our focus of work is the shock/boundary-layer interaction region in inlet duct as shown in Fig. 6.1b, where the cowl shock interacts with boundary layer on vehicle wall to form a separation bubble. The computed shock-structure inside the inlet duct is shown in Fig. 6.4 in terms of the normalized mean dilatation contours. The shock structure is similar to that obtained in the interaction of an incident oblique shock with a flat plate boundary layer, shown in Fig. 6.5. The incident shock, separation shock, induced shock, transmitted shock and reflected shock follow the same pattern in the two flows. The differences are the additional shock generated by the hinge and the reflection of the induced shock from the top wall. These are not present in the isolated shock impingement case shown in Fig. 6.5.

The flow solution computed for the impingement of an oblique shock on a turbulent bound-

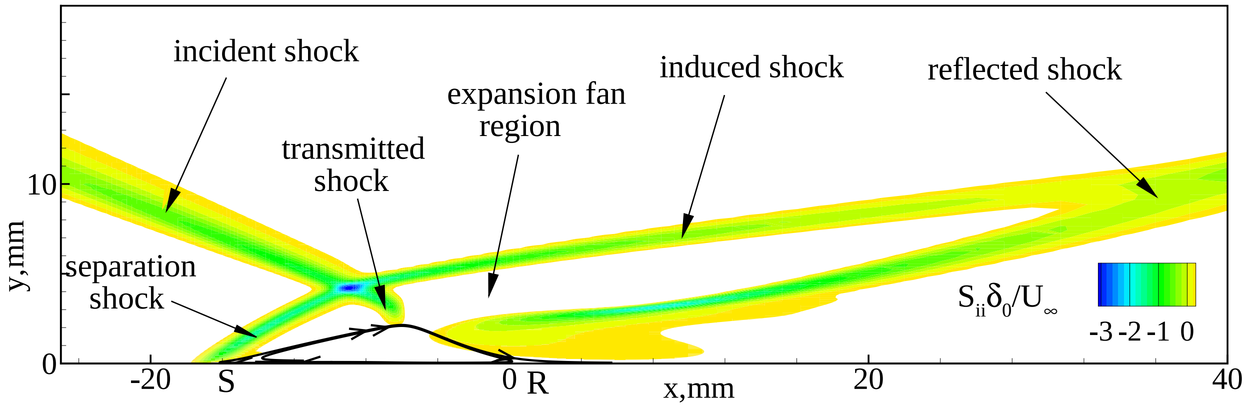

Figure 6.5: Computed normalized dilatation contours identifying shock regions using standard Spalart-Allmaras model [75] for isolated oblique shock/boundary-layer interaction with deflection angle of 14° and M_∞ = 5.

ary layer is shown in Fig. 6.6. The data corresponds to the 14° shock generator case studied in Chapter 5. The results are similar to those presented in Sec. 5.4, except for the fact that the Spalart-Allmaras model is used here instead of the k-ω turbulence model earlier. Note that the standard Spalart-Allmaras model yields too small separation bubble compared to the experimental data.

The variation of surface pressure in the interaction region is plotted in Fig. 6.7, where the initial pressure rise at $x \approx -38$ mm represents the separation location. It is apparent that the standard Spalart-Allmaras model predicts a delayed separation ($x \approx -20$ mm) as compared to the experiment. The shock-unsteadiness correction reduces the turbulent eddy viscosity at the separation shock and thus enhances flow separation. Solutions computed using different values of the shock-unsteadiness parameter c'_{b_1} are also plotted in Fig. 6.7. A higher magnitude of c'_{b_1} yields a larger separation, and c'_{b_1} = -2.0 is found to match the experimental separation location closely. Also the flow topology matches the experimental schlieren image better than the standard model (see Fig. 6.6). This value of the shock-unsteadiness parameter results in a close match of the separation location for a range of shock strengths, and therefore it is used in the study of cowl shock impingement.

6.5 Flowfield and wall data

Figure 6.8 shows the Mach contours on the forebody ramps. An oblique shock is generated at the nose tip and a second oblique shock forms at the corner between the two ramps. The two

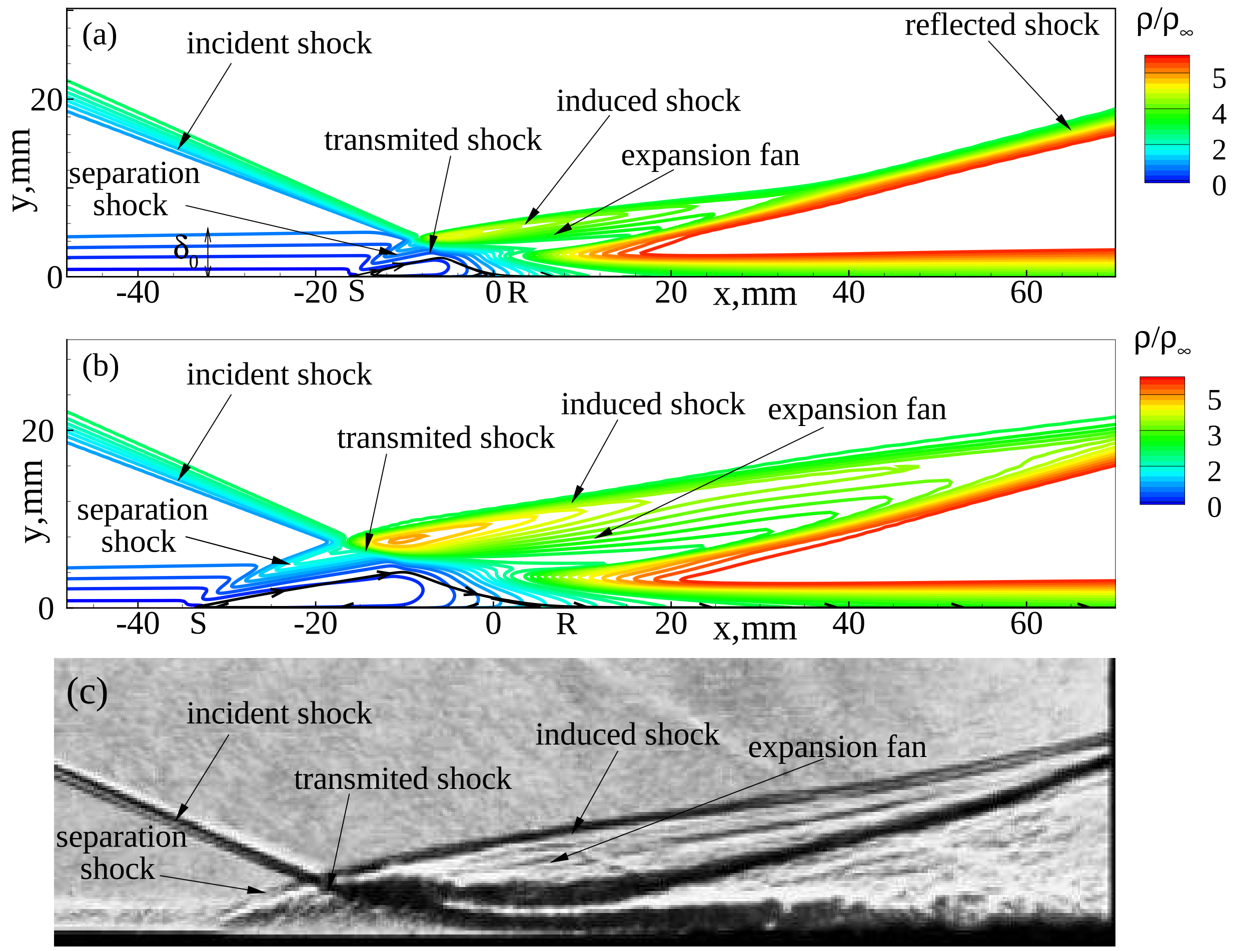

Figure 6.6: Computations showing normalized density contours using (a) standard Spalart-Allmaras model [75] and (b) shock-unsteadiness modified Spalart-Allmaras model [12] for oblique shock/boundary-layer interaction with deflection angle of $14°$ and M_∞ = 5, compared with (c) experimental shadowgraph [14].

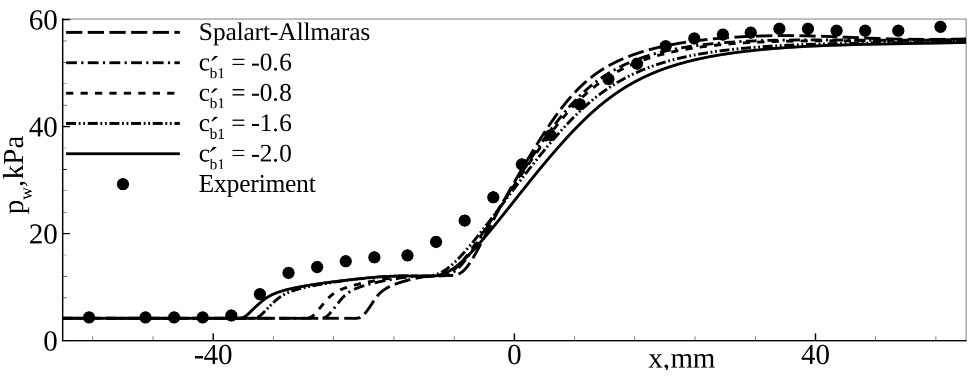

Figure 6.7: Computed wall pressure using standard Spalart-Allmaras model [75] and shock-unsteadiness modified Spalart-Allmaras model [12] with deflection angle of 14° and $M_\infty = 5$, compared with experiments [14].

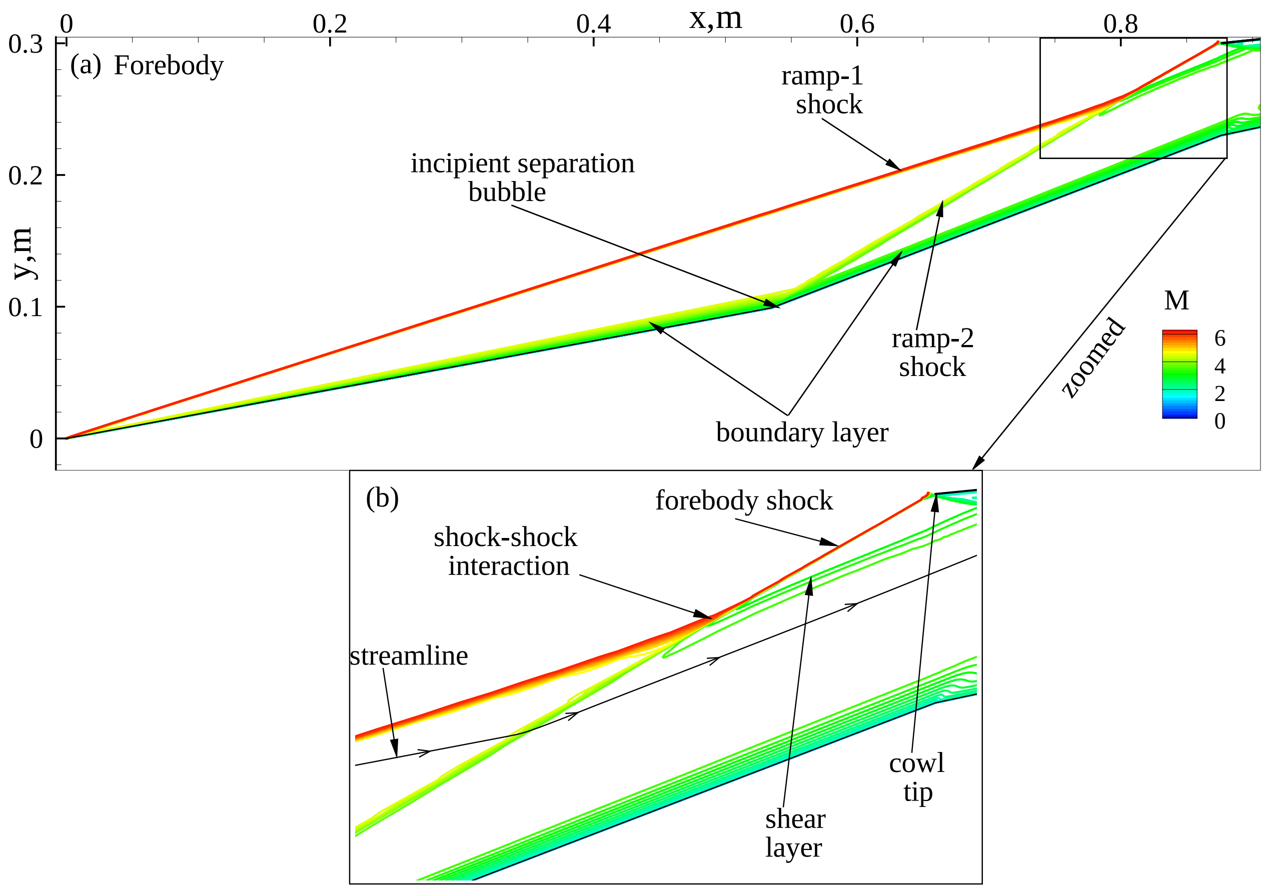

Figure 6.8: Computations showing variation of Mach contours in forebody with M_∞ = 6.5. The inset shows the enlarged view of shock-shock interaction region.

shocks intersect to form a single forebody shock of higher strength close to the cowl tip. A shear layer and an expansion fan emanates at the Edney type-VI shock-shock interaction [40] and is shown clearly in Fig. 6.8b. The shear layer enters the inlet duct and forebody shock passes slightly upstream of the cowl tip. A boundary layer develops along the ramp surfaces and an incipient separation bubble is formed at the ramp corner. An average value of Mach number = 3.64 is observed at exit of forebody and the turbulent boundary layer thickness is 10.8 mm before the expansion corner.

Fig. 6.9 shows the normalized pressure along a streamline passing through the inviscid region across the forebody shock waves. The mean pressure is normalized with the inlet freestream pressure. The computed pressure jump across the ramp-1 and ramp-2 shocks are slightly higher compared to the inviscid theory because of boundary layer displacement effect.

Figure 6.10 shows the shock structure of inviscid simulations in terms of pressure contours. The cowl shock and hinge shock interact to from a combined shock wave. The combined shock reflects from the vehicle wall to from a straight reflected shock. The expansion fans

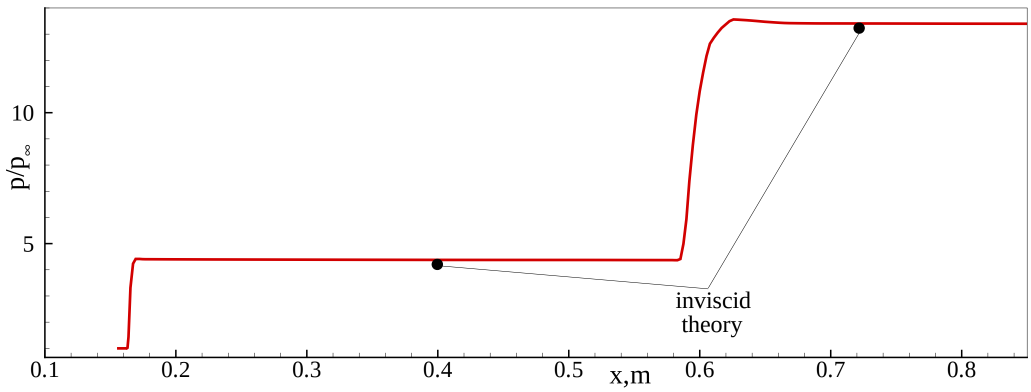

Figure 6.9: Computations showing normalized pressure jump across ramp-1 and ramp-2 shocks in the inviscid region of forebody with M_∞ = 6.5.

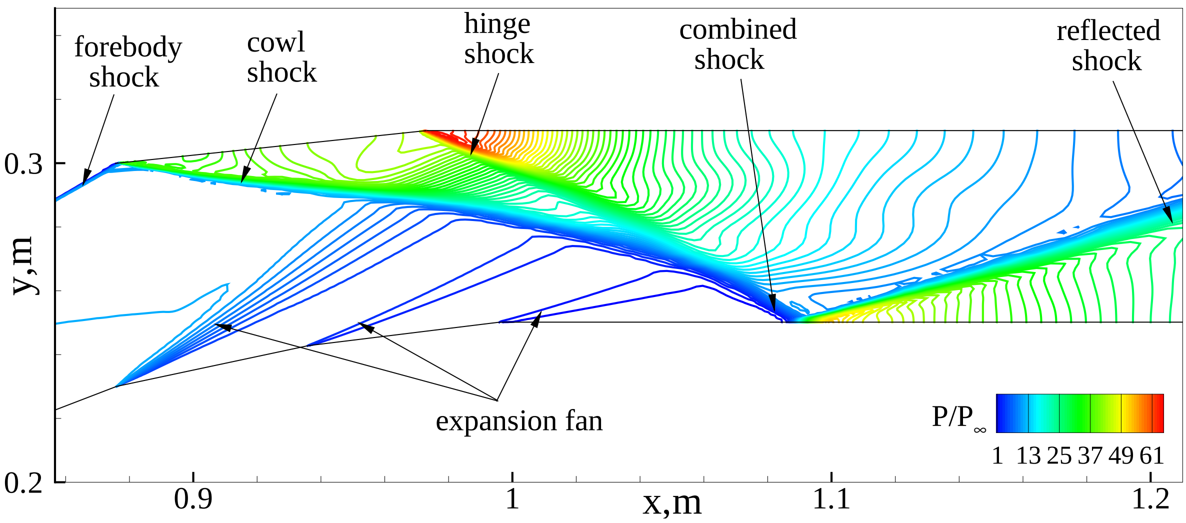

Figure 6.10: Inviscid computations showing normalized pressure contours in inlet duct.

generated at the three expansion corners bend the shock waves downwards. The flow expands across the corner expansion fans and increases the local Mach number. The expansion fans reflect between the cowl wall and the vehicle wall to from an expansion fan train.

The computed pressure and Mach contours (Figure 6.11) shows a complex flowfield in the inlet duct with large separation bubble for viscous flow. The cowl and hinge shocks impinge on the turbulent boundary layer on the vehicle wall and form a recirculation region. A separation shock is formed at the separation point and a shear layer develops over the separation bubble. Intersection of the separation and incident shocks generate the induced and transmitted shock waves. The flow turns over the separation bubble to generate an expansion fan. The compression waves generated by flow reattachment coalesce to form the reflected shock. There are multiple reflections of shocks and expansion waves in the duct.

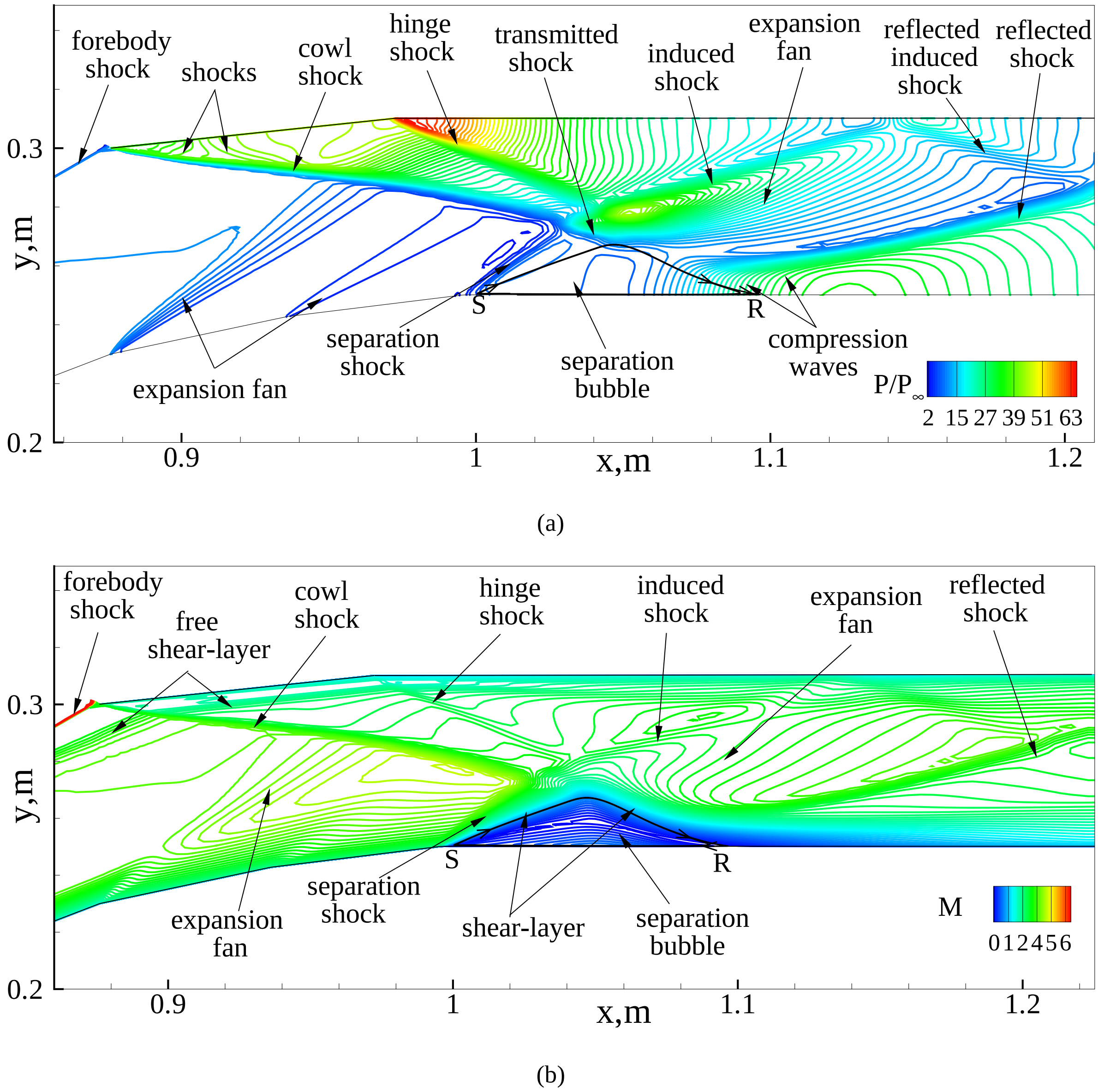

Figure 6.11: Computations showing (a) normalized pressure and (b) Mach contours in inlet duct using shock-unsteadiness modified Spalart-Allmaras model [12].

The surface pressure and skin-friction coefficient along the inlet bottom wall is shown in Fig. 6.12. The wall pressure is normalized with freestream pressure. The wall pressure drops across the two expansion corners at x = 0.86 m and x = 0.94 m. The expansion fan at the third expansion corner (see Fig. 6.10) is cancelled by the separation shock. Pressure rises at flow separation, remains approximately constant along the separation bubble and rises to peak values in the reattachment region. The skin friction data shows a large negative region between the separation (S) and reattachment (R) points. The separation bubble is 104 mm long in the streamwise direction and extends to about one third of the duct height.

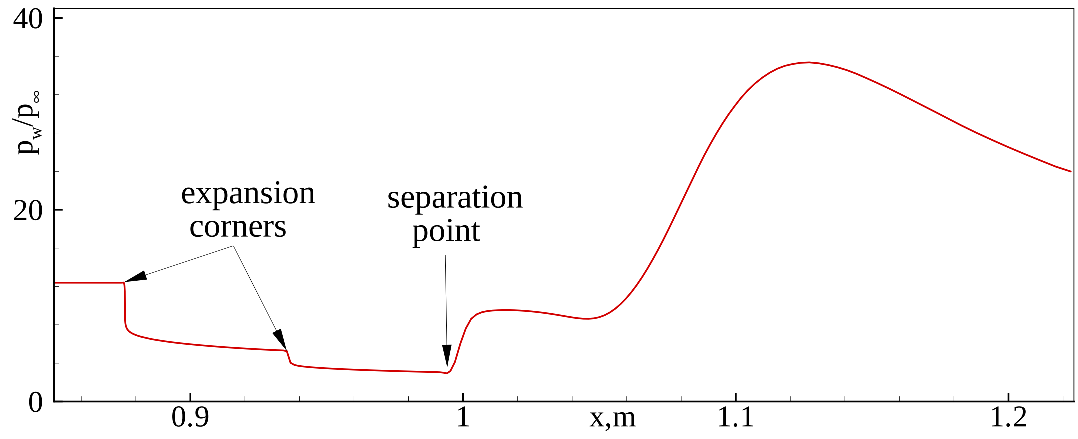

(a)

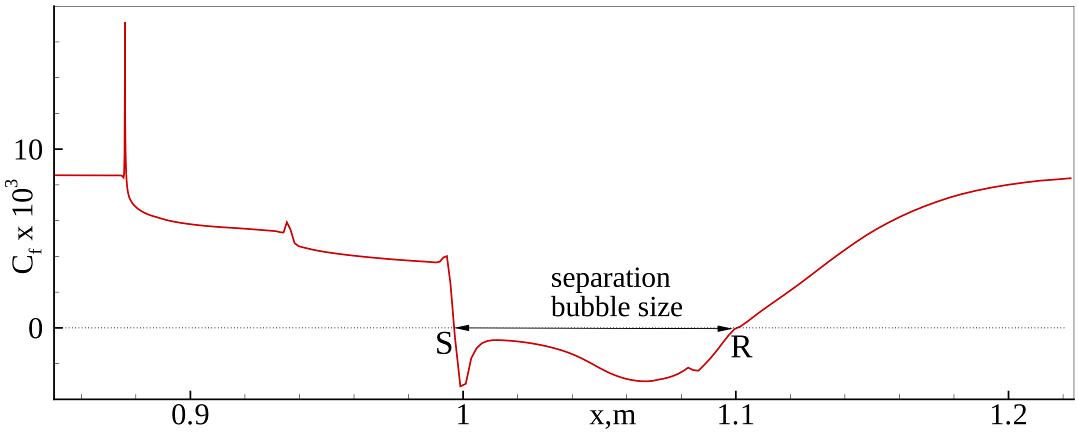

(b)

Figure 6.12: Computed (a) normalized wall pressure and (b) skin friction on vehicle wall of inlet duct using shock-unsteadiness modified Spalart-Allmaras model [12].

6.6 Comparison of separation bubble size with experiments

In this section, the computed separation bubble size is compared with available experimental data to ascertain the accuracy of the results. In the absence of experimental data for the current geometry, the data reported by Schulein [14] is used for validation. Specifically, the size of the separation bubble predicted in the inlet duct is compared with those reported in the oblique shock impingement experiments. The variations due to differences in the inflow conditions are accounted for three cases reported in Ref. [14], which correspond to shock generator angles of 14°, 10° and 6° placed in a Mach 5 flow with density of 0.2043 $\mathrm{kg/m^3}$ and temperature of 68.3 K. By comparison, the flow conditions at the entrance of the inlet duct correspond to a Mach number of 3.4, density of 0.089 $\mathrm{kg/m^3}$ and temperature of 382.2 K. These are the inviscid conditions downstream of the forebody ramp shock.

Parameters	Inlet	Oblique shock impingement		
		case-1	case-2	case-3
Free stream Mach number, M_∞	3.4	5	5	5
Deflection angle, θ°	15	14	10	6
Inviscid incident shock strength, p_2/p_1	11.34	13.62	7.63	3.76
Unit Reynolds number, $Re_{1\infty} \times 10^7$, m^{-1}	0.74	3.7	3.7	3.7
Upstream boundary layer thickness, δ_0, mm	22.7	4.66	4.66	4.66
Separation bubble size, Δs, mm	104	34	12	-
Normalized separation bubble size, $\Delta s/\delta_0$	4.58	7.30	2.58	-

Table 6.2: Comparison of flow parameters between the scramjet inlet simulations and oblique shock impingement cases [14].

The extent of flow separation in a shock/boundary-layer interaction mainly depends on the shock strength and the Reynolds number of the flow. A stronger incident shock wave results in a larger separation bubble and vice versa. On the other hand, a higher Reynolds number results in a higher level of turbulence. This in turn leads to a fuller boundary layer profile, thus resulting in delay of flow separation. Also, the separation bubble size is found to scale with the boundary layer thickness upstream of the interaction. These parameters are listed for the current configuration and for the three test cases of Schulein [14] in Table 6.2.

Deflection of a Mach 3.4 flow by the cowl shock results in a pressure rise of 11.34. A comparison of the inviscid pressure rise values places the shock/boundary-layer interaction in the inlet duct between the experimental test cases 1 and 2. The recirculation bubble in the inlet duct is however much larger than those reported in the experiments. This is because of a thicker boundary layer than that in the experimental cases. On normalizing the separation bubble size with the incoming boundary layer thickness, the simulation results compare well with the experimental data. From above analysis, $\Delta s/\delta_0$ = 4.58 for the inlet duct lies in between the experimental test cases 1 and 2.

The upstream unit Reynolds number in the current simulation is five times lower than that of Schulein's [14] cases. A lower Reynolds number increases the size of the separation bubble, and therefore $\Delta s/\delta_0$ in the inlet duct is found to be 78% higher than that in case 2, whereas the inviscid shock strengths vary by 49%. Thus, the simulation reproduces the effect of Mach number, Reynolds number and upstream boundary layer thickness on the shock/boundary-layer interaction correctly. Thus, the computations reproduce the experimentally observed trends in predicting flow separation in the inlet duct.

6.7 Inlet performance parameters

The variation of computed velocity, Mach number and static pressure at exit of inlet duct are shown in Fig. 6.13 for inviscid and viscous simulations. The inviscid computation yields an approximately uniform streamwise velocity of (1500-1600 m/s). The variation at y $\simeq$ 0.29 m is due to the reflected shock wave. The velocity profile obtained by the viscous simulations matches the inviscid result in the core flow, and has lower velocity in the boundary layer. The boundary layer thickness δ on vehicle wall is = 16 mm and on cowl wall is = 14 mm. Overall the viscous effects are present in 50% of the inlet duct cross section. A similar variation is observed in the Mach distribution at the exit plane with the core flow Mach number varying between 3.0 and 3.6.

The exit plane pressure data shows similar variation in the inviscid and viscous simulations. There is a large variation in pressure between y = 0.284 m and 0.29 m, which is caused by the reflected shock passing through the exit station. The difference between the inviscid and viscous simulation at y $\simeq$ 0.28 m is caused by the induced shock. The induced shock is generated by flow separation and therefore absent in the inviscid simulations. A reflection of the induced shock results in a higher pressure on the cowl wall than that in the inviscid solution.

	$P_{0\ \mathrm{inlet}}$, MPa	$P_{0\ \mathrm{exit}}$, MPa	π_{d}	M_{exit}
Inviscid	2.68	1.03	0.38	2.89
Viscous	2.66	0.62	0.23	2.0

Table 6.3: Inlet efficiency parameters for inviscid and viscous simulations of inlet duct.

An average value of total pressure and Mach number (see Fig. 6.13b) is calculated from the profiles and listed in Table 6.3. The inlet performance parameters [104] for both inviscid and viscous simulations are listed in Table 6.3. The pressure recovery factor π_{d} is calculated as ratio of average value of total pressure at duct exit to duct inlet. In an inviscid simulations 62% losses occur across different shock waves. The viscous simulations show higher losses of 77% and this additional loss of 15% compared to an inviscid one is due to viscous effects.

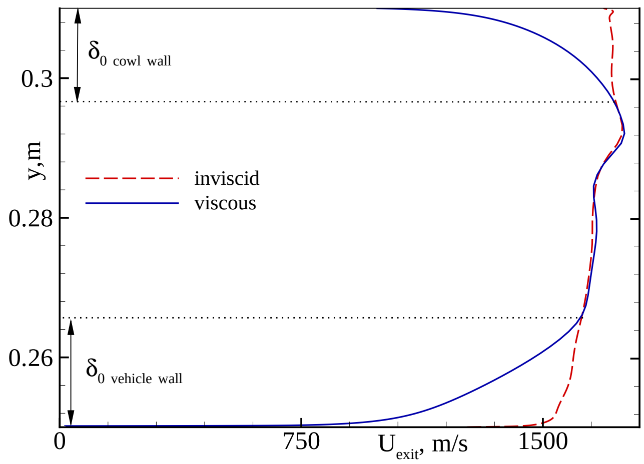

(a)

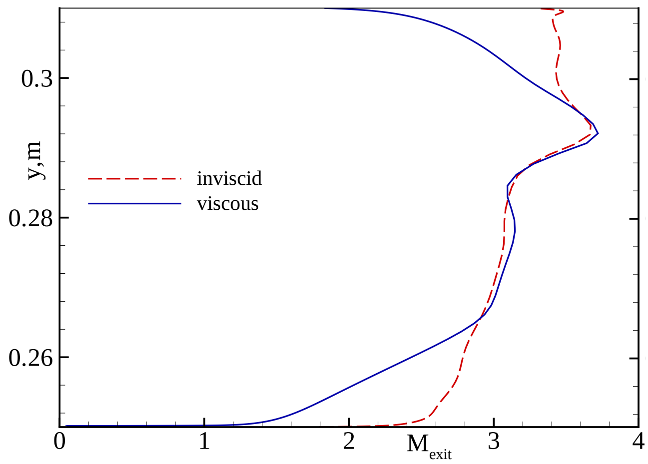

(b)

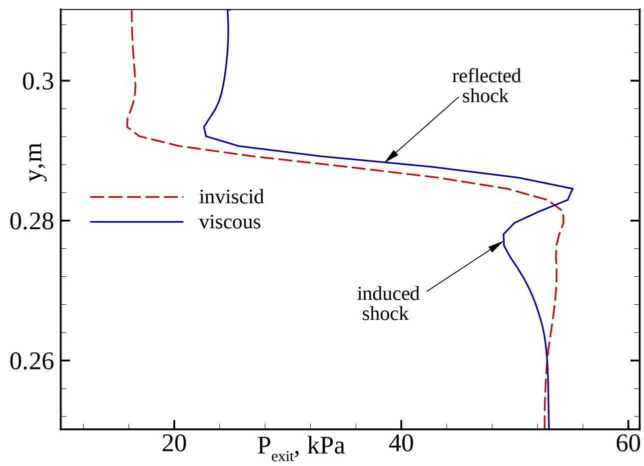

(c)

Figure 6.13: Computed flow variable profiles for inviscid and viscous simulations at exit of inlet duct: (a) velocity (b) Mach number and (c) static pressure.

6.8 Summary

Two-dimensional simulations are performed for a practical scramjet inlet geometry using the shock-unsteadiness modified Spalart Allmaras turbulence model. The inlet geometry consists of two forebody ramps, followed by expansion corners leading to the inlet duct. The cowl is hinged at 6° with respect to the inlet duct. The oblique shocks generated by the cowl and the hinge location interact with the turbulent boundary on the opposite wall to result in a large separation bubble. The presence of multiple shocks and expansion waves, their reflection inside the inlet duct, along with the recirculation region and free shear layers result in a complex flow pattern. The computed solution is used to obtain a detailed understanding the flow field, specifically the separation bubble formed inside the inlet duct.

The shock-unsteadiness parameter is calibrated against the experimental data for the different oblique shock impingement cases listed in Chapter 5, and then used in the current simulation. The separation bubble size is further validated against available experimental data for similar interactions.

Finally, the performance parameters of the scramjet inlet are obtained using the computed flow solution. The viscous effects are present in 50% of the inlet duct cross section. The viscous effects contribute additional $\approx 15\%$ of total pressure loss in inlet duct as compared to an inviscid case.

Chapter 7

Three-dimensional single-fin configuration

7.1 Introduction

The most fundamental three-dimensional shock/boundary-layer interaction is generated on a single-fin configuration. It consists of a flat plate with a sharp fin mounted perpendicular to it. The oblique shock wave generated by the fin interacts with the turbulent boundary layer on the plate and results in flow separation. The three-dimensional vortical flow thus generated alters the inviscid flow pattern. Additional shock-waves, expansion regions and free shear layers are generated that result in a complex flow in the interaction region. Practical applications of single-fin configuration include scramjet inlets, where the oblique shock generated by the cowl interacts with the side wall boundary layer.

In this chapter, the flow in a three-dimensional single-fin configuration is studied using Spalart-Allmaras model [75] and shock-unsteadiness modified Spalart-Allmaras [12] model. First, the test case is described, which is followed by the simulation methodology. Next, the flowfield is explained for the strongest shock strength case with fin deflection angle of $23°$ and M_∞ = 5. Next, the shock-unsteadiness correction to Spalart-Allmaras model is applied and the computed wall pressure and skin friction are compared with the experiments [14]. Lastly, the computed results for deflection angles of $18°$, $12°$ and $8°$ at Mach 5 are presented.

7.2 Test case

The schematic of the experimental single-fin configuration used by Schulein [14] is shown in Fig. 7.1a. The fin is inclined with deflection angle of θ to the flow direction. Different fin

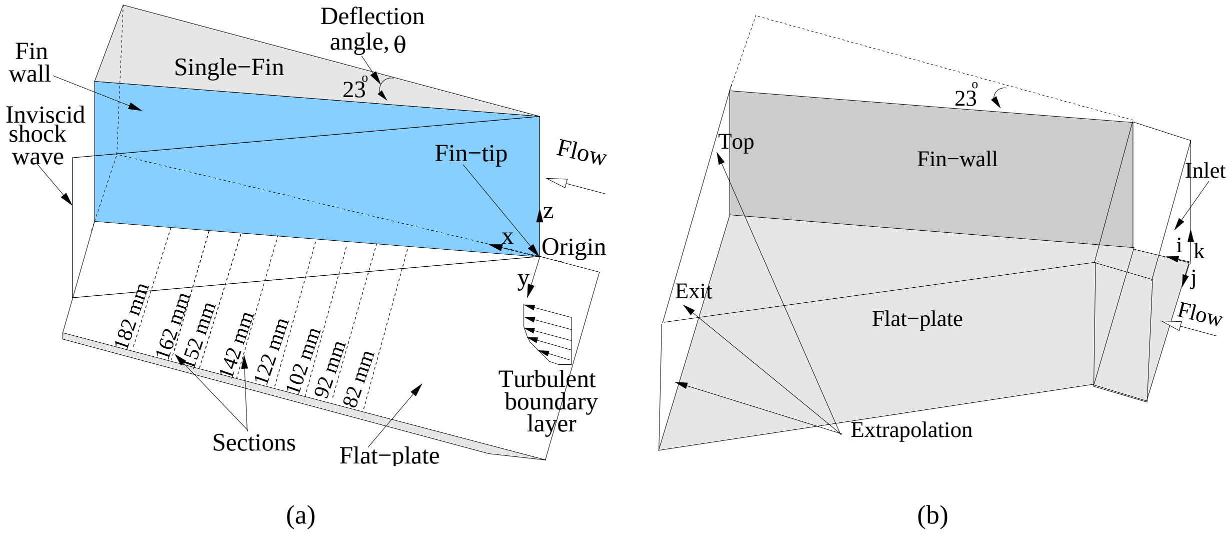

Figure 7.1: (a) Three-dimensional single-fin configuration with fin mounted on the flat-plate. The surface measurements [14] were taken along the dashed lines. (b) Computational domain with appropriate boundary conditions.

deflection angles between $8°$ and $23°$ are taken with stagnation temperature, $T_0 = 410$ K and stagnation pressure, $P_0 = 2.12$ MPa at $M_\infty = 5$. The fin height is 100 mm normal to the flat plate and the fin-tip starts at a distance of 286 mm downstream of the flat plate edge. Both the flat plate and fin wall are maintained under isothermal condition of 300 K. The flow is turbulent, upstream of the interaction region with a unit Reynolds number of $Re_{1\infty}$ = 37×10^6 m^{-1}. Wall data like pressure, skin friction and heat-transfer rates were measured at different cross sections in the shock-wave/turbulent boundary-layer interaction region (see Fig. 7.1a). The undisturbed turbulent boundary-layer properties measured on the flat plate at 20 mm upstream of the fin tip are δ = 3.8 mm, δ^* = 1.6 mm, θ = 0.16 mm and C_f = 1.35×10^{-3}.

7.3 Simulation methodology

We solve the three-dimensional RANS equations for the mean flow, as presented in Ref. [76]. The standard Spalart-Allmaras (SA) model [75] and shock-unsteadiness modified Spalart-Allmaras [12] without any compressibility corrections is used for calculating the eddy viscosity. In-house code of Sinha *et al.* [84] is used in the simulations. The governing equations are discretized in a finite-volume formulation where the inviscid fluxes are computed using a modified (low-dissipation) form of the Steger-Warming flux-splitting approach [85]. The method is second order accurate both in streamwise and wall-normal directions. The other details of the code are described in

Section 3.3.

The freestream conditions are $T_\infty = 68.3$ K and $p_\infty = 4008.5$ N/m^2. The computational domain and boundary conditions are identified in Fig. 7.1b. At the fin wall and flat plate, an isothermal wall with no-slip condition is applied. An extrapolation boundary condition is assigned at top and exit planes. The freestream and wall boundary conditions for the turbulence model variables are discussed in Subsection 3.2.3. Inlet profiles for the computations are obtained from separate two-dimensional flat plate simulation at freestream and wall boundary conditions identical to those listed above. The value of the momentum thickness reported in the experiments [14] is matched to obtain the mean flow and turbulence profiles at the inlet boundary of the computational domain.

A single-block grid is generated using a FORTRAN code. A structured Cartesian mesh with exponential stretching normal to the plate and fin walls is used to span the computational domain. The origin is taken at tip of single-fin and the grid is stretched exponentially in the upstream and downstream directions of origin. A careful grid refinement study is performed by systematically varying the number of grid points in each direction, as well as refining the cell size in critical regions. A converged grid of $140 \times 160 \times 160$ is obtained with 140 points along the streamwise direction, 160 points transverse to the flow and 160 points normal to the plate. At the wall the minimum distance of 1×10^{-6} m is taken, in wall-normal direction. The y_2^+ varies between 0.06 in the undisturbed boundary-layer to a maximum value of $y_2^+ < 0.6$ in the shock/boundary-layer interaction region. This value of y_2^+ is sufficient to capture the high gradients of mean and turbulent variables in the boundary-layer in the wall-normal direction, especially at the reattachment region.

In the computations, a CFL of 0.05 is used at the beginning and it is gradually increased to 10 in the first 3500 iterations. It is further increased to 100 at 6000 iterations and to 1000 at 8000 iteration. A maximum CFL of 5000 is used after 10000 iterations. The corresponding time steps vary from 2×10^{-12} sec for the initial iterations to 2×10^{-5} sec at steady state solution. It takes 190 cpu-hours to reach the steady state solution in 30,000 iterations.

7.4 Flow physics

An isometric view of the flow solution computed for the 23° fin is shown in Fig. 7.2. The normalized pressure contours are taken at two x-sections of 92 and 183 mm to identify the

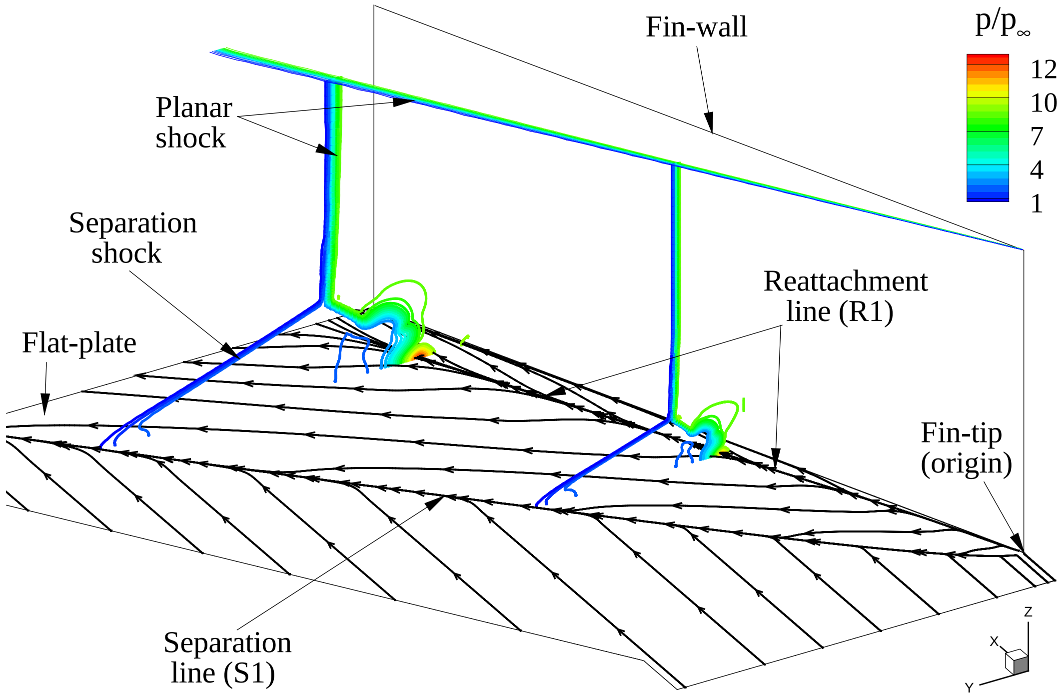

Figure 7.2: Flow solution in a single-fin shock/boundary-layer interaction in terms of the computed surface streamlines on the plate. The shock structure is shown by normalized pressure contours at x-sections = 92 mm and 183 mm.

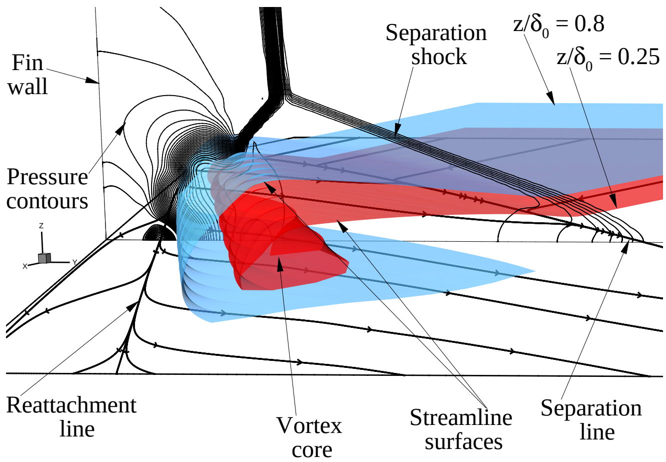

Figure 7.3: Computed stream-surfaces starting at z/δ_0 = 0.8 and z/δ_0 = 0.25 showing vortex region, and the normalized pressure contours at x-section = 83 mm, as viewed from the downstream direction.

shock structure. The flow pattern is depicted by streamlines taken at the cell adjacent to the flat plate. Very near to the wall these streamlines behave similar to the skin-friction lines.

A planar shock-wave generated by the fin interacts with the turbulent boundary-layer on the plate. It separates the boundary-layer and results in the formation of separation shock. The flow separates at primary separation line S1 and attaches at primary reattachment line R1

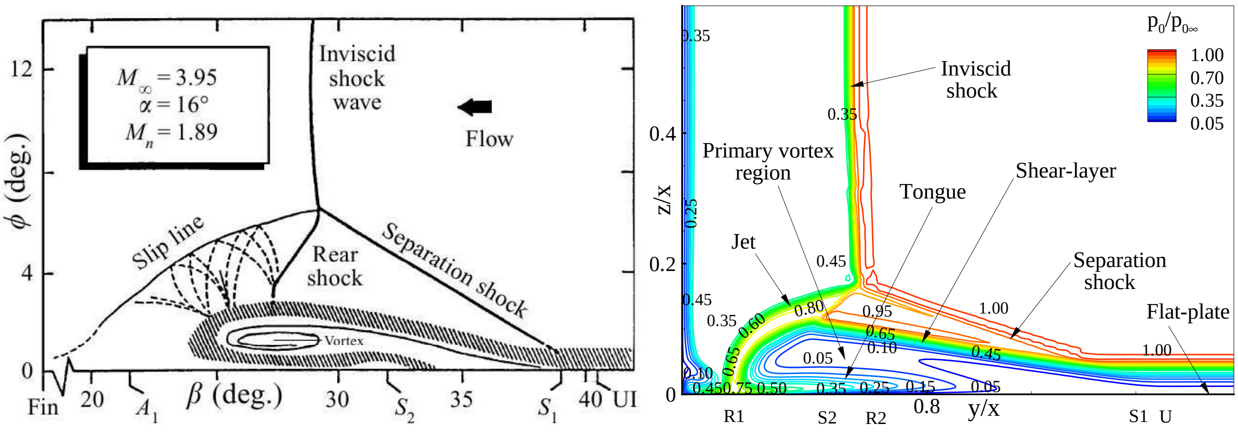

(a) (b)

Figure 7.4: (a) Experimental [106] pictorial diagram for deflection angle $\alpha = 16°$ and $M_\infty = 3.95$. (b) Computed normalized stagnation pressure contours at x-section = 123 mm, for $\theta = 23°$ and $M_\infty = 5$.

near the fin wall. The streamlines converge at separation line S1 and the fluid moves upwards normal to the plate and then turns in counter clockwise direction to form a helical flow as shown in Fig. 7.3. Two stream surfaces originating at z/δ_0 = 0.8 and z/δ_0 = 0.25 are shown, where z is the normal distance from the plate and δ_0 is the undisturbed boundary-layer thickness. At the reattachment line the fluid impinges on the plate from top, making the streamlines diverge in either direction. The inviscid shock-wave in Fig. 7.3 bifurcates into a lambda structure and encloses the vortex region.

The experimental [106] flowfield schematic is shown in Fig. 7.4a. The inviscid shock bifurcates and forms a separation shock and a rear shock, and results in the formation of lambda structure. The boundary layer separates across the separation shock and forms a conical vortical flow (displayed by shaded region) underneath the lambda shock structure. A slip line is generated from the triple point of intersection of three shock waves and a set of compression and expansion waves are formed between the shear layer and the slip line. The computed contours of local stagnation pressure P_0 is normalized with the freestream stagnation pressure P_{0_∞} and is shown in Fig. 7.4b. The computed flow features match qualitatively with flowfield diagram in Fig. 7.4a. The shear-layer is observed over the vortex region, which emanates from the separation point and interacts with the rear shock-wave and then rolls up and turns back to from a tongue. A secondary flow separation region was observed in the experiments of Schulein [14]. In the present computation, secondary flow is not predicted, but its effect is observed in the region beneath the tongue.

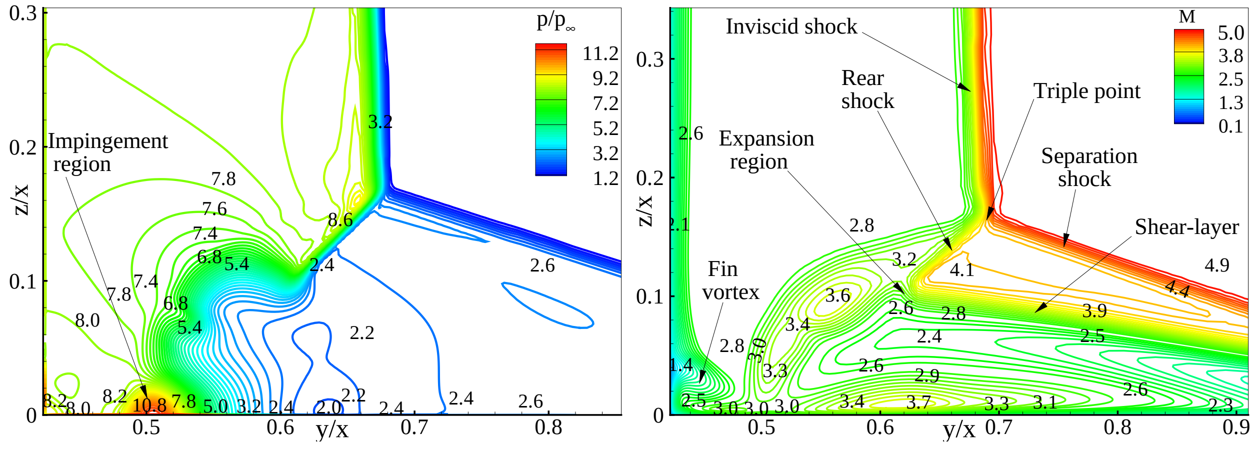

(a) (b)

Figure 7.5: (a) Enlarged region of computed (a) pressure contours (b) Mach contours at x-section = 123 mm.

The computed normalized pressure contours are shown in Fig. 7.5a. An expansion fan is generated when the rear shock-wave reflects from the shear layer. The computed Mach contours are shown in Figure 7.5b. A type-IV shock-shock interaction [40] is observed at the triple point. The alternate increase and decrease in Mach contours in the region between shear layer and jet represents the weak compression and expansion waves corresponding to as observed in Fig. 7.4a. The flow remains supersonic in the separated region. Small subsonic pockets are observed near the corner region of fin wall and plate. The supersonic jet (shear-layer) emanating from the triple point of shock-shock interaction impinges on the flat plate. High values of pressure is observed in the impingement region marked in Fig. 7.5a. A small fin-vortex is formed when the fluid coming from the inviscid region interacts with fin wall and turns in the clockwise direction, as viewed from the downstream direction. A corner-vortex was observed in the vapour screen images of the experiments [57].

7.5 Comparison of computed wall data with experiments

In Fig. 7.6, the computed normalized pressure and velocity contours are overlapped with the normalized wall pressure and skin friction on the flat plate at x-section = 123 mm. The surface data is taken along the dashed lines as shown in Fig. 7.1a. The distance along y-axis is normalized with the corresponding x-section distance measured from the fin-tip. The wall pressure remains constant in the undisturbed boundary-layer before the interaction region. The separation shock affects the upstream flow at point of influence U and the wall pressure rises

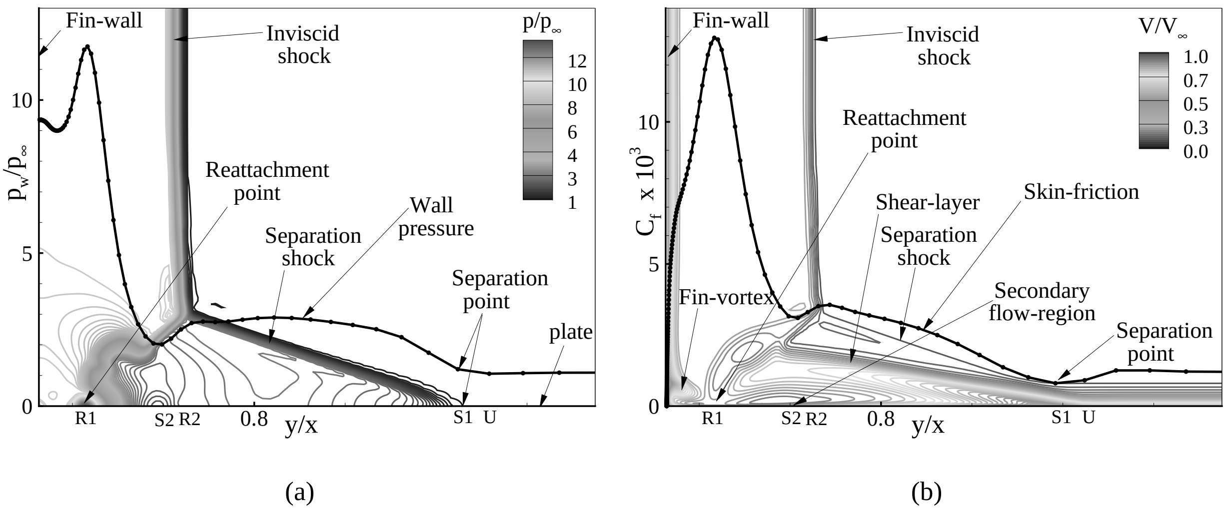

Figure 7.6: Computed (a) normalized pressure contours overlapped with normalized wall pressure and (b) normalized velocity contours overlapped with skin-friction coefficient, at x-section = 123 mm.

effectively across the separation shock at primary separation point S1. It remains constant in the separated vortex flow and rises to peak values at primary reattachment R1. The wall pressure then decreases away from the reattachment region and rises near the fin-plate junction. The skin friction does not vary significantly in the unperturbed boundary-layer before the region of influence U. The boundary-layer is compressed across the separation shock wave, hence it increases the velocity gradient and thereby increases skin friction. An additional rise of skin friction in R2 region is due to higher levels of the eddy-viscosity. It then rises between S2 and R1. At the reattachment point R1, skin friction reaches to peak value due to high values of the velocity gradient.

Figure 7.7 shows comparison of the computed wall pressure and skin friction with the experimental data [14]. The experiments give initial pressure rise location at y/x = 1.22, where as the standard Spalart-Allmaras model predicts a delayed separation at y/x = 1.14. The computed surface pressure compares well with experiments in the primary vortex and reattachment point R1. The skin fiction coefficient also shows a similar trend, but the peak skin friction at reattachment is underpredicted. The computed locations of primary separation point S1 and reattachment point R1 are compared with the experimental data at different x-sections in Table 7.1. It is observed that, at all the x-sections, the standard SA model predicts initial pressure rise location downstream as compared to the experiment.

Next, the shock-unsteadiness correction of Sinha *et al.* [12] is applied to the complex region of three-dimensional shock/boundary-layer interaction. The shock-unsteadiness parameter

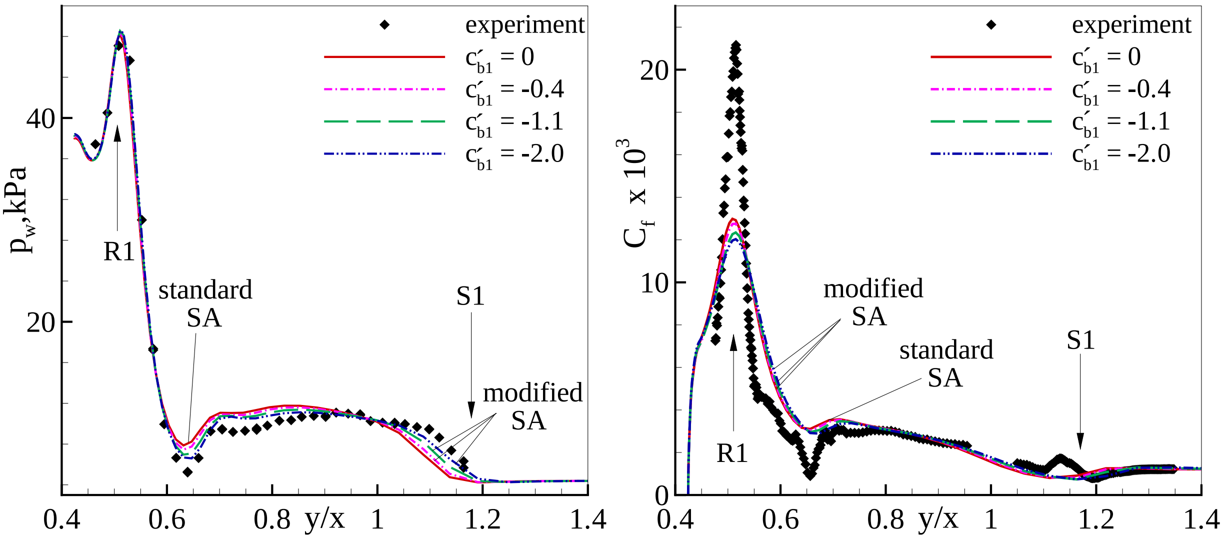

(a) (b)

Figure 7.7: Comparison of computed (a) wall pressure at x-section = 154 mm and (b) skin friction at x-section = 123 mm with experiments [14] using standard Spalart-Allmaras model [75] and modified Spalart-Allmaras model [12].

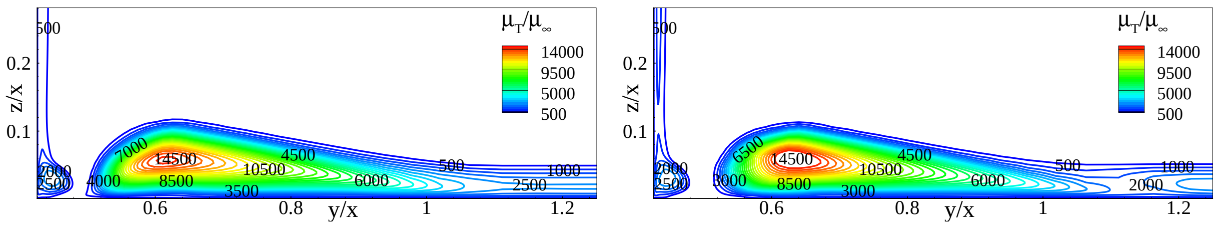

(a) (b)

Figure 7.8: Computed normalized eddy-viscosity contours at x-section = 123 mm using (a) standard SA model and (b) shock-unsteadiness modified SA model with c'_{b_1} = -2.0.

c'_{b_1} (see Section 4.5.2) is a function of the upstream normal Mach number M_{1n} and needs to be evaluated at each shock wave so as to implement the shock-unsteadiness correction. The three dimensional shock structure in the single fin configuration is quite complex. It is not easy to find the orientation of the different shock waves and the inclination of the upstream flow at each shock. Therefore, it is a difficult task to calculate the mean value of M_{1n}. An alternate approach is to use different values of c'_{b_1} in the current single-fin case to improve the flow predictions. Similar approach by Gaitonde *et al.* [105] was used for simulating three-dimensional double-fin shock/boundary-layer interaction. The turbulence model constants were varied by limiting the value of production term in standard k-ϵ turbulence model. A smaller value of model constant resulted in lower turbulent kinetic energy. Hence, the computed solution resulted in a larger separated region and matched well with the experimental flowfield and wall pressure.

	S1			R1		
x-section, mm	Exp	SA	modified SA	Exp	SA	modified SA
82	1.3	1.24	1.3	-	0.5	0.5
92	1.27	1.22	1.27	-	0.51	0.51
122	1.23	1.16	1.21	-	0.51	0.51
152	1.22	1.14	1.2	0.52	0.52	0.52
162	-	1.13	1.18	-	0.51	0.51
182	-	1.12	1.15	0.52	0.52	0.52

Table 7.1: Computed primary separation point S1 and reattachment point R1 compared with the experiments [14] at different x-sections on the flat plate.

In the present case, different values of the shock-unsteadiness parameter c'_{b_1} taken in the simulations are shown in Fig. 7.7. The shock-unsteadiness correction reduces the turbulent eddy viscosity in the region of the separation shock as depicted Fig. 7.8. A higher magnitude of c'_{b_1} = -2.0 yields a larger separation, and is found to match the experimental initial pressure rise location closely. This causes increase in the length of the separation shock and hence brings the separation point predictions close to the experiments. The modification also predicts lower values of μ_T/μ_∞ in the region of y/x $\simeq$ 0.72, as compared to the standard SA model and improves the pressure distribution in the region between S2 and R2. The pressure distribution is well predicted in the reattachment region and corner region of the plate-fin junction. Overall, the modified SA model matches experimental data better than the standard SA model at all locations (see table 7.1).

The skin friction is underpredicted by 42% at R1 and is over predicted between S2 and R2 in Fig. 7.7b. A vortex region is calculated based on the distance between S1 and R1. The standard SA model predicts vortex region of 74 mm whereas the modified SA model predicts 79 mm which is close to experimental value of 82 mm. The y/x values of primary separation point S1 and primary reattachment point R1 can be obtained from computed skin friction plots similar to that listed in table 7.1. The shock-unsteadiness model improves the location of S1 and matches well with experiments.

Computations are performed for fin deflection angles θ = 18°, 12° and 8° at Mach 5.

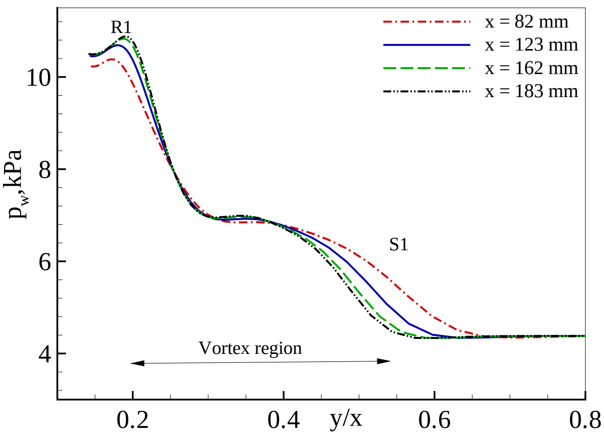

(a)

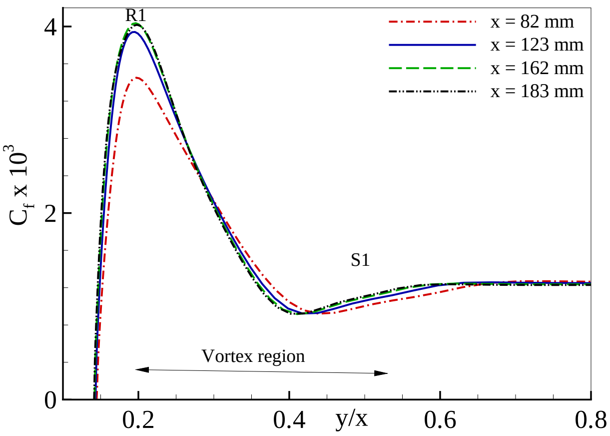

(b)

Figure 7.9: Computed (a) surface pressure and (b) skin-friction at different x-sections for single-fin configuration with $M_\infty = 5$ and deflection angle, θ = 8°.

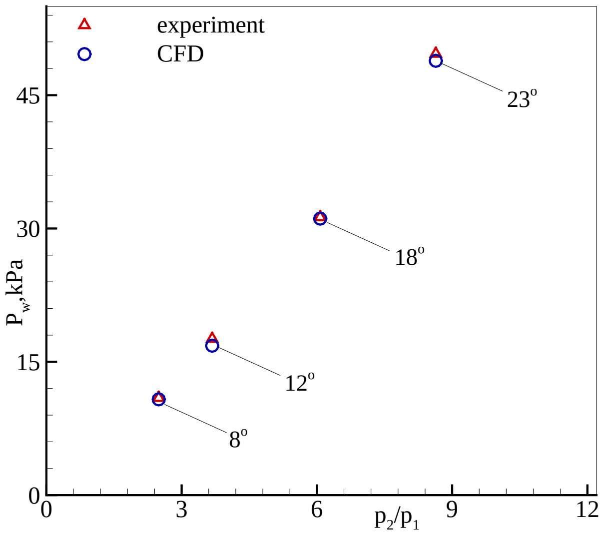

Figure 7.10: Variation of computed peak pressures at reattachment point R1 with inviscid shock strength p_2/p_1 compared with experiments [14] for different fin angles θ = 23°, 18°, 12° and 8°.

The wall pressure and skin friction variation is presented in Fig 7.9 for the weakest interaction case, where the standard SA and shock-unsteadiness models match. The figure shows that the flow exhibits quasiconical nature in the interaction region. The maximum pressure is 4.5 times less and maximum skin friction is of 3 times less as compared to the $23°$ case. A maximum vortex region of 41 mm is observed at x-section = 183 mm. The experiments [14] have been performed for these cases but the surface data of pressure and skin friction is not accessible due to the non-disclosure policy. The only data available is peak pressures at reattachment point R1 versus inviscid shock strength p_2/p_1 for different angles and is shown in Fig. 7.10. Here p_1 and p_2 are the inviscid pressure values in the freestream and post shock regions of single-fin configuration. The computed peak pressures at R1 match the experiments for different deflection angles ranging from 8° to 23°.

7.6 Summary

Three-dimensional shock-wave/turbulent boundary-layer interaction in single-fin configurations at Mach 5 with deflection angles of 23°, 18°, 12° and 8° are presented. RANS equations with standard and modified Spalart-Allmaras model are used in the computations. The inviscid shock generated by the fin interacts with boundary layer on the adjacent flat plate to form a conical vortex. The inviscid shock bifurcates and forms a lambda shock structure, one edge being the separation shock and the other being the rear shock. The inviscid shock, separation shock and rear shock interact to form Edney-type IV shock-shock interaction.

The wall pressure distribution using shock-unsteadiness model matches well for 23° case. Specifically, the primary separation point is predicted close to the experiments. The secondary flow region also shows improvement. The skin friction plot predicted by shock-unsteadiness model also shows agreement with experiments compared to the standard model, except at reattachment point where it is under predicted. The computations match the peak reattachment pressures reported in the experiments for a range of fin angles.

Chapter 8

Shock/boundary-layer interaction on a cone-flare geometry

8.1 Introduction

The majority of the research on shock/turbulent boundary-layer interaction is in the Mach 1-5 regime. At higher Mach numbers the shock waves generated by flow deflection are much stronger than those at supersonic speeds. Therefore the shock/boundary-layer interactions observed in hypersonic flows are usually stronger, resulting in larger separation bubble and higher peak pressure than the supersonic ones. Further, hypersonic flows are often characterized by multiple shock waves interacting with each other. These shock-shock interactions generate additional compression and expansion waves, and free shear-layers. Simulating all the flow features and the underlying flow physics make it harder to predict hypersonic shock/boundary-layer interactions than their supersonic counterparts.

In this chapter, shock/boundary-layer interaction on axisymmetric cone-flare is studied at Mach numbers in the range of 11-13. A naturally developing turbulent boundary-layer on a long cone with a small cone angle interacts with an oblique shock generated at the cone-flare junction. Tests were conducted with different flare angles at varying freestream conditions [15]. The resulting experimental data set spans a range of shock/boundary-layer interactions, from weak ones with no flow separation at the corner to strong interactions with a large separation bubble at the cone-flare junction.

The experimental test cases are presented in the next section and simulation methodology is described subsequently. This is followed by a detailed grid refinement study. The solutions computed for the experimental test cases using the standard and modified turbulence models are discussed in the subsequent section. A detailed description of the mean flow field and a comparison of the computed surface data to the experimental measurements is presented for each case.

8.2 Test cases

The configuration studied by Holden [15] is a 2.66 m long cone with a $6°$ half-cone angle and a flare of length 0.23 m (see Fig. 8.1). Two flare angles were considered and the models were tested in the Calspan 96-inch shock tunnel. The flare angle is measured with reference to the cone surface, and the cone-flare junction is placed at x = 0. Thus, negative values of x correspond to the cone surface and the flare has positive x values. Flow prediction in the shock/boundary-layer interaction region identified in Fig. 8.1, is the primary focus of this work.

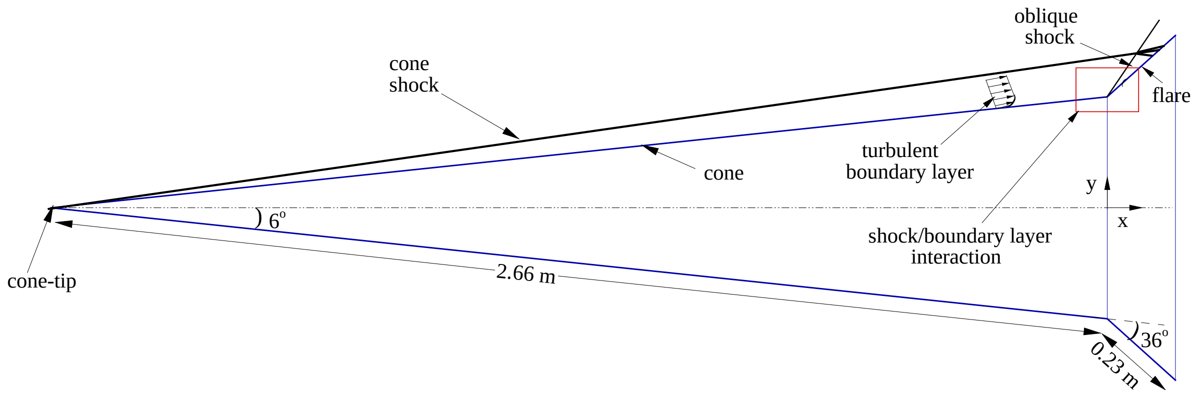

Figure 8.1: Geometric configuration with flow schematic for hypersonic shock-wave turbulent boundary-layer interaction test cases of Holden [15].

Models with two flare angles, $30°$ and $36°$, were tested at two Mach numbers, nominally 11 and 13, resulting in four test cases. The freestream and geometric parameters for different cases are listed in Table 8.1. Constant wall temperature of 294.44 K is taken along the cone-flare surface for all the cases. The resulting T_w/T_{aw} values for each case are also listed in the table. Note that a recovery factor of 0.89 is used to compute the adiabatic wall temperature. Air is used as test gas in these runs and perfect gas assumption is applicable owing to low stagnation enthalpy.

A single-pass schlieren system was used for flow visualization. Static pressure was measured along the model using piezoelectric pressure transducers and platinum thin-film gages

Test cases	1	2	3	4
Cone-flare angle	$36°$	$36°$	$30°$	$30°$
Freestream Mach number M_∞	13.1	10.97	12.92	10.98
Freestream temperature T_∞, K	57.0	65.4	60.9	67.4
Freestream pressure P_∞, kPa	0.51	0.62	0.5	0.63
Unit Reynolds number $Re_{1\infty} \times 10^6$, m^{-1}	1.385	1.145	1.219	1.113
Wall temperature/Adiabatic wall temperature, T_w/T_{aw}	0.15	0.17	0.14	0.17
Stagnation enthalpy, H_0, MJ/kg	2.0	1.6	2.1	1.7

Table 8.1: Freestream conditions and flare-angles for hypersonic cone-flare configurations.

were used to obtain the heat transfer rate on the surface. The uncertainties associated with the pressure and heating rate data were estimated to be $\pm3\%$ and $\pm5\%$ respectively. Surface pressure data is a good indicator of the separation point and has a one-to-one correspondence with the shock structure observed in the schlieren images. The majority of the comparison between numerical simulations and experimental data is therefore based on the pressure measurements. A limited comparison with surface heat flux data is also done [107].

8.3 Simulation methodology

The axisymmetric form of the Reynolds-averaged Navier-Stokes equations, as presented by Wilcox [76] are solved for the mean flow. The standard k-ω and Spalart-Allmaras, and shock-unsteadiness modified turbulence models are used in the simulations. The details of the numerical method are presented in Section 3.3. The computational domain used in the simulations is shown in Fig. 8.2a. It spans the region between the cone tip and the end of flare in the wall-parallel i-direction. In the wall-normal j-direction it extends from the cone-flare surface to the outer boundary, which is placed in the freestream flow outside the shock waves. The flow solution is insensitive to the actual location of the outer boundary as long as the shock wave generated by the cone-flare geometry do not intersect it. The inclination of the outer boundary is tailored such that the grid lines in the vicinity of the oblique shock generated by the cone tip are parallel to the shock wave. This eliminates any grid-induced distortion of the oblique shock along the length of the cone until it reaches the shock/boundary-layer interaction region.

A FORTRAN code is used to generate a single-block structured Cartesian grid as shown in

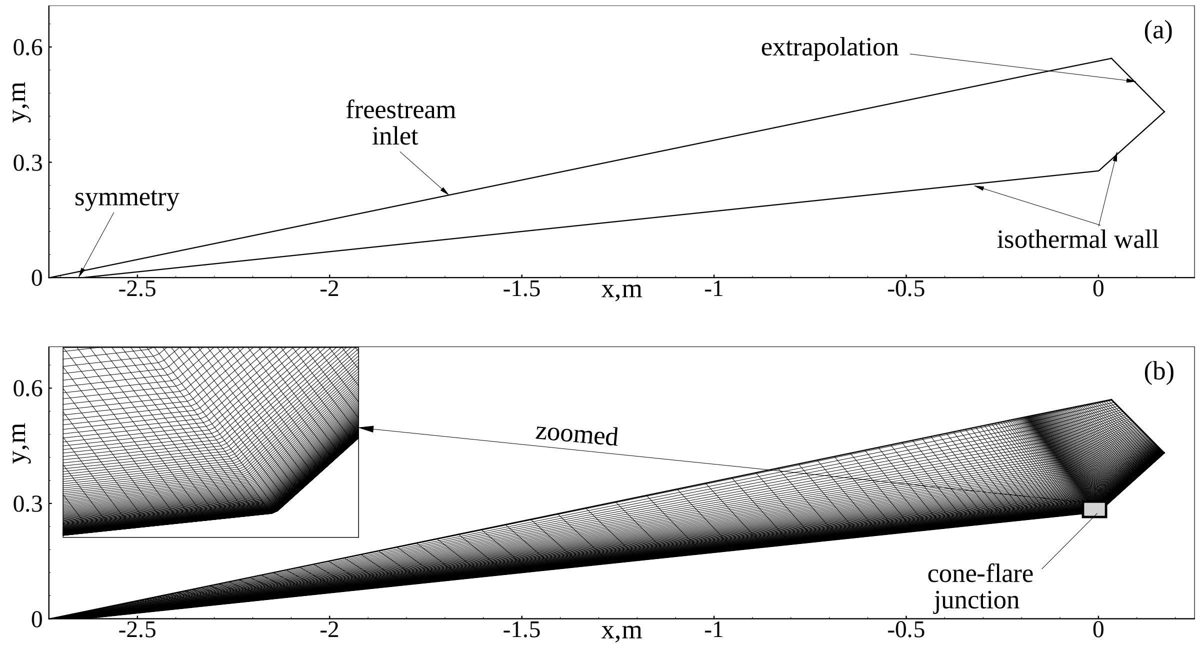

Figure 8.2: (a) Computational domain and boundary conditions used in the simulations. (b) A typical computational mesh showing every third point in each direction. Inset shows a magnified view of the cone-flare junction.

Fig. 8.2b. A typical grid has about 600 points in the stream-wise direction and 500 exponentially-stretched points in the wall-normal direction. The grid points are clustered in the vicinity of the cone-tip and at the cone-flare junction, such that there are about 300×375 points in the interaction region. The sensitivity of the solution to the computational grid is described below.

8.3.1 Grid refinement study

Flowfield solutions are computed using computational meshes with varying number of points in the wall-parallel and wall-normal directions. Also, the cell sizes in high-gradient regions, like shock waves, cone-flare junction, separation point and reattachment location, are systematically varied to study their effect on the computed solution. A detailed grid convergence study of the $36°$ flare at Mach 13 using the shock-unsteadiness modified Spalart-Allmaras model is presented below. This is followed by a similar study for the shock-unsteadiness modified k-ω model. The computational solution obtained using the standard turbulence models is found to be less sensitive to the variation in computational grid than those obtained using the modified turbulence models.

For the baseline grid size of 600×500 points, the normal spacing adjacent to the wall is varied between 5×10^{-6}m and 1×10^{-6}m, and the results computed using the modified Spalart-

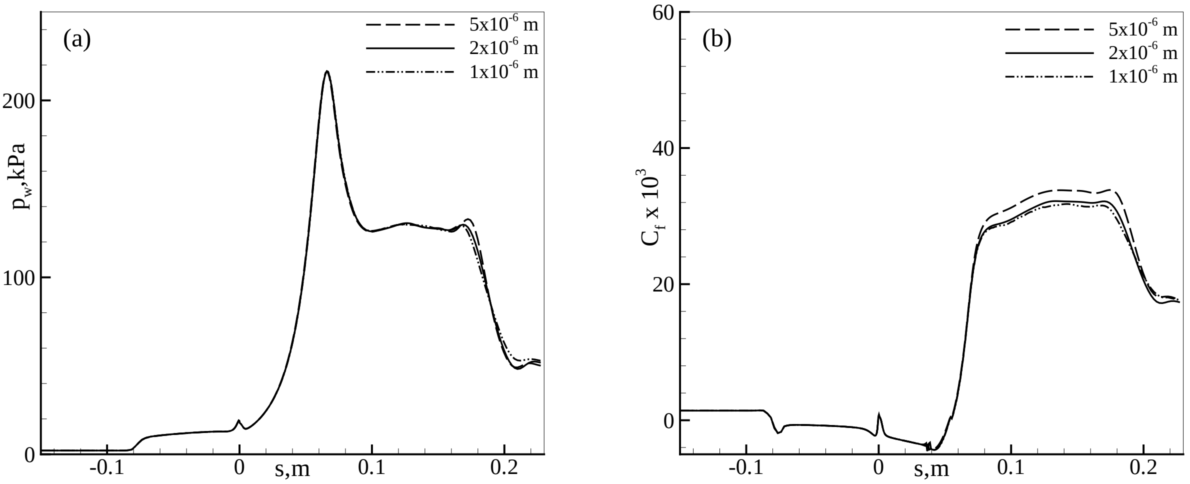

Figure 8.3: Effect of variation in wall-normal spacing on (a) wall pressure and (b) skin friction, using modified Spalart-Allmaras model for $36°$ flare at Mach 13.1.

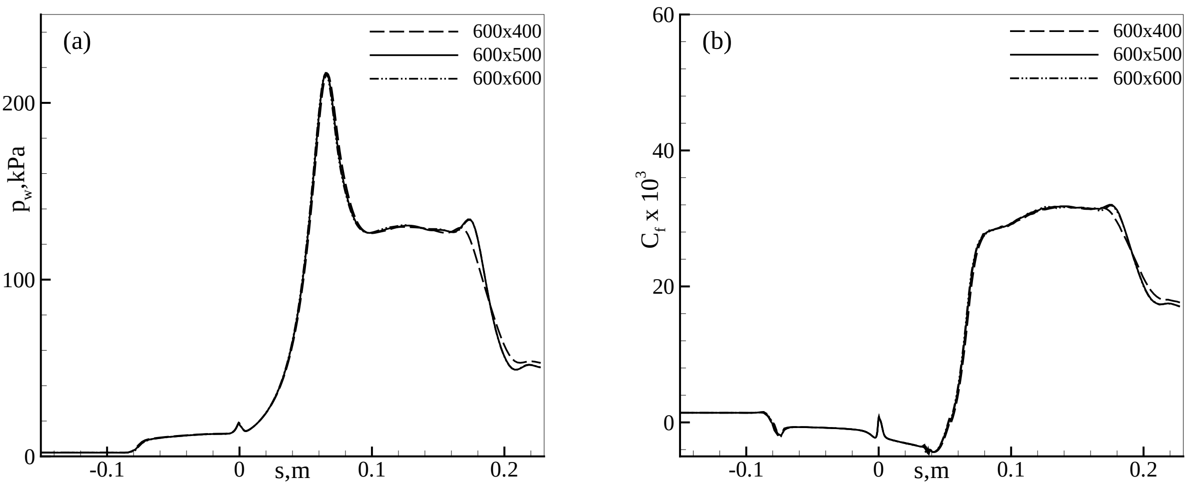

Figure 8.4: Effect of varying the number of wall-normal grid points on (a) wall pressure and (b) skin friction, using modified Spalart-Allmaras model for $36°$ flare at Mach 13.1.

Allmaras model are presented in Fig. 8.3. The corresponding y_2^+ values range from 0.04 to 0.2 on the cone and from 1.4 to 7.6 on the flare. The surface pressure is mostly insensitive to the near-wall grid point distribution, except near the end of the computational domain. The variation in surface pressure in this region ($s \simeq 0.17$ m) is due to the impingement of the expansion fan generated by the shock-shock interaction outside the boundary layer. Refining the near-wall grid for a fixed number of grid-points in the wall-normal direction results in a coarser mesh in the outer inviscid region. The consequent effect on the inviscid shock-shock interaction and the resulting surface pressure distribution can be seen in Fig. 8.3. The skin-friction coefficient, as expected, is more sensitive to the wall-normal spacing than the surface pressure, especially on the flare. There is about 2% variation between the two fine grids for 0.08 m $< s < 0.18$ m.

There is somewhat larger deviation further downstream, which is an effect of the outer inviscid interaction.

Next, the number of points in the wall-normal direction are varied and the results are presented in Fig. 8.4. Three exponentially stretched grids with 400, 500 and 600 grid points, with identical cell-size adjacent to the wall, are used. This results in a stretching factor of 1.023, 1.018, and 1.014, respectively for the three grids. The majority of the variation is in the outer inviscid zone and the near-wall grid is affected to a smaller extent. The surface data are almost identical over the entire geometry, except for the later part of the flare. This is once again caused by variation of the grid point density in the outer inviscid region, as explained above. The two finer grids yield overlapping results for the entire domain.

A similar procedure is followed in the wall-parallel direction by systematically varying the number of points along the wall. The surface properties are found to be less sensitive to the changes in the wall-parallel grid than that in the wall-normal direction, and 600 points are found to be adequate to obtain an accurate solution. Based on above study, a computational mesh of 600×500 points with a wall-normal spacing of 2×10^{-6}m at the wall is chosen for computations using the standard and modified Spalart-Allmaras models. The corresponding y_2^+ value is about 0.08 on the cone and less than 3 on the flare.

The flowfield solution obtained using the k-ω model is more sensitive to the computational mesh than that of the Spalart-Allmaras model. The k-ω solution requires substantially larger number of wall-parallel grid points (more than 1000) to attain grid independence. Even with finer grids, the changes in surface properties with successive refinement (presented in Figs. 8.5-8.7) are found to be appreciably higher than the corresponding Spalart-Allmaras model results. Further, the k-ω computations are found to be prone to numerical instability, which restricts the time steps used in the simulation. The highest Courant-Friedrichs-Lewy (CFL) achievable for the k-ω model calculations (see Sec. 8.4) is significantly lower than those used for the Spalart-Allmaras computations.

The results obtained by varying the cell size adjacent to the wall and the number of grid points in the wall-normal and wall-parallel directions is presented next. Note that the pressure data computed using the modified k-ω model appears similar to that of the modified Spalart-Allmaras model, but the skin-friction coefficient has a local maximum near the reattachment point ($s \simeq 0.07$m) that is not present in the modified Spalart-Allmaras model solutions.

The variation of skin-friction coefficient (Fig. 8.5b), when the wall-normal spacing at the

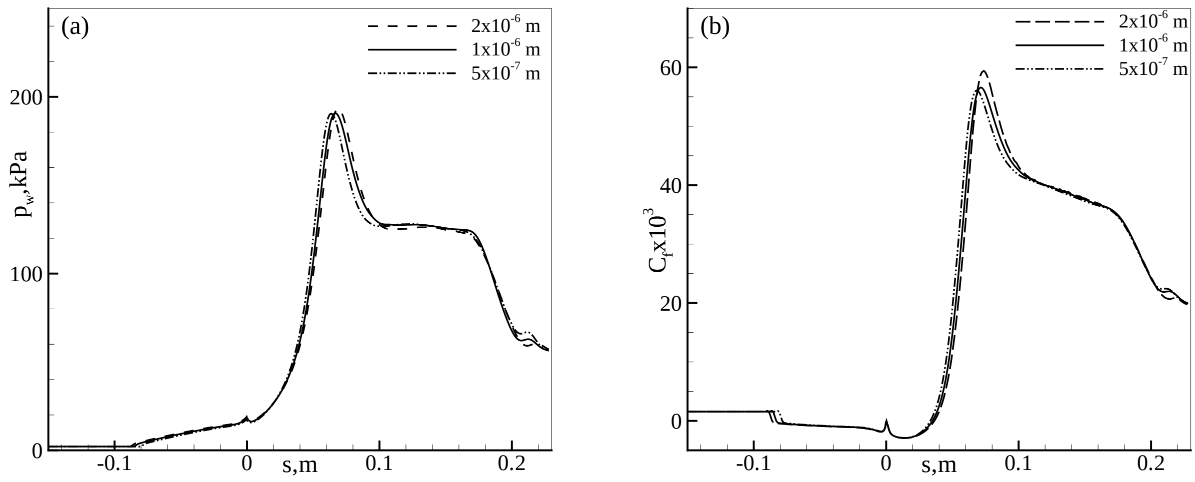

Figure 8.5: Effect of varying wall-normal spacing on computed (a) wall pressure and (b) skin-friction coefficient, using modified k-ω model for 36° flare at Mach 13.1.

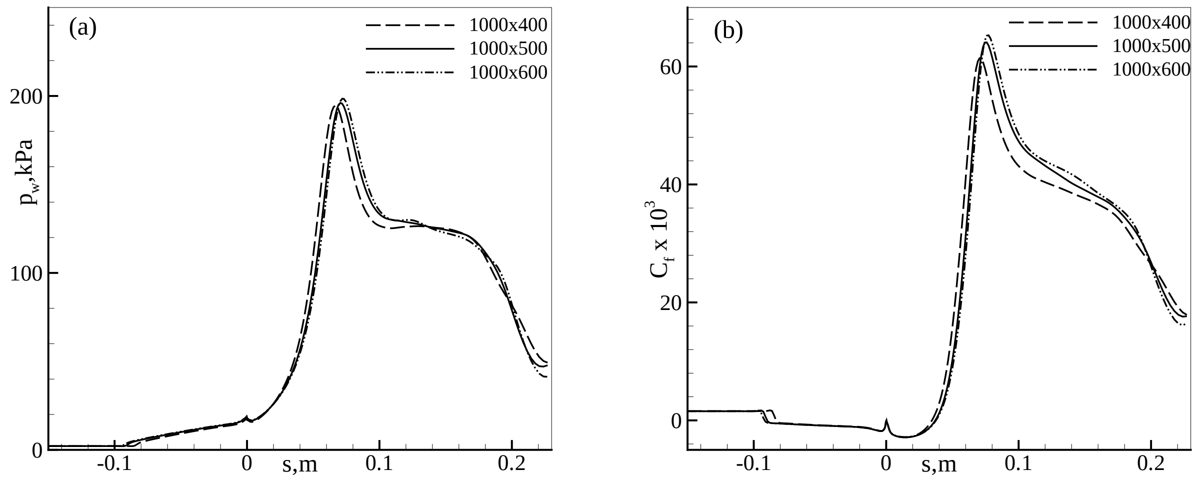

Figure 8.6: Effect of varying number of wall-normal grid points on computed (a) wall pressure and (b) skin-friction coefficient, using modified k-ω model for 36° flare at Mach 13.1.

wall is decreased from 2×10^{-6}m to 0.5×10^{-6}m shows a converging trend. The maximum deviation between the two finer grid predictions is 3%. The separation point located at s = -0.085 m changes by a small amount (0.005 m) for the three grids. The pressure data (Fig. 8.5a) shows a similar trend, with the location of the reattachment pressure peak at s = 0.07 m shifted by 0.003 m between the two finer grids. The value of the peak pressure remains almost identical for all the three grids.

Figure 8.6 shows the data obtained using grids with varying number of points in the wall-normal direction and identical normal spacing at the wall. The location of the peak pressure and C_f on the flare shifts downstream by 0.005 m, when the number of wall-normal grid points is increased from 400 to 500. Their locations do not change appreciably when the grid size

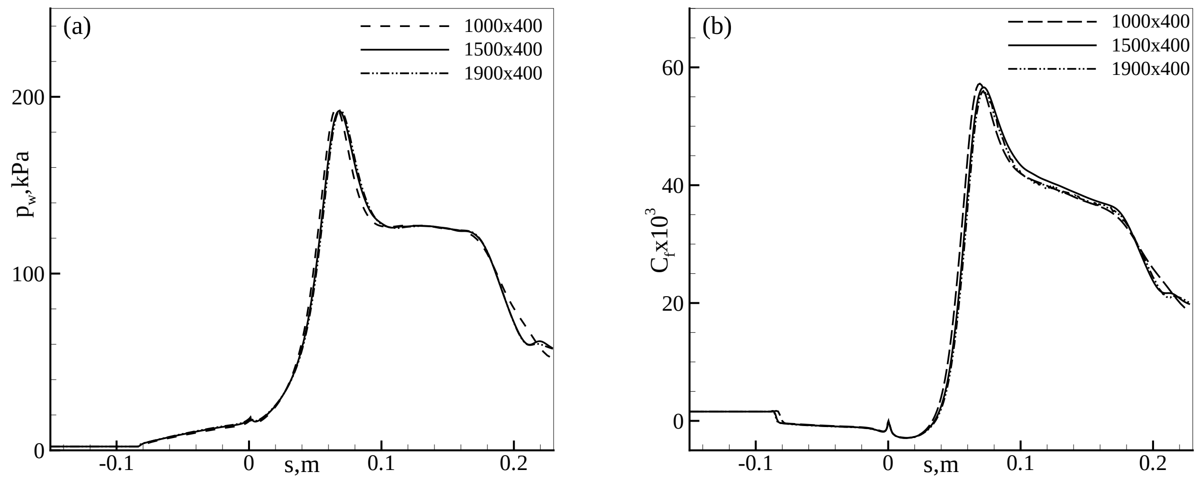

Figure 8.7: Effect of varying wall-parallel grid points on computed (a) wall pressure and (b) skin-friction coefficient, using modified k-ω model for $36°$ flare at Mach 13.1.

is increased further to 600 points. The peak values of pressure and C_f vary less than 2% for the two finer grids. The flow solutions upstream of the corner, including the separation point location, are almost identical for the 1000×500 and 1000×600 cases.

The data computed using successively higher number of wall-parallel grid points is presented in Fig. 8.7. The location of peak pressure and C_f shifts slightly downstream with the first refinement from 1000 to 1500 points, but there are almost no visible difference when the grid is further refined to 1900 points. Thus, 1500 points in the wall-parallel direction and 500 points in the wall-normal direction are adequate for computations using the standard and modified k-ω turbulence models. However, it is found that k-ω simulations using fine grids like 1500×500 require very small time steps for integration, such that a steady state solution cannot be obtained in a reasonable computational time. By comparison, simulations on the 1500×400 grid are more robust and therefore selected for all the k-ω results presented below. Based on the data presented in Fig. 8.6, using 400 points in the wall-normal direction will result in a slightly higher uncertainty, around 0.006 m in the location of the reattachment peak pressure and 7% in the peak skin-friction coefficient level, in the k-ω solutions. The wall-normal spacing at the wall is set at 1×10^{-6}m, which is equivalent to a y_2^+ value of 0.03 on the cone and less than 1.2 on the flare.

8.4 Simulation results

In this section, numerical solutions for the four test cases are presented in the decreasing order of the strength of the shock/boundary-layer interaction (see Table 8.2). Initially, the standard Spalart-Allmaras and k-ω models are used in the computation. The shock-unsteadiness correction is then applied to show improvement in results over the standard models. The flow physics details are emphasized and the computed wall pressure in the interaction region is compared with the experimental measurements.

The results presented below are computed on a 600×500 grid for the standard and modified Spalart-Allmaras models, and on a 1500×400 grid for the standard and modified k-ω models. These grids are chosen (Sec. 8.3.1) based on a detailed grid refinement study for the 36° flare at Mach 13. The other three test cases are either at a lower Mach number, a lower flare angle, or both. The shock/boundary-layer interaction is therefore strongest for the first case, and the grid refinement study for this flow is expected to be sufficient for the other three flows.

The flowfield variables are initialized to freestream values over the entire domain and the solution is advanced in time to reach a steady state. In the computations using the standard and modified Spalart-Allmaras models, a CFL of 0.05 is used at the beginning of iterations and it is increased to 10 in the first 2500 iterations. Next, it is increased to 500 at 8000 iterations and a maximum CFL of 1500 is used after 125000 iterations. The time step is 3×10^{-11} sec at the beginning of iterations and reaches to 3×10^{-6} sec at steady state solution. In the computations using the standard and modified k-ω models, a CFL of 0.05 is used at the beginning of iteration, later it is increased to 10 at 500 iterations. Further it is increased to a value of 30 at 15000 iterations and a maximum CFL of 50 is used at 35000 iterations. All the simulations are run in parallel using 16 cpu-cores of a 2.66 GHz Intel processor based machine. It takes approximately 92 cpu-hours (80,000 iterations) to reach steady state solution using the Spalart-Allmaras model and about 625 cpu-hours (1,80,000 iterations) for the k-ω model.

8.4.1 36° flare at Mach 13.1

The experimental schlieren image corresponding to the 36° flare at Mach 13.1 is shown in Fig. 8.8a. The boundary layer on the cone is marked by mild density variation and is identified in the figure. The boundary layer separates at the cone-flare junction and a separation shock is located upstream of the corner. The separation shock is not clearly visible inside the cone

	$36°$ flare		$30°$ flare	
	Mach 13	Mach 11	Mach 13	Mach 11
Mach number at incoming boundary-layer edge	10.37	9.1	10.27	9.1
Mach number normal to oblique shock, M_{1n}	6.75	5.94	5.72	5.08
Inviscid pressure rise at corner, p_2/p_1	56.0	43.4	40.0	31.7

Table 8.2: Shock/boundary-layer characteristics for the cone-flare configuration. The subscripts *1* and *2* correspond to inviscid conditions upstream and downstream of an assumed oblique shock at the cone-flare junction.

boundary layer, but a distinct separation shock is observed outside the boundary layer. It is followed by a steeper shock on the flare downstream of reattachment. The clarity of the schlieren image is limited in the reattachment region, but distortions in the flare shock can be clearly seen. The flowfield exhibits some degree of unsteadiness and the schlieren image corresponds to a single time realization of the unsteady flow field. The oblique shock generated at the tip of the cone intersects the flare shock at the top right corner of the visualization window. The details of this shock-shock interaction is described below.

The numerical solution obtained using the standard Spalart-Allmaras turbulence model is presented in Fig. 8.8b. The normalized density contours plotted in the figure shows the interaction of the cone shock and the flare shock clearly. The resulting shock-shock interaction generates a third shock and a free shear layer. Also, an expansion fan emanates from the triple point, and reflects off the flare surface. The flow features generated by the intersection of the cone and flare shocks are reproduced well by the numerical simulation and they match the experimental schlieren image qualitatively. On the other hand, the computational solution differs markedly from the schlieren image at the cone-flare junction. The shock/boundary-layer interaction in this region and the underlying flow physics is the main focus of this work. The numerical solution predicts an oblique shock at the corner as opposed to a separation shock observed in the experiment. This is because the incoming boundary-layer in the simulation does not separate upstream of the corner.

The difference in the flow topology between the experimental image and the computed solution results in a large mismatch between the corresponding surface pressure distributions plotted in Fig. 8.9. The numerical solution with a single attached shock results in a distinct jump in pressure at the corner ($s \simeq 0$). On the other hand the experimental data shows a pressure rise upstream of the corner (at $s \simeq -0.08$ m). This pressure rise corresponds to the separa-

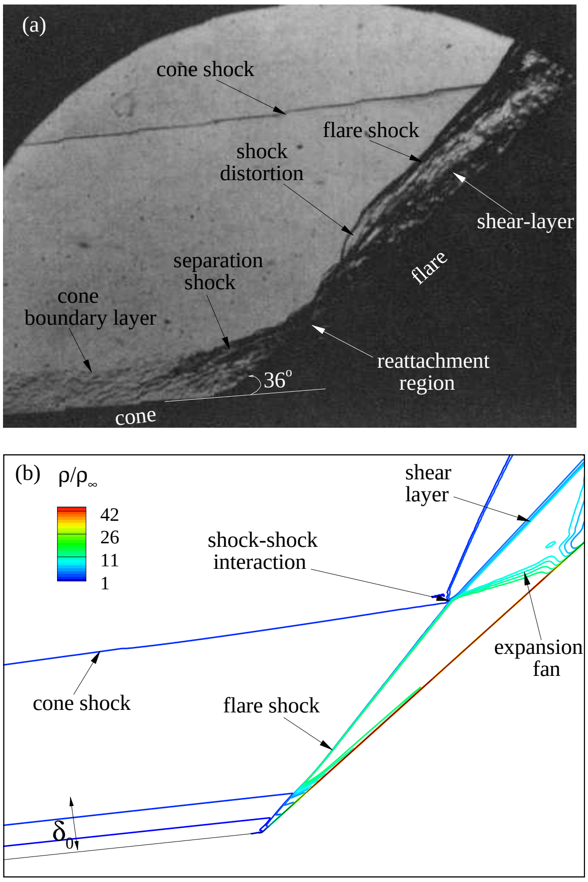

Figure 8.8: Shock-wave/boundary-layer interaction on a $36°$ flare at Mach 13.1: (a) experimental schlieren image [15] and (b) computed density contours using standard Spalart-Allmaras model.

tion shock and is followed by a pressure plateau in the separation bubble. A further rise in the surface pressure downstream of the corner is due to flow reattachment on to the flare surface. Both the experimental data and the computed pressure on the cone are found to match the theoretical estimate of Taylor and Maccoll [108] upstream of the interaction region. Downstream of reattachment, the simulation results compare well with measurements on the flare wall, but over-predict the theoretical pressure rise obtained using oblique shock relations. The simulations predict a drop in surface pressure at the location $s \simeq 0.16$ m, where the expansion fan from the shock-shock interaction reflects from the flare wall.

Note that the wall pressure is plotted on a log-scale in Fig. 8.9 to emphasize its variation in the vicinity of the separation point. In the absence of direct measurement of the separation location, it is estimated from an extrapolation of the initial pressure rise on the cone. As pointed earlier, predicting the location of flow separation accurately is crucial to obtain the correct shock structure and flow topology in the interaction region.

The pressure data computed using the standard k-ω model is also presented in Fig. 8.9

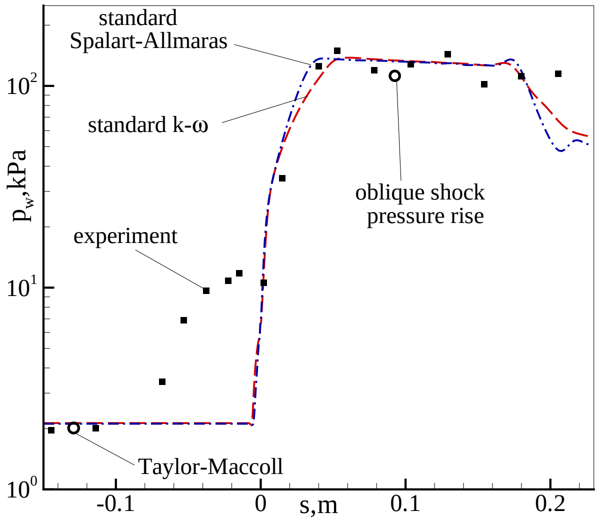

Figure 8.9: Comparison of computed wall pressure with experiments [15] for $36°$ flare at Mach 13.1. The standard Spalart-Allmaras and standard k-ω models are used in the simulations.

and it matches the results obtained using the Spalart-Allmaras turbulence model closely. The flowfield structure obtained using the k-ω model is also similar to the one presented in Fig. 8.8b. Both models fail to predict flow separation at the cone-flare junction, and therefore result in a significant disparity with the experimental shock structure and pressure data in this region. We attempt to improve the model predictions using the shock-unsteadiness correction proposed by Sinha *et al.* [10].

Application of the shock-unsteadiness modification

The detail formulation of shock-unsteadiness correction [12] to k-ω and Spalart-Allmaras turbulence models are presented in Sections 4.5.1 and 4.5.2. The implementation of the model is given below.

The shock-unsteadiness correction is a function of the shock-normal Mach number upstream of the shock wave. This is calculated by,

$$M_{1n} = \frac{\mathbf{u_1} \cdot \nabla p}{a_1 |\nabla p|} \tag{8.1}$$

Here $\mathbf{u_1}$ and a_1 are the velocity vector and the speed of sound upstream of the shock wave, and ∇p is the pressure gradient at the shock.

The velocity and temperature values in the incoming boundary layer are plotted as a function of the wall-normal distance in Fig. 8.10a. The resulting distribution of the upstream Mach number is also shown in the figure. The shock wave generated at the cone-flare junction is

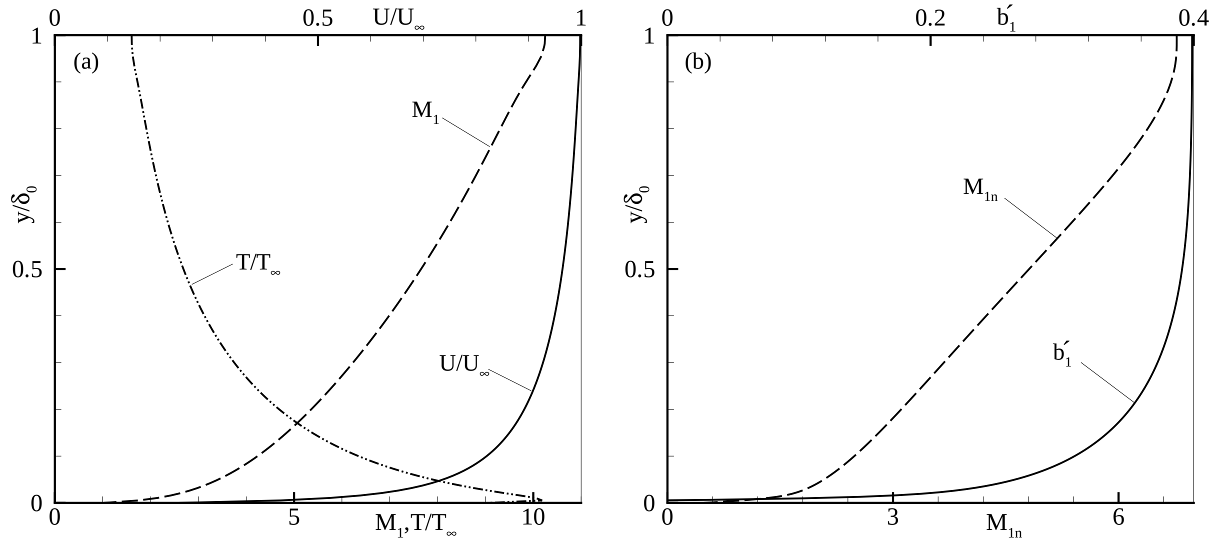

Figure 8.10: (a) Distribution of upstream Mach number, M_1, normalized velocity, U/U_∞ and normalized temperature T/T_∞ in the undisturbed boundary-layer upstream of the shock/boundary-layer interaction region. (b) Variation of shock-normal upstream Mach number M_{1n} and shock-unsteadiness model parameter b_1' in the boundary layer.

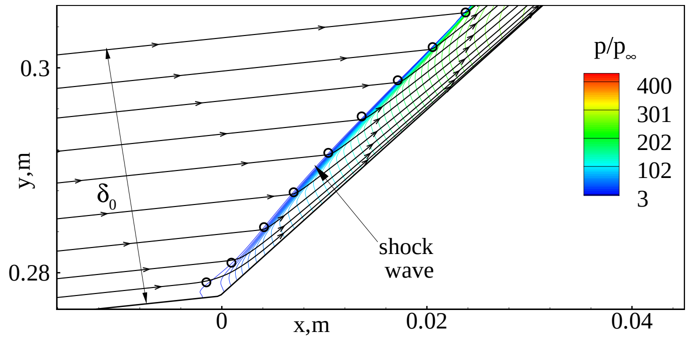

Figure 8.11: Normalized pressure contours showing the shock wave in the interaction region of the 36° flare geometry. A set of points are identified along the shock wave and M_{1n} is calculated using the upstream values along the respective streamlines.

plotted in terms of the normalized pressure contours in Fig. 8.11. The scale of the figure is magnified to highlight the incoming boundary-layer on the cone. The value of M_{1n} along the shock is thus calculated using the upstream values along the local streamlines. The upstream Mach number varies between subsonic values near the wall to about 10 at the boundary-layer edge. The component of the upstream Mach number normal to the shock varies between 1.0 to 6.67 (see Fig. 8.10b). The shock-unsteadiness parameter b_1' computed using these values of M_{1n} is also plotted in the figure. It approaches zero in the near-wall region and attains a limiting value of 0.4 at the boundary-layer edge. For the Spalart-Allmaras model, the shock-unsteadiness parameter c_{b_1}' is evaluated using Eq. 4.51 (see Section 4.5.2). It varies between 0.42 near the

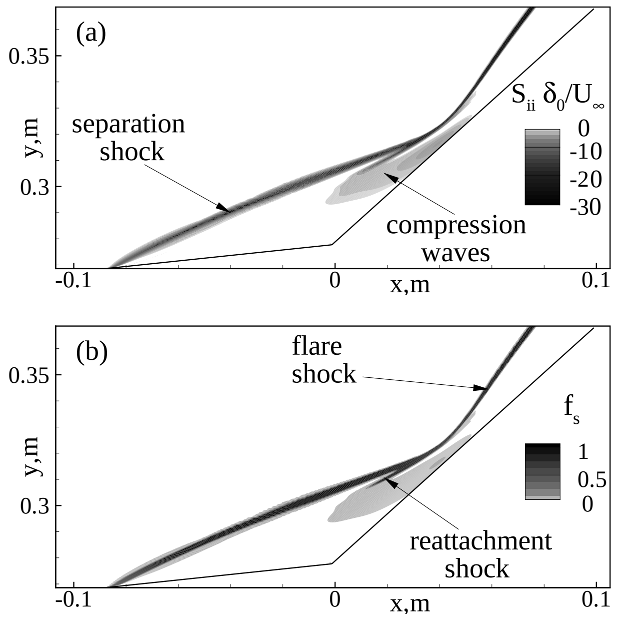

Figure 8.12: Variation of (a) normalized mean dilatation, S_{ii} and (b) shock-identifying function, f_s showing different shocks and compression waves in the shock/boundary-layer interaction region.

wall to -0.79 at the boundary-layer edge. In the following, the shock-unsteadiness correction is applied by using an average value of c'_{b_1} = -0.32 and b'_1 = 0.32 for the Spalart-Allmaras and k-ω models respectively. The average is calculated over a set of points distributed uniformly along the shock wave in the region where it overlaps with the incoming boundary layer. Solution obtained by implementing a detailed variation of the shock-unsteadiness parameter is discussed subsequently.

In shock-unsteadiness modified Spalart-Allmaras model, the parameter c'_{b_1} can take either positive or negative values depending on the upstream Mach number. As per Eq. 4.50 (see Section 4.5.2), the amplification of the eddy viscosity ν_T across a shock is given by the ratio of k^2-amplification to ϵ-amplification. At supersonic Mach numbers the amplification of k^2 is larger than that of ϵ, and therefore results in an increase in ν_T across the shock wave. This corresponds to a positive value of c'_{b_1} and a positive source term $-c'_{b_1}\bar{\rho}\tilde{\nu}S_{ii}$ in the model equation. A higher turbulence eddy viscosity results in reduction of the separation bubble size in supersonic shock/boundary-layer interactions [12] . At hypersonic Mach numbers, the amplification of ϵ increases monotonically with M_{1n}, where as k^2-amplification saturates for $M_{1n} >$ 1.8. This results in decrease of ν_T across a shock wave at hypersonic conditions. A lower value of ν_T increases the separation bubble size in hypersonic shock/boundary-layer interaction and is opposite to that observed at supersonic Mach numbers.

In shock-unsteadiness modified k-ω model, f_s is the empirical function that locates the region of shock wave in terms of the mean dilatation S_{ii}. The functional form of f_s is identical to that used in Ref. [12], except for the fact that S_{ii} is normalized by U_∞/δ_0 instead of the local value of S.

$$f_s = \frac{1}{2} - \frac{1}{2}\tanh\left[5\left(\frac{S_{ii}\delta_0}{U_\infty}\right) + 3\right]. \quad (8.2)$$

The quantity U_∞/δ_0 is found to be more robust than S in Ref. [90]. The characteristic length δ_0 and freestream velocity U_∞ are known *a priori* for a given simulation and can be specified as user input. The function f_s takes a value of one in shock and high compression regions of the flow field and in other regions it becomes zero and the standard form of k-ω model is recovered.

The function f_s identifies the shock waves and high compression regions in the flow in terms of the mean dilatation S_{ii}. These regions are highlighted in the modified k-ω solution in Fig. 8.12a. The near-wall region of the turbulent boundary layer also has non-zero S_{ii}, but care is taken to make f_s negligible in boundary-layer flows, where the standard model predictions are well validated. Figure 8.12b shows the distribution of f_s in the interaction region and it captures the shock waves correctly. Depending on the level of compression, it smoothly varies between 0 and 1, where f_s = 0 corresponds to the standard model.

Modified turbulence model predictions

The shock-unsteadiness corrected Spalart-Allmaras model with a negative c'_{b_1} results in a decrease of the turbulent kinematic eddy viscosity at the shock wave. Lower levels of turbulence leads to an earlier separation of the boundary layer on the cone. The separation bubble in the numerical solution is identified in terms of a few characteristic streamlines in Fig. 8.13a and the separation and reattachment points are marked by S and R respectively. A separation shock is formed as the incoming boundary layer is deflected over the separation bubble. As the flow over the bubble reattaches the flare surface, a series of compression waves are generated. The resulting reattachment shock intersects the separation shock close to the flare surface (see magnified view in Fig. 8.13b) and forms a Edney type-VI shock-shock interaction [40]. The flow pattern in the interaction region is shown schematically in Fig. 8.14. An oblique shock is generated at the triple point and an expansion fan propagates towards the flare wall. The flow pattern is similar to that obtained in the shock-shock interaction further downstream on the flare, but the scale is smaller due to its proximity to the solid boundary. The shear layer generated at the triple point travels parallel to the flare surface and is marked by density contours in Fig. 8.13c. Also,

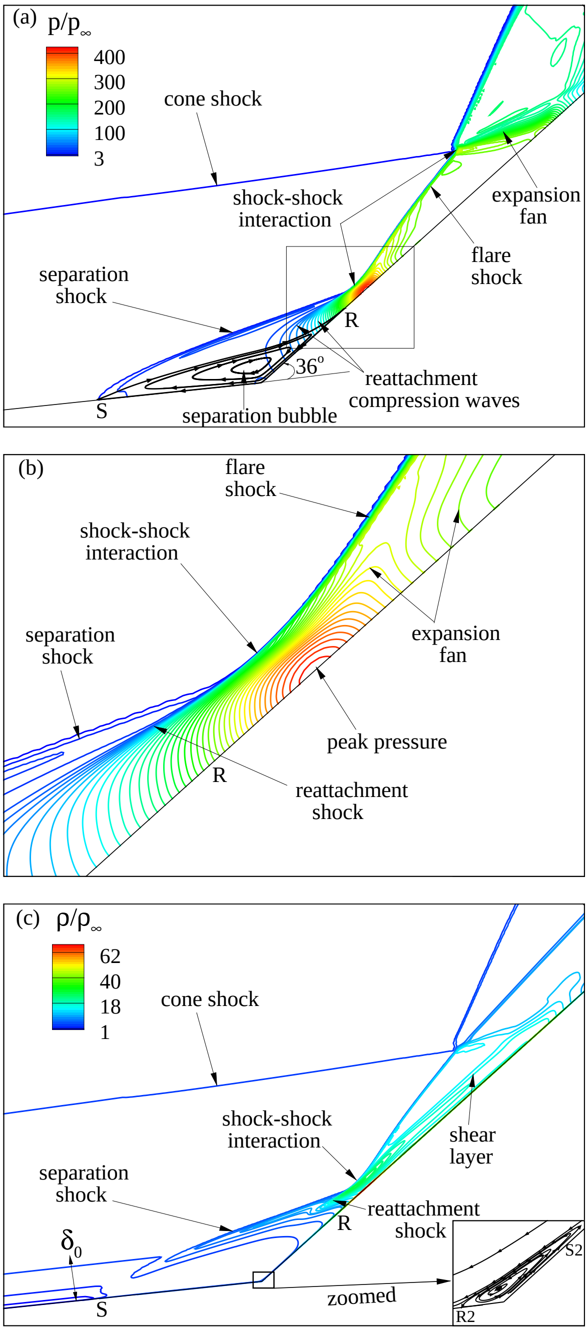

Figure 8.13: Computed flow pattern using shock-unsteadiness modified Spalart-Allmaras model [12] for 36° flare at Mach 13.1: (a) normalized pressure contours, and (b) magnified view of the reattachment region and (c) normalized density contours.

a small secondary separation bubble formed at the corner is shown in the inset.

The density contours in Fig. 8.13c has strong resemblance with the experimental schlieren image in Fig. 8.8a. The density gradient in the upstream boundary layer is marked by contour lines of the time-averaged density parallel to the cone surface. In the vicinity of the separation point (S), the boundary layer density variation overlaps with the separation shock contour lines. A similar effect is seen in the experimental schlieren image, and the separation shock

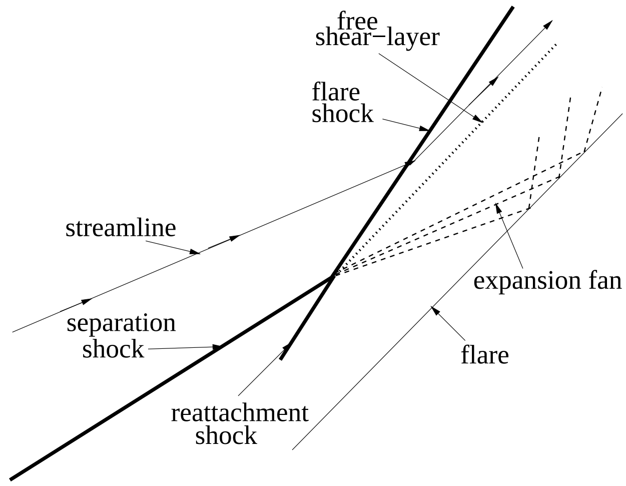

Figure 8.14: Schematic sketch of Edney type-VI shock-shock interaction [40].

is not distinctly visible inside the cone boundary layer. The density contours clearly mark the separation shock outside the boundary layer, and a small reattachment shock is visible on the flare. The reattachment shock cannot be discerned in the schlieren image, but the overall shock structure near the reattachment location matches the computed shock-shock interaction pattern closely. The flare shock generated at the triple point goes on to intersect the cone shock further downstream. The dark band in Fig. 8.8a along the flare wall downstream of reattachment is probably the free shear layer marked in the numerical solution. As expected, the flare shock in the RANS solution is steady, whereas distortions of the flare shock are visible in the experiment. These shock distortions appear to reduce significantly before the flare shock intersects the oblique shock from the cone tip.

The pressure data obtained using shock-unsteadiness corrected Spalart-Allmaras model is shown in Fig. 8.15a. Comparison with the standard Spalart-Allmaras model results show two marked differences. First, the single pressure rise at the corner is replaced by a pressure rise due to the separation shock at $s = -0.08$ m, followed by a pressure plateau and another pressure rise at the reattachment point on the flare. A sharp peak at $s = 0$ is due to a small secondary separation bubble formed at the corner (see Fig. 8.13c). Secondly, there is a local pressure peak immediately downstream of the reattachment point. This is caused by the shock-shock interaction in this region. The flow over the separation bubble gets over-compressed on passing through the separation and reattachment shock/compression waves. The pressure reaches a local maximum and then reduces when the expansion fan from the triple point reflects off the flare surface. There is indication of a local pressure peak in the experimental data, but the location of

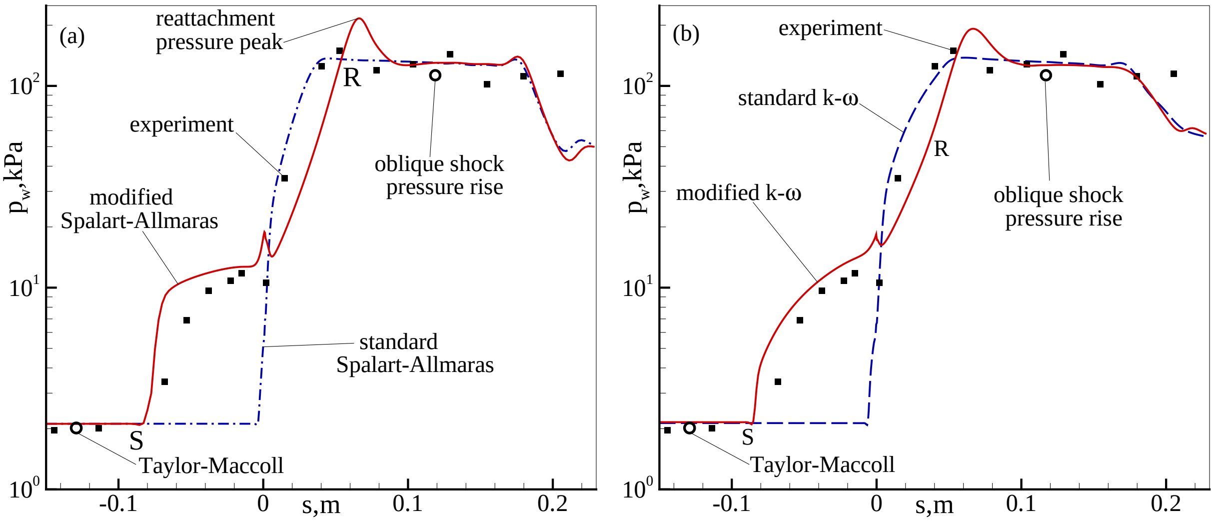

Figure 8.15: Computed wall pressure is compared with experiments [15] for $36°$ flare at Mach 13.1. Shock-unsteadiness correction [12] applied to (a) Spalart-Allmaras model and (b) k-ω model.

the peak and the reattachment pressure rise is somewhat upstream of the numerical prediction. The simulation also yields a slightly earlier separation than the experimental measurement. The locations of initial pressure rise on the cone, as obtained from experiment and computation, are listed in Table 8.3. The separation bubble size, as estimated by the separation shock pressure rise and the reattachment pressure peak, is over-predicted by the modified Spalart-Allmaras model.

The modified k-ω model shows similar improvement over the standard k-ω model (see Fig. 8.15b). The shock-unsteadiness correction damps the turbulent kinetic energy at the shock, and therefore results in a sizable recirculation bubble at the cone-flare junction. The separation shock pressure rise is located somewhat upstream of the experiment. Also, the reattachment pressure rise and the local pressure peak on the flare are downstream of the experimental data. The flowfield in the interaction region, including the separation bubble and the shock-shock interaction past reattachment, are very similar to that obtained using the modified Spalart-Allmaras model (Fig. 8.13). On the whole, the shock-unsteadiness correction, irrespective of the base turbulence model, reproduces the separation bubble at the cone-flare junction and the shock/expansion wave topology in the interaction region correctly. In spite of differences with the experimental data, the shock-unsteadiness corrected models yield significant improvement (see Table 8.3) in the surface pressure prediction over the standard Spalart-Allmaras and k-ω turbulence models.

	36° flare		30° flare	
	Mach 13	Mach 11	Mach 13	Mach 11
Experiment, mm	-80.1	-71.3	-37.8	-
Standard k-ω model, mm	-6.2	-7.5	-3.7	-3.7
Standard Spalart-Allmaras model, mm	-5.2	-6.5	-3.6	-3.6
Modified k-ω model, mm	-86.3	-86.1	-15.3	-15.0
Modified Spalart-Allmaras model, mm	-84.1	-83.9	-4.1	-4.0

Table 8.3: Experimental and computed separation shock locations.

Wilcox presents a k-ω stress-limiter model [8] that limits turbulent kinetic energy production in a shock wave. The value of the limiter is set as C_{lim} = 7/8 for the new k-ω model. In a normal shock, the stress limiter model yields TKE production of the form

$$P_k = c\rho k|S_{ii}| \tag{8.3}$$

with c = 1.15. A value of C_{lim} = 1 corresponds to the SST model [77] with c = 1.09. By comparison, the shock-unsteadiness correction yields a production term of the form given by Eq. (4.36) (see Section 4.4), with c = 2/3 $(1 - b_1')$. A lower (higher) value of b_1' results in a higher (lower) value of c, which in turn increases (decreases) TKE production and suppresses (enhances) flow separation. In the simulations presented below, the shock-unsteadiness parameter b_1' is around 0.3, which corresponds to $c \simeq$ 0.46. A relatively higher value of c used in the new k-ω and SST models may, therefore, result in a smaller separation bubble compared to that obtained using the shock-unsteadiness correction.

8.4.2 $36°$ flare at Mach 10.97

Next, we consider the shock/boundary-layer interaction on a $36°$ flare at Mach 10.97. A lower freestream Mach number compared to the first test case leads to a lower boundary-layer edge Mach number on the cone, upstream of the interaction. The inviscid pressure rise assuming a single oblique shock at the corner and the corresponding Mach number normal to the shock-wave are appreciably lower than the earlier case (see Table 8.2). This is expected to result in a weaker shock/boundary-layer interaction at the cone-flare junction. The strength of the interaction directly influences the extent of flow separation at the corner. The separation point in the experiment, as indicated by the location of initial pressure rise on the cone (see Table 8.3), is downstream in the Mach 11 flow than the higher Mach number case. On the other hand, the Mach 13 flow is found to have a relatively colder wall (T_w/T_{aw} = 0.15) than the current test case (T_w/T_{aw} = 0.17). A colder wall with smaller values of T_w/T_{aw} increases the local Reynolds number and hence reduces the separation bubble size. Also, a lower unit Reynolds number in this flow (Table 8.1) compared to the earlier test case tends to increase the size of the separation bubble. The Reynolds number and cold wall effects counteract the trend observed due to the variation in Mach number in the later case, but are found to have a minor effect on the shock/boundary-layer interaction. Overall, the second configuration results in a weaker interaction, in terms of a smaller separation bubble at the corner and a lower peak pressure at reattachment, than the first case.

The computed solution, in terms of the normalized pressure contours, is compared with the experimental schlieren image in Fig. 8.16. The simulation results correspond to the standard and modified k-ω turbulence models. The results obtained using the Spalart-Allmaras turbulence model are almost identical, and therefore not presented. The trends observed in this flow are very similar to those in the higher Mach number case presented earlier. The standard k-ω model suppresses flow separation, leading to a single oblique shock at the cone-flare junction. The solution does not match the experimental flow topology in this region. The shock-unsteadiness correction, by comparison, predicts a recirculation bubble at the corner. The flow topology is identical to that in Fig. 8.13, and it matches the shock structure observed in the schlieren image (Fig. 8.16a). Note that the corrugations in the flare shock are relatively weaker in this flow than the previous case (Fig. 8.8a), possibly due to the reduced strength of the shock/boundary-layer interaction.

The surface pressure computed using the standard k-ω and Spalart-Allmaras turbulence models match the experimental and theoretical values on the cone (see Fig. 8.17a). The attached shock at the corner results in a single pressure jump at s = 0 to reach a uniform pressure on the flare. The computed pressure on the flare is comparable to the experimental measurements. There is a small dip in surface pressure towards the end of the flare, where the expansion fan from the second shock-shock interaction hits the wall.

The shock-unsteadiness correction (see Fig. 8.17b) yields an increase in the pressure at the separation point upstream of the corner. The separation locations for the two turbulence models are almost identical. The separation bubble is marked by a pressure plateau, followed by a further rise in pressure at reattachment. Similar to the earlier case, a local pressure peak is

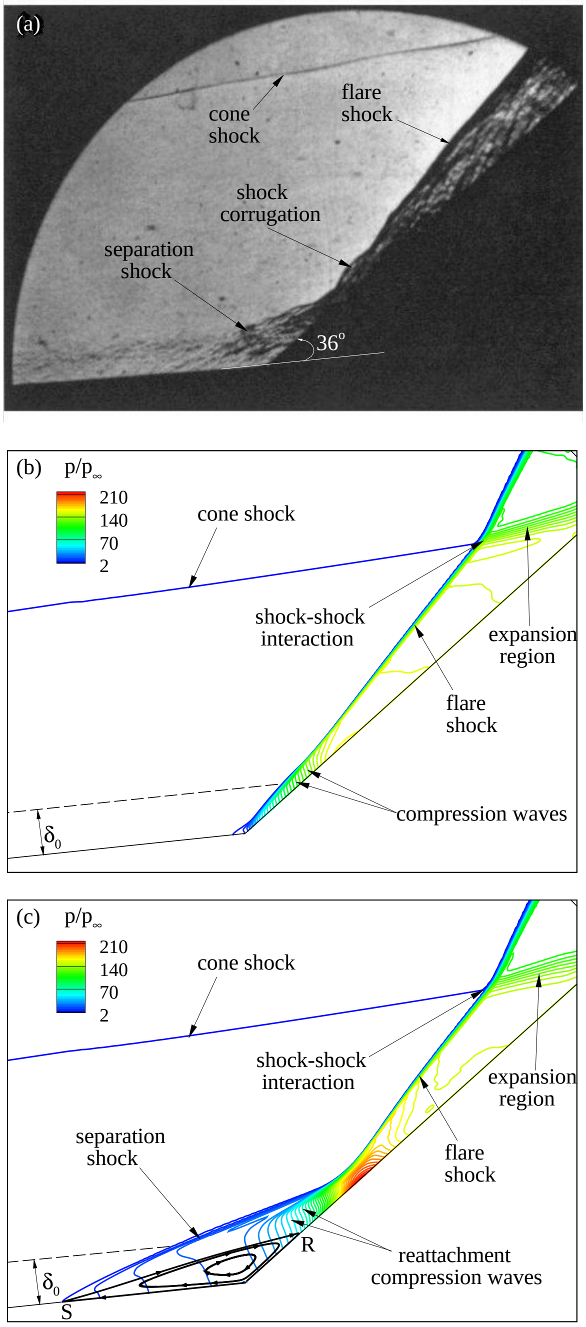

Figure 8.16: Shock-wave/boundary-layer interaction on a 36° flare at Mach 10.97: (a) experimental schlieren image [15], and computed normalized pressure contours using (b) standard k-ω model and (c) shock-unsteadiness modified k-ω model.

observed in the reattachment region due to the interaction between the separation and reattachment shock waves. The separation point identified in terms of the location of initial pressure rise on the cone is listed in Table 8.3. The shock-unsteadiness corrected turbulence models predict a separation point that is upstream of the experimental location. The experimental data also appears to indicate a steeper pressure rise at reattachment. An earlier separation and a later reattachment in the computation yields a larger separation bubble than the experiment. The

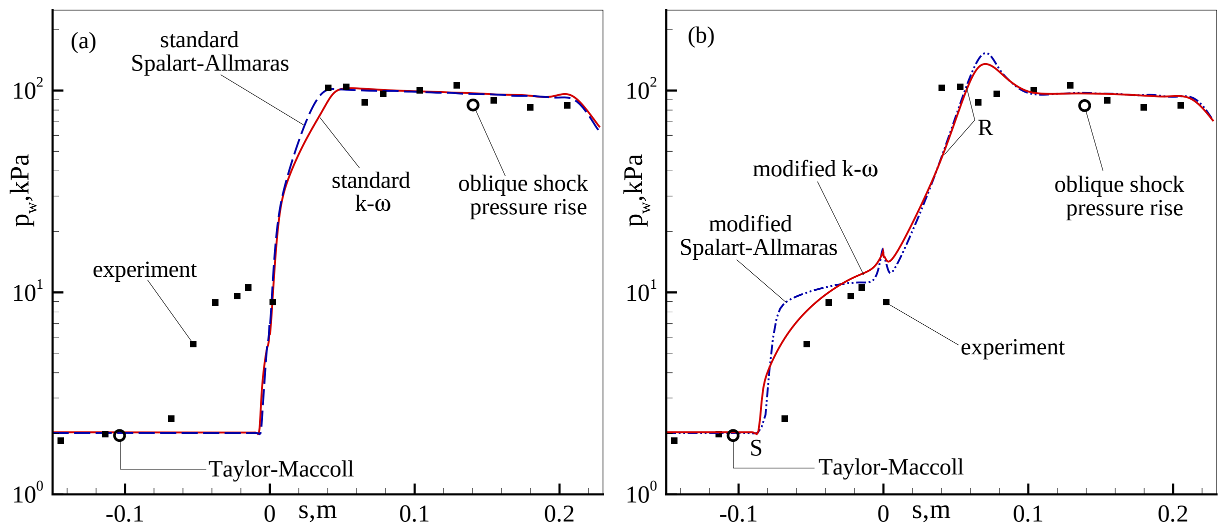

Figure 8.17: Comparison of computed wall pressure using (a) standard and (b) shock-unsteadiness modified turbulence models with experimental measurements [15] for $36°$ flare at Mach 10.97.

simulations, however, reproduce the pressure plateau level in the recirculation region. This indicates that the inclination of the free shear layer enclosing the recirculation bubble is predicted correctly.

The implementation of the shock-unsteadiness correction in this flow follows the same procedure as outlined in the earlier case (Section 8.4.1). The upstream Mach number normal to the shock varies from sonic value near the wall to about 6 at the edge of the boundary layer. The corresponding variation in b_1' is in the range 0 to 0.4. An average value of b_1' = 0.31 is used for this case. This results in the damping of the turbulent kinetic energy at the shock, which promotes flow separation at the cone-flare junction. The parameter c_{b_1}' varies between 0.4 near the wall to -0.79 at the boundary-layer edge. Positive values of c_{b_1}' in the near wall region promotes turbulent eddy viscosity amplification, where as negative values in the outer part of the boundary-layer tends to suppress the turbulence. The overall effect due to average c_{b_1}' = -0.3 is to reduce the turbulence level compared to the standard Spalart-Allmaras model and thus increase the size of the recirculation bubble at the cone-flare junction.

A comparison of the schlieren images in Figs. 8.8a and 8.16a shows that the cone shock is shifted outward at the lower Mach number. A lower post-shock Mach number on the cone in the second case (Table 8.2) also results in a steeper flare shock for the same deflection at the corner. The shock-shock interaction point is therefore shifted outward in the Mach 11 flow than the higher Mach number case. The triple point is placed outside the visualization window at the lower Mach number (Fig. 8.16a), whereas it is located at the top right corner of the visualization window for the Mach 13 case. The numerical solutions show the same effect. The cone shock and the flare shock intersect at x = 0.09 m in the Mach 13 flow (Fig. 8.13c), and the interaction point is shifted downstream to x = 0.11 m for the Mach 11 flow (Fig. 8.16c). Note that there is a negligible effect of flow separation at the cone-flare junction on the location of the flare shock and its interaction with the cone shock. The triple point locations obtained using the standard and modified turbulence models are, therefore, identical in Figs. 8.16b and 8.16c.

It is difficult to make a quantitative comparison of the triple point location between the numerical solutions and the experimental results, due to the lack of scale information for the schlieren images. A qualitative comparison, however, can be made by matching the size with the interaction region in the pressure data and approximate location of the separation shock in the schlieren image. It appears that the cone shock is placed higher in the experiment than the numerical solution. This could be because of the nose bluntness effects. The 6° half-angle cone used in the experiments has a nose radius of 3.8 cm, which is about 1.3% of the model length. The computations neglect this small nose radius and assume a sharp nose for the cone-flare geometry. A rounded nose of the experimental model results in a detached shock at the cone tip, which may be shifted outward compared to the attached shock predicted by computation. The location of the shock-shock interaction will also be moved accordingly, and can explain the discrepancy between the numerical solution and the experimental image. A difference in the location of the cone shock is not expected to alter the post-shock conditions on the cone and the shock/boundary-layer interaction at the cone-flare junction, which is the main focus of the current study.

8.4.3 30° flare at Mach 12.92

The next test case corresponds to the 30° flare at Mach 12.92. The inviscid pressure rise through a single oblique shock at the corner and the corresponding upstream normal Mach number (listed in Table 8.2) are slightly lower than those for the 36° flare at Mach 11. A higher flare angle, but a lower Mach number, in the previous case results in an inviscid shock strength slightly higher than the current flow. The shock/boundary-layer interaction in the current case is, therefore, expected to be slightly weaker than, but comparable to, the interaction on the 36° flare at Mach 10.97. The values of the unit Reynolds number and T_w/T_{aw} for this case (Table 8.1) are in the same range as the earlier test cases, and minor differences in their values

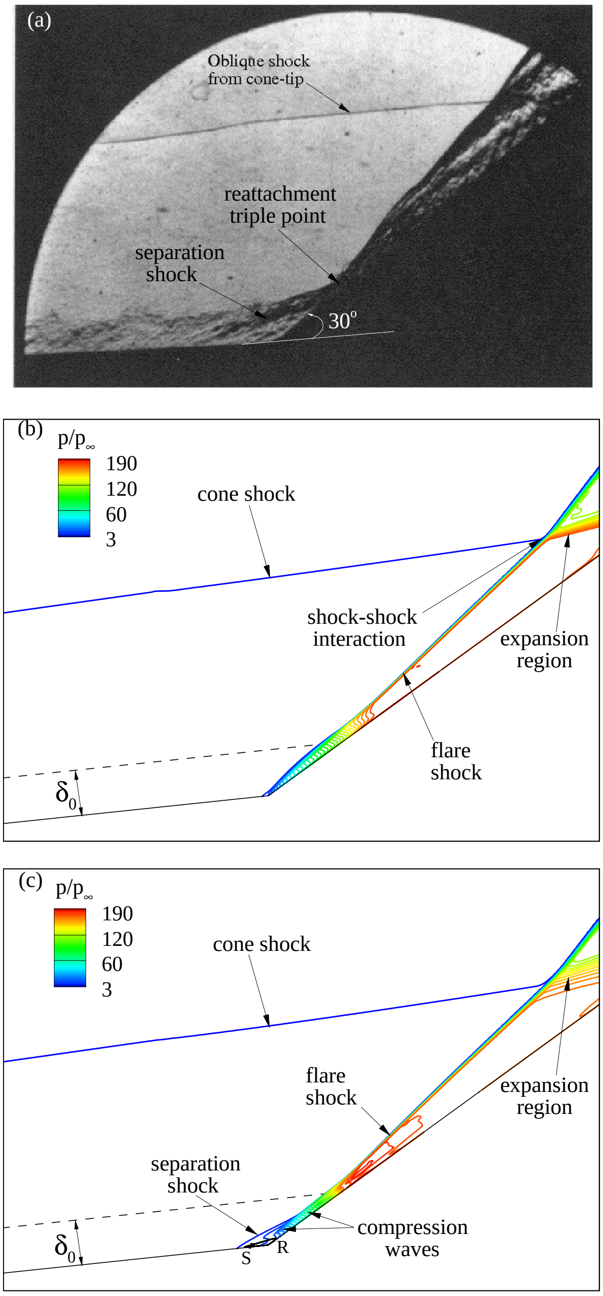

Figure 8.18: Shock-wave/boundary-layer interaction on a 30° flare at Mach 12.92: (a) experimental schlieren image [15], and computed normalized pressure contours using (b) standard k-ω model and (c) modified k-ω model.

may not alter the strength of the shock/boundary-layer interaction dramatically.

The experimental data for this flow shows an interesting pattern. The schlieren image in Fig. 8.18a is similar to that in the earlier cases in terms of the separation shock and the triple point observed at reattachment. However, the pressure data shows no distinct jump at the separation shock location (see Fig. 8.19). There is a gradual, but low, rise in surface pressure closer to the corner. This may be because of large-scale unsteadiness of the corner flow.

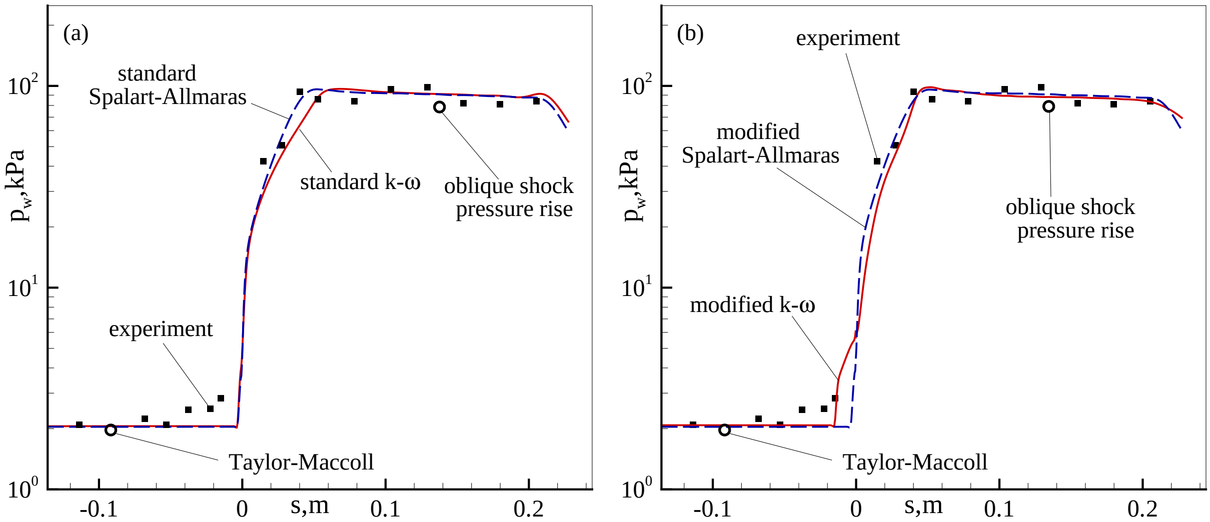

Figure 8.19: Comparison of computed wall pressure using (a) standard and (b) shock-unsteadiness modified Spalart-Allmaras and k-ω turbulence models with experimental measurements [15] for $30°$ flare at Mach 12.92.

The shock/boundary-layer interaction may oscillate between a separated flow similar to that observed in the schlieren image and an attached flow without a recirculation bubble at the corner. The schlieren image is a single time realization of the flow-field, whereas the pressure data is representative of the mean flow and captures the time-averaged effect of any possible separation-bubble unsteadiness.

The RANS simulation yields a time-averaged flowfield solution. The standard Spalart-Allmaras and k-ω turbulence models predict an attached flow up to the corner (Fig. 8.18b), like the earlier cases. The surface pressure, presented in Fig. 8.19a, shows a similar trend. The shock-unsteadiness corrected Spalart-Allmaras model also predicts an attached flow at the junction and a single oblique shock on the flare. The solution is therefore identical to the standard Spalart-Allmaras model. The initial pressure is located slightly upstream of the corner ($s \simeq -0.004$ m) for both the models (see Table 8.3).

The shock-unsteadiness correction in the k-ω model, on the other hand, results in a small region of separated flow (see Fig. 8.18c). A separation shock wave can be seen in the figure, but the reattachment compression waves and their interaction with the separation shock are not clearly discernable because of the small scale of the interaction region. The pressure data obtained using the modified k-ω model (Fig. 8.19b) shows a pressure rise upstream of the corner (at s = -0.015 m). A small pressure plateau and a slight overshoot in the surface pressure at reattachment can also be observed. The pressure variation in the interaction region is similar to that obtained in earlier cases, but is smaller in scale. It does not match the pressure measurements in the separation bubble (-0.04 m $< s <$ 0). The non-uniform variations in the experimental data in this region is probably due to the intermittent nature of the separation bubble. RANS methods, even with shock-unsteadiness correction, do not reproduce such intermittency effects.

8.4.4 30° flare at Mach 10.98

The last test case corresponds to a 30° flare at Mach 10.98. Based on the pressure ratio and M_{1n} values presented in Table 8.2, it is the weakest of all the interactions considered in this work. The experimental schlieren image for this flow (Fig. 8.20a) shows a single oblique shock on the flare, with no indication of the flow separation at the corner. The pressure data on the cone (Fig. 8.21a) is uniform up to the cone-flare junction and is followed by a single pressure jump corresponding to the corner shock. This corroborates the fact that there is no boundary-layer separation in this case. This is reproduced well by both the standard and modified Spalart-Allmaras model computations. The computed density contours (Fig. 8.20b) matches the schlieren image closely. The computed surface pressure also compares very well with the experimental measurements (Fig. 8.21a).

A magnified view of the pressure contours in the corner region (inset in Fig. 8.20b) shows the corner shock more clearly. The oblique shock is slightly curved in the region where there is a gradient in the upstream Mach number due to the incoming boundary layer on the cone. A turning of the low Mach number flow in the near-wall region on to the flare is achieved by a steeper shock compared to the outer part of the boundary layer, where a higher Mach number flow is deflected by the same angle through a more inclined shock wave. There is also a smaller pressure rise in the lower Mach number near-wall region and a higher post-shock pressure as the high Mach number flow is deflected in the outer part of the boundary layer. This variation in the surface pressure can be seen both in the experiment and computation (Fig. 8.21a). There is a sharp increase in pressure at the corner (from 2 to 13 kPa) followed by a gradual build up on the flare up to s = 0.05 m. Beyond this point, the uniform inviscid flow outside of the boundary layer (Mach number = 9.03) is deflected by 30° and the flare pressure is close to the corresponding oblique shock value.

The standard k-ω model solution is identical to the Spalart-Allmaras model result presented in Fig. 8.20b. The shock-unsteadiness corrected k-ω model yields a small separation bubble at the corner. The pressure rise at the separation point located at s = -0.015 m, pres-

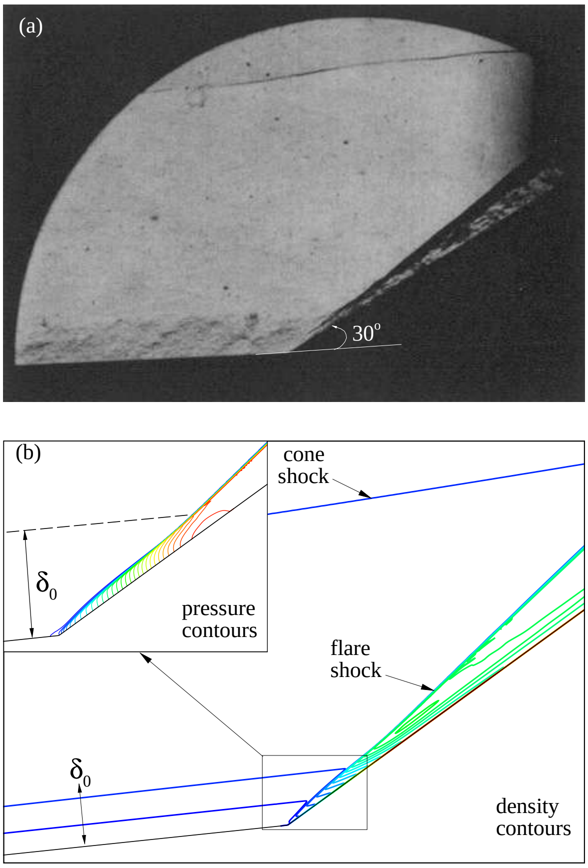

Figure 8.20: Shock/wave boundary-layer interaction on a $30°$ flare at Mach 10.98: (a) experimental schlieren image [15] and (b) computed density and pressure field using standard Spalart-Allmaras model.

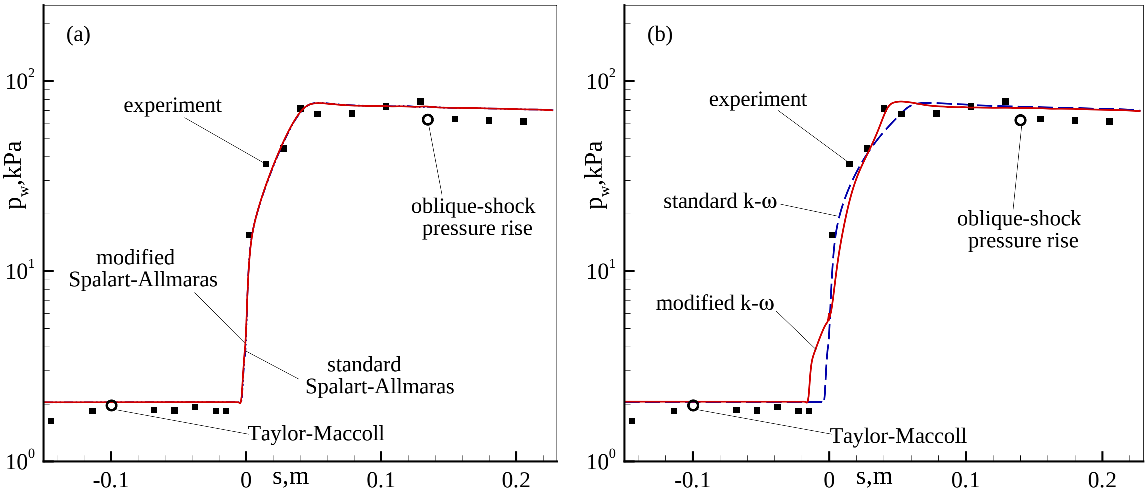

Figure 8.21: Shock-unsteadiness correction [12] applied to (a) Spalart-Allmaras and (b) k-ω turbulence models. Computed wall pressure is compared with experimental measurements [15] for $30°$ flare at Mach 10.98.

sure plateau in the recirculation zone and a small overshoot in pressure at reattachment (see Fig. 8.21b) are similar to the previous case of $30°$ flare at Mach 12.92 (Fig. 8.19b). The shock-structure in the interaction region is also similar to that observed at the higher Mach number (Fig. 8.18c), and is not repeated here. The shock-unsteadiness correction in this flow is applied with an average value of $b_1' = 0.29$. The corresponding value of c_{b_1}' in the modified Spalart-Allmaras simulation is -0.26.

8.4.5 Heat flux predictions

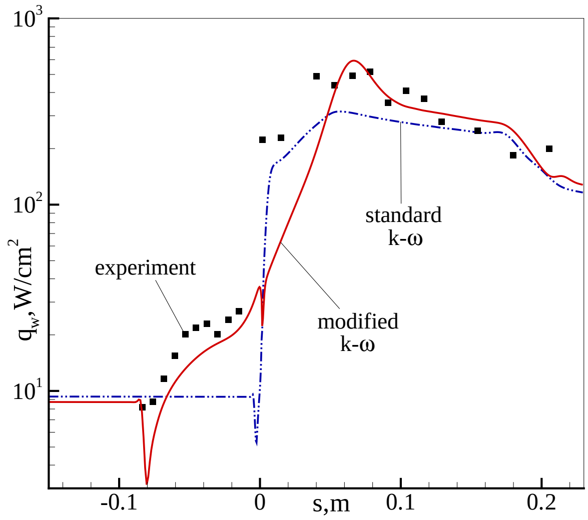

Figure 8.22: Comparison of computed heat flux using standard and shock-unsteadiness modified k-ω turbulence models with experimental measurements [15] for $36°$ flare at Mach 13.1.

Figure 8.22 presents the surface heat flux computed using the standard and modified k-ω turbulence models for the strongest interaction case. The heat flux variation follows a trend similar to that of the corresponding surface pressure data (see Fig. 8.15b). The standard model predicts a sharp rise in heat flux at the corner, whereas the shock-unsteadiness modification results in an elevated heating rate due to flow separation on the cone and a local peak at reattachment. Heat flux prediction is thus closely related to the flow topology, and obtaining the separation bubble at the corner and the shock-shock interaction near reattachment results in significant improvement in heat flux prediction. Nevertheless, there are noticeable differences between the computed and experimental data, and they are discussed below.

The shock-unsteadiness modification applied to the Spalart-Allmaras turbulence model leads to similar trends in heat flux prediction, as in Fig. 8.22. However, the enhancement in heating rate due to flow separation and the peak heating at reattachment are lower than the modified k-ω predictions. Overall, the discrepancies with the experimental measurements are significantly larger than the k-ω model. The heat transfer results for the $36°$ flare at Mach 10.97

are qualitatively similar to that described above. For the remaining two cases with $30°$ flare, there are no major differences between the flow topologies computed using the standard and modified turbulence models (see Sections. 8.4.3 and 8.4.4). The effect of the shock-unsteadiness modification on the surface heat flux is also quite small.

Note that all the computations show a dip in surface heat flux at separation point (for example, at s = -0.086 m in Fig. 8.22) that is not observed in the experimental data. There are additional discrepancies between the measured and computed heating rates on the flare. Standard turbulence models like k-ϵ and k-ω show large error in heat flux predictions in shock-dominated hypersonic flows [6]. The recent k-ω model with stress limiter [8] also exhibits similar trends. As pointed out by Wilcox [8], this limitation is typical of all turbulence models that use Reynolds analogy and model the turbulent heat-flux vector in terms of a turbulent Prandtl number. This is true for the standard and modified turbulence models considered in this paper, and the error margin may be reduced by improving upon the constant turbulent Prandtl number assumption.

8.5 Summary

In this work, the hypersonic shock/turbulent boundary-layer interactions on cone-flare geometries are studied numerically. Four configurations with varying flare angles and freestream Mach numbers are simulated using the Reynolds-averaged Navier-Stokes methodology. The test cases range from strong interactions with large flow separation at the cone-flare junction to weak one with attached flow at the corner.

The standard Spalart-Allmaras and k-ω turbulence models suppress flow separation at the corner, and therefore do not reproduce the correct shock structure in the interaction region. This is probably due to a high level of turbulence predicted at the shock wave. By comparison, the shock-unsteadiness correction damps turbulence amplification at the shock. It reproduces the separation bubble observed experimentally, and matches the surface pressure measurements well. The shock-unsteadiness corrected turbulence models also predict the flow topology in the interaction region, including the Edney Type VI shock-shock interaction at reattachment, correctly. The magnitude of correction decreases with the strength of the shock/boundary-layer interaction, such that it has a negligible effect for weak interactions, where the standard models perform reasonably well.

Chapter 9

Conclusions

Reynolds-averaged Navier-Stokes simulations are used to study shock/turbulent boundary-layer interactions at high Mach number. Standard turbulence models like k-ϵ, k-ω and Spalart-Allmaras often predict incorrect separation bubble for strong shock interaction cases. The shock-unsteadiness correction has been found to show improvement in the separation bubble size and the wall pressure. Earlier, the correction has been restricted to compression corner configurations at supersonic Mach number. In the current research work, the shock-unsteadiness correction is applied to other, more complex configurations at significantly higher Mach numbers. The focus is to predict the separation bubble size accurately. Simulations are performed for a range of Mach numbers and deflection angles for four shock-wave/boundary-layer interaction configurations: (i) two-dimensional oblique shock boundary-layer interaction; (ii) two-dimensional scramjet inlet; (iii) three-dimensional single-fin configuration; and (iv) axisymmetric cone-flare configuration. The flow physics is studied in detail in each case and the computed wall data in the interaction region is compared with the experimental measurements.

In the first case, the impingement and reflection of oblique shock wave on a turbulent boundary layer developed on the flat plate is studied. Three configurations with shock generator angles of 14, 10 and 6 are chosen at Mach 5. The flow in the interaction region is complex due to the presence of multiple shock and expansion waves along with local flow separation and reattachment. The standard Spalart-Allmaras and k-ω models predict smaller separation bubble, a delayed initial pressure rise location and yields too high skin friction at reattachment. The shock-unsteadiness correction dampens the turbulence at the shock, hence moves the separation location much closer to the experiment. This in turn results in close matching of the shock structure, wall pressure and skin friction with the measurements.

Next, a practical scramjet inlet geometry is simulated at Mach 6.5. The cowl shock impingemes on the opposite wall to result in a shock/boundary-layer interaction, which is the focus of work. The flow is similar to the above canonical oblique shock/boundary-layer interaction. However, the geometry of the inlet generates additional shocks and expansion waves and adds complexity to the flowfield. The shock-unsteadiness modified Spalart-Allmaras model is used in the simulations. The model parameter is calibrated against the experimental data for different canonical oblique shock impingement cases. The simulations predict a large separation bubble inside the inlet duct. The computed separation bubble size is validated against available experimental data for canonical flow configurations. The performance parameters of the scramjet inlet are then obtained using the computed flow solution.

Three-dimensional shock/boundary-layer interaction is studied in single-fin configurations at Mach 5 and deflection angles of $23°$, $18°$, $12°$ and $8°$. The inviscid shock generated by the fin interacts with the boundary layer on the adjacent flat plate to form a complex three-dimensional flowfield. The boundary layer separates to form a conical vortex and the inviscid shock bifurcates to form a lambda structure. Peak values of wall pressure and skin friction are observed along the reattachment line near the corner region of plate-fin junction. The standard model predicts delayed initial pressure rise location, and the shock-unsteadiness modification improves the separation point location and matches the wall pressure distribution with the experiments.

Finally, shock/turbulent boundary-layer interactions are numerically studied on cone-flare geometries at high Mach numbers. Four test cases with flare angles of $36°$ and $30°$, and two Mach numbers of 11 and 13 are considered. The high Mach numbers results in stronger shock waves and therefore larger separation bubble compared to supersonic interactions. The shocks are also more inclined to the flare surface. A shock-shock interaction is observed close on the flare and it results in localized peak values of pressures in the reattachment region. These peak pressures are absent in supersonic flows. The standard turbulence models suppress flow separation at the corner, and therefore do not reproduce the correct shock structure in the interaction region. The shock-unsteadiness correction reproduces the separation bubble observed experimentally, and matches the surface pressure measurements well. The shock-unsteadiness corrected turbulence models also predict the flow topology in the interaction region, including the Edney Type VI shock-shock interaction at reattachment, correctly.

Overall, the thesis presents a detailed study of shock/boundary-layer interactions. The physics-based shock-unsteadiness modification of Sinha *et al.* [10] is used to improve the turbulence model predictions. Specifically, the contributions of the thesis are as follows.

1. The shock-unsteadiness modification is shown to improve the prediction of flow separation, pressure distribution and flow topology significantly for different geometries at varying freestream conditions.

2. The implementation of the correction in the presence of multiple intersecting shocks and expansion waves is presented. It is shown that a detailed calculation of the shock-unsteadiness parameter based on the local shock strength is not essential. An average value of the parameter yields comparable results.

3. Application of the shock-unsteadiness correction to predict flow separation in a scramjet intake shows its potential in real-life applications.

In summary, it is found that a robust implementation of the shock-unsteadiness modification yields significant improvement in flow prediction, irrespective of the baseline turbulence model. The improvements are consistent over a range of geometric and flow parameters. The shock-unsteadiness correction, therefore, proves to be useful for simulating shock/turbulent boundary-layer interactions in practical configurations.

Appendix A

Navier-Stokes equations

The instantaneous continuity, momentum and energy equations for compressible flows can be written in tensor notation as,

$$\frac{\partial \rho}{\partial t} + \frac{\partial}{\partial x_i}(\rho u_i) = 0 \tag{A.1}$$

$$\frac{\partial (\rho u_i)}{\partial t} + \frac{\partial}{\partial x_j}(\rho u_j u_i) = -\frac{\partial p}{\partial x_i} + \frac{\partial t_{ij}}{\partial x_j} \tag{A.2}$$

$$\frac{\partial}{\partial t}[\rho(e + \frac{1}{2}u_i u_i)] + \frac{\partial}{\partial x_j}[\rho u_j(h + \frac{1}{2}u_i u_i)] = \frac{\partial}{\partial x_j}(u_i t_{ij}) - \frac{\partial q_j}{\partial x_j} \tag{A.3}$$

Here ρ is the density of fluid, u_i is instantaneous velocity in the i direction $(i = 1, 2, 3)$, p is the pressure and t_{ij} is the viscous shear stress acting on a fluid element, e is specific internal energy, $h = e + p/\rho$ is specific enthalpy and q_j is the scalar heat flux. The left hand side (LHS) of Eqs. A.1, A.2 and A.3 represent the unsteady and convective transport terms. The terms on right hand side (RHS) of Eq. A.2 represent the pressure forces and viscous forces. The first term on RHS of Eq. A.3 gives the work done due to shear stress, where t_{ij} is governed by Newton's law of viscosity as,

$$t_{ij} = 2\mu s_{ij} - \zeta \frac{\partial u_k}{\partial x_k}\delta_{ij} \tag{A.4}$$

where s_{ij} is instantaneous strain rate tensor and ζ is second viscosity. The ζ is related to molecular viscosity μ as $\zeta = -\frac{2}{3}\mu$, where the molecular viscosity μ variation with temperature is calculated from Sutherland's formula [91] of viscosity (for air) as,

$$\mu = \left[\frac{(1.45 \times T^{3/2})}{(T + 110)} \times 10^{-6}\right] \tag{A.5}$$

Here T is temperature in Kelvin and δ is the Kronecker delta function defined as $\delta_{ij} = 1$ if $i = j$ and $\delta_{ij} = 0$ if $i \neq j$. The second term in RHS of Eq. A.3 represents the heat flux due to conduction and is calculated from Fourier's law as,

$$q_j = -\kappa \frac{\partial T}{\partial x_j} = -\frac{\mu}{Pr_L} \frac{\partial h}{\partial x_j} \tag{A.6}$$

where κ is thermal conductivity of fluid and the Prandtl number is given as $Pr_L = C_p \mu/\kappa$.

In many fluid flow cases the intermolecular forces between the molecules is neglected and the fluid is assumed to be perfect gas which satisfy the following equation of state.

$$p = \rho R T \tag{A.7}$$

$$e = C_v T \tag{A.8}$$

$$h = C_p T \tag{A.9}$$

where R is characteristic gas constant, C_v and C_p are the specific heats at constant volume and pressure respectively. The characteristic gas constant can be expressed as ratio of universal gas constant $\overline{R}$, and molecular weight M, of gas as, $R = \overline{R}/M$. The universal gas constant has same value of 8.314 kJ/(kg mol.K) for all gases. The value of R is different for different gases and for air it's value is equal to 287.1 J/K.

References

[1] Ganesh, A. T. K., Thiagarajan V. and Panneerselvam, S. "Improvements in Intake Starting Characterization for a Hypersonic Cruise Vehicle," Chapter 33, Symposium on Applied Aerodynamics and Design of Aerospace Vehicle (SAROD 2009) December 10-12, Bangalore, India, 2009. pp. 336-343.

[2] Horstman, C. C., "Prediction of Hypersonic Shock-Wave/Turbulent Boundary-Layer Flows," AIAA Paper 1987-1367, June 1987.

[3] Huang, P. G., and Coakley, T. J., "Turbulence Modeling for Complex Hypersonic Flows," AIAA Paper 1993-0200, Jan. 1993.

[4] Roy, C. J., and Blottner, F. G., "Review and Assessment of Turbulence Models for Hypersonic Flows," *Progress in Aerospace Sciences*, Vol. 42, Issues 7-8, 2006, pp. 469-530.

[5] Sarkar, S., Erlebacher, G., Hussaini, and Kreiss, H. O., "The Analysis and Modelling of Dilatation Terms in Compressible Turbulence," *Journal of Fluid Mechanics*, Vol. 227, 1991, pp. 473-493.

[6] Coakley, T. J., and Huang, P. G., "Turbulence Modeling for High Speed Flows," AIAA Paper 1992-0436, Jan. 1992.

[7] Catris, S., and Aupoix, A., "Density Corrections for Turbulence Models," *Progress in Aerospace Sciences*, Vol. 4, Issue 1, 2000, pp. 1-11.

[8] Wilcox, D. C., "Formulation of the k-ω Turbulence Model Revisited" *AIAA Journal*, Vol. 46, No. 11, 2008, pp. 2823-2838.

[9] Knight, D., Yan, H., Panaras, A.G., and Zheltovodov, A., "Advances in CFD Prediction of Shock Wave Turbulent Boundary Layer Interactions," *Progress in Aerospace Sciences*, Vol. 39, Issues 2-3, 2003, pp. 121-184.

[10] Sinha, K., Mahesh, K., and Candler, G. V., “Modeling Shock-Unsteadiness in Shock/Turbulence Interaction,” *Physics of Fluids*, Vol. 15, No. 8, 2003, pp. 2290-2297.

[11] Mahesh, K., Lele, S. K., and Moin, P., “The Inuence of Entropy Fluctuations on the Interaction of Turbulence with a Shock Wave,” *Journal of Fluid Mechanics*, Vol. 334, 1997, pp. 353-379.

[12] Sinha, K., Mahesh, K., and Candler, G. V., “Modeling the Effect of Shock-Unsteadiness in Shock/Turbulent Boundary-Layer Interactions,” *AIAA Journal*, Vol. 43, No. 3, 2005, pp. 586-594.

[13] Steger, J. L., and Warming, R. F., “Flux Vector Splitting of the Inviscid Gasdynamic Equations with Application to Finite-Difference Methods,” *Journal of Computational Physics*, Vol. 40, No. 2, 1981, pp. 263-293.

[14] Schulein, E., “Optical Skin Friction Measurements in Short-duration Facilities”, *AIAA Journal*, Vol. 44, No.8, 2006, pp.1732-1742.

[15] Holden, M. S., “Studies of the Mean and Unsteady Structure of Turbulent Boundary-Layer Separation in Hypersonic flow,” AIAA Paper 1991-1778, June 1991.

[16] “Special Course on Shock-Wave/Boundary-Layer Interactions in Supersonic and Hypersonic Flows,” AGARD Advisory Report 792, 1993.

[17] Knight, D. D., and Degrez, G., “Shock Wave Turbulent Boundary Layer Interactions in High Mach Number Flows—A Critical Survey of Current Numerical Prediction Capabilities,” AGARD Advisory Report 319, Vol. 2, Chapter 1, 1998, pp. 1-35.

[18] Dussauge, J. P., Dupont, P., and Debieve, J. F., “Unsteadiness in Shock Wave Boundary-layer Interactions with Separation,” *Progress in Aerospace Sciences*, Vol. 10, Issue 2, 2006, pp. 85-91.

[19] Panaras, A.G., “Review of the Physics of Swept-Shock/Boundary Layer Interactions,” *Progress in Aerospace Sciences*, Vol. 32, Issues 2-3, 1996, pp. 173-244.

[20] Thivet, F., Knight, D. D., Zheltovodov, A. A., and Maksimov, A. I., “Analysis of Observed and Computed Crossing Shock Wave Turbulent Boundary Layer Interactions,” *Progress in Aerospace Sciences*, Vol. 6, Issue 1, 2002, pp. 3-17.

[21] Knight, D., Yan, H., Panaras, A. G., and Zheltovodov, A., "RTO WG 10: CFD Validation for Shock Wave Turbulent Boundary Layer Interactions," AIAA Paper 2002-0437, Jan. 2002.

[22] Holden, M. S., and Wadhams, T. P., "A Database of Aerothermal Measurements in Hypersonic Flow in "Building Block" Experiments for CFD Validation," AIAA Paper 2003-1137, Jan. 2003.

[23] Holden, M. S., "Historical Review of Experimental Studies and Prediction Methods to describe Laminar and Turbulent Shock Wave/Boundary Layer Interactions in Hypersonic Flows," AIAA Paper 2006-494, Jan. 2006.

[24] Delery, J. M., "Shock-Wave/Turbulent Boundary-Layer Interaction and its Control," *Progress in Aerospace Sciences*, Vol. 22, Issue 7, 1985, pp. 209-280.

[25] Arnal, D., and Delery, J. M., "Laminar-Turbulent Transition and Shock-Wave/Boundary-Layer Interaction," RTO-EN-AVT-116, Chapter 4, 2004, pp. 1-46.

[26] Zheltovodov, A. A., Maksimov, A. I., Thivet, F., Knight, D. D., Gaitonde, D. V., and Schmisseur, J. D., "Experimental and Computational Studies of Crossing Shock-Wave/Turbulent Boundary-Layer Interactions," Proceedings of International Conference, RDAMM, Vol. 6, 2001, pp. 153-162.

[27] Zheltovodov, A., "Some Advances in Research of Shock Wave/Boundary Layer Interactions," AIAA Paper 2006-496, Jan. 2006.

[28] Settles, G. S., and Dodson, L. J., "Supersonic and hypersonic Shock/Boundary Layer Interaction Data Base," *AIAA Journal*, Vol. 32, No. 7, 1994, pp. 1337-1383.

[29] Wilcox, D. C., "Supersonic Compression-Corner Applications of a Multiscale Model for Turbulent Flows," *AIAA Journal*, Vol. 28, No. 7, 1990, pp. 1194-1198.

[30] Haidinger, F. A., and Friedrich, R., "Computation of Shock Wave Turbulent Boundary Layer Interactions Using a Two Equation Model with Compressibility Corrections," *Applied Scientific Research*, Vol. 51, Nos. 1-2, 1993, pp. 501-505.

[31] Forsythe, J., Hoffmann, K., and Damevin, H. M., "Several Turbulence Models for Supersonic Compression Ramp Flow," AIAA Paper 98-2648, 1998.

[32] Liou, W. W., Huang, P. G., and Shih, T-H., “Turbulence Model Assessment for Shock Wave Turbulent Boundary Interaction in Transonic and Supersonic Flows,” *Computers and Fluids*, Vol. 29, Issue 3, 2000, pp. 275-299.

[33] Gerolymos, G.A., Sauret, E., and Vallet, I., “Oblique Shock-Wave/Boundary Layer Interaction using Near-Wall Reynolds Stress Models,” *AIAA Journal*, Vol. 42, No. 6, 2004, pp. 1089-1100.

[34] Oliver, A. B., Lillard, R. P., Blaisdell, G. A., and Lyrintzis, A. S., “Effects of Three-Dimensionality in Turbulent Compression Ramp Shock-Boundary Layer Interaction Computations,” AIAA Paper 2008-720, 2008.

[35] Wilcox, D. C., “Reassessment of the Scale-Determining Equation for Advanced Turbulence Models,” *AIAA Journal*, Vol. 26, No. 11, 1988, pp. 1299-1310.

[36] Launder, B. E., and Sharma, B. I., “Application of the Energy Dissipation Model of Turbulence to the Calculation of Flow near a Spinning Disc,” *Letters in Heat and Mass Transfer*, Vol. 1, No. 2, 1974, pp. 131-138.

[37] Wilcox, D. C., “Prediction of Channel and Boundary-Layer Flows with a Low-Reynolds-Number Turbulence model,” *AIAA Journal*, Vol. 20, No. 1, 1982, pp. 33-38.

[38] Wilcox, D. C., “Progress in Hypersonic Turbulence Modeling,” AIAA Paper 91-1785, 1991.

[39] “Hypersonic Experimental and Computational Capability, Improvement and Validation,” AGARD Advisory Report 319, Vol. 1, 1996.

[40] Edney, B. E., “Anomalous Heat Transfer and Pressure Distributions on Blunt Bodies at Hypersonic Speeds in the Presence of an Impinging Shock,” FFA Rept. 115, The Aeronautical Research Institute of Sweden, Stockholm, Feb. 1968.

[41] Kussoy, M. I., and Hostman, C. C., “Documentation of Two- and Three dimensional Hypersonic Shock-Wave/Turbulent Boundary-Layer Interaction Flows,” NASA Report TM 101075, 1989.

[42] Settles, G. S., and Dodson, L. J., “Hypersonic Shock/Boundary layer Interaction database,” NASA Report CR 17757, Vol. 1, 1991.

[43] Coleman, G. T., and Stollery, J. L., "Heat Transfer From Hypersonic Flow at a Wedge of Compression Corner," *Journal of Fluid Mechanics*, Vol. 56, Part 4, 1972, pp. 741-752.

[44] Elfstrom, G. M., "Turbulent hypersonic Flow at a Wedge- Compression Corner," *Journal of Fluid Mechanics*, Vol. 53, Part 1, 1972, pp. 113-127.

[45] Horstman, C. C., "Hypersonic Shock-Wave/Turbulent Boundary Layer Interaction Flows," AIAA Paper 1991-1760, 1991.

[46] Bedarev, I. A., Borisov, A. V., and Fedorova, N. N., "Modeling of Supersonic Turbulent Flows in the Vicinity of Axisymmetric Congurations," *Journal of Applied Mech Tech Physics*, Vol. 43, No. 6, 2002, pp. 861-866.

[47] Holden, M. S., Wadhams, T. P., and MacLean, M., "Experimental Studies in Hypersonic Flows for Facility and Code Validation," AIAA Paper 2007-1304, 2007.

[48] Oliver, A. B., Lillard, R. P., Schwing, A. M., Blaisdell, G. A., and Lyrintzis, A. S., "Assessment of Turbulent Shock-Boundary Layer Interaction Computations Using the OVERFLOW Code," AIAA Paper 2007-104, 2007.

[49] Jones, W. P., and Launder, B. E., "The Prediction of Laminarization with a Two-Equation Model of Turbulence,"*International Journal of Heat Mass Transfer*, Vol. 15, No. 9, 1972, pp. 301-314.

[50] MacLean, M., Wadhams, T., Holden, M., and Johnson, H., "A Computational Analysis of Ground Test Studies of the HIFiRE-1 Transition Experiment," AIAA Paper 2008-0641, 2008.

[51] Reda, D. C., and Murphy, J. D., "Shock Wave/Turbulent Boundary-layer Interaction in Rectangular Channels," *AIAA Journal*, Vol. 11, No. 2, 1973, pp. 139-140.

[52] Bachalo, W. D, Modaress, D., and Johnson, D. A., "Experiments on Transonic and Supersonic Turbulent Boundary Layer Separation," AIAA Paper 77-47, 1977.

[53] Murty, V. S., and Rose, W. C., "Wall Shear Stress Measurements in a Shock-Wave Boundary-Layer Interaction," *AIAA Journal*, Vol. 16, No. 7, 1978, pp. 667-672.

[54] Holden, M. S., "A Study of Flow Separation in Regions of Shock Wave-Boundary Layer Interaction in Hypersonic Flow," AIAA Paper 78-1169, 1978.

[55] Lindbad, I. A. A., Wallin, S., Johanson, A., Freiedrich, R., Lechner, R., Krogmann, P., Schulein, E., Courty, J., Ravachol, M., and Giordano, D., "A Prediction Method for High Speed Turbulent Separated Flows with Experimental Verification," AIAA Paper 98-2547, 1998.

[56] Wilcox, D. C., "Simulation of Transition with a Two-Equation Turbulence Model," *AIAA Journal*, Vol. 32, No. 2, 1994, pp. 247-255.

[57] Kubota, H., and Stollery, J., "An Experimental Study of the Interaction Between a Glancing Shock Wave and a Turbulent Boundary Layer," *Journal of Fluid Mechanics*, Vol. 116, No. 1, 1982, pp. 431-58.

[58] Alvi, F.S., and Settles, G., "Structure of Swept Shock Wave Boundary Layer Interactions using Conical Shadowgraphy," AIAA Paper 1990-1644, 1990.

[59] Kim, K. S., Lee, Y. S., Alvi, F. S., Settles, G. S., and Horstman, C. C., "Laser Skin Friction Measurements and CFD Comparison of Weak to Strong Shock Boundary Layer interaction," AIAA Paper 90-0378, 1990.

[60] Zheltovodov, A. A., "Regimes and Properties of Three Dimensional Separation Flows Initiated by Skewed Compression Shocks," *Journal of Applied Mech Tech Physics*, Vol. 23, No. 3, 1982, pp. 2474-2475.

[61] Knight, D. D., "Numerical Simulation of 3-D Shock-Wave/Turbulent Boundary-Layer Interactions," AGARD Advisory Report 792, Chapter 3, 1993, pp. 1-32.

[62] Doling, D. S., "Unsteady Phenomenon in Shock-Wave/Boundary-Layer Interaction," AGARD Advisory Report 792, Chapter 4, 1993, pp. 1-46.

[63] Settles, G. A., "Swept Shock/Turbulent Boundary-Layer Interactions - Scaling Laws, Flowfield Structure, and Experimental Methods," AGARD Advisory Report 792, Chapter 1, 1993, pp. 1-40.

[64] Degrez, G., "Swept Shock Wave/Laminar Boundary-Layer Interactions, Experimental and Numerical Results," AGARD Advisory Report 792, Chapter 2, 1993, pp. 1-19.

[65] Thivet, F., "Lessons Learned from RANS Simulations of Shock Wave/Boundary Layer Interactions," AIAA Paper 2002-0583, 2002.

[66] Edwards, J. R., and Chandra, S., “Comparison of Eddy Viscosity-Transport Turbulence Models for Three-Dimensional Shock-Separated Flowfields,” *AIAA Journal*, Vol. 34, No. 4, 1996, pp. 756-763.

[67] Zheltovodov, A., Schulein, E., and Yakovlev, E., “Development of Turbulent Boundary Layer under Conditions of Mixed Interaction of Shock and Expansion Waves,” Preprint No. 2883, Institute of Theoretical and Applied Mechanics, USSR Academy of Sciences, Siberian Division, 1983.

[68] Zheltovodov, A., Schulein, E., and Yakovlev, E., “Investigation of Development of Compressible Turbulent Boundary Layer in the Vicinity of Compression/Expansion Corner Combination,” Preprint No. 1397, Institute of Theoretical and Applied Mechanics, USSR Academy of Sciences, Siberian Division, 1983.

[69] Dolling, D. S., and Or, C.T., “Unsteadiness of Shock Wave Structure in Attached and Separated Compression Ramp Flows,” *Experiments in Fluids*, Vol. 3, 1997, pp. 24-32.

[70] Andreopoulos, Y., and Muck K. C., “Some New Aspects of the Shock Wave Boundary Layer Interaction in Compression Ramp Corner,” *Journal of Fluid Mechanics*, Vol. 180, 1987, pp. 405-428.

[71] Beresh, S. J., Clemens, N. T., and Dolling, D. S., “Relationship Between Upstream Turbulent Boundary-Layer Velocity Fluctuations and Separation Shock Unsteadiness,” *AIAA Journal*, Vol. 40, No. 12, 2002, pp. 2412-2422.

[72] Dolling, D. S., “High-speed Turbulent Separated Flows: Consistency of Mathematical Models and Flow Physics,” *AIAA Journal*, Vol. 36, No. 5, 1998, pp. 725-732.

[73] Durbin, P. A., “On the k-ϵ Stagnation Point Anomaly,” *International Journal of Heat and Fluid Flow*, Vol. 17, No. 1, 1996, pp. 89-90.

[74] Thivet, F., Knight, D. D., Zheltovodov, A. A., and Maksimov, A. I., “Insights in Turbulence Modeling for Crossing-shock Wave/Boundary-Layer Interactions,” *AIAA Journal*, Vol. 39, No. 6, 2002, pp. 985-995.

[75] Spalart, P. R., and Allmaras, S. R., “A One-equation Turbulence Model for Aerodynamic Flows,” AIAA Paper 1992-0439, Jan. 1992.

[76] Wilcox, D. C., *Turbulence Modeling for CFD*, DCW Industries, 2^{nd} ed., 2000, pp. 491-492.

[77] Menter, F. R., "Two-Equation Eddy-Viscosity Turbulence Models for Engineering Applications," *AIAA Journal*, Vol. 32, No. 8, 1994, pp. 1598-1605.

[78] Hirsch, C., *Numerical Computation of Internal and External Flows*, Vol. 1 and Vol. 2, John Wiley and Sons, 1991.

[79] Chung, T. J., *Computational Fluid Dynamics*, Cambridge University Press, 2002.

[80] Leveque, R. J., *Finite Volume Methods for Hyperbolic problems*, Cambridge University Press, 2002.

[81] Blazek, J., *Computational Fluid Dynamics: Principles and Applications*, Amsterdam: Elsevier, 2005.

[82] Laney, C. B., *Computational Gas Dynamics*, Cambridge University Press, 1998.

[83] Toro, E. F., *Riemann Solvers and Numerical Methods for Fluid Dynamics: A Practical Introduction*, Cambridge University Press, 1998.

[84] Sinha, K., and Candler, G. V., "Convergence Improvement of Two-equation Turbulence Model Calculations," AIAA Paper 1998-2649, June 1998.

[85] MacCormack, R. W., and Candler, G. V., "The Solution of the Navier-Stokes Equations Using Gauss-Siedel Line Relaxation," *Computers and Fluids*, Vol. 17, Issue 1, 1989, pp. 135-150.

[86] Wright, M. J., Candler, G. V., and Bose, D., "Data-Parallel Line Relaxation Method for the Navier-Stokes Equations," *AIAA Journal*, Vol. 36, No. 9, 1998, pp. 1603-1609.

[87] Wright, M. J., Candler, G. V., and Prampolini, M., "Data-Parallel Lower-Upper Relaxation Method for the Navier-Stokes Equations," *AIAA Journal*, Vol. 34, No. 7, 1996, pp. 1371-1377.

[88] Druguet, M.C., Candler, G,V. and Nompelis, I., "Effect of Numerics on Navier-Stokes Computations of Hypersonic Double-Cone Flows," *AIAA Journal*, Vol. 43, No. 3, 2005, pp. 616-623.

[89] Reddy, D. S. K., and Sinha, K., "Hypersonic Turbulent Flow Simulation of FIRE II Reentry Vehicle Afterbody," *Journal of Spacecraft and Rockets*, Vol. 46, No. 4, 2009, pp. 745-757.

[90] Pasha, A. A., and Sinha, K., "Shock-Unsteadiness Model Applied to Oblique Shock-Wave/Turbulent Boundary-Layer Interaction," *International Journal of Computational Fluid Dynamics*, Vol. 22, No. 8, 2008, pp. 569-582.

[91] Shames, E., *Mechanics of Fluid Flow*, McGraw-Hill, Inc., 4th ed., 2003.

[92] Wright, M., Dinesh., Prabhu, K., Edward., and Martinez, R, "Analysis of Apollo Command Module Afterbody Heating part I: AS-202," *Journal of Thermophysics and Heat Transfer*, Vol. 20, No. 1, 2006, pp. 16-30.

[93] Mahesh, K., Moin, P., and Lele, S. K., "The Interaction of a Shock Wave with a Turbulent Shear Flow," Report TF-69, Thermosciences Division, Mechanical Engineering Department, Stanford University, 1996.

[94] Ribner, H. S., "Convection of a Pattern of Vorticity through a Shock Wave," NACA TN 2864, 1953.

[95] Fabre, D., and Jacquin, L., "Linear Interaction of a Cylindrical Entropy Spot with a Shock," *Physics of Fluids*, Vol. 13, No. 8, 2001, pp. 2403-2422.

[96] Wouchuk, J. G., Ruiz de Lira, C. H., and Velikovich, A. L., "Analytical Linear Theory for the Interaction of a Planar Shock Wave with an Isotropic Turbulent Vorticity Field," *Physical Review*, Vol. 79, No. 066315, 2010, pp. 1-35.

[97] Hannappel, R., and Friedrich, R., "Direct Numerical Simulation of a Mach 2 Shock Interacting with Isotropic Turbulence," *Applied Sciences Research*, Vol. 54, 1995, pp. 205-221.

[98] Jamme, S., Cazalbou, J. B., Torres, F., and Chassaing, P., "Direct Numerical Simulation of the Interaction between a Shock Wave and Various Types of Isotropic Turbulence," *Turbulence and Combustion*, Vol. 68, 2000, pp. 227-268.

[99] Larssona, J., and Lele, S. K., "Direct Numerical Simulation of Canonical Shock/Turbulence Interaction," *Physics of Fluids*, Vol. 21, 2009, pp. 126101-1-12.

[100] Smits, A. J., and Muck, K. C., “Experimental Study of Three Shock Wave/Turbulent Boundary Layer Interactions,” *Journal of Fluid Mechanics*, Vol. 182, 1987, pp. 294-314.

[101] Fedorova, N. N., and Fedorchenko, I. A., “Computations of Interaction of Incident Oblique Shock Wave with a Turbulent Boundary Layer on a Flat Plate, ” *Journal of Applied Mechanics and Technical Physics*, Vol. 45, No. 3, 2004, pp. 358-366.

[102] Xiao, X., Hassan, H. A., Edwards, J. R., and Gaffney Jr. R.L., “Role of Turbulent Prandtl Numbers on Heat Flux at Hypersonic Mach Numbers,” *AIAA Journal*, Vol. 45, No. 4, 2007, pp. 806-813.

[103] Gridgen Version 15.16, “http://www.pointwise.com/gridgen,” 2011.

[104] Van Wie, D. M., “Scramjet Inlets, Scramjet Propulsion, edited by E. T. Curran and S. N. B. Murthy,” *Progress in Astronautics and Aeronautics*, 2000, pp. 447511.

[105] Gaitonde, D. V., Visbal, M. R., Shang J., Zheldovodov, A., and Maksimov, A., “Sidewall Interaction in an Asymmetric Simulated Scramjet Inlet Configuration,” *Journal of Propulsion and Power*, Vol. 17, No. 3, 2001, pp. 579-584.

[106] Alvi, F.S., and Settles, G., “Physical Model of the Swept Shock Wave/Boundary-Layer Interaction Flowfield,” *AIAA Journal*, Vol. 30, No. 9, 1992, pp. 2252-2258.

[107] Sinha, K. “Shock-Unsteadiness Model Applied to Hypersonic Shock-Wave/Turbulent Boundary-Layer Interactions,” AIAA Paper 2006-0126, 2006.

[108] Anderson Jr., J. D., *Modern Compressible Flow: With Historical Perspective*, McGraw-Hill, Inc., 3rd ed., 2003, pp. 366-371.

List of publications based on present work

Refereed Journals

1. **Amjad Ali Pasha**, Krishnendu Sinha, "Shock-unsteadiness model applied to hypersonic shock-wave/turbulent boundary-layer interactions" *Journal of Propulsion and Power*, 2010 (under review).

2. **Amjad Ali Pasha**, Krishnendu Sinha, "Shock-unsteadiness model applied to oblique shock wave/turbulent boundary-layer interaction" *International Journal of Computational Fluid Dynamics*, Volume 22, Issue 8, 569-582, September 2008.

Conference Proceedings

1. **Amjad Ali Pasha**, C. Vadivelan, Krishnendu Sinha, "Simulation of a practical scramjet inlet using shock-unsteadiness model" 28^{th} International Symposium on Shock Waves, The University of Manchester, United Kingdom, 17-22 July 2011 (accepted for oral presentation).

2. **Amjad Ali Pasha**, Krishnendu Sinha, "Simulation of hypersonic shock/turbulent boundary-layer interactions using advanced turbulence models" *In Proceedings of the* 8^{th} *Asian Computational Fluid Dynamics Conference*, Hong Kong, China, 10-14 January 2010.

3. **Amjad Ali Pasha**, Krishnendu Sinha, "Simulation of three-dimensional shock/boundary-layer interaction in a single-fin configuration" *In Proceedings of* 11^{th} *Annual AeSI Computational Fluid Dynamics Symposium*, IISc., Bangalore, India, Aug. 11-12, 2009.

4. **Amjad Ali Pasha**, Krishnendu Sinha, "Shock-unsteadiness modification applied to oblique shock wave/turbulent boundary-layer interaction" *In Proceedings of* 34^{th} *conference on Fluid Mechanics and Fluid Power*, BITS, Ranchi, Dec.10-12, 2007.

Acknowledgments

I take this opportunity to express my deep sense of gratitude to my guide **Prof. Krishnendu Sinha**. I would like to convey my sincere thanks to him for his consistent help, valuable guidance, scholarly encouragement, selflessness time investment and thought provoking discussions which inspired me to make this report fruitful.

I am also grateful to my research progress committee members Prof. A. W. Date, Prof. A. G. Marathe, Prof. A. Chatterjee, Prof. Viren Menezes, Prof. Atul Sharma and Prof. K. Sudhakar for their valuable suggestions.

I would like to express my sincere thanks to all my colleagues and friends for their valuable help. Lastly, I would like to express my deepest sense of gratitude to my family members, especially my parents and elder brother, who motivated me and provided their moral support and encouragement during my career.

Date: ____________________ Amjad Ali Pasha